1998

Collision-induced dissociation reactions and pulsed field ionization photoelectron studies

Stephanie Lynn Stimson
Iowa State University

INFORMATION TO USERS

This manuscript has been reproduced from the microfilm master. UMI films the text directly from the original or copy submitted. Thus, some thesis and dissertation copies are in typewriter face, while others may be from any type of computer printer.

The quality of this reproduction is dependent upon the quality of the copy submitted. Broken or indistinct print, colored or poor quality illustrations and photographs, print bleedthrough, substandard margins, and improper alignment can adversely affect reproduction.

In the unlikely event that the author did not send UMI a complete manuscript and there are missing pages, these will be noted. Also, if unauthorized copyright material had to be removed, a note will indicate the deletion.

Oversize materials (e.g., maps, drawings, charts) are reproduced by sectioning the original, beginning at the upper left-hand corner and continuing from left to right in equal sections with small overlaps. Each original is also photographed in one exposure and is included in reduced form at the back of the book.

Photographs included in the original manuscript have been reproduced xerographically in this copy. Higher quality 6" x 9" black and white photographic prints are available for any photographs or illustrations appearing in this copy for an additional charge. Contact UMI directly to order.

UMI

A Bell & Howell Information Company
300 North Zeeb Road, Ann Arbor MI 48106-1346 USA
313/761-4700 800/521-0600

Collision-induced dissociation reactions and pulsed field ionization photoelectron studies

by

Stephanie Lynn Stimson

A dissertation submitted to the graduate faculty

in partial fulfillment of the requirements for the degree of

DOCTOR OF PHILOSOPHY

Major: Physical Chemistry

Major Professor: Cheuk-Yiu Ng

Iowa State University

Ames, Iowa

1998

Graduate College
Iowa State University

This is to certify that the Doctoral dissertation of

Stephanie Lynn Stimson

has met the dissertation requirements of Iowa State University

Signature was redacted for privacy.

Major Professor

Signature was redacted for privacy.

For the Major Program

Signature was redacted for privacy.

For the Graduate College

To my beloved Mother, family, and friends

TABLE OF CONTENTS

GENERAL INTRODUCTION

Dissertation Organization

This dissertation is composed of four papers formatted for journal publication. Each paper contains an abstract, introduction, experiment, results and discussion, and conclusion section. The experimental conditions for each experiment are reported within each separate paper and only pertain to that paper. In addition, references, tables, and figures within each paper also pertain only to that individual paper. Following the last paper is a general conclusion.

Introduction

The first paper contains the collision-induced dissociation (CID) study of the methanethiol cation $CH_3SH^+(1^2A'')$ with Ar. This experiment was performed on a triple-quadrupole double-octopole photoionization apparatus located at Iowa State University. As an important atmospheric pollutant emitted from combustion, industrial, and oceanic sources,[1-8] the photochemistry of CH_3SH has recently received a great deal of experimental and theoretical attention.[9] Being the simplest alkyl mercapton cation, the structure, energetics, and dissociation dynamics of CH_3SH^+ have also been the focus of many theoretical[10-12] and experimental[13-24] efforts. The dissociation dynamics of CH_3SH^+, which addresses the fundamental question of hydrogen scrambling, has been investigated previously by charge exchange,[21] mass spectrometry,[13,17,19,20] and photoelectron-photoion coincidence (PEPICO)[22] techniques. In a similar energy range above the ground state of CH_3SH^+, the major product ions observed in the charge exchange and photoionization studies are in agreement. The products include CH_2SH^+ (CH_3S^+), CH_2S^+, HCS^+, HS^+, and CH_3^+.[19-22]

In this study the absolute total cross sections for the product ions CH_2SH^+ (CH_3S^+), CH_2S^+, HCS^+, HS^+, CH_3^+, and CH_2^+ produced by CID were measured. The relative yields for the product ions formed in the CID reaction, which strongly favor the C-S bond scission process leading to the formation of $CH_3^+ + SH$, are significantly different from those measured in previous photoionization and charge exchange studies. Since the $CH_3^+ + SH$ channel is not among the most stable product channels, this observation shows that the collision-induced dissociation of CH_3SH^+ is non-statistical. The high yield for $CH_3^+ + SH$ observed in CID is attributed to the more efficient translational to vibrational energy transfer for the C-S stretch than for C-H stretches of CH_3SH^+, and to weak couplings between the low frequency C-S and high frequency C-H stretching vibrational modes of CH_3SH^+. The differences in excitation mechanisms for CH_3SH^+ via collision activation, photoionization, and charge exchange are responsible for the different fragment ion distributions from CH_3SH^+ observed in these experiments.

The second, third, and fourth papers contain the vacuum ultraviolet pulsed field ionization photoelectron (VUV-PFI-PE) spectroscopy studies of OCS ($X^1\Sigma^+$), H_2 ($X^1\Sigma_g^+$), and HD ($X^1\Sigma^+$) respectively. These experiments were performed on the Chemical Dynamics Beamline at the Advanced Light Source (ALS) at Lawrence Berkeley National Laboratory.

Recently, we have developed a high resolution monochromatic vacuum ultraviolet undulator synchrotron radiation source associated with the Chemical Dynamics Beamline at the ALS with a tunable energy range from 5 to 27 eV.[28,29] An experimental scheme for PFI-PE detection using a multibunch synchrotron source has also been implemented.[30-33] The PFI-PE technique provides a means for spectroscopic and energetic characterization of gaseous ionic species. As demonstrated in recent PFI-PE experiments[31-33] on Ne, Ar, Kr, and O_2, the photoelectron energy resolution achieved was 3-6 cm^{-1} (FWHM). This is comparable to the resolution obtained in VUV laser studies.[24,25,27] Although VUV laser radiation with useful intensities can in principle be generated up to ≈17.7 eV, the processes involved remain inefficient for routine experimentation[24-27] compared with the ease in tuning VUV synchrotron radiation.

Carbonyl sulfide (OCS) is a linear molecule with the dominant ground state electronic configuration[34] $...(6\sigma)^2\ (7\sigma)^2\ (8\sigma)^2\ (9\sigma)^2\ (2\pi)^4\ (3\pi)^4\ \ X^1\Sigma^+$. Taking into account the spin-orbit interaction, the removal of an electron from the highest occupied 3π-orbital (mostly having the sulfur 3p character)[34] results in the formation of the $OCS^+(X^2\Pi_{3/2,1/2})$ spin-orbit states. The OCS^+ cation has been investigated previously by many experimental techniques, including dispersed fluorescence,[35-40] laser-induced fluorescence,[41] photodissociation,[42] photoionization,[43,44] and HeI[45-48] and threshold photoelectron (TPE) spectroscopy.[44,49] High resolution spectroscopic data for the $OCS^+(X^2\Pi_{3/2,1/2})$ states have been obtained recently by laser ion photodissociation techniques.[50]

The VUV-PFI-PE bands of $OCS^+(X^2\Pi)$ in the energy region of 11.09-11.87 eV were measured using the high-resolution monochromatic synchrotron radiation of the Chemical Dynamics Beamline at the ALS. The ionization energies (IEs) for the formation of the (0,0,0) $X^2\Pi_{3/2}$ and (0,0,0) $^2\Pi_{1/2}$ states of OCS^+ were determined to be 11.1831±0.0005 eV and 11.2286±0.0005 eV, respectively, yielding a value of 367±1.2 cm^{-1} for the spin-orbit splitting.

C. Destandau, G. Chambaud, and P. Rosmus from the Theoretical Chemistry Group at the Université de Marne-la-Vallée in France used the internally contracted multi-reference configuration interaction approach to generate three-dimensional potential energy functions (PEFs) for the $OCS^+(X^2\Pi)$ state which were then used in variational Renner-Teller calculations of the vibronic states. The energies of all

vibronic states (J=P) for J = 1/2, 3/2, 5/2, and 7/2 were computed in the energy range of ≈4000 cm^{-1} above the IE[$OCS^+(X^2\Pi_{3/2})$] for the assignment of the experimental spectrum.

Being the simplest neutral and cationic molecular system, the potential energy surfaces and spectroscopic constants for H_2 and H_2^+ and their isotopes in their ground and excited rovibronic states have been calculated with high accuracy.[51-60] Reliable and extensive predictions for the bound rovibronic energies of H_2^+ and HD^+ have been obtained at different levels of theory.[52-55]

The rotationally resolved PFI-PE spectra of H_2 and HD at a resolution of ≈7 cm^{-1} FWHM (full-width-half-maximum) in the photon energy range of 15.30-18.11 eV were obtained. The rotational transitions for the $H_2^+(X^2\Sigma_g^+, v^+ = 0\text{-}18)$ and the $HD^+(X^2\Sigma^+, v^+ = 0\text{-}21)$ vibronic bands were assigned and then simulated using the Buckingham-Orr-Sichel (BOS) model. From the experimental data, $\Delta G(v^+ + 1/2)$, B_{v^+}, and D_{v^+} were determined and used to calculate the ionic vibrational and rotational constants (ω_e, $\omega_e x_e$, $\omega_e y_e$, $\omega_e z_e$, B_e, and α_e), the internuclear separation (r_e), and the dissociation energy (D_0).

References

1. S. W. Benson, *Chem. Rev.* **78**, 23 (1978).
2. A. Levy, E. L. Merryman, W. T. Reid, *Environ. Sci. Technol.* **4**, 653 (1970).
3. C. F. Cullis, M. F. R. Mulcahy, *Combust. Flame* **18**, 225 (1975).
4. S. Hatakeyama, H. Akimoto, *J. Phys. Chem.* **87**, 2387 (1983).
5. A. A. Turnipseed, S. B. Barone, A. R. Ravishankara, *J. Phys. Chem.* **97**, 5926 (1993).
6. T. S. Bates, B. K. Lamb, A. Guenther, J. Dignon, and R. E. Stroiber, *J. Atmos. Chem.* **14**, 315 (1992).
7. P. A. Spiro, D. J. Jacob, and J. A. Logan, *J. Geophys. Res.* **97**, 6023 (1992).
8. R. J. Charlson and T. M. L. Wigley, *Sci. Am.* **270**, No. 2, 48 (1994).
9. C. Y. Ng, Advances in Photochemistry, **22**, 1 (1997); and references therein.
10. S.-W. Chiu, W.-K. Li, W.-B. Tzeng, and C. Y. Ng, *J. Chem. Phys.* **97**, 6557 (1992).
11. R. H. Nobes, W. J. Bouma, L. Radom, *J. Am. Chem. Soc.* **106**, 2774 (1984).
12. L. A. Curtiss, R. H.Nobes, J. A. Pople, and L. Radom, *J. Chem. Phys.* **97**, 6766 (1992).
13. D. Amos, R. G. Gills, J. L. Occolowitz, and J. F. Pisani, *Org. Mass Spectr.* **2**, 209 (1969).
14. B. G. Keyes and A. G. Harrison, J. Am. Chem. Soc. **90**, 5671 (1968); A. G. Harrison, *J. Am. Chem. Soc.* **100**, 4911 (1978).
15. D. C. Frost, F. G. Herring, A. Katrib, C. A. McDowell, and R. A. N. McLean, *J. Phys. Chem.* **76**, 1030 (1972).
16. S. Cradock and P. A. Whiteford, *J. Chem. Soc. Faraday II*, **68**, 281 (1972).

17. J. L. Holmes, F. P. Lossing, J. K. Terlouw, and P. C. Burgers, *J. Am. Chem. Soc.* **104**, 2931 (1982); J. K. Terlouw, W. Heerma, G. Dijkstra, J. L. Holmes, and P. C. Burgers, *Int. J. Mass Spectrom. Ion Phys.* **47**, 147 (1983); J. L. Holmes, F. P. Lossing, J. K. Terlouw, and P. C. Burges, *Can. J. Chem.* **61**, 2305 (1983).

18. "Handbook of Helium I Photoelectron Spectra of Fundamental Organic Molecules", edited by K. Kimura, S. Katsumata, Y. Achiba, T. Yamazaki, and S. Iwata (Halsted, New York, 1981).

19. M. E. Akopyan, Y. L. Serhiev, and F. I. Vilesov, *Klim. Vys. Energy* **4**, 305 (1970).

20. R. E. Kutina, A. K. Edwards, J. Berkowitz, *J. Chem. Phys.* **77**, 5508 (1982).

21. B.-Ö. Jonsson and J. Lind, *J. Chem. Soc. Faraday Trans. II* **70**, 1399 (1974).

22. S. Nourbakhsh, K. Norwood, H.-M. Yin, C.-L. Liao, and C. Y. Ng, *J. Chem. Phys.* **95**, 945 (1991).

23. Y.-S. Cheung, C.-W. Hsu, J.-C. Huang, W.-K. Li, and S.-W. Chiu, *Int. J. Mass. Spectrom. Ion Proc.* **159**, 13 (1996).

24. C. Y. Ng, in "The Structure, Energetics, and Dynamics of Organic Ions", edited by T. Baer, C. Y. Ng, and I. Powis, Wiley Series in Ion Chemistry and Physics (Wiley, Chichester, 1996), Chap. 2, p. 35; and references therein.

25. F. Merkt and T. P. Softley, in "High Resolution Laser Photoionization and Photoelectron Studies", edited by I. Powis, T. Baer, and C. Y. Ng, *Wiley Series in Ion Chem. and Phys.* (Wiley, Chichester, 1995), p. 119.

26. J. W. Hepburn, in "Vacuum Ultraviolet Photoionization and Photodissociation of Molecules and Clusters", edited by C. Y. Ng (World Scientific, Singapore, 1991), p. 435.

27. J. W. Hepburn, in "Laser Techniques in Chemistry", edited by A. Meyers and T. R. Rizzo (Wiley, New York, 1994).

28. C.-W. Hsu, M. Evans, P. Heimann, K. T. Lu, and C. Y. Ng, *J. Chem. Phys.* **105**, 3950 (1996).

29. P. Heimann, M. Koike, C.-W. Hsu, M. Evans, K. T. Lu, C. Y. Ng, A. Suits, and Y. T. Lee, *Rev. Sci. Instrum.*, **68**, 1945 (1997).

30. M. Evans, C. Y. Ng, C.-W. Hsu, and P. Heimann, *J. Chem. Phys.* **106**, 978 (1997).

31. C.-W. Hsu, M. Evans, P. A. Heimann, and C. Y. Ng, *Rev. Sci. Instrum.*, **68**, 1694 (1997).

32. C.-W. Hsu, P. A. Heimann, M. Evans, S. Stimson, T. Fenn, and C. Y. Ng, *J. Chem. Phys.* **106**, 8931 (1997).

33. C.-W. Hsu, P. A. Heimann, M. Evans, S. Stimson, and C. Y. Ng, *Chem. Phys.*, accepted.

34. M.-J. Hubin-Franskin, J. Delwiche, P.-M. Guyon, M. Richard-Viard, M. Lavollée, O. Dutuit, J.-M. Robbe, and J.-P. Flament, *Chem. Phys.* **209**, 143 (1996).

35. M. Horani, S. Leach, and J. Rostas, *J. Chim. Phys.* **63**, 1015 (1966).
36. J. P. Maier and F. Thommen, *Chem. Phys.* **51**, 319 (1980).
37. D. L. Judge and M. Ogawa, *J. Chem. Phys.* **51**, 2035 (1969).
38. D. L. Judge and L. C. Lee, *Int. J. Mass Spectrom. Ion Proc.* **17**, 329 (1975).
39. C. Y. R. Wu, T. S. Yih, and D. L. Judge, *Int. J. Mass Spectrom. Ion Proc.* **68**, 303 (1986).
40. M. Tsuji and J. P. Maier, *Chem. Phys. Lett.* **137**, 421 (1987).
41. M. Ochsner, M. Tsuji, and J. P. Maier, *Chem. Phys. Lett.* **115**, 373 (1985).
42. R. Kakoschke, U. Boesl, J. Herman, and E. W. Schlag, *Chem. Phys. Lett.* **119**, 467 (1985).
43. Y. Ono, E. A. Osuch and C. Y. Ng, *J. Chem. Phys.* **74**, 1645 (1981).
44. J. Delwiche, M. J. Hubin-Franskin, G. Caprace, P. Natalis, and D. Roy, *J. Electron Spectrosc. Relat. Phenom.* **21**, 205 (1980).
45. C. R. Brundle and D. W. Turner, *Int. J. Mass Spectrom. Ion Phys.* **2**, 195 (1969).
46. A. W. Potts and G. H. Fattahallah, *J. Phys.* **B13**, 2545 (1980).
47. B. Kovac, *J. Chem. Phys.* **78**, 1684 (1983).
48. L.-S. Wang, J. E. Reutt, Y. T. Lee, and D. A. Shirley, *J. Electron Spectrosc. Relat. Phenom.* **47**, 167 (1988).
49. R. Frey, B. Gotchev, W. B. Peatman, H. Pollak, and E. W. Schlag, *Int. J. Mass Spectrom. Ion Phys.* **26**, 137 (1978).
50. R. Weinhauf and U. Boesl, *J. Chem. Phys.* **101**, 8482 (1994).
51. K. P. Huber and G. Herzberg, "Molecular Spectra and Molecular Structure, Vol. IV, Constants of Diatomic Molecules" (Van Nostrand, New York, 1979).
52. G. Hunter, A. W. Yau, and H. O. Pritchard, *At. Data Nucl. Data Tables* **14**, 11 (1974).
53. C. L. Beckel, B. D. Hansen, and J. M. Peek, *J. Chem. Phys.* **53**, 3681 (1970).
54. G. Hunter and H. O. Pritchard, *J. Chem. Phys.* **46**, 2153 (1967).
55. L. Wolniewicz and J. D. Poll, *Mol. Phys.*, **59**, 953-964, (1986).
56. D. M. Bishop and L. M. Cheung, *Phys. Rev.* A**16**, 640 (1977)
57. D. M. Bishop, *Mol. Phys.* **28**, 1397 (1974).
58. D. M. Bishop and L. M. Cheung, *J. Chem. Phys.* **75**, 3155 (1981).
59. P. M. Dehmer and W. A. Chupka, *J. Chem. Phys.* **65**, 2243 (1976).
60. P. M. Dehmer and W. A. Chupka, *J. Chem. Phys.* **79**, 1569 (1983).

A STUDY OF THE DISSOCIATION OF CH_3SH^+ BY COLLISIONAL ACTIVATION: OBSERVATION OF NON-STATISTICAL BEHAVIOR*

A paper accepted by The Journal of Physical Chemistry

P. T. Fenn,[1] S. Stimson,[1] Y.-J. Chen,[1] and C. Y. Ng[1,2]

Abstract

We have measured the absolute total cross sections for $CH_2SH^+(CH_3S^+)$, CH_2S^+, HCS^+, HS^+, CH_3^+, and CH_2^+ produced by the collision-induced dissociation (CID) reaction of $CH_3SH^+(1^2A'') + Ar$ in the center-of-mass collision energy range of 1-36 eV. While the onset for CH_3^+ is consistent with the thermochemical threshold for the formation of $CH_3^+ + SH$, the onsets for other product ions are higher than their corresponding thermochemical thresholds. Using the charge transfer probing technique, we concluded that the m/e = 47 amu ions observed in the CID reaction have mostly the CH_2SH^+ structure. The relative yields for CH_2SH^+, CH_2S^+, HCS^+, HS^+, CH_3^+, and CH_2^+ formed in the CID reaction, which strongly favor the C-S bond scission process leading to the formation of $CH_3^+ + SH$, are significantly different from those measured in previous photoionization and charge exchange studies. Since the $CH_3^+ + SH$ channel is not among the most stable product channels, this observation shows that the collision-induced dissociation of CH_3SH^+ is non-statistical. The high yield for $CH_3^+ + SH$ observed in CID is attributed to the more efficient translational to vibrational energy transfer for the C-S stretch than for C-H stretches of CH_3SH^+, and to weak couplings between the low frequency C-S and high frequency C-H stretching vibrational modes of CH_3SH^+. The differences in excitation mechanisms for CH_3SH^+ via collision activation, photoionization, and charge exchange are responsible for the different fragment ion distributions from CH_3SH^+ observed in these experiments.

---

* Dedicated to Prof. Yuan T. Lee on the occasion of his 60th Birthday.

[1] Ames Laboratory, USDOE and Department of Chemistry, Iowa State University, Ames, IA 50011, USA.

[2] Author to whom correspondence should be addressed. E-mail addresses:
CYN: <CYNG@Ameslab.gov>.

Introduction

As an important atmospheric pollutant emitted from combustion, industrial, and oceanic sources,[1-8] the photochemistry of methylmercapton (CH_3SH) has recently received a great deal of experimental and theoretical attention.[9] Being the simplest alkyl mercapton cation, the structure, energetics, and dissociation dynamics of CH_3SH^+ have also been the focus of many theoretical[10-12] and experimental[13-24] efforts. The dissociation dynamics of CH_3SH^+, which addresses the fundamental question of hydrogen scrambling, has been investigated previously by charge exchange,[21] mass spectrometry,[13,17,19,20] and photoelectron-photoion coincidence (PEPICO)[22] techniques. In a similar energy range above the ground state of CH_3SH^+, the major product ions observed in the charge exchange and photoionization studies are in agreement, including CH_2SH^+ (CH_3S^+), CH_2S^+, HCS^+, HS^+, and CH_3^+.[19-22]

The *ab initio* potential-energy profile for the rearrangement and fragmentation reactions involving CH_3SH^+ has been calculated.[11] The dissociation mechanisms are partially rationalized by the isomerization equilibrium between CH_3SH^+ and $CH_2SH_2^+$ prior to fragmentation. The existence of the stable $CH_2SH_2^+$ isomer is also supported by experimental studies.[17] At the time of this calculation[12] and of many previous experimental studies,[13,19-22] the energetics for the CH_3S^+ and CH_2SH^+ isomers were not yet accurately established. Without this energetic information for these isomeric ions, the previous investigations of the dissociation mechanisms for CH_3SH^+ must be considered as incomplete.

It is interesting that the breakdown diagrams of CH_3SH^+ obtained in the charge exchange[21] and PEPICO[22] study and that estimated in the photoionization mass spectrometric experiment[20] are in qualitative agreement with the prediction[20] of the quasiequilibrium theory (QET). Since CH_3SH^+ in electronic excited states can be formed readily by charge exchange and photoionization processes, the results of the charge exchange and photoionization studies indicate that the couplings between the electronic states and the dissociating degrees of freedom of CH_3SH^+ are good, resulting in efficient energy flow between the internal electronic and vibrational modes of CH_3SH^+.

The energetics (Table 1) and structures for the CH_nS and CH_nS^+ (n=1-4) systems have been accurately determined in recent experimental[9,24-33] and theoretical[10-12] investigations. Motivated by this available information, we have undertaken a study of the CH_3SH^+ + Ar collision-induced dissociation (CID) reaction. The primary goal of this study is to compare the nature of product ions and their relative yields produced in CID, charge exchange[21], and photoionization[19,20,22]. Collisional activation mainly involves translational to rotational and vibrational energy transfer in the ground potential energy

surface of CH_3SH^+. At low collisional energies, collisional activation should be equivalent to thermal excitation. Considering the fact that translational to electronic energy transfer is inefficient, whether collisional activation can access excited electronic states from the ground electronic energy surface of CH_3SH^+ is highly questionable. If the region of phase space available to collisional activation is different from that available to charge exchange and photoionization, the branching ratios for the dissociation product channels observed in CID should be different from those formed in the other modes of excitation. In other words, the mechanism for CID may not be statistical in nature. The comparison of the dissociation product ions observed in CID, charge exchange, and photoionization presented here has revealed fundamental information about the CID mechanism. We have also probed the structure of the m/e=47 amu (mass 47) product ions formed in the CID reaction of $CH_3SH^+ + Ar$ by using the charge exchange probing scheme. The question of hydrogen scrambling[13,17,20,21] during the decomposition of excited CH_3SH^+ has been investigated here by examining the CID reaction of $CH_3SD^+ + Ar$.

In the present experiment, the reactant CH_3SH^+ is prepared by photoionization of CH_3SH at its ionization threshold. By using a sufficiently high photon energy resolution, the reactant CH_3SH^+ is formed in its ground vibronic state. Furthermore, since the CH_3SH sample is introduced into the photoionization ion source in the form of a supersonic jet in this experiment, CH_3SH^+ thus formed is also rotationally cold. This is the result of the fact that photoionization only involves small changes in rotational angular momentum. This approach of forming reactant ions by photoionization has many advantages over that by electron impact ionization of a supersonic jet. Due to the lower energy resolution used in electron impact ionization, together with the fact that supersonic expansion is inefficient for vibrational relaxation, reactant ions thus formed may contain considerable vibrational excitations.

On the basis of the self-consistent-field molecular orbital calculation using the 4-31G basis set,[18] the main electronic configuration for CH_3SH is predicted to be

$$....(8a')^2(2a'')^2(9a')^2(10a')^2(3a'')^2.$$

The 3a" orbital is a nonbonding orbital (n_S) localized on the S atom. The 10a' and 9a' orbitals are σ-bonding in character and are mainly localized along the C-S (σ_{CS}) and S-H (σ_{HS}) bonds, respectively. The first to fifth photoelectron bands observed in previous HeI photoelectron spectroscopic

studies[15,16,18] have been assigned to the removal of an electron from the 3a″, 10a′, 9a′, 2a″, and 8a′ orbitals, resulting in the $1^2A''$, $1^2A'$, $2^2A'$, $2^2A''$, $3^2A'$, for CH_3SH^+. The vertical IEs for these corresponding states are 9.46, 12.05, 13.73, 15.08, and 15.53 eV.[18] As expected, the vertical and adiabatic IEs for the formation of the ground $CH_3SH^+(1^2A'')$ state are nearly identical due to the similar geometries of CH_3SH and $CH_3SH^+(1^2A'')$.[10] We note that the reactant $CH_3SH^+(1^2A'')$ prepared by photoionization in this experiment has the charge localized mostly on the S atom.

Experiment

The arrangement of the triple-quadrupole double-octopole (TQDO) photoionization ion-molecule reaction apparatus (Fig. 1) and procedures used to perform state-selected absolute total cross section measurements have been described in detail previously.[34-37] The TQDO apparatus essentially consists of, in sequential order, a vacuum ultraviolet (VUV) photoionization ion source, an electron impact ion source (1), a reactant quadrupole mass spectrometer (QMS) (5), a lower radio frequency (RF) octopole ion guide reaction gas cell (RFOIGGC) [(6) + (7)], a middle QMS (10), an upper RFOIGGC [(11) + (14)], a product QMS (15), and a modified[38] Daly-type scintillation ion detector [(17) + (19) + (20)]. The electron impact ion source is not used in this experiment. The TQDO apparatus is partitioned into five chambers, which are separately evacuated by liquid nitrogen-trapped diffusion pumps.

The photoionization ion source consists of a 0.2 m VUV monochromator (McPherson 234), a hydrogen discharge lamp, and a photoelectric VUV light detector. The recent high resolution non-resonant two-photon pulsed field ionization photoelectron (N2P-PFI-PE) study of CH_3SH near the ionization threshold yields a value of 9.4553±0.0006 eV (1311±0.08 Å) for the ionization energy (IE) of CH_3SH.[23] The N2P-PFI-PE spectrum also revealed a vibrational progression corresponding to excitation of the C-S stretching mode (ν_2^+=687 cm^{-1}) of $CH_3SH^+(1^2A'')$.[23,39] Methanethiol is introduced into the photoionization source as a free jet formed by supersonic expansion through a nozzle with a diameter of 75 μm at a stagnation pressure of ≈120 Torr. By setting the photoionization wavelength at 1310 Å with a wavelength resolution of 6 Å [full-width-at-half-maximum (FWHM)], the CH_3SH^+ reactant ions were formed in their ground vibronic states. The rotational temperature of CH_3SH^+ thus formed is expected to be ≤ 150 K, characteristic of the neutral CH_3SH jet.

For absolute total cross section measurements, the reactant CH_3SH^+ ions were extracted and guided by the lower QMS (operated in the RF only mode) and the lower RF octopole ion guide to the middle QMS. The middle QMS, functioning as a mass filter, passed only the desired CH_3SH^+ ions to

the upper RFOIGGC, where collision-induced dissociation occurred with Ar. The pressure of Ar in the upper RFOIGGC was monitored with an MKS Baratron manometer, and maintained at 2-3x10^{-4} Torr. In this pressure range, the CID product ion intensity was found to have a linear dependence on the Ar gas cell pressure. The reactant ions and the product ions formed in the upper RFOIGGC were then mass selected by the product QMS and detected with the modified Daly-type scintillation ion detector.

The reactant ion beam energies were determined by the retarding potential method, using the upper octopole ion guide to retard the reactant CH_3SH^+ ions. The retarding potential curve thus obtained was differentiated to yield the most probable laboratory kinetic energy (E_{lab}) of the reactant ions and the FWHM of the kinetic energy distribution. The E_{lab} resolution for CH_3SH^+ achieved in this experiment was in the range of ±0.2 eV. The collection efficiencies for reactant and product ions were maximized at each center-of-mass collision energy (E_{cm}) by optimizing the dc voltage settings applied to the ion lenses, the octopole ion guides, and the QMSs.

To probe the structure of the mass 47 ions formed in the CID reaction of CH_3SH^+ + Ar, we used both the lower and upper RFOIGGCs. Reactant CH_3SH^+ ions prepared by photoionization of CH_3SH were first selected by the reactant QMS to enter the lower RFOIGGC, where the CID reaction of CH_3SH^+ + Ar took place. The Ar gas cell pressure used was 5x10^{-4} Torr. The mass 47 product ions thus formed in the E_{cm} range of 4.5-6.5 eV were selected by the middle QMS and guided into the upper RFOIGGC, in which the structure for the mass 47 ions was probed by the charge transfer reaction with benzene (C_6H_6) at $E_{cm} \leq 2$ eV. Charge transfer product $C_6H_6^+$ ions, if formed, were detected by the product QMS. The C_6H_6 pressure used in the upper gas cell was 3x10^{-4} Torr. The IEs for CH_3S, CH_2SH, and C_6H_6 are known to be 9.2649±0.0010 eV (Ref. 26), 7.536±0.003 eV (Ref. 27), and 9.243842±0.000006 eV (Ref. 40), respectively (see Table 1). Using these IE values, we calculated that the charge transfer reaction (1) for CH_3S^+ is slightly exothermic by 0.0211eV, whereas the charge transfer reaction (2) for CH_2SH^+ is endothermic by more than 1.7 eV. The $\Delta H°_0$ values given in reactions (1) and (2) are the corresponding heats of reaction at 0 K.

$$CH_3S^+ + C_6H_6 \rightarrow CH_3S + C_6H_6^+ \qquad \Delta H°_0 = -0.0211 \text{ eV} \qquad (1)$$

$$CH_2SH^+ + C_6H_6 \rightarrow CH_2SH + C_6H_6^+ \qquad \Delta H°_0 = 1.708 \text{ eV} \qquad (2)$$

Because near-resonant charge transfer reactions usually have large cross sections, we should observe the formation of $C_6H_6^+$ if the mass 47 ions have the CH_3S^+ structure, while the charge transfer cross

section should be negligibly small if CH_2SH^+ ions are produced in the CID reaction of $CH_3SH^+(1^2A'') + Ar$.

It is known that CH_2SH^+ ions are produced at the onset by photoionization of CH_3SH.[19,21,22] This conclusion is based on the fact that the thermochemical threshold of $\Delta H°_0 = 11.541$ eV for process (3) is very close to the appearance energy (AE) of ≈11.55 eV for the mass 47 ion observed in the dissociative photoionization of CH_3SH.

$$CH_3SH + h\nu \rightarrow CH_2SH^+ + H. \qquad \Delta H°_0 = 11.541 \text{ eV} \qquad (3)$$

To test the charge transfer detection scheme, we prepared CH_2SH^+ in the photoionization ion source by process (3) at $h\nu < 12.4$ eV, and measured the charge transfer cross section for reaction (2) using the upper RFOIGGC. No $C_6H_6^+$ ions were observed, confirming that CH_2SH^+ is indeed produced by process (3) at $h\nu < 12.4$ eV. Since the IE(CH_3SH)[23] and IE(CH_3S)[20] are similar (see Table 1), we have also measured the charge transfer cross section for reaction (4).

$$CH_3SH^+(1^2A'') + C_6H_6 \rightarrow CH_3SH + C_6H_6^+ \qquad \Delta H°_0 = -0.2115 \text{ eV} \qquad (4)$$

As expected from the small $\Delta H°_0$ value of -0.2115 eV, we obtained a cross section of ≈19 $Å^2$ for reaction (4) at $E_{cm} \approx 4$-6 eV, yielding a significant intensity of $C_6H_6^+$.

The data acquisition for the TQDO apparatus has recently been upgraded to be controlled by a Pentium PC system.[11] This improvement allows computer control of the QMS and monochromator scans, the voltage settings applied to individual components of the ion optics system, the reactant ion kinetic energy determination, and the background corrections in absolute total cross section measurements. The procedures outlined above were conducted mostly in an automatic mode.

The methanethiol and benzene were obtained from Aldrich Chemical Co. and Fisher Scientific with purities of 99.5% and 99.9%, respectively. The Ar gas is from Air Products and has a purity of 99.998%.

To examine the aspect concerning H-scrambling in the dissociation of CH_3SH^+, we have also measured the relative intensities of the masses 47 and 48 ions formed in the CID reaction of

$CH_3SD^+(1^2A'')$ + Ar. The CH_3SD was obtained from CDN Isotope with a quoted isotopic purity of >91%.

Results and Discussion

Absolute total cross sections and identification of CID product channels

The product ions observed in the CID reaction of $CH_3SH^+(1^2A'')$ + Ar are CH_2SH^+ (CH_3S^+), CH_2S^+, CHS^+, HS^+, CH_3^+, and CH_2^+. The absolute total cross sections for these product ions in the E_{cm} range of 1.9-37 eV are plotted in Fig. 2(a). Figure 3 depicts the mass spectrum observed for the CID reaction of CH_3SH^+ + Ar at E_{cm}=7.3 eV by scanning the product quadrupole mass spectrometer, showing that CH_3^+ and CH_2SH^+ (CH_3S^+) are the major product ions. The cross section curves for CH_3^+ and CH_2SH^+ (CH_3S^+) have a similar E_{cm} dependence and exhibit a maximum at E_{cm} = 11-14 eV. The maximum cross section for CH_3^+ is 3.4 Å^2, which is approximately 3 times higher than the maximum cross section of 1.2 Å^2 for CH_2SH^+ (CH_3S^+). A magnified view of the cross section curves for the minor product ions, all of which have cross sections $\leq$0.5 Å^2, are depicted in Fig. 2(b). The profiles for the cross section curves of these minor product ions are also similar, i.e., they increase very slowly from their onsets as E_{cm} is increased.

The CID reactions that may be responsible for the production of the observed product ions are given below.

$CH_3SH^+ + Ar$	$\rightarrow CH_2SH^+ + H + Ar$	$\Delta H°_0 = 2.09 \pm 0.09$ eV	(5)
	$\rightarrow CH_3S^+ + H + Ar$	$\Delta H°_0 = 3.54 \pm 0.09$ eV	(6)
	$\rightarrow CH_2S^+ + H_2 + Ar$	$\Delta H°_0 = 1.28 \pm 0.09$ eV	(7a)
	$\rightarrow CH_2S^+ + H + H + Ar$	$\Delta H°_0 = 5.75 \pm 0.09$ eV	(7b)
	$\rightarrow CHS^+ + H_2 + H + Ar$	$\Delta H°_0 = 3.46 \pm 0.08$ eV	(8)
	$\rightarrow HS^+ + CH_3 + Ar$	$\Delta H°_0 = 4.12 \pm 0.03$ eV	(9)
	$\rightarrow CH_3^+ + SH + Ar$	$\Delta H°_0 = 3.53 \pm 0.02$ eV	(10)
	$\rightarrow CH_2^+ + H_2S + Ar$	$\Delta H°_0 = 4.89$ eV	(11a)
	$\rightarrow CH_2^+ + HS + H + Ar$	$\Delta H°_0 = 8.8$ eV	(11b)

All atomic and molecular species in reactions (5)-(11) are assumed to be in their ground states. Using the thermochemical data listed in Table 1, we have calculated the corresponding $\Delta H°_0$ values for these reactions. With the exception of minor differences, the nature of the product ions observed in the present CID study are similar to those in previous photoionization[19,20,22] and charge exchange[21] studies in the same energy range.

One of the most important pieces of information obtained in a low energy CID study, such as this, is the AEs of the product ions, from which upper limits of the bond dissociation energies involved can be calculated. Although the energetics for the CH_3SH^+ + Ar reaction are well known, it is still of interest to compare the observed CID AE [AE(CID)] values for product ions with their corresponding thermochemical thresholds. Such a comparison is helpful for identifying the product ions with specific product channels as listed in reactions (5)-(11). We have listed in Table 2 the AE(CID) values for CH_2SH^+ (CH_3S^+), CH_2S^+, HCS^+, HS^+, CH_3^+, and CH_2^+ determined by the cross section curves of Figs. 2(a) and 2(b). Below these AE(CID) values, the intensities for the corresponding product ions are at the background level. Other than the AE(CID) values for CH_3^+ and CH_2SH^+ (CH_3S^+), the AE(CID) value for a minor product ion is given in an E_{cm} range, covering the uncertainty range of the measurement. We note that these AE(CID) values given in Table 2 represent upper limits for the true thermochemical thresholds of the processes involved. We have also fit the absolute total cross sections for the CID product ions near their onsets using the semi-empirical cross section expression,[42]

$$\sigma = \sigma_0 \frac{(E_{cm} - E_0)^n}{E_{cm}} \qquad (12)$$

where σ_0, E_0, and n are adjustable parameters. The E_0 value is the onset or AE of the process involved. The best fit values for these parameters are also listed in Table 2. The fits to the total cross sections for CH_2SH^+(CH_3S^+) and CH_3^+ are most straightforward and reliable, covering the E_{cm} ranges from their respective onsets to ≈12 eV. The E_0 values for CH_2SH^+ (CH_3S^+) (3.84 eV) and CH_3^+ (3.37 eV) are essentially identical to the respective AE(CID) values of 3.9 and 3.5 eV. Fitting the cross sections for the other minor product ions is complicated by the very gradual rise of the cross section curves near their onsets. The parameters given in Table 2 provide satisfactory fits to the cross section curves for CH_2S^+, HCS^+, HS^+, and CH_2^+, covering the E_{cm} ranges of 5-10, 6-16, 6-15, and 8-15 eV, respectively. The E_0 values for these minor product ions are mostly higher than, but consistent with

their corresponding AE(CID) values. The n values for CH_2SH^+ (CH_3S^+) and CH_3^+ are close to unity, which is consistent with a hard-sphere line-of-centers model for energy transfer.[43,44] The n values for other product ions are in the range of 1.5-1.8, which reflect the nonimpulsive character of the collisions at $E_{c.m.}$'s near their thresholds.[44]

The AE values for CH_2SH^+(CH_3S^+), CH_2S^+, HCS^+, and CH_3^+ have been reported in previous photoionization studies[19,20,22] of CH_3SH. The photoionization AE [AE(PI)] values represent ionization transition energies with respect to the neutral ground state of CH_3SH. In order to compare these values with the AE(CID) values, it is necessary to subtract the IE(CH_3SH) value (9.4553 ± 0.0006 eV)[23] from the AE(PI) values. Thus, the values for $\Delta(PI) = AE(PI) - IE(CH_3SH)$ given in Table 2 represent the excitation energies measured with respect to CH_3SH^+ in its ground vibronic state. The Δ(PI) values for CH_2SH^+ (CH_3S^+) and CH_2S^+ are in the ranges of 1.8-2.16 eV and 1.12-1.34 eV,[19,20,22] which are in good agreement with the thermochemical thresholds of 2.09±0.09 eV and 1.28±0.09 eV for the formation of $CH_2SH^+ + H$ and $CH_2S^+ + H_2$, respectively. This observation indicates that these product channels are formed in the photoionization experiments at photon energies near the AE(PI)'s of CH_2SH^+ and CH_2S^+. As described in the experimental section, no charge transfer product $C_6H_6^+$ was found in the reaction of C_6H_6 with the mass 47 ion formed in the photoionization of CH_3SH. Such an observation is in accord with the conclusion that the mass 47 ions formed by photoionization have mostly the CH_2SH^+ structure. Although the Δ(PI) values for HCS^+ (<4.15 eV)[20] and CH_3^+ (3.9 eV)[20] are higher by ≈0.5 eV than the respective thermochemical thresholds of 3.46±0.08 eV and 3.53±0.02 eV for the formation of $HCS^+ + H_2 + H$ and $CH_3^+ + SH$, we may still conclude that these product channels are responsible for the production of HCS^+ and CH_3^+ near their photoionization onsets. With the exception of Δ(PI) values for CH_3^+, which is higher than the AE(CID) value for CH_3^+, the Δ(PI) values for CH_2SH^+, CH_2S^+, and HCS^+ are lower than the corresponding AE(CID) values. The AE(PI) values for HS^+ and CH_2^+ were not measured in previous photoionization studies.[19,20,22]

As shown in Figs. 2(a) and 2(b), both the CID onsets for CH_2SH^+ (CH_3S^+) and CH_3^+ are relatively sharp compared to those observed for the other minor product ions, suggesting that CH_3^+, in addition to CH_2SH^+ (CH_3S^+), is formed directly in the CID reaction instead of by secondary decomposition. This conclusion is consistent with the observation that the AE(CID) value of 3.5 ± 0.2 eV for CH_3^+ is in excellent agreement with the thermochemical threshold of $\Delta H^\circ_0 = 3.53 \pm 0.02$ eV for reaction (10). The substantial curvatures and very gradual rises observed for the cross sections of the other minor product

ions are mostly indicative of a sequential decomposition or an elimination reaction mechanism involving a tight transition state.

Although the AE(CID) value of 3.9 ± 0.2 eV for the mass 47 ion is higher than the thermochemical threshold of $\Delta H°_0 = 2.09 \pm 0.09$ eV for reaction (5), it is close to that of $\Delta H°_0 = 3.54 \pm 0.09$ eV for reaction (6). It is tempting to speculate that CH_3S^+ is formed near the CID onset for the mass 47 ion. To shed light on the possible structure of the mass 47 ion formed in the CID reaction of CH_3SH^+ + Ar, we have carried out the charge transfer probing experiment using the double RFQIGGC scheme as described in the experimental section. On the basis of the energetics of reactions (1) and (2), we expect to observe charge transfer $C_6H_6^+$ if the mass 47 ion has the CH_3S^+ structure, whereas no $C_6H_6^+$ ions should be formed if the mass 47 ion possesses the CH_2SH^+ structure. Since no charge transfer product $C_6H_6^+$ ions are observed, we conclude that the mass 47 ions formed in the CID reaction of $CH_3SH^+(1^2A'')$ + Ar at E_{cm} = 4.5-6.4 eV have mostly the CH_2SH^+ structure. This experiment indicates that the closeness between the AE(CID) value for the mass 47 ion and the $\Delta H°_0$ value for reaction (6) is fortuitous.

At the AE(CID) of ≈5.5 eV for HS^+, the product channel should correspond to reaction (9). As pointed out above, the charge of $CH_3SH^+(1^2A'')$ is mainly localized on the S atom. The dissociation of the C-S bond in $CH_3SH^+(1^2A'')$ should result in the formation of CH_3 + SH^+. However, during the breakage of the C-S bond, the charge on HS^+ may hop to CH_3, resulting in the formation of CH_3^+ + SH [reaction (10)]. Considering that the IE for CH_3 (9.8380±0.0004 eV)[33] is significantly lower than that of HS (10.4682±0.0002 eV)[32], we expect that the production of CH_3^+ + SH is more favorable than that of CH_3 + SH^+, in good accord with the experimental observation.

The AE(CID) value of 5.0-5.5 eV for CH_2S^+ are significantly higher than the thermochemical threshold of $\Delta H°_0$ = 1.28±0.09 eV for reaction (7a), but lower than that of $\Delta H°_0$ = 5.75±0.09 eV for reaction (7b). Thus, we concluded that CH_2S^+ + H_2 are formed at the AE(CID) for CH_2S^+. At E_{cm} > 5.75 eV, the formation of CH_2S^+ + 2H is possible. We note that the mass 46 ion can exist as *trans*-$HCSH^+$ and *cis*-$HCSH^+$, which are estimated to be 1.1 eV higher in energy than CH_2S^+.[12,20,30] We cannot exclude the formation of these structures for the mass 46 ion observed in the CID reaction.

Although the AE(CID) value for HCS^+ determined in the range of 5.0-5.5 eV is higher than the thermochemical threshold of $\Delta H°_0$ = 3.46±0.08 eV for reaction (8), we may conclude that the formation of HCS^+ is accompanied by H_2 + H at the AE(CID) for HCS^+. The CSH^+ isomer is predicted by Gaussian-2 (G2) *ab initio* calculation to be 3.16 eV higher in energy than that of HCS^+.[12] Thus, the formation of CSH^+

is also possible at higher E_{cm}'s. The formation of $HCS^+ + H_2 + H$ is likely the result of a stepwise dissociation mechanism, i.e., HCS^+ may be produced by the further dissociation of internally excited CH_2SH^+ (CH_3S^+) initially formed by reaction (5) [reaction (6)]. Product HCS^+ may also be produced by the decomposition of internally excited CH_2S^+ formed in reaction (7a). However, judging by the significantly higher cross sections for reaction (5) compared to reaction (7a), we favor excited CH_2SH^+ to be the precursor of HCS^+ formed in reaction (8).

The AE(CID) for CH_2^+ is determined to be ≈5.0 eV, which is slightly higher than the thermochemical threshold of $\Delta H^\circ_0 = 4.89$ eV for reactions (11a). This observation indicates that $CH_2^+ + H_2S$ are formed at the CID onset for CH_2^+. Since the IE for CH_2 (10.396±0.003 eV)[30] is only slightly lower than that for H_2S (10.4682±0.0002 eV)[31], it is surprising that H_2S^+ was not observed in the CID reaction. The formation of $CH_2^+ + HS + H$ [reaction (11b)] is possible at higher E_{cm}'s. Reaction (11b) may result from the further dissociation of excited CH_2SH^+ initially formed by reaction (5) and/or the further dissociation of H_2S formed in reaction (11a).

The aspect concerning H-scrambling in the dissociation of excited CH_3SH^+ has been examined in previous dissociation studies[13,14,20,21] by measuring the relative intensities for product ions from CD_3SH^+. The dissociation product ions observed in these experimental studies indicate that H/D-scrambling may occur before or after the fragmentation processes. We have examined the CID reaction of $CH_3SD^+(1^2A'') + Ar$ at E_{cm} = 10 and 15 eV. Masses 48 and 47 ions are observed with the intensity ratios of ≈ 4:1 and ≈ 2:1 at E_{cm} = 10 and 15 eV, respectively, favoring the formation of mass 48. From the results of the charge exchange probing experiment, we expect the mass 48 ion to be CH_2SD^+ and the mass 47 ion to be CH_2SH^+. The observed ratios of CH_2SD^+ to CH_2SH^+ are in agreement with the ratios of CD_2SH^+ to CD_2SD^+ from CD_3SH^+ reported in previous mass spectrometric studies.[13,14] The ratio for CH_3^+ to CH_2D^+ from the CID reaction of CH_3SD^+ is also found to decrease from ≈ 4:1 to 2.5:1 as E_{cm} is increased from 10 to 15 eV. These findings unambiguously show that H/D-scrambling occurs during the collision-induced dissociation of $CH_3SD^+(1^2A'')$.

Potential-energy profile for rearrangement and dissociation reactions of CH_3SH^+

The *ab initio* potential-energy profile for the rearrangement and dissociation reactions of CH_3SH^+ has been calculated at the MP3/6-31G(d,p)//4-31G level of theory.[11,45] The calculations indicate that $CH_2SH_2^+$ (methylenesulfonium radical cation) is a stable isomer, which can be formed by 1,2-hydrogen shift from $CH_3SH^+(1^2A'')$. The existence of $CH_2SH_2^+$ is supported by collisional-activation mass spectrometric

experiments.[17] According to the recent G2 *ab initio* calculation,[12] $CH_2SH_2^+$ is a higher energy isomer which lies 0.8 eV above $CH_3SH^+(1^2A'')$. This value is in good agreement with that obtained in Ref. 11. Using the G2 energetic value for $CH_2SH_2^+$, together with the known energetics for the other molecular species involved, we have constructed a potential energy diagram in Fig. 4 which shows the rearrangement and dissociation pathways of the CH_3SH^+ system.

The transition structure (1) shown in Fig. 4 for 1,2-hydrogen shift between CH_3SH^+ and $CH_2SH_2^+$ is predicted to lie ≈1.97 eV above the energy for $CH_3SH^+(1^2A'')$.[11] Hence, at low excitation energies [<1.97 eV with respect to the energy for $CH_3SH^+(1^2A'')$], these two isomeric ions cannot interconvert. However, the AE(CID) values of all the product ions are above the potential barrier for 1,2-hydrogen shift. Therefore, both CH_3SH^+ and $CH_2SH_2^+$ should be accessible in this CID experiment. An interesting consequence of the existence of these isomers is that $CH_2SH^+ + H$ can be formed via H-eliminations from the C atom of CH_3SH^+ as well as from the S atom of $CH_2SH_2^+$. The corresponding transition structures (2) and (3) for these elimination processes have also been calculated to have energies of ≈0.16 eV and ≈0.34 eV above that for $CH_2SH^+ + H$, respectively.[11] We note that the previous *ab initio* calculations predict an energy of ≈1.84 eV[11] for $CH_2SH^+ + H$ with respect to that for $CH_3SH^+(1^2A'')$, which is lower than the known experimental value of 2.09 eV [$\Delta H°_0$ of reaction (5)] by ≈0.25 eV. Based on the highest Δ(PI) value of 2.16 eV[20] for CH_2SH^+ (see Table 2), we estimate a potential barrier of ≤ 0.07 eV , as compared to the *ab initio* value of ≈0.16 eV with respect to the energy for $CH_2SH^+ + H$. The experimental estimate of ≤ 0.07 eV is used to locate the energy of (2) in Fig. 3. We have calculated the energies for (2) and (3) at the G2 level of theory.[46] The G2 energies for (2) and (3) are found to be 2.10 eV higher than that for $CH_3SH^+(1^2A'')$, indicating that the reverse potential barrier for the formation of formation of $CH_2SH^+ + H$ from $CH_3SH^+(1^2A'')$ ($CH_2SH_2^+$) is negligibly small. Thus, the G2 prediction is in agreement with the observed AE(PI) values[19,20,22] for CH_2SH^+.

The energy for $CH_3S^+ + H$ is also shown in Fig. 3. The ground state for CH_3S^+ is a triplet $^3A_1$ state, which is known to lie 1.45 eV above the ground $CH_2SH^+(^1A')$ state.[10,12] The formation of $CH_3S^+(^3A_1)$ has been demonstrated in photoionization[27-29] and photoelectron[26] experiments. The detailed mechanism for the conversion between $CH_3S^+(^3A_1)$ and $CH_2SH^+(^1A')$ is not known. The rearrangement from $CH_3S^+(^3A_1)$ to $CH_2SH^+(^1A')$ necessarily involves intersystem crossing from the triplet to the single manifolds, i.e., the coupling between the triplet and singlet potential energy surfaces. The result of the charge exchange probing experiment, which uses reactions (1) and (2) designed to probe the existence CH_3S^+, is negative. This

observation is consistent with the previous suggestion that the rearrangement from CH_3S^+ to CH_2SH^+ occurs at a sufficiently high internal energy.[47]

As expected, the *ab initio* calculations of Ref.11 show that the formations of $CH_3^+ + SH$ from CH_3SH^+ and $CH_2^+ + H_2S$ from $CH_2SH_2^+$ involve loose transition complexes and the reverse activation energies for such processes are zero. Similarly, the formation of $HS^+ + CH_3$ from CH_3SH^+ should also occur without a reverse activation energy. The formation of HCS^+ necessarily involves a two-step dissociation mechanism. Hence, the $HCS^+ + H_2 + H$ channel is not shown in Fig. 4.

The Δ(PI) value for CH_2S^+ observed in previous photoionization experiments[19,20,22] are in close agreement with the thermochemical threshold for $CH_2S^+ + H_2$ (see Table 2), indicating that the formation of $CH_2S^+ + H_2$ via 1,2-H_2 elimination from CH_3SH^+ may proceed without a reverse potential energy barrier. The thermochemical threshold (1.28 eV) for the formation of $CH_2S^+ + H_2$ from CH_3SH^+ is lower than the potential energy barrier of 1.97 eV for isomerization from CH_3SH^+ to $CH_2SH_2^+$. Thus, the CH_2S^+ ions observed at the AE for CH_2S^+ in photoionization cannot be formed from $CH_2SH_2^+$. However, the AE(CID) value of 5.0-5.5 observed here is significantly higher than the energy barrier of 1.97 eV for isomerization between CH_3SH^+ and $CH_2SH_2^+$. Hence, the formation of $CH_2S^+ + H_2$ by H_2-elimination from the S atom of $CH_2SH_2^+$ is possible at AE(CID) for CH_2S.

We have obtained the transition structure (4) for 1,2-H_2 elimination from CH_3SH^+ at the MP2/6-311G(d, p) level of theory.[48] The G2 energy[46] for (4) is found to be 2.08 eV higher than that of CH_3SH^+, which yield a reverse potential energy barrier of 0.8 eV. This prediction is contrary to the photoionization measurements.[19,20,22] A careful examination of the photoionization efficiency spectrum for CH_2S^+ reveals that the yield for CH_2S^+ increased sharply at ≈1075 Å. The photoionization yields below 1075 Å are small. The PEPICO measurement for CH_2S^+ shows negligible yields at photon energies below 1180 Å. Taking this value as the AE for CH_2S^+, we calculated a Δ(PI) value of 2.02 eV for CH_2S^+.[22] Thus, the PEPICO measurement for CH_2S^+ seems to support the G2 prediction. On the basis of the threshold photoelectron spectrum for CH_3SH, the adiabatic IE for the formation of the excited $CH_3SH^+(1^2A')$ is estimated to be ≈1075 Å (11.53 eV) or Δ(PI) ≈ 2.08 eV. The sharp increases in photoionization yields for CH_2S^+ as well as CH_2SH^+ at ≈1075-1080 Å may correlate with the onset of the excited $CH_3SH^+(1^2A')$ state.

As pointed out in Ref. 11, since the potential energy barriers for the 1,2-hydrogen shift connecting CH_3SH^+ and $CH_2SH_2^+$ and those for H-eliminations from CH_3SH^+ and $CH_2SH_2^+$ to give $CH_2SH^+ + H$ are similar, H/D-scrambling may take place prior to fragmentation. This provides a rationalization for the observation of mixed H/D product ions in the dissociation reactions of CD_3SH^+ and CH_3SD^+.

Comparison of relative abundance for product ions observed in CID, charge exchange, and photoionization

Figure 5 depicts the plot of the relative abundance in percentages for the observed CID product ions $CH_2SH^+(CH_3S^+)$, CH_2S^+, HCS^+, HS^+, CH_3^+, and CH_2^+. Here, the sum of the abundance for all product ions at a specific E_{cm} is normalized to 100%. As shown in the figure, the relative abundance of CH_3^+ decreases monotonically from 100% to ≈30% as E_{cm} is increased from 3.5 eV to 36 eV. In the same E_{cm} range, the relative abundance of $CH_2SH^+(CH_3S^+)$ remains in the range of 15-25%. The relative abundance for other minor product ions is negligibly small at $E_{cm} < 6$ eV, and increase gradually as a function of E_{cm} to ≤ 15% at $E_{cm} = 36$ eV.

Table 3 compares the relative abundance for CH_3SH^+, $CH_2SH^+(CH_3S^+)$, CH_2S^+, HCS^+, HS^+, and CH_3^+ observed in this CID experiment with those reported in the previous charge exchange[21] and photoionization mass spectrometric[20] studies in the energy range of 2.7-12 eV. In order to compare the abundance observed in charge exchange and photoionization with those in CID, the recombination energies (RE) of the charge exchange experiment and the photon energies (PHE) in the photoionization experiment are converted to excitation energies (E_{ex}) with respect to the ground vibronic state of $CH_3SH^+(1^2A'')$. That is, the E_{ex} values given in Table 3 are equal to E_{cm} in CID, RE - IE(CH_3SH) in charge exchange, and PHE - IE(CH_3SH) in photoionization. At a specific E_{ex}, the sum of the abundance for all product ions except that for CH_3SH^+ is arbitrarily set to 100%. The abundance of CH_3SH^+ for the CID study is not included in the table because CH_3SH^+ is the reactant ion in this case. Furthermore, since CH_2^+ was not observed in the charge exchange and photoionization studies, the comparison of the abundance for CH_2^+ was also excluded from the table.

Considering that charge exchange favors processes with small energy defects between the reactant and product states, it is essentially a state- or energy-selected technique. However, photoionization mass spectrometry and CID are not. Thus, the comparison in Table 3 between the abundance of product ions observed in CID, charge exchange, and photoionization experiments should be viewed only as qualitative in nature. The small abundance for CH_3SH^+ observed in the charge exchange study is consistent with the expectation that the overwhelming fraction of CH_3SH^+ initially formed are in dissociative excited states, yielding a low intensity for stable CH_3SH^+.

The charge exchange study used Xe^+, CO_2^+, CO^+, Kr^+, N_2^+, Ar^+, and Ne^+ as the charge transfer reactant ions, covering the E_{ex} range of 2.7-12 eV.[21] As shown in Table 3, at $E_{ex} < 4.0$ eV,

$CH_2SH^+(CH_3S^+)$ and CH_2S^+ are the only product ions formed in the charge exchange study, with the abundance (98%) for $CH_2SH^+(CH_3S^+)$ significantly greater than that (2%) for CH_2S^+. The lower yield for CH_2S^+ has been rationalized by QET calculations as due to the tight transition state (4) involved in the 1,2-H_2 elimination of CH_3SH^+. At E_{ex}>4.0 eV, HCS^+ and CH_3^+ are also observed in the charge exchange experiment. The abundance for CH_3^+ remains small ≤ 3% in the E_{ex} range of 4-12 eV. Product HS^+, which appears at E_{ex} > 6.0 eV, is also minor, with abundance below 4%. At E_{ex} = 4-12 eV, HCS^+ becomes the dominant product ion. The growth of HCS^+ and CH_2S^+ at higher E_{ex}'s is at the expense of CH_2SH^+. At E_{ex} = 12 eV, S^+ and CS^+ with the respective abundance of 2% and 4% are also reported in the charge exchange study.[21]

The relative abundance for fragment ions formed in the photoionization of CH_3SH have been measured at 800 and 744 Å,[20] which are equivalent to E_{ex} = 6.0 and 7.2 eV, respectively. In qualitative agreement with the charge exchange study, the abundance for CH_2SH^+ (68%) and HCS^+ (22%) are found to be the dominant product ions. The photoionization mass spectrometric experiment also reported the observation of a small abundance (0.03%) of CH_4^+.

As shown in Table 3, the relative abundance for product ions measured in this CID study reveals CH_3^+ as the major fragment ion with an abundance in the range of 65-85% at E_{ex} = 4-12 eV. This abundance is significantly greater than those observed in charge exchange[21] and photoionization studies[20]. Considering that the endothermicities for the formation of CH_2SH^+ + H [reaction (5)], $CH_2S^+ + H_2$ [reaction (7a)], and $HCS^+ + H_2 + H$ [reaction (8)] are lower than that for reaction (10), we expect the abundance for CH_2SH^+, CH_2S^+, and HCS^+ to be greater than that for CH_3^+, as were observed in previous photoionization[19,20,22] and charge exchange[21] experiments. The high abundance for CH_2SH^+, CH_2S^+, and HCS^+ were also predicted by the QET calculations.[20] For a detailed comparison between breakdown diagrams obtained in QET calculations and those derived from the charge exchange and photoionization studies, readers are referred to Ref. 20.

Dissociation mechanism for collision activated CH_3SH^+

The observation that CH_3^+ + SH [reaction (10)] is the dominant product channel over the full $E_{c.m.}$ range of 2-36 eV is most interesting. Such an observation is contrary to the prediction of QET calculations. The two basic assumptions of a statistical model, such as QET, are that a critical configuration or transition state controls the reaction rate, and that the internal energy of the reactant is randomly distributed in the molecule's active degrees of freedom. This favors the most stable product

channel. Hence, the result of the present CID experiment is strong evidence, indicating that the CID dissociation of CH_3SH^+ is not compatible with the energy randomization assumption of a statistical model. However, a finite degree of energy flow within CH_3SH^+ clearly takes place, as indicated by the isotopically mixed product ions observed due to H/D-scrambling in the CID measurement of CH_3SD^+.

The statistical model describes, at least qualitatively, the fragmentation resulting from charge exchange and photoionization well, but fails for the fragmentation resulting from collisional activation. The difference between the results of these experiments is in how the necessary internal energy for fragmentation is added to CH_3SH^+. It is known that collisional activation in the E_{cm} range of this experiment is highly inefficient for electronic excitation. A collisional activation process mainly involves translational to rotational and vibrational energy transfer.[43,44] We expect that the low frequency vibrational modes of CH_3SH^+ are preferentially excited in such a process.[43] The four highest vibrational frequencies[10] of $CH_3SH^+(1^2A'')$ correspond to CH_3 and SH stretching modes, ranging from ≈2556-3035 cm^{-1}, while the C-S stretch[10,39] is the second lowest vibrational mode with a frequency of 687 cm^{-1}. Thus, the internal vibrational energy resulting from collisional activation is predominantly deposited in the C-S stretch mode instead of the CH_3 stretching modes of CH_3SH^+. Furthermore, the size factor, i.e., the size of S and C are significantly greater than that of H, may also contribute to the more efficient excitation of the C-S bond in CH_3SH^+. Owing to the large differences in vibrational frequencies between the C-S and CH_3 stretching modes of CH_3SH^+, the C-S and CH_3 stretching modes are only weakly coupled, resulting in inefficient energy flow between the C-S and CH_3 (SH) vibrational modes of CH_3SH^+. As a consequence, the product CH_3^+ ion, which results from the breakage of the C-S bond, is favored over those due to the breakage of the C-H (S-H) bonds of CH_3SH^+. This conclusion may be tested in CID studies of larger molecular ions, such as $CH_3CH_2SH^+$, which contains a C-C bond as well as a C-S bond. In addition to the expected efficient excitation of the C-C and C-S stretching modes via collision activation, the coupling between the C-C and C-S modes of $CH_3CH_2SH^+$ should also be good. Hence, product channels arising from the breakage of the C-S and C-C bonds should dominate in the collision activated dissociation of $CH_3CH_2SH^+$.

The observation that the abundance of product ions formed in charge exchange and photoionization are consistent with statistical predictions indicates that the energy randomization assumption is mostly valid when the internal energy of CH_3SH^+ is deposited by electronic excitation. It appears that in the photoionization[20,22] and charge exchange[21] experiment the onsets of all dissociation product ions are found in the first and second excited photoelectronic bands of CH_3SH^+, i.e., the $CH_3SH^+(1^2A', 2^2A')$

states. As pointed out above, these excited states correspond mainly to the removal of an electron from the σ_{CS} and σ_{HS} bonding orbitals. To a first approximation, the excitations of the C-S and C-H stretching modes of $CH_3SH^+(1^2A')$ and $CH_3SH^+(2^2A')$ are to be expected upon the ejection of an electron from the σ_{CS} and σ_{HS} orbitals of CH_3SH, respectively. Owing to the delocalized nature of these orbitals, such ionization processes are also expected to affect the bonding of the S-H and C-H bonds of CH_3SH^+, resulting in finite excitation of the vibrational modes involving the C-H and S-H bonds. The extent of vibrational excitations in the electronic excited $CH_3SH^+(1^2A', 2^2A')$ states may be assessed by comparing the differences between the equilibrium geometries of the neutral ground CH_3SH state and those of the electronically excited $CH_3SH^+(1^2A', 2^2A')$ states.[23] The more efficient excitation of the low frequency C-S as well as high frequency CH_3 and S-H vibrational modes of CH_3SH^+ via electronic excitations may promote better couplings between these vibrational modes. The Franck-Condon factors for ionization transitions from CH_3SH to the excited $CH_3SH^+(1^2A')$ and $CH_3SH^+(2^2A')$ states favor the excitation of a long progression in the C-S and S-H stretching modes, respectively. If several quanta of the C-S stretching mode are excited, the couplings between the C-S and CH_3 (SH) stretching modes should improve. It is known that collisional activation at the $E_{c.m.}$ range of this experiment is highly inefficient for electronic excitation.

The CID technique has been used extensively for bond dissociation energy determinations of ionic species.[49] The present study indicates that the CID technique would provide higher sensitivity for the determination of dissociation energies involving bonds of heavy atoms with lower vibrational frequencies. For a dissociation process that proceeds via a tight transition state or a stepwise dissociation mechanism, the experimental onset would most likely provide only an upper bound for the dissociation energy for the bond involved.[44]

Conclusions

We have examined the CID reaction of CH_3SH^+ + Ar in the $E_{c.m.}$ range of 2-36 eV. The fragment ions observed were in general agreement with those observed in previous charge exchange and photoionization studies. The most interesting observation of this CID study was that CH_3^+ + SH was found to be the dominant product channel, which is contrary to the QET prediction and results of previous charge exchange and photoionization measurements. Stemming from the fact that the dissociation energy for the CH_3-SH bond is greater than that of the H-CH_2SH^+ bond, this observation

clearly indicates non-statistical behavior in the CID of $CH_3SH^+(1^2A'')$. In effect, this system is an example of bond selective dissociation via collisional activation.

Acknowledgements

This work was supported by the National Science Foundation Grant No. ATM-9521558. S.S. acknowledges the GAANN Fellowship support for 1994-1995 and 1996-1997.

References

1. S. W. Benson, *Chem. Rev.* **78**, 23 (1978).
2. A. Levy, E. L. Merryman, W. T. Reid, *Environ. Sci. Technol.* **4**, 653 (1970).
3. C. F. Cullis, M. F. R. Mulcahy, *Combust. Flame* **18**, 225 (1975).
4. S. Hatakeyama, H. Akimoto, *J. Phys. Chem.* **87**, 2387 (1983).
5. A. A. Turnipseed, S. B. Barone, A. R. Ravishankara, *J. Phys. Chem.* **97**, 5926 (1993).
6. T. S. Bates, B. K. Lamb, A. Guenther, J. Dignon, and R. E. Stroiber, *J. Atmos. Chem.* **14**, 315 (1992).
7. P. A. Spiro, D. J. Jacob, and J. A. Logan, *J. Geophys. Res.* **97**, 6023 (1992).
8. R. J. Charlson and T. M. L. Wigley, *Sci. Am.* **270**, No. 2, 48 (1994).
9. C. Y. Ng, Advances in Photochemistry, **22**, 1 (1997); and references therein.
10. S.-W. Chiu, W.-K. Li, W.-B. Tzeng, and C. Y. Ng, *J. Chem. Phys.* **97**, 6557 (1992).
11. R. H. Nobes, W. J. Bouma, L. Radom, *J. Am. Chem. Soc.* **106**, 2774 (1984).
12. L. A. Curtiss, R. H.Nobes, J. A. Pople, and L. Radom, *J. Chem. Phys.* **97**, 6766 (1992).
13. D. Amos, R. G. Gills, J. L. Occolowitz, and J. F. Pisani, *Org. Mass Spectr.* **2**, 209 (1969).
14. B. G. Keyes and A. G. Harrison, J. Am. Chem. Soc. **90**, 5671 (1968); A. G. Harrison, *J. Am. Chem. Soc.* **100**, 4911 (1978).
15. D. C. Frost, F. G. Herring, A. Katrib, C. A. McDowell, and R. A. N. McLean, *J. Phys. Chem.* **76**, 1030 (1972).
16. S. Cradock and P. A. Whiteford, *J. Chem. Soc. Faraday II*, **68**, 281 (1972).

17. J. L. Holmes, F. P. Lossing, J. K. Terlouw, and P. C. Burgers, *J. Am. Chem. Soc.* **104**, 2931 (1982); J. K. Terlouw, W. Heerma, G. Dijkstra, J. L. Holmes, and P. C. Burgers, *Int. J. Mass Spectrom. Ion Phys.* **47**, 147 (1983); J. L. Holmes, F. P. Lossing, J. K. Terlouw, and P. C. Burges, *Can. J. Chem.* **61**, 2305 (1983).

18. "Handbook of Helium I Photoelectron Spectra of Fundamental Organic Molecules", edited by K. Kimura, S. Katsumata, Y. Achiba, T. Yamazaki, and S. Iwata (Halsted, New York, 1981).

19. M. E. Akopyan, Y. L. Serhiev, and F. I. Vilesov, *Klim. Vys. Energy* **4**, 305 (1970).

20. R. E. Kutina, A. K. Edwards, J. Berkowitz, *J. Chem. Phys.* **77**, 5508 (1982).

21. B.-Ö. Jonsson and J. Lind, *J. Chem. Soc. Faraday Trans. II* **70**, 1399 (1974).

22. S. Nourbakhsh, K. Norwood, H.-M. Yin, C.-L. Liao, and C. Y. Ng, *J. Chem. Phys.* **95**, 945 (1991).

23. Y.-S. Cheung, C.-W. Hsu, J.-C. Huang, W.-K. Li, and S.-W. Chiu, *Int. J. Mass Spectrom. Ion Proc.* **159**, 13 (1996).

24. C. Y. Ng, in "The Structure, Energetics, and Dynamics of Organic Ions", edited by T. Baer, C. Y. Ng, and I Powis, Wiley Series in Ion Chemistry and Physics (Wiley, Chichester, 1996), Chap. 2, p. 35; and references therein.

25. J. M. Nicovich, K. D. Kreutter, C. A. van Dijk, and P. H. Wine, *J. Phys. Chem.* **96**, 2516 (1992).

26. C.-W. Hsu and C. Y. Ng, *J. Chem. Phys.* **101**, 5596 (1994).

27. B. Ruscic and J. Berkowitz, *J. Chem. Phys.* **97**, 1818 (1992).

28. B. Ruscic and J. Berkowitz, *J. Chem. Phys.* **98**, 2568 (1993).

29. S. Nourbakhsh, K. Norwood, G.-Z. He, and C. Y. Ng, *J. Am. Chem. Soc.* **113**, 6311 (1991).

30. S. G. Lias, J. E. Bartmess, J. L. Holmes, R. D. Levin, and W. G. Mallard, *J. Phys. Chem.* Ref. Data, **17**, Supp. 1.

31. I. Fischer, A. Lochschmidt, A. Strobel, G. Niedner-Schatteburg, K. Muller-Dethlefs, and V. E. Bondybey, *J. Chem. Phys.* **98**, 3592 (1993).

32. C.-W. Hsu, D. BP. Baldwin, C.-L. Liao, and C. Y. Ng, *J. Chem. Phys.* **100**, 8047 (1994).

33. J. A. Blush, P. Chen, R. T. Wiedmann, M. G. White, *J. Chem. Phys.* **98**, 3557 (1993).

34. J.-D. Shao and C. Y. Ng, *J. Chem. Phys.* **84**, 4317 (1986); J.-D. Shao, Y. G. Li, G. D. Flesch, and C. Y. Ng, *J. Chem. Phys.* **86**, 170 (1987); G. D. Flesch and C. Y. Ng, *J. Chem. Phys.* **94**, 2372

(1991); G. D. Flesch, S. Nourbakhsh, and C. Y. Ng, *J. Chem. Phys.* **92**, 3490 (1990); G. D. Flesch and C. Y. Ng, *J. Chem. Phys.* **92**, 3235 (1990).

35. C. Y. Ng, in "State-Selected and State-to-State Ion-Molecule Reaction Dynamics: I. Experiment", edited by C. Y. Ng and M. Baer (Wiley, New York, 1992), *Adv. Chem. Phys.* **82**, p. 401-500.

36. X. Li, Y.-L. Huang, G. J. Flesch, and C. Y. Ng, *Rev. Sci. Instrum.* **65**, 3724 (1994); ibid. **66**, 2871 (1995).

37. X. Li, Y.-L. Huang, G. J. Flesch, and C. Y. Ng, *J. Chem. Phys.* **106**, 564 (1997).

38. H. M. Gibbs and E. D. Cummins, *Rev. Sci. Instrum.* **37**, 1385 (1966).

39. The non-resonant two photon PFI-PE spectrum for CH_3SH obtained in Ref. 34 also reveal a very small peak at 178 cm^{-1} (0.022 eV) above the IE of CH_3SH, which is assigned as excitation of the ν_1^+ (torsional) mode of $CH_3SH^+(1^2A'')$.

40. R. Linder, K. Müller-Dethlefs, E. Wedum, K. Haber, and E. R. Grant, *Science* **271**, 1698 (1996); L. A. Chewter, M. Sander, K. Müller-Dethlefs, and E. W. Schlag, *J. Chem. Phys.* **86**, 4737 (1987); R. Linder, H. Sekiya, B. Beyl, and K. Müller Dethelefs, *Angew Chem., Int. Ed. Engl.* **32**, 603 (1993); R. G. Neuhauser, K. Siglow, and H. J. Neusser, *J. Chem. Phys.* **106**, 896 (1997).

41. X. Li, Ph.D. Thesis, 1996, Iowa State University.

42. M. E. Weber, J. L. Elkind, and P. B. Armentrout, *J. Chem. Phys.* **84**, 1521 (1986).

43. B. H. Mahan, *J. Chem. Phys.* **52**, 5221 (1970).

44. P. de Sainte Claire, G. H. Peslherbe, and W. L. Hase, *J. Phys. Chem.* **99**, 8147 (1995); P. de Sainte Claire and W. L. Hase, *J. Phys. Chem.* **100**, 8190 (1996).

45. For CH_4S^+ species, the MP3/6-31G(d, p) energies were estimated by using additivity relationships (see Ref. 11).

46. The G2 energies for CH_3SH^+, (**2**), (**3**), and (**4**) are -437.800900, -437.723698, -437.723698, and -437.724606 hartree, respectively. See Ref. 11 for the structures of (**2**), and (**3**).

47. The structure of mass 47 ions formed in the CID $CH_3SH^+(1^2A'')$ at E_{cm} = 4.5-6.5 eV are probed in the charge exchange probing experiment. This E_{cm} range corresponds to the internal excitation energy range of 1-3 eV for $CH_3S^+(^3A_1)$.

48. The geometric parameters for the MP2/6-311G(d,p) structure of (**4**) are: r(CS) = 1.589 Å, r(SH) = 1.477 Å, r[CH(1)] = 3.079 Å, r[CH(2)] = r[CH(3)] = 1.091 Å, ∠CSH = 96.1°, ∠H(1)CS = 55.4°, ∠H(2)CS = 123.6°, ∠H(3)CS = 118.6°, ∠H(1)CSH = ∠H(2)CSH = 0.0°, ∠H(3)CSH = 180.0°, where r's and ∠'s are bond distances and bond angles, respectively. The transition structure id planar, with one of hydrogen atoms, H(1), originally bound to the C atom is stretched to combine with the H atom on the S atom. The S-H bond is increased by 0.12 Å from the equilibrium value in CH_3SH^-.

49. P. B. Armentrout and T. Baer, *J. Phys. Chem.* **100**, 12866 (1996).

Table 1. Current recommended experimental $\Delta_f H°_0$ and IE values for CH_3SH, CH_2SH_2, CH_2SH, CH_3S, CH_2S, CHS, CH_3, CH_2, CH_3SH^+, $CH_2SH_2^+$, CH_2SH^+, CH_3S^+, CH_2S^+, $HCSH^+$, CHS^+, CSH^+, CH_3^+, and CH_2^+.[a]

Species	$\Delta_f H°_0$ (kcal/mol)	IE (eV)
Neutrals		
CH_3SH	-3.0 ± 0.1[b,c]	9.4553 ± 0.0006[d]
CH_2SH_2	61.3[e]	7.48[e]
CH_2SH	37.7 ± 2.0[b]	7.536 ± 0.003[h]
CH_3S	31.4 ± 0.5[f]	9.2649 ± 0.0010[g]
		9.2330 ± 0.0010[g]
CH_2S	28.3 ± 2.0[h]	9.376 ± 0.003[h]
HCS	71.7 ± 2.0[h]	7.412 ± 0.007[h]
H_2S	-4.2 ± 0.2	10.4682 ± 0.0002[i]
HS	34.0 ± 0.6[f]	10.4218 ± 0.0004[j]
CH_3	35.6 ± 0.3	9.8380 ± 0.0004[k]
CH_2	93	10.396 ± 0.003
H	51.63	13.598
Cations		
CH_3SH^+	215.0 ± 0.1[b,d]	
$CH_2SH_2^+$	221, 233.8	
CH_2SH^+	211.5 ± 2.0[b]	
CH_3S^+	245.0 ± 0.5[f,g]	
CH_2S^+	244.5 ± 2.0[h]	
trans-$HCSH^+$	≈270,[l] 275[e]	
cis-$HCSH^+$	≈270,[l] 277[e]	
HCS^+	243.2 ± 1.9[h]	
CSH^+	314.6[e]	
H_2S^+	237.2 ± 0.2[e,i]	
HS^+	274.3 ± 0.6[f,j]	
CH_3^+	262.5 ± 0.3[e,k]	
CH_2^+	332	

a) Unless specified, the $\Delta_f H°_0$ and IE values are obtained from Ref. 30. b) Reference 27. c) Reference 30. d) Reference 23. e) Gaussian-2 calculations (see Ref. 12). f) Reference 25. g) Reference 26. h) Reference 28. i) Reference 31. j) Reference 32. k) Reference 33. l) References 20 and 30.

Table 2. Appearance energies determined in CID and photoionization and parameters [(E_0, σ_0, and n, see Eq. (12)] for the fittings of the CID cross sections for CH_2SH^- (CH_3S^-), CH_2S^-, CHS^-, CH_3^-, and CH_2^- near their onsets.

Product Ions	AE(CID)[a] (eV)	E_0[b] (eV)	σ_0 ($Å^2$)	n	Δ(PI)[c] (eV)
CH_2SH^-/CH_3S^-	3.9 ± 0.2	3.84	1.00	1.23	2.16[d] 1.8[e] 1.9[f]
CH_2S^-	5.0-5.5	4.65	0.02	1.74	1.15[d] 1.12[e] 1.34[f]
HCS^-	5.0-5.5	6.36	0.11	1.77	<4.15[d]
HS^-	5.5-6.0	5.85	0.12	1.47	—
CH_3^-	3.5 ± 0.2	3.37	2.44	1.28	3.90[d]
CH_2^-	5.0-6.0	6.50	0.08	1.54	—

a) This work. Appearance energy determined in the CID study of $CH_3SH^-(1^2A'') + Ar$. The uncertainties represent the precision of the measurements. The uncertainties for CH_2S^-, HCS^-, HS^-, CH_2^- are by the energy ranges given in the table.

b) See Eq. (12). E_0 is the onset or AE of the process involved.

c) Appearance energy AE(PI) determined in photoionization mass spectrometric studies of CH_3SH. Δ(PI) = AE(PI) - IE(CH_3SH).

d) Reference 20.

e) Reference 22.

f) Reference 19.

Table 3. Comparison of relative abundance in percentage[a] for CH_3SH^+, CH_2SH^+, CH_3S^+, CH_2S^+, CHS^+, CH_3^+, and CH_2^+ formed at excitation energies E_{ex} = 2.7-12 eV[b] in collisional activation (CA),[c] charge exchange (CE),[d] and photoionization (PI)[e].

E_{ex} (eV)	Expt.	CH_3^+ (15 amu)	HS^+ (33 amu)	HCS^+ (45 amu)	CH_2S^+ (46 amu)	CH_2SH^+ (47 amu)[f]	CH_3SH^+ (48 amu)
2.7	CE	0	0	0	2	98	3
	CA	**0**	**0**	**0**	**0**	**0**	—
4.0	CE	0	0	0	2	98	3
	CA	**85**	**0**	**0**	**0**	**15**	—
4-5	CE	2	0	10	6	82	1.5
	CA	**81**	**0**	**0**	**0**	**19**	—
6-7	CE	3	2	77	8	10	2
	CA	**76**	**1**	**1**	**1**	**21**	—
	PI	*3*	*1*	*22*	*6*	*68*	*30*
12	CE	3	4	71	10	6	5
	CA	**65**	**3**	**5**	**3**	**22**	—

a) The sum of the abundance for all product ions except that for CH_3SH^+ is set to 100%.

b) E_{ex} is the excitation of CH_3SH^+. $E_{ex} = E_{c.m.}$ in CID. RE - IE(CH_3SH) in charge exchange, and PHE - IE(CH_3SH) in photoionization, where RE and PHE are the recombination and photon energies, respectively.

c) This work. The numbers in bold fonts are CID values. The CID % abundance for CH_3SH^+ is not given in the table because CH_3SH^+ is the reactant ion. At E_{ex} = 12 eV, 2% of CH_2^+ is observed in CID.

d) Reference 21. The numbers in normal fonts are % abundance observed in charge exchange. At E_{ex} = 12 eV, 2% S^+ and 4% CS^+ are reported in Ref. 21.

e) Reference 20. The number in italics are % abundance observed in photoionization. At 800 and 744 Å, 0.03% of CH_4 is also observed in Ref. 20.

f) The structure of the mass 47 ion is expected to be CH_2SH^+. We cannot rule out the formation of CH_3S^+.

Figure Captions

Figure 1. Schematic diagram of the TQDO apparatus. (1) electron impact ionization ion source. (2) atomic or molecular nozzle beam. (3) to freon-trapped 6" diffusion pump (DP). (4) to liquid-nitrogen (LN_2)-trapped 6" DP. (5) reactant QMS. (6) lower RF octopole ion guide. (7) lower RFOIGGC. (8) to LN_2-trapped 6" DP. (9) the lower RF octopole ion guide chamber. (10) middle QMS. (11) upper RF octopole ion guide. (12) to LN_2-trapped 4" DP. (13) upper RF octopole ion guide chamber. (14) upper RFOIGGC. (15) product QMS. (16) detector chamber. (17) plastic scintillator window. (18) to LN_2-trapped 2" DP. (19) photomultiplier tube. (20) aluminum ion target.

Figure 2. (a) Absolute total cross section curves for CH_2SH^+ (CH_3S^+) (•), CH_2S^+ (O), HCS^+ (Δ), HS^+(∇), CH_3^+ (■), and CH_2^+ (□) formed in the CID reaction of CH_3SH^+ + Ar at E_{cm} = 2-36 eV. (b) Magnified absolute cross section curves for CH_2S^+(O), HCS^+(Δ), HS^+(∇), CH_3^+ (■), and CH_2^+ (□).

Figure 3. Mass spectrum in the mass range of m/e = 12-49 amu for the CID reaction of CH_3SH^+ + Ar obtained at E_{cm} = 7.3 eV. The mass peak for m/e = 48 amu has been scaled by a factor of 0.06.

Figure 4. Schematic of the potential energy profile for rearrangement and dissociation reactions for CH_3SH^+. For the detailed structures for transition structures (1), (2), and (3), readers are referred to Ref. 11. See Ref. 48 for the structure of (4). The energy for (2) is based on the photoionization AE for CH_2SH^+ (Ref. 20). The energies for (3) and (4) are based on G2 calculations, and that for (1) is from Ref. 11. The energies for other species are based on thermochemical data of Table 1. See the text.

Figure 5. Relative abundance in percentage for CH_2SH^+ (CH_3S^+) (•), CH_2S^+ (O), HCS^+ (Δ), HS^+(∇), CH_3^+ (■), and CH_2^+ (□) formed in the CID reaction of CH_3SH^+ + Ar at E_{cm} = 3.5-36 eV. The sum of all the product ions is arbitrarily set to 100%.

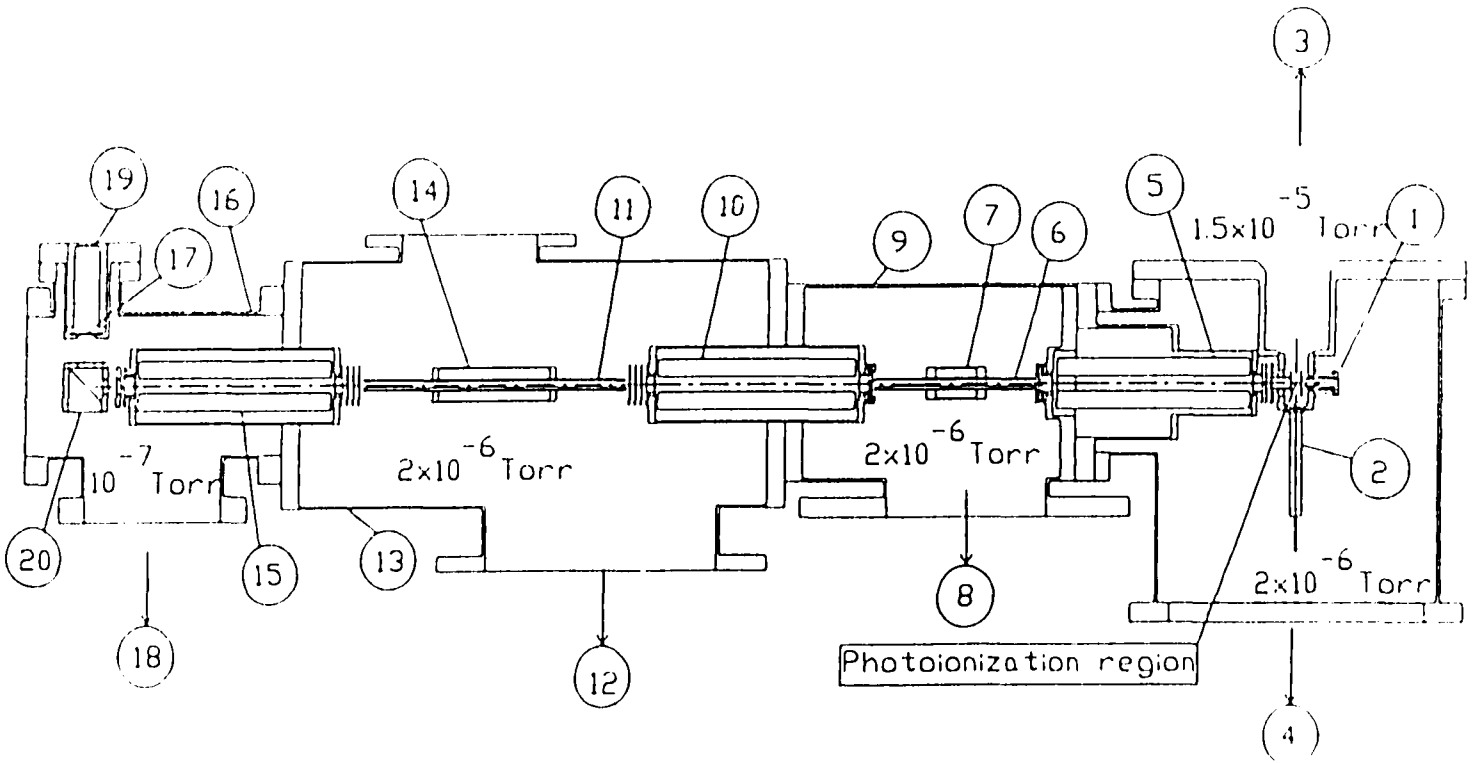
3
19
16
14
11
10
9
7
6
5
1.5x10 -5 Torr
1
17
10 -7 Torr
2x10 -6 Torr
2x10 -6 Torr
2
20
15
13
8
2x10 -6 Torr
18
12
Photoionization region
4

Figure 1.

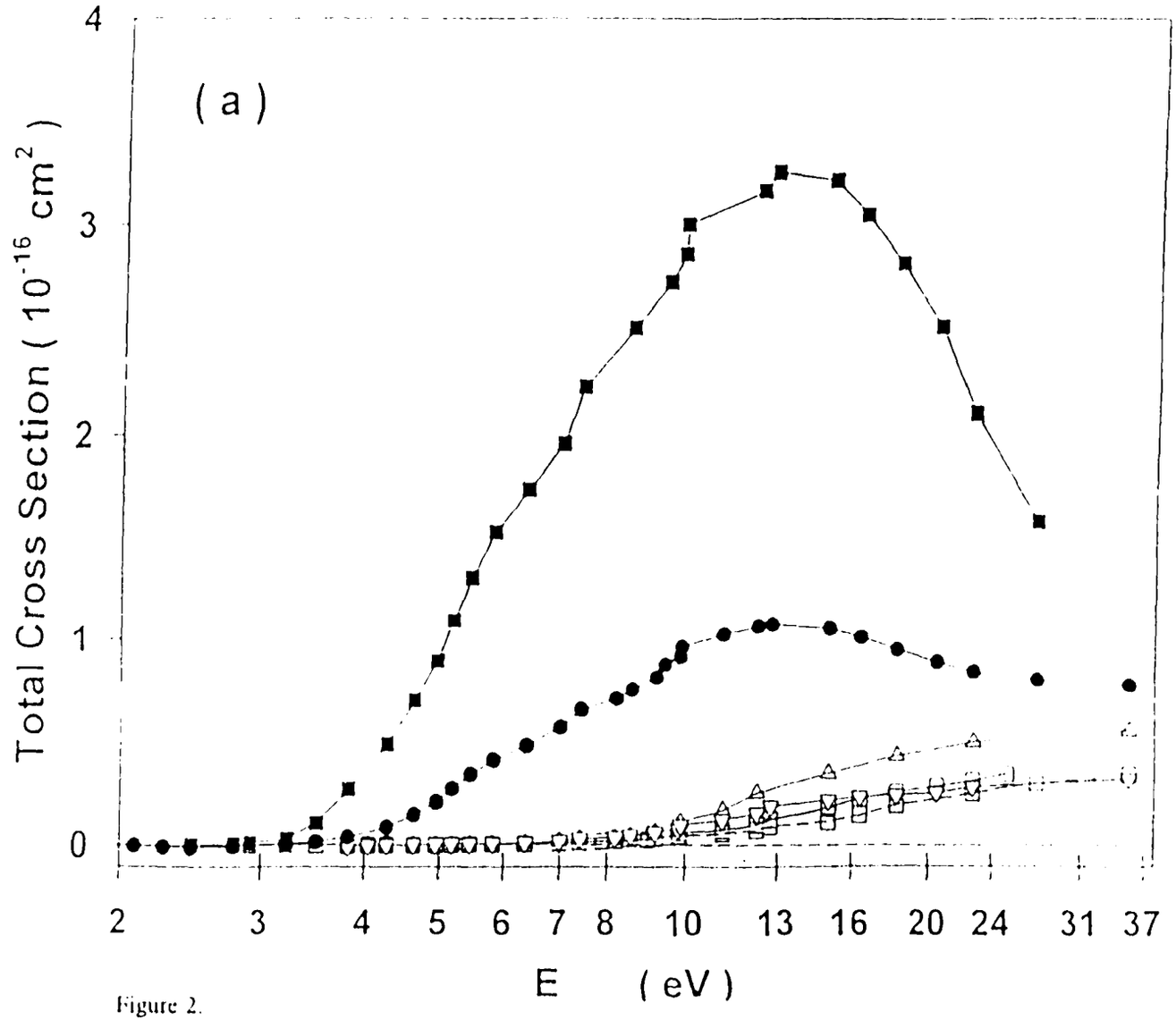
(a)
Total Cross Section (10^{-16} cm^2)
0
1
2
3
4
2
3
4
5
6
7
8
10
13
16
20
24
31
37
E (eV)

Figure 2.

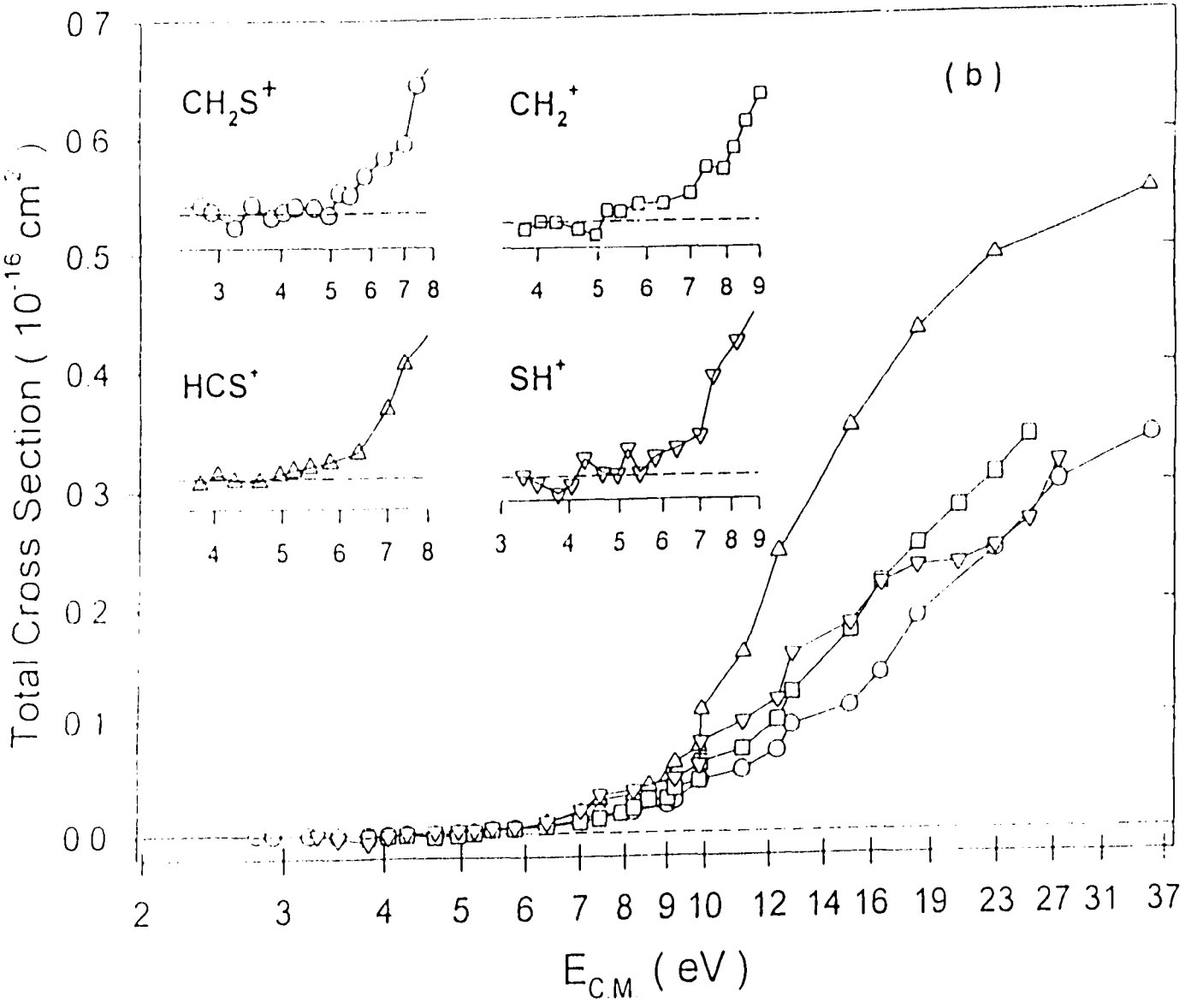

Figure 2. (continued)

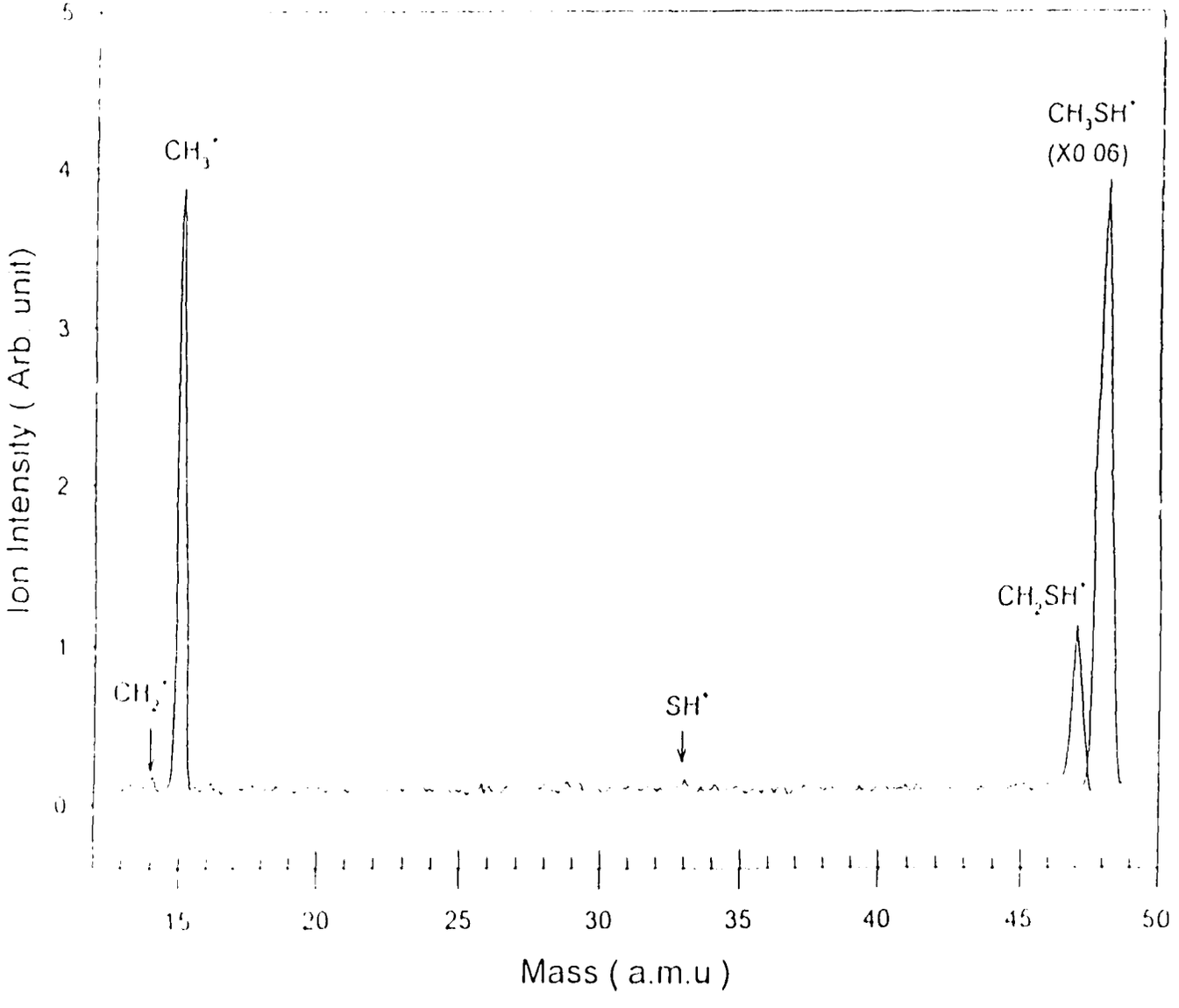
Ion Intensity (Arb. unit)
5
4
3
2
1
0
$CH_3^{\bullet}$
$CH_2^{\bullet}$
$SH^{\bullet}$
$CH_2SH^{\bullet}$
$CH_3SH^{\bullet}$
(X0 06)
15
20
25
30
35
40
45
50
Mass (a.m.u)

Figure 3.

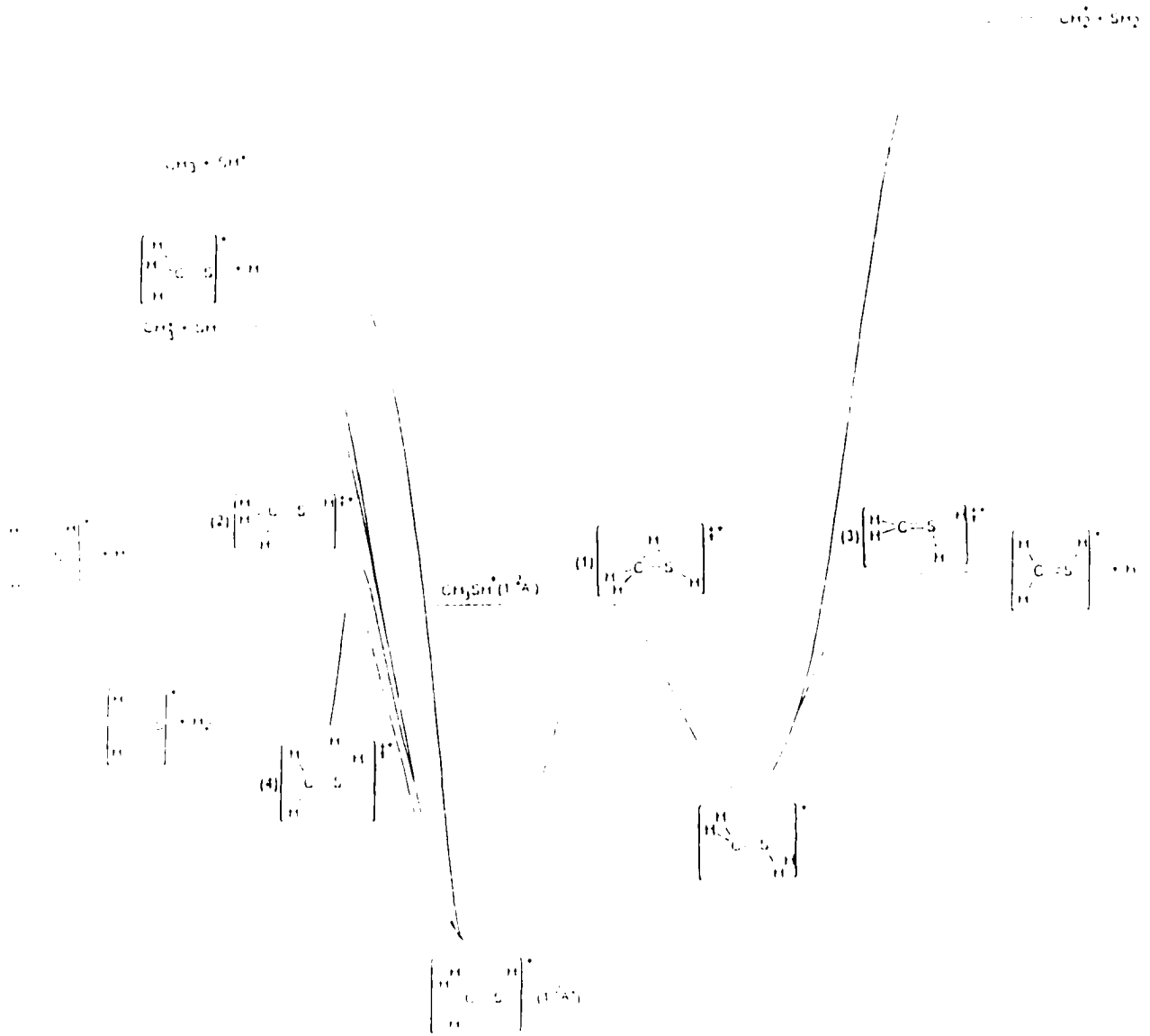

Figure 4

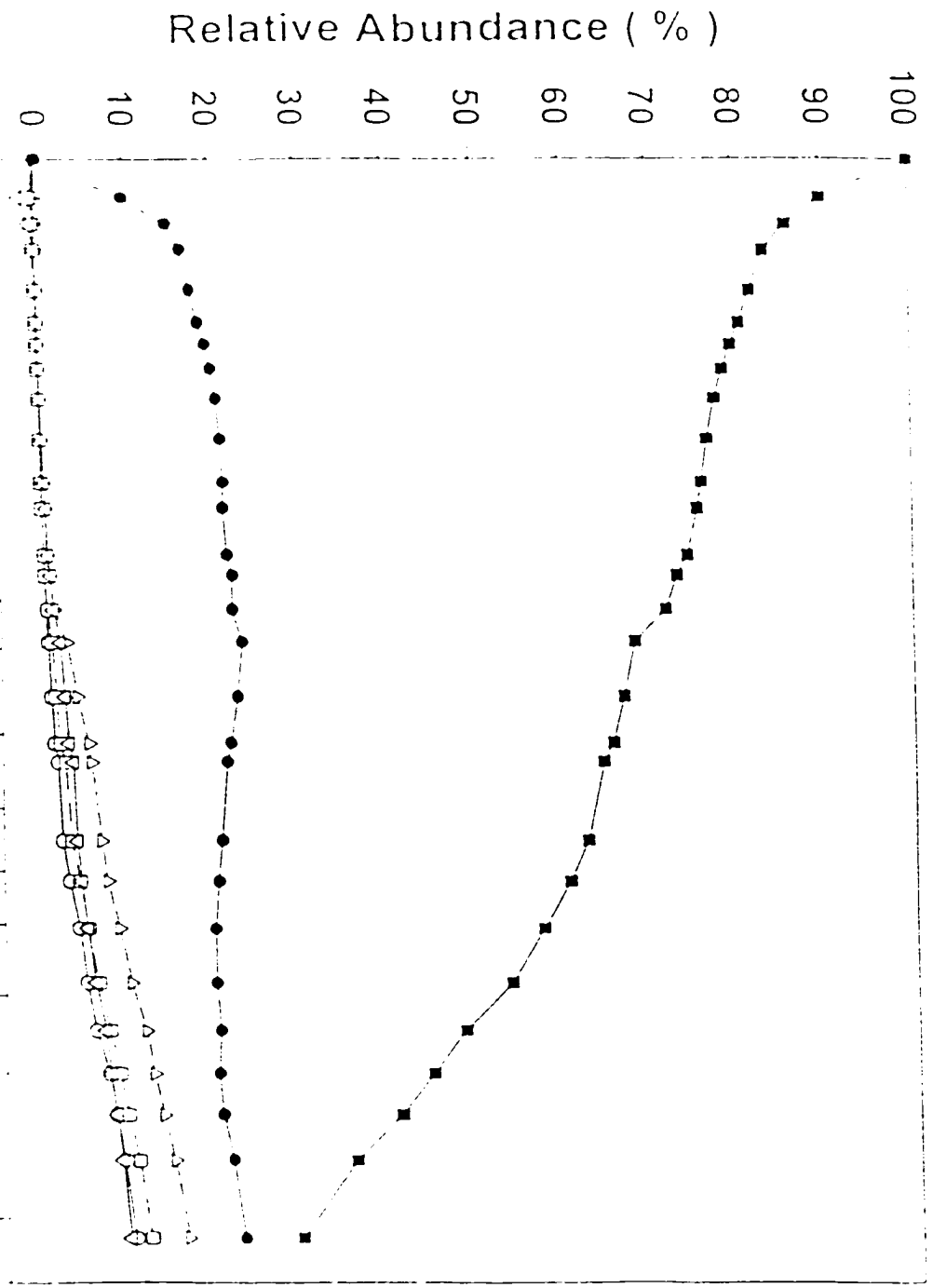
Relative Abundance (%)
0
10
20
30
40
50
60
70
80
90
100
4
5
6
7
8
9
10
12
14
16
18
21
25
29
34
E C.M. (eV)

Figure 5.

HIGH RESOLUTION VACUUM ULTRAVIOLET PULSED FIELD IONIZATION PHOTOELECTRON BAND FOR $OCS^+(X^2\Pi)$: AN EXPERIMENTAL AND THEORETICAL STUDY

A paper accepted by The Journal of Chemical Physics

S. Stimson,[1] M. Evans,[1] C.-W. Hsu,[2] P. Heimann,[2] C. Y. Ng,[1,4] C. Destandau,[3] G. Chambaud,[3] and P. Rosmus[3,4]

Abstract

The vacuum ultraviolet pulsed field ionization photoelectron (PFI-PE) band for $OCS^+(X^2\Pi)$ in the energy region of 11.09-11.87 eV has been measured using high-resolution monochromatic synchrotron radiation. The ionization energies (IEs) for the formation of the (0,0,0) $X^2\Pi_{3/2}$ and (0,0,0) $^2\Pi_{1/2}$ states of OCS^+ were determined to be 11.1831±0.0005 eV and 11.2286±0.0005 eV, respectively, yielding a value of 367±1.2 cm^{-1} for the spin-orbit splitting. Using the internally contracted multi-reference configuration interaction approach, three-dimensional potential energy functions (PEFs) for the $OCS^+(X^2\Pi)$ state have been generated and used in the variational Renner-Teller calculations of the vibronic states. The energies of all vibronic states (J=P) for J = 1/2, 3/2, 5/2, and 7/2 have been computed in the energy range of ≈4000 cm^{-1} above the IE[$OCS^+(X^2\Pi_{3/2})$] for the assignment of the experimental spectrum. By a minor modification of the *ab initio* PEFs, good correlation was found between the experimental and theoretical Renner-Teller structures. Similar to the PFI-PE bands for CO_2^+ ($X^2\Pi_g$) and $CS_2^+(X^2\Pi_g)$, weak transitions have been detected in the PFI-PE band for $OCS^+(X^2\Pi)$, which are forbidden in the Franck-Condon approximation. The non-vanishing single-photon ionization cross sections involving the excitation of the bending vibrational modes of OCS^+, CO_2^+, and CS_2^+ in their ground electronic states are attributed to the symmetries of the geometry dependent electronic transition dipole operator components.

[1] Ames Laboratory, USDOE and Department of Chemistry, Iowa State University, Ames, IA 50011, USA.

[2] Chemical Sciences Division and Advanced Light Source Accelerator and Fusion Research Division, Lawrence Berkeley National Laboratory, Berkeley, CA 94720, USA.

[3] Theoretical Chemistry Group, Université de Marne-la-Vallée, F-93166 Noisy le Grand, France.

[4] Authors to whom correspondence should be addressed. E-mail addresses: CYN: <CYNG@Ameslab.gov> and PR: <p@rosmus.univ-mlv.fr>.

Introduction

Carbonyl sulfide (OCS) is a linear molecule with the dominant ground state electronic configuration[1] ...$(6\sigma)^2 (7\sigma)^2 (8\sigma)^2 (9\sigma)^2 (2\pi)^4 (3\pi)^4$ $X^1\Sigma^+$. Taking into account the spin-orbit interaction, the removal of an electron from the highest occupied 3π-orbital (mostly having the sulfur 3p character)[1] results in the formation of the $OCS^+(X^2\Pi_{3/2,1/2})$ spin-orbit states. The OCS^+ cation has been investigated previously by many experimental techniques, including dispersed fluorescence,[2-7] laser-induced fluorescence,[8] photodissociation,[9] photoionization,[10,11] and HeI[12-15] and threshold photoelectron (TPE) spectroscopy.[11,16] High resolution spectroscopic data for the $OCS^+(X^2\Pi_{3/2,1/2})$ states have been obtained recently by laser ion photodissociation techniques.[17]

The accurate quantum mechanical calculations of the rovibronic levels for degenerate open shell electronic states of linear triatomic molecules, e.g., the $X^2\Pi_{3/2,1/2}$ states of CO_2^+, OCS^+, and CS_2^+, requires the consideration of interactions, such as the Renner-Teller effect due to the coupling of electronic, electron spin, and bending vibrational angular momenta.[18-20] One of the important goals of high resolution spectroscopic studies of these molecular ions has been to search for the rovibronic structures, which may be used as a sensitive test for *ab initio* calculations.[17-20] The Renner-Teller structures for $CO_2^+(X^2\Pi)$ and $CS_2^+(X^2\Pi)$ have been identified in detail in the recent pulsed field ionization photoelectron (PFI-PE) spectroscopic studies[21,22] of CO_2 and CS_2 at resolutions of 1-3 cm^{-1} (full-width-at-half-maximum, FWHM).

To date, experimental information about electronically degenerate open shell states of the triatomic molecules has not been sufficient to derive accurate three-dimensional potential energy functions (PEFs). Frequently, the shapes of such PEFs have been characterized only along an effective bending coordinate, which, however, cannot be used if strong anharmonic coupling effects are present. This is the case in the 15-valence-electron molecules such as CO_2^+, OCS^+, and CS_2^+.[23-25] Due to the lack of high resolution spectroscopic data for $OCS^+(X^2\Pi)$, even the one dimensional bending treatment of the Renner-Teller effect has not yet been reported.

We have obtained the vacuum ultraviolet (VUV) PFI-PE spectrum for OCS using the newly developed high resolution photoelectron spectrometer of the Chemical Dynamics Beamline at the Advanced Light Source (ALS).[26-29] We have also generated accurate three-dimensional PEFs for the two Renner-Teller components of the $OCS^+(X^2\Pi)$ state, and used them in variational calculations of the vibronic states. Similar theoretical calculations for $CO_2^+(X^2\Pi)$[23] and $CS_2^+(X^2\Pi)$[25] have been reported previously. On the basis of the comparison of experimental and theoretical results, we have satisfactorily assigned the Renner-Teller structures resolved in the $OCS^+(X^2\Pi)$ PFI-PE band. Furthermore, the comparison between experimental

PFI-PE features and theoretical predictions has resulted in some improvement of the three dimensional PEFs for the $OCS^-(X^2\Pi)$ state.

Experiment

The design and combined performance of the high resolution monochromatic VUV synchrotron source and the photoion-photoelectron apparatus has been described previously.[26-31] The high resolution VUV synchrotron source essentially consists of an undulator with a 10 cm period (U10), a gas harmonic filter, and a 6.65m off-plane Eagle mounted monochromator. The photon energy corresponding to the U10 undulator fundamental peak can be tuned easily to cover the energy range of 8-25 eV. Using Ne (pressure ≈ 30 Torr) as the filter gas in the present experiment, VUV radiation due to higher undulator harmonics with photon energy above the ionization energy (IE) of Ne (21.56 eV) was greatly suppressed (suppression factor = 10^{-4}) before entering the monochromator. Thus, the present experiment was essentially free from interference by photoionization and photoexcitation effects caused by higher order undulator radiation. The grating employed was an Os coated 4800 l/mm grating (Hyperfine Inc.) with a dispersion of 0.32 Å/mm.[26] The monochromator entrance/exit slits used vary in the range of 75-400 μm, which correspond to wavelength resolutions of 0.024-0.128 Å (FWHM).

The OCS sample was obtained from Aldrich Chemical Co. with a purity of greater than 96%. A continuous molecular beam of pure OCS was produced by supersonic expansion from a room temperature nozzle (diameter = 0.127 mm) at a stagnation pressure of ≈760 Torr. The molecular beam was skimmed by a home made conical skimmer (diameter = 1 mm) before intersecting the dispersed VUV photon beam 7 cm downstream in the photoionization region. The beam source chamber and photoionization chamber were evacuated by turbomolecular pumps with pumping speeds of 3000 l/s and 1200 l/s, respectively. During the experiment, the pressures in the beam source chamber and the photoionization chamber were maintained at $\approx 1\times10^{-4}$ and 2×10^{-6} Torr, respectively.

The experimental scheme designed for PFI-PE measurements using multibunch synchrotron radiation has been described in detail.[27,29,31] The key to the success of this method is the use of a high resolution [0.8 meV (FWHM)] zero kinetic energy photoelectron (ZEKE-PE) spectrometer for filtering prompt background electrons. The ZEKE-PE spectrometer used here consists of a steradiancy analyzer (drift length = 12.8 cm, entrance and exit apertures = 3 mm) and a hemispherical energy analyzer arranged in tandem. When the electron spectrometer is tuned to maximize the transmission of PFI-PEs, prompt electrons

slightly dispersed in space are greatly discriminated. Our analysis shows that for a stray field of ≈0.1 V/cm, it only requires a delay of ≈8 ns for prompt electrons to escape from the detection of the ZEKE-PE spectrometer. This in essence overcomes the requirement for a delay in the μs range as in laser PFI-PE studies.

The ALS synchrotron ring period is 656 ns. In a normal ALS multibunch (464 MHz) operation, the entire orbit contains 304 bunches or buckets. Each bunch has a duration of 50 ps. The separation between adjacent bunches is 2 ns. A 48-ns dark gap exists between adjacent ring periods for ejecting background ions in the ring orbit. In this experiment, the nominal dc electrostatic field at the photoionization region was zero by setting the repeller plates at the same potential before the application of the electric field pulse. The application of the electric field pulse (0.67 V/cm, 40 ns) is delayed by 8 ns with respect to the beginning of the 48-ns dark gap. Similar to the previous experiment,[27-29] the time interval between adjacent electric field pulses is 1.31 μs, or two synchrotron ring periods. After passing through the ZEKE-PE spectrometer, the PFI-PEs were detected by a two-stage microchannel plate detector. The hemispherical energy analyzer of the ZEKE-PE spectrometer is situated in the photoelectron chamber, which was evacuated by a turbomolecular pump with a pumping speed of 400 l/s. The pressure of the photoelectron chamber was maintained at 6-x10^{-7} Torr during the experiment. All electrostatic optics for electron detection were coated with graphite and enclosed by two layers of μ-metal shielding.

The OCS PFI-PE spectra were calibrated using the PFI-PE spectra of the $Kr^+(^2P_{3/2})$ and $Xe^+(^2P_{3/2})$ bands obtained at the same experimental conditions.[26-29] This calibration scheme assumes that the Stark shifts for IEs of OCS and the rare gases are identical. The calibration for the OCS PFI-PE spectrum was made before and after the experiment. Two well known Ar absorption lines at 11.6237 and 11.8282 eV due to the presence of a small impurity of Ar in the harmonic gas filter were identified, and were also used to calibrate the OCS PFI-PE spectrum. In this case, we have taken into account the Stark shift of the OCS PFI-PE peaks in the energy calibration. By comparing the results of these different calibration schemes and our previous experience of energy calibrations involving other experiments,[28,29,31] we estimate that the accuracy of the energy calibration is better than 1 meV.

The PFI-PE resolutions achieved are 0.6 and 1.2 meV (FWHM) using monochromator entrance/exit slits of 75 and 200 μm, respectively, as indicated by the PFI-PE spectra of Ar. We have examined the actual OCS PFI-PE resolutions when the monochromator slit sizes were varied from 75 to 400 μm. We find that the OCS spectra obtained in the photon energy range of 11.09-11.36 eV at

100, 150, and 200 μm are essentially identical with a width of ≈2.8 meV (FWHM). The actual resolution for the OCS PFI-PE spectrum achieved using 400 μm monochromator slits is ≈3.0-3.5 meV (FWHM), only slightly poorer than those obtained using 100-200 μm. Since an instrumental resolution of 0.7-1.0 meV used here is not capable of resolving rotational structures in the OCS spectrum, we believe that the actual resolution observed for the OCS PFI-PE spectrum is predominantly limited by rotational excitations due to a finite rotational temperature of the OCS molecular beam. Using similar supersonic expansion conditions, a rotational temperature of ≈100 K was observed for O_2.[29,31] The rotational temperature for OCS achieved here should be lower than that of O_2 because of the smaller rotational constants for OCS.

After replacing the home made skimmer with an electroformed skimmer (Beam Dynamics, Inc.), we have achieved a lower rotational temperature (≈50 K) for O_2.[31] We have reexamined the PFI-PE spectrum for OCS in the energy region of 11.155-11.292 eV using monochromator slits of 75 μm. The PFI-PE peaks thus measured have a width of 2.2 meV (FWHM).

Depending on the monochromator slit sizes used, the photon energy step size and counting time used at each photon energy were in the range of 0.15-0.5 meV and 1-10 s, respectively. The OCS spectra presented here have been recorded at least twice and the structures resolved in the spectrum were reproducible.

Electronic Structure Calculations

The electronic structure calculations were performed with complete active space self-consistent field (CASSCF)[32] and internally contracted multi-reference configuration interaction (MRCI)[33,34] approaches. For mapping the PEFs in three dimensions, the spdf(vqz) basis set[35] for O, C, and S has been used, which resulted in 142 contracted functions. The active space comprised all valence molecular orbitals except the lowest σ valence molecular orbital. For the MRCI calculations the reference wavefunctions were selected according to a coefficient threshold of 0.02 in the CASSCF configuration expansion. In the MRCI calculations all valence electrons were correlated. All electronic structure computations were done with the MOLPRO program suite.[36]

The calculated MRCI energies for 26 near equilibrium geometries were fit by quartic polynomial functions

$$V(R_1, R_2, \alpha) = \sum C_{ijk} (q_1)^i (q_2)^j (q_3)^k. \qquad (1)$$

In the PEFs the bond lengths R_1 and R_2, and the included angle α are expressed as linear combinations of the products $(q_1)^i(q_2)^j(q_3)^k$. The coordinates q_1 and q_2 have the form $q = r - r^{ref}$, and the coordinate $q_3 = \alpha - \alpha^{ref}$. The PEFs have been expanded at their computed linear equilibrium geometries, with $r^{ref}(CO) = 2.1344$ and $r^{ref}(CS) = 3.1112$ bohr. Symmetry restrictions demand k to be even. For $\alpha^{ref} = 180^\circ$, both the A' and A" components have a common part of the PEFs resulting in equal expansion coefficients for k=0. The expansion coefficients are given in Table 1. These analytical functions define the PEFs of OCS^+ in the geometry range 2.7 bohr $\leq r(CS) \leq$ 3.7 bohr, 1.8 bohr $\leq r(CO) \leq$ 2.8 bohr, and $130^\circ \leq \alpha \leq 180^\circ$. Some coefficients have been modified in order to improve agreement with structures observed in the high resolution PFI-PE spectrum. In the original *ab initio* MRCI PEFs these coefficients were: $C_{200} = 0.137147$, $C_{020} = 0.593042$, and $C_{002}(A') = 0.050910$ and $C_{002}(A'') = 0.065543$.

The PEF expansions have been used to calculate the quartic force field in internal coordinates, which have been transformed by the *l*-tensor algebra to the quartic force fields in dimensionless normal coordinates. The force field of OCS^+ is compared with similar force fields of CO_2^+ and CS_2^+ in Table 2. We refer to the previous work[37] where such force fields for other 15-valence-electron molecules are discussed. These data allow the calculation of effective spectroscopic constants frequently used in the interpretation of Renner-Teller spectra, such as the Renner-Teller splitting parameter ε, the Fermi resonance parameters W_1 and W_2, and the g_4 constants describing the anharmonic effects along the effective bending coordinate. In the present case, the parameter ε has been calculated to be -0.225. In other 15 valence degenerate electronic ground states the ε varies between -0.190 (CO_2^+) and -0.124 (NCO). For OCS^+, the value is larger, but experience has shown that the *ab initio* ε-values are usually slightly too small. So far, there is not enough experimental data to improve the present PEFs along the bending coordinate. The rotational constant B_0 in the (0,0,0) $^2\Pi_{3/2}$ ground state has been determined[17] to be 0.1936 cm^{-1}, and our calculated value is 0.1932 cm^{-1}, which is in very good agreement with this latest measurement (all α_r values are calculated to be smaller 0.001 cm^{-1}).

In the Renner-Teller variational calculations, the approach of Carter and Handy has been employed, in which the full dimensionality, anharmonicity, rotation-vibration, and electronic and spin angular momenta coupling effects are accounted for (cf. Refs. 38 and 39 for details). In the present application the basis set was comprised of 15 one-dimensional harmonic oscillator functions for each stretching mode and 41 associated Legendre polynomials for the bending mode. The effective spin-orbit parameter A_{so} has been kept constant ($A_{so}^{eff} = -374.2$ cm^{-1}). This value reproduced the experimental splitting between the (0,0,0) $^2\Pi_{3/2}$ and (0,0,0) $^2\Pi_{1/2}$ states well. Here (0,0,0) represents the ($v_1^+=0$, $v_2^+=0$, $v_3^+=0$) level, where v_1^+, v_2^+, and v_3^+ are the harmonic vibrational quantum numbers for the C-S stretching mode, the bending mode, and the C-O

stretching mode of OCS^+, respectively. In the Hamiltonian, the $A_{so}LS$ term has been replaced by $A_{so}L_zS_z$. The L_x and L_y operators and the variation of the L_z and L_z^2 operators have been neglected. The expectation values of the L_z and L_z^2 operators were set to unity. Such approximations can be considered to be well founded as demonstrated[18,20] for CO_2^+ and CS_2^+.

Results and Discussion

Experimental VUV-PFI-PE spectrum for OCS

Figures 1(a) and 1(b) show the PFI-PE spectrum for OCS in the energy region of 11.09-11.87 eV obtained using monochromator slits of 200 and 400 μm. As mentioned above, the observed width of 2.5-2.8 meV (FWHM) for the PFI-PE peaks are believed to be limited by the rotational temperature (≈100 K) of the OCS gas sample. A section of this spectrum in the energy region of 11.155-11.292 eV measured using a colder OCS sample (rotational temperature ≈50 K) and monochromator slits of 75 μm is plotted in Fig. 2. The PFI-PE peak widths observed in this spectrum are 2.2 meV (FWHM). However, the structures resolved in the spectra of Figs. 1(a) and 2 are essentially identical.

The strong features observed in these figures are similar to those reported in previous TPE and HeI photoelectron spectroscopic studies.[11,15,16] However, the fine structures between the strong peaks in the PFI-PE spectra were not observed in these previous experiments. Since rotational transitions[17] are not resolved in this experiment, the observed PFI-PE peak contours are mainly the result of overlapping rotational branches in the photoionization transition. The rotational profiles appear to shade toward the red, consistent with the fact that the C-S bond distance in $OCS^+(X^2\Pi)$ is longer than that in $OCS(X^1\Sigma^+)$.

Theoretical predictions of Renner-Teller vibronic levels

For a linear molecule, such as $OCS^+(X^2\Pi)$, with v_2^+ bending quanta, the vibrational angular momenta along the molecular axis can have values $l_v\hbar$, where $l_v = v_2^+, v_2^+-2, \ldots, 1$, or 0. Since the electronic orbital angular momentum has a nonzero projection of $\Lambda\hbar$ along the molecular axis, the Renner-Teller coupling between Λ and l_v forms a new quantum number, $K = |\Lambda \pm l_v|$. Including coupling of the projection of the spin angular momentum on the molecular axis (Σ), the projected angular momentum is $P = \Lambda + l_v + \Sigma$. In Table 3, the calculated vibronic levels for the electronic ground state of OCS^+ are given for energies up to ≈4000 cm^{-1} above the (0,0,0) $X^2\Pi_{3/2}$ ground state. In the present work, we have performed calculations for J = 1/2, 3/2, 5/2, and 7/2, i.e., K could take values 0, 1, 2, and 3 (Σ, Π, Δ, and Φ vibronic states), and only the J=P levels (each having its own rotational stack) are given. The μ levels can be approximately associated

with the lower potential component (A'), and the κ levels with the higher one (A''). The energies [Δν(theo) in cm^{-1}] in Table 3 for the vibronic levels, (v_1^+, v_2^+, v_3^+) $^2\Sigma_{1/2}^+$ ($^2\Sigma_{1/2}^+$, $^2\Pi_{v2,1/2}$, $^2\Delta_{v2,5/2}$, and $^2\Phi_{v2,7/2}$), of the $OCS^+(X^2\Pi)$ state are given with respect to the energy of the (0,0,0) $^2\Pi_{3/2}$ level.

Due to the Renner-Teller coupling and the strong anharmonic resonances, the assignments of the calculated vibronic levels of $OCS^+(X^2\Pi)$ to (v_1^+, v_2^+, v_3^+) harmonic vibrational states are not straightforward except for the levels lying within ≈1700 cm^{-1} above the (0,0,0) $X^2\Pi_{3/2}$ state of OCS^+. The harmonic vibrational quantum numbers were attributed to particular states by inspection of the contour plots for both vibrational parts and the weights of the basis functions in the vibronic wavefunctions. In the $^2\Sigma$ states, we could assign all levels to Fermi polyads, even though in some cases the $^2\Sigma^+$ members of a polyad were found to interact with different $^2\Sigma^-$ members of another polyad. The same situation is found in the $^2\Pi$ and $^2\Delta$ states, where in some cases strong interactions between different polyads in the μ and κ states exist. In the $^2\Phi_{5/2}$ states the distinction between the μ and κ states is hardly possible and, therefore, has not been included in the assignment of the PFI-PE peaks of the OCS spectrum shown in Figs. 1(a) and 1(b). We find also in many cases K-coupling (i.e., the $^2\Pi$ states mix with the $^2\Delta$ states etc.). A reliable analysis of this effect requires more accurate PEFs than those of the present work. Referring to Table 3, the levels with the corresponding unique level designations are marked by asterisks. Fermi polyad members are designated by a, b, c....etc. The numerical value, such as 05, designates $v_3^+ = 0$, and $2v_1^+ + v_2^+ = 5$ (i.e., polyad five) etc. The prime in, e.g., 07', designates the upper Renner-Teller polyad. The equal sign means that the level belongs to two polyads. Generally, for all higher energy levels the assignments with harmonic quantum numbers are only tentative.

As an example, we show in Fig. 3 the three members of the $2v_1^+ + v_2^+ = 5$ polyad in the $^2\Delta_{5/2}$ symmetry. The unique level (2,1,0) shows hardly any mixing with the two other members (1,3,0), and (0,5,0), which exhibit a strong anharmonic resonance. For illustration also, a $^2\Phi_{7/2}$ level, at 3758 cm^{-1} which belongs to a polyad 10, is depicted in Fig. 4. In this case the assignment with vibrational quantum numbers v_1^+ and v_2^+ becomes practically meaningless.

Assignment of Renner-Teller structures in the VUV-PFI-PE band for OCS

Since the Renner-Teller states were not known, along with the relatively low photoelectron energy resolutions used, the photoelectron spectra for OCS reported previously have not yet been assigned in terms of the Renner-Teller vibronic states.[11-16] The tentative assignments were made previously for separate $^2\Pi_{3/2}$ and $^2\Pi_{1/2}$ stacks, and the fact that the C-S bond becomes longer than the C-O bond in the ion relative to the

neutral molecule was used to attribute the intense progression to the C-S stretching mode and the less intense progression to the C-O stretching mode.[15] Many spectroscopy techniques, such as ion photodissociation[17] and dispersed fluorescence,[2-7] are capable of providing information about part of the existing vibronic states in $OCS^+(X^2\Pi)$ ground state. In comparison, the high resolution single-photon TPE and PFI-PE spectroscopic techniques are the most general for detection of the Renner-Teller states.[19,21,22] As shown below, many such states have been detected in the present PFI-PE experiment.

In accordance with previous assignments, the strong PFI-PE features can be ascribed to the $(v_1^+, 0, v_3^+)$ levels of the $^2\Pi_{3/2}$ and $^2\Pi_{1/2}$ symmetries,[11,15,16] where v_1^+=0-2 and v_3^+=0-2 are observed [see Figs. 1(a) and 1(b)]. As shown in Fig. 2, the first peaks of these symmetry levels at 11.1831±0.0005 eV and 11.2286±0.0005 eV are assigned to be the ionization energies (IE) for the formation (0, 0, 0) $X^2\Pi_{3/2}$ and (0, 0, 0) $^2\Pi_{1/2}$ states of OCS^+, respectively, from the ground $OCS(X^1\Sigma^+)$ state, yielding a value of 367.0±1.2 cm^{-1} for the spin-orbit splitting. These IE values and the spin-orbit splitting represent the average of two independent measurements. We find that the energy calibrations by using the Ar absorption lines (11.6237 and 11.8282 eV) and the PFI-PE bands for the rare gas atoms [$Xe^+(^2P_{3/2})$, $Kr^+(^2P_{3/2})$, and $Ar^+(^2P_{3/2})$] are in agreement with a deviation of <0.8 meV. The IE values determined here are lower than those obtained in the previous HeI photoelectron measurement of Wang *et al.*[15] and the TPE study of Frey *et al.*[16], but higher than the TPE study of Delwiche *et al.*[11] The spin-orbit splitting obtained here has an uncertainty determined by the photon energy step size (0.15 meV) used in the experiment, and is in excellent agreement with the value of 368 cm^{-1} obtained by Kakoschke *et al.*[40]

Table 4 lists the photon energies of the PFI-PE peaks resolved in Figs. 1(a), 1(b), and 2. By comparing the peak energies [$\Delta\nu$(expt) in cm^{-1}] with respect to the (0, 0, 0) $^2\Pi_{3/2}$ to the $\Delta\nu$(theo) values calculated for the Renner-Teller states, we have assigned the PFI-PE peaks to ionization transitions as shown in Table 4. These assignments are also marked in Figs. 1(a) and 1(b). Interestingly, all the PFI-PE structures can be assigned to unique Renner-Teller levels as indicated by asterisks in Table 3. We note that the assignments of the weak, unresolved PFI-PE features marked by "sh" in Table 4 are tentative and require future experimental confirmation. With a few exceptions of the weak PFI-PE structures, where their $\Delta\nu$(expt) values deviate from the corresponding $\Delta\nu$(theo) values by 20-34 cm^{-1}, the deviations found for other PFI-PE peaks are less than 20 cm^{-1}. In fact, the majority of the theoretical predictions are within 10 cm^{-1} of the experimental observations. Considering that the PFI-PE peak positions may not be the origin of the photoelectron bands, we conclude that the assignments are satisfactory. This good comparison of the experimental and theoretical results implies that other predicted vibronic states, which are not observed in the

present experiment, should have the similar error bound of about 10 cm^{-1}. The calculated Renner-Teller levels should be valuable for future spectroscopic studies of $OCS^+(X^2\Pi)$.

The (3, 0, 0) $^2\Pi_{3/2}$ and (3, 0, 0) $^2\Pi_{1/2}$ states are predicted to lie 24 and 13 cm^{-1} lower than the (0, 0, 1) $^2\Pi_{3/2}$ and (0, 0, 1) $^2\Pi_{1/2}$ states, respectively. On the basis of the observed trend of the Franck-Condon factors for the (v_1^+, 0, 0) $^2\Pi_{3/2,1/2}$ states, v_1^+=0-2, we expect that the PFI-PE bands for the (3, 0, 0) $^2\Pi_{3/2,1/2}$ states are weak. The weak PFI-PE bands for these states are likely buried under the low energy shoulders of the strong PFI-PE bands for the (0, 0, 1) $^2\Pi_{3/2,1/2}$ states.

The v_1(C-S) stretching, v_2 bending, and v_3(C-O) stretching frequencies for $OCS(X^1\Sigma^+)$ are 859, 520, and 2062 cm^{-1}, respectively.[41] At room temperature, we expected the population for v_1=1 to be ≈1.5%, while that for v_2=1 to be ≈7.5%. Since the beam expansion conditions used in the present experiment are inefficient for vibrational relaxation, we expect that hot band transitions originating from v_1=1 and v_2=1 are observable in the PFI-PE spectrum of OCS. As shown in Figs. 1(a) and 1(b), PFI-PE peaks due to the transitions, 2_1^0, 1_1^1, $1_0^1 2_1^0$, $2_1^0 3_0^1$, and $1_0^1 2_1^0$, are clearly identified for the $^2\Pi_{3/2}$ and $^2\Pi_{1/2}$ symmetry states.

Additional weaker PFI-PE peaks can be attributed to the ionization transitions to the $^2\Sigma_{1/2}^+$, $^2\Sigma_{1/2}^-$, $^2\Delta_{3/2}$, and $^2\Delta_{5/2}$ symmetry states. All of these states involve excitation of the v_2^+ mode of $OCS^+(X^2\Pi)$. The presence of hot bands starting from the bending mode of the neutral molecule gives additional information about the position of the bending levels reflecting the Renner-Teller coupling. It is clear from the spectrum of Figs. 1(a) and 1(b) that PFI-PE peaks due to the transitions, 2_1^1, 2_0^1, $1_0^1 2_1^1$, $1_0^1 2_0^1$, $1_0^2 2_1^1$, $1_0^2 2_0^1$, $1_0^3 2_1^1$, $2_0^1 3_0^1$, and $1_0^1 2_1^1 3_0^1$ etc. are identifiable. The inspection of the calculated vibronic levels in Table 3 shows that in some cases the observed peaks could be attributed to several close lying states. For example, the peak at 11.4885 eV could contain the states (3,1,0) $^2\Sigma^+$ and (3,1,0) $^2\Delta_{5/2}$ (see Table 4).

In the direct photoionization transition between a linear neutral and a linear ionic state, the bending modes of ungerade symmetry are not Franck-Condon active. Only if in the region of the observed vibrational progression these bending modes are coupled to the stretching modes, for instance, in Fermi polyads, information about the polyad members including the bending can be observed in a direct photoionization process according to the Franck-Condon approximation. The electronic ground state of OCS^+ exhibits strong anharmonic resonances of the above type, nonetheless not in the lowest part of the spectrum. The fact that for instance, the weak peak at 11.2351 eV corresponding to the 2_0^1 transition has been unambiguously assigned, means that the corresponding photoionization cross section, though small, is not negligible. The inspection of the vibronic wavefunctions shows that the $\Sigma_{1/2}$ levels belong to a large and extend to just one

PEF component. This assignment implies that the Franck-Condon approximation, which would predict zero intensity for this transition is not valid.

As discussed below, the reason why several transitions of this type (e.g., 2_1^0, 2_0^1....) are seen can be attributed to the dependence of the electronic part of the integral for the photoionization cross section on the bending coordinate. The integral determining the photoionization cross section contains the three Cartesian components of the dipole operator. The electronic transition dipole component along the bending coordinate changes sign along the positive or negative displacement along the bending coordinate. Hence, this component in the one-dimensional picture is of ungerade symmetry, as are the one-dimensional cuts of the vibrational bending modes with odd quantum numbers. This is why the transition becomes weakly allowed, as observed also in the photoelectron bands for the electronic ground state of CO_2^+ and CS_2^+.[19-22] It has been argued previously that the autoionization from a Rydberg state or Herzberg-Teller intensity borrowing might be responsible for this effect, which, however, can be simply explained, as given above, by the geometry dependence of the electronic transition dipole operator. Mixings in the Rydberg manifold could be partially responsible for the appearance of these bending excitations. These effects have been and are still discussed actively in the high resolution PFI-PE literature.[17,42] The fact that Renner-Teller components have been found in Rydberg spectra of OCS implies that Renner-Teller components can also be found in the photoelectron band of $OCS^+(X^2\Pi)$.[42-45] We note that the detailed assignment of the vibronic bands for $CO_2^+(X^2\Pi_g)$, $OCS^+(X^2\Pi)$ and $CS_2^+(X^2\Pi_g)$ represents an important step for using VUV photoionization to prepare mode-specific $CO_2^+(X^2\Pi_g)$, $OCS^+(X^2\Pi)$ and $CS_2^+(X^2\Pi)$ reactant ions for ion-neutral reaction dynamics studies.[46]

The weak PFI-PE features observed in the energy range of 11.75-11.87 eV have not been assigned. As pointed out above, the theoretical calculations indicate the Renner-Teller states at this energy range are highly mixed states and the assignment to one set of (v_1^+, v_2^+, v_3^+) harmonic frequencies is not meaningful. The PFI-PE peaks at 11.7861 eV [Δv(expt) = 4863 cm^{-1})] and 11.8233 eV [Δv(expt) = 5163 cm^{-1}] most likely correspond to the 11.7835 eV [Δv(expt)= 4825 cm^{-1}] and 11.8284 eV [Δv(expt)=5187 cm^{-1}] photoelectron bands reported in a previous HeI study.[15] We note that these latter photoelectron bands were assigned as $(1,0,2)\ ^2\Pi_{3/2}$ and $(1,0,2)\ ^2\Pi_{1/2}$ by Wang et al.[15]

Conclusions

We have obtained a high resolution PFI-PE spectrum for OCS in the energy range of 11.09-11.87 eV. In addition to strong photoelectron bands assigned to $(v_1^+, 0, v_3^+)\ ^2\Pi_{3/2}$ and $(v_1^+, 0, v_3^+)\ ^2\Pi_{1/2}$ for $OCS^+(X^2\Pi)$, weaker Renner-Teller structures were observed for the first time. Accurate theoretical predictions for the

Renner-Teller levels for the $OCS^+(X^2\Pi)$ state have also been obtained. The observed transitions in the PFI-PE spectrum were assigned satisfactorily by using the calculated energy positions of the vibronic levels.

Acknowledgements

This work was supported by the Director, Office of Energy Research, Office of Basic Energy Sciences, Chemical Science Division of the U.S. Department of Energy under Contract No. W-7405-Eng-82 for the Ames Laboratory, Contract No. DE-AC03-76SF00098 for the Lawrence Berkeley National Laboratory and the EC Grant ERFMRXCT960088. The electronic structure calculations were made on CRAY computers at the computer center of IDRIS and UMLV. M.E. acknowledges the GAANN Fellowship for 1994-1997 and Dow Chemical Fellowship for 1997, and S.S. acknowledges the GAANN Fellowship for 1994-1997.

References

1. M.-J. Hubin-Franskin, J. Delwiche, P.-M. Guyon, M. Richard-Viard, M. Lavollée, O. Dutuit, J.-M. Robbe, and J.-P. Flament, *Chem. Phys.* **209**, 143 (1996).
2. M. Horani, S. Leach, and J. Rostas, *J. Chim. Phys.* **63**, 1015 (1966).
3. J. P. Maier and F. Thommen, *Chem. Phys.* **51**, 319 (1980).
4. D. L. Judge and M. Ogawa, *J. Chem. Phys.* **51**, 2035 (1969).
5. D. L. Judge and L. C. Lee, *Int. J. Mass Spectrom. Ion Proc.* **17**, 329 (1975).
6. C. Y. R. Wu, T. S. Yih, and D. L. Judge, *Int. J. Mass Spectrom. Ion Proc.* **68**, 303 (1986).
7. M. Tsuji and J. P. Maier, *Chem. Phys. Lett.* **137**, 421 (1987).
8. M. Ochsner, M. Tsuji, and J. P. Maier, *Chem. Phys. Lett.* **115**, 373 (1985).
9. R. Kakoschke, U. Boesl, J. Herman, and E. W. Schlag, *Chem. Phys. Lett.* **119**, 467 (1985).
10. Y. Ono, E. A. Osuch and C. Y. Ng, *J. Chem. Phys.* **74**, 1645 (1981).
11. J. Delwiche, M. J. Hubin-Franskin, G. Caprace, P. Natalis, and D. Roy, *J. Electron Spectrosc. Relat. Phenom.* **21**, 205 (1980).
12. C. R. Brundle and D. W. Turner, *Int. J. Mass Spectrom. Ion Phys.* **2**, 195 (1969).
13. A. W. Potts and G. H. Fattahallah, *J. Phys.* **B13**, 2545 (1980).
14. B. Kovac, *J. Chem. Phys.* **78**, 1684 (1983).

15. L.-S. Wang, J. E. Reutt, Y. T. Lee, and D. A. Shirley, *J. Electron Spectrosc. Relat. Phenom.* **47**, 167 (1988).

16. R. Frey, B. Gotchev, W. B. Peatman, H. Pollak, and E. W. Schlag, *Int. J. Mass Spectrom. Ion Phys.* **26**, 137 (1978).

17. R. Weinhauf and U. Boesl, *J. Chem. Phys.* **101**, 8482 (1994).

18. M. Brommer, G. Chambaud, E.-A. Reinsch, P. Rosmus, A. Spielfieldel, N. Feautrier, H.-J. Werner, *J. Chem. Phys.* **94**, 8070 (1991).

19. P. Baltzer, F. T. Chau, J. H. D. Eland, L. Karlsson, M. Lundqvist, J. Rostas, K. Y. Tam, H. Veenhuizen, and B. Wannberg, *J. Chem. Phys.* **104**, 8922 (1996).

20. M. Brommer and P. Rosmus, *J. Chem. Phys.* **98**, 7746 (1993).

21. F. Merkt, S. R. Mackenzie, R. J. Rednall, and T. P. Softley, *J. Chem. Phys.* **99**, 8430 (1993).

22. J.-C. Huang, Y.-S. Cheung, M. Evans, C.-X. Liao, C. Y. Ng, C.-W. Hsu, P. Heimann, H. Lefebvre-Brion, and C. Cossart-Magos, *J. Chem. Phys.* **106**, 864 (1997).

23. G. Chambaud, W. Gabriel, P. Rosmus, and J. Rostas, *J. Phys. Chem.* **96**, 3285 (1992).

24. M. Brommer and P. Rosmus, *J. Chem. Phys.* **98**, 7748 (1993).

25. M. Brommer and P. Rosmus, *Chem. Phys. Lett.* **206**, 540 (1993).

26. P. Heimann, M. Koike, C.-W. Hsu, M. Evans, K. T. Lu, C. Y. Ng, A. Suits, and Y. T. Lee, *Rev. Sci. Instrum.* **68**, 1945 (1997).

27. C.-W. Hsu, M. Evans, C. Y. Ng, P. Heimann, *Rev. Sci. Instrum.* **68**, 1694 (1997).

28. C.-W. Hsu, M. Evans, P. Heimann, K. T. Lu, and C. Y. Ng, *J. Chem. Phys.* **105**, 3950 (1996).

29. C.-W. Hsu, M. Evans, S. Stimson, C. Y. Ng, and P. Heimann, *J. Chem. Phys.* **106**, 8931 (1997).

30. M. Evans, C. Y. Ng, C.-W. Hsu, and P. Heimann, *J. Chem. Phys.* **106**, 978 (1997).

31. C.-W. Hsu, P. Heimann, M. Evans, S. Stimson, and C. Y. Ng, *Chem. Phys.*, submitted.

32. P. J. Knowles and H.-J. Werner, *Chem. Phys. Lett.* **115**, 259 (1985).

33. H.-J. Werner and P. J. Knowles, *J. Chem. Phys.* **89**, 5803 (1988).

34. P. J. Knowles and H.-J. Werner, *Chem. Phys. Lett.* **145**, 514 (1988).

35. T. H. Dunning, *J. Chem. Phys.* **90**, 1007 (1989).

36. MOLPRO is a package of *ab initio* programs written by H.-J. Werner, P. J. Knowles, with contributions from J. Almlöf, R. D. Amos, M. J. O. Deegan, S. T. Elbert, C. Hampel, W. Meyer, K. Peterson, R. Pitzer, A. J. Stone, and P. R. Taylor.

37. H. Gritli, G. Chambaud, M. Brommer, and P. Rosmus, *J. Chim. Phys.* **91**, 151 (1994).

38. S. Carter and N. C. Handy, *Mol. Phys.* **52**, 1367 (1984).

39. S. Carter, N. C. Handy, P. Rosmus, and G. Chambaud, *Mol. Phys.* **71**, 608 (1990).

40. R. Kakoscke U. Boesl, J. Hermann, and E. W. Schlag, *Chem. Phys. Lett.* **119**, 467 (1985).

41. G. Herzberg, "Molecular Spectra and Molecular Structure III" (van Nostrand, Princeton, 1966); G. Guelachvili and K. N. Rao, "Handbook of Infrared Standards" (Academic, New York, 1986).

42. R. Weinkauf and U. Boesl, *J. Chem. Phys.* **98**, 4459 (1993).

43. B. Yang, M. H. Eslami, and S. L. Anderson, *J. Chem. Phys.* **89**, 5527 (1988).

44. B. Leclerc, A. Poulin, D. Roy, M.-J. Hubin-Franskin, and J. Delwiche, *J. Chem. Phys.* **75**, 5329 (1981).

45. I. Kopp, *Can. J. Phys.* **45**, 4001 (1967).

46. S. L. Anderson, in "State-Selected and State-to-State Ion-Molecule Reaction Dynamics, Part 1: Experiment", edited by C. Y. Ng and M. Baer (Wiley, New York, 1992), *Adv. Chem. Phys.* **82**, p. 177.

Table 1. Expansion coefficients of the three dimensional near equilibrium potential energy functions for the two Renner-Teller components of the $X^2\Pi$ state of OCS^- (in atomic units).

Lower component A′					
C_{000}	-510.501 559	C_{200}	0.145 000	C_{110}	0.084 661
C_{020}	0.585 000	C_{002}	0.043 000	C_{300}	- 0.159 504
C_{210}	-0.093 958	C_{120}	0.030 851	C_{030}	- 0.741 174
C_{102}	-0.034 119	C_{012}	- 0.027 903	C_{400}	0.093 695
C_{310}	0.167 354	C_{220}	- 0.145 212	C_{130}	0.003 467
C_{040}	0.331 148	C_{202}	0.032 713	C_{112}	0.033 281
C_{022}	0.004 398	C_{004}	- 0.002 769		
Upper component A″					
C_{000}	-510.501 559	C_{200}	0.145 000	C_{110}	0.084 661
C_{020}	0.585 000	C_{002}	0.068 000	C_{300}	- 0.159 504
C_{210}	-0.093 958	C_{120}	0.030 851	C_{030}	- 0.741 174
C_{102}	-0.054 048	C_{012}	- 0.025 803	C_{400}	0.093 695
C_{310}	0.167 354	C_{220}	- 0.145 212	C_{130}	0.003 467
C_{040}	0.331 148	C_{202}	0.025 160	C_{112}	0.080 255
C_{022}	-0.016 556	C_{004}	- 0.001 515		

Table 2. Quartic force field of the lower A′ (upper A″) component of the $X^2\Pi$ states of OCS^-, CO_2^-, and CS_2^- in dimensionless normal coordinates.[a]

	OCS^-	CO_2^-	CS_2^-
ω_1	708.7	1284.5	647.0
ω_2	395.8 (497.8)	461.4 (564.8)	313.1 (374.9)
ω_3	2124.2	1397.9	1200.4
ϕ_{111}	-232.4	-328.1	-111.7
ϕ_{333}	-747.9	—	—
ϕ_{122}	84.2 (47.1)	268.7 (192.4)	119.0 (86.3)
ϕ_{223}	379.1 (303.1)	—	—
ϕ_{133}	-80.7	-599.2	-347.17
ϕ_{113}	80.8	—	—
ϕ_{1111}	60.2	27.5	14.23
ϕ_{2222}	227.6 (133.7)	177.5 (104.0)	80.4 (47.2)
ϕ_{3333}	89.8	1924.9	400.7
ϕ_{1122}	-21.8 (-16.7)	-92.1 (-70.9)	-28.1 (-21.5)
ϕ_{2233}	-189.9 (-157.0)	-128.1 (-120.3)	-76.2 (-72.8)
ϕ_{1133}	-13.9	109.3	42.6
ϕ_{1113}	-13.5	—	—
ϕ_{1223}	-2.8 (1.6)	—	—
ϕ_{1333}	37.8	—	—

a) All values are in cm^{-1}. Factorials have been excluded.

Table 3. Predicted energies for vibronic levels (v_1^-, v_2^-, v_3^-) $^2\Sigma_{1/2}^-$ ($^2\Sigma_{1/2}^-$, $^2\Pi_{v2\,1/2}$, $^2\Delta_{v2\,5/2}$, $^2\Phi_{v2\,7/2}$) of the $OCS^-(X^2\Pi)$ state.[a,b]

(v_1^-, v_2^-, v_3^-)	$\Delta\nu$(theo) (cm^{-1})	(v_1^-, v_2^-, v_3^-)	$\Delta\nu$(theo) (cm^{-1})
$^2\Sigma_{1/2}^-$		$^2\Sigma_{1/2}^-$	
(0,1,0)	418.8	(0,1,0)	837.0
(1,1,0)	1103.1	(1,1,0)	1528.0
(0,3,0)	1249.1	(0,3,0)	1763.8
(2,1,0) a 05	1782.3	(2,1,0) a 05'	2208.5
(1,3,0) b 05	1919.0	(1,3,0) b 05'/07	2435.2
(0,5,0) c 05	2072.1	(0,5,0) c 05'/07	2672.1
(3,1,0) a 07	2457.6	(3,1,0) a 07'	2882.1
(0,1,1)	2488.9	(0,1,1)	2906.4
(2,3,0) b 07	2580.7	(2,3,0) b 07'/09	3098.1
(1,5,0) c 07	2759.6	(1,5,0) c 07'/09	3313.4
(0,7,0) d 07	2897.1	(4,1,0) a 09'	3552.0
(4,1,0) a 09	3128.1	(1,1,1)	3597.8
(1,1,1)	3172.9	(0,7,0) d 07'/09	3743.9
(3,3,0) b 09	3235.1	(3,3,0) b 09'/011	3754.6
(0,3,1)	3313.4	(0,3,1)	3826.9
(2,5,0) c 09/07'	3431.9	(2,5,0) c 09'/011	4088.5
(0,9,0) d 09	3499.8		
(1,7,0) e 09/07'	3653.6		
(5,1,0) a 011/09'	3793.2		
(2,1,1) a 15	3853.6		
(4,3,0) b 011/09'	3883.2		
(3,5,0) c 011	3966.2		
(1,3,1) b 15	3984.8		
(2,7,0) d 011/15	4127.3		
(0,5,1) c 15	4135.5		
$^2\Pi_{v2}$		$^2\Pi_{1/2}$	
*(0,0,0)	0.0	*(0,0,0)	368.1
*(1,0,0)	691.2	(0,2,0)μ	847.2
(0,2,0)μ	836.3	*(1,0,0)	1063.4
(0,2,0)κ	1306.6	(0,2,0)κ	1284.4
*(2,0,0) a 04 = a 04'	1374.4	(1,2,0)μ	1521.7
(1,2,0)μ b 04	1511.4	(0,4,0)μ	1673.0
(0,4,0)μ c 04	1657.4	*(2,0,0) a 04'	1750.3
(1,2,0)κ b 04'	1990.4	(1,2,0)κ b 04'	1969.9
*(3,0,0) a 06 = a 06'	2050.4	(2,2,0)μ a 06/04'	2187.1

Table 3. (continued)

*(0,0,1)	2074.6	(0,4,0)κ c 04'/06	2213.5
(2,2,0)μ b 06	2178.7	(1,4,0)μ b 06	2241.5
(0,4,0)κ c 04'/06	2241.5	*(3,0,0) c 06 = a 06'	2429.1
(1,4,0)μ c 06	2325.8	*(0,0,1)	2442.0
(0,6,0)μ d 06	2476.3	(0,6,0)μ d 06	2498.1
(2,2,0)κ b 06'	2666.6	(2,2,0)κ b 06'	2647.8
*(4,0,0) a 08 = a 08'	2720.3	(3,2,0)μ a 08/06'	2845.4
*(1,0,1)	2765.0	(1,4,0)κ c 06'/08	2885.0
(3,2,0)μ b 08	2836.1	(0,2,1)μ	2914.2
(0,2,1)μ	2903.7	(2,4,0)μ b 08/06'	3002.1
(1,4,0)κ c 06'/08	2908.3	(0,6,0)κ d 06'/08	3086.5
(2,4,0)μ c 08/06'	2987.6	*(4,0,0) c 08 = a 08'	3102.2
(1,6,0)μ d 08	3096.9	*(1,0,1)	3137.7
(0,6,0)κ d 06'/08	3213.5	(1,6,0)μ d 08/06'	3203.0
(0,8,0)μ e 08/06'	3300.6	(3,2,0)κ b 08'	3317.8
(3,2,0)κ b 08'	3335.8	(0,8,0)μ e 08/06'	3332.4
(0,2,1)κ	3372.5	(0,2,1)κ	3350.6
*(5,0,0) a 010 = a 010'	3385.2	(3,4,0)μ a 010/08'	3497.6
*(2,0,1) a 14	3451.2	(4,2,0)μ b 010/08'	3547.8
(3,4,0)μ b 010	3489.2	(1,2,1)μ	3588.5
(4,2,0)μ c 010/08'	3567.3	(1,8,0)μ c 010/08'	3654.5
(1,2,1)μ b 14	3578.8	(2,6,0)μ d 010	3724.2
(2,4,0)κ c 08'/010	3642.7	(0,4,1)μ	3736.0
(0,4,1)μ c 14	3720.0	*(5,0,0) e 010 = a 010'	3769.2
(2,6,0)μ d 010	3732.9	*(2,0,1)	3828.2
(1,6,0)κ d 08'	3890.8	(1,6,0)κ c 08'	3880.5
(0,10,0)μ e 010	3905.1	(0,10,0)μ f 010	3909.2
(4,2,0)κ b 010'	3998.9	(4,2,0)κ b 010'	3983.6
		(1,2,1)κ	4036.7

$^{2}\Delta_{52}$ $^{2}\Delta_{52}$

*(0,1,0)	437.6	*(0,1,0)	793.7
*(1,1,0)	1119.9	(0,3,0)μ	1279.5
(0,3,0)μ	1255.9	*(1,1,0)	1488.0
(0,3,0)κ	1773.5	(0,3,0)κ	1721.0
*(2,1,0) a 05 = a 05'	1796.0	(1,3,0)μ a 05	1947.6
(1,3,0)μ b 05	1921.8	(0,5,0)μ b 05	2104.6
(0,5,0)μ c 05	2069.8	*(2,1,0) c 05 = a 05'	2173.5
(1,3,0)κ b 05'/07	2448.5	(1,3,0)κ b 05'	2402.1
*(3,1,0) a 07 = a 07'/05'	2468.4	(1,5,0)μ a 07/05'	2604.0
*(0,1,1)	2507.5	(0,5,0)κ c 05'	2642.9

Table 3. (continued)

˙(1,5,0)˙μ b 07/05˙	2579.8	(2,3,0)μ b 07	2773.6
(0,5,0)κ c 05˙/07	2695.3	*(3,1,0) c 07 = a 07˙	2853.2
˙(0,7,0)μ c 07/05˙	2753.4	*(0,1,1)	2864.1
˙(2,3,0)˙μ d 07	2884.2	(0,7,0)μ d 07	2932.9
(2,3,0)κ b 07˙/09	3112.7	(2,3,0)κ b 07˙	3075.6
*(4,1,0) a 09 = a 09˙/07˙	3138.3	(2,5,0)μ a 09/07˙	3253.8
*(1,1,1)	3189.3	(3,3,0)μ b 09/07˙	3305.4
˙(2,5,0)˙μ b 09	3231.8	(0,3,1)μ	3343.5
(0,3,1)μ	3320.6	(1,7,0)μ c 09/07˙	3434.1
(3,3,0)μ c 09/07˙	3342.4	(0,9,0)μ d 09	3499.9
(1,5,0)κ c 07˙/09	3423.1	*(4,1,0) e 09 = a 09˙	3526.5
˙(0,9,0)˙μ d 09	3507.9	*(1,1,1)	3558.7
˙(1,7,0)˙ μ e 09/07˙	3675.3	˙(1,5,0)˙κ c 07˙/09	3643.7
(0,7,0)κ d 07˙/09	3716.4	(3,3,0)κ b 09˙/011	3742.3
(4,3,0)μ a 011/09˙	3769.6	(0,7,0)κ d 07˙/09	3777.2
*(5,1,0) b 011 = a 011˙/09˙	3804.4	(0,3,1)κ	3783.9
(0,3,1)κ	3836.4	(2,7,0)μ a 011/09˙	3899.0
*(2,1,1) a 15 = a 15˙	3865.4	(4,3,0)μ b 011/09˙	3961.2
˙(3,5,0)˙μ c 011/15	3880.4	(1,3,1)μ	4011.1
˙(2,7,0)˙μ d 011/15	3981.7		
(1,3,1)μ b 15	3990.7		

$^{2}\Phi_{72}$

*(0,2,0)	870.2
*(1,2,0) a 04 = a 04˙	1541.8
(0,4,0)μ b 04	1673.7
*(2,2,0) a 06 = a 06˙	2205.5
(0,4,0)κ b 04˙	2242.5
˙(1,4,0)˙μ b 06	2333.4
˙(0,6,0)˙μ c 06	2488.7
˙(2,4,0)˙μ a 08	2861.1
˙(1,4,0)˙κ b 06˙	2919.2
*(0,2,1)	2936.9
*˙(3,2,0)˙ b 08 = a 08˙	2986.7
(0,6,0)κ c 06˙	3211.3
(1,6,0)μ c 08/06˙	3296.2
(3,4,0)μ a 010	3514.5
˙(2,4,0)˙κ b 08˙/010	3586.7
*(1,2,1) a 14	3606.4
*(4,2,0) b 010/08˙	3629.8
(0,4,1)μ b 14	3737.3

$^{2}\Phi_{v2}$

*(0,2,0)	1210.7
(0,4,0)	1716.5
*(1,2,0)	1907.1
(0,6,0) a 06	2150.0
(1,4,0) b 06/08	2375.2
(0,8,0) a 08/06	2538.9
*(2,2,0) c 06	2596.8
(1,6,0) b 08	2826.7
(2,4,0) c 08/010	3022.2
(0,10,0) a 010/08	3067.2
(1,8,0) b 010/012/08	3207.2
*(3,2,0) d 08/12	3274.0
*(0,2,1) a 12	3279.3
(0,12,0) a 012/010	3372.1
(2,6,0) c 010/012/08	3495.1
(2,8,0) b 012/010/014	3664.7
(3,4,0) d 010/012/014	3722.8
(0,4,1)	3777.8

Table 3. (continued)

c 010^{z}	3757.8	(1,12,0)	a 014/012/010	3867.6
d 010^{z}	3876.8	(0,14,0)	b 014/012/010	3912.6
e $010'$	3923.5	*(4,2,0)	e 010/012	3951.1
		*(1,2,1)		3974.8

x) Fermi polyad members are designated by a, b, c,... etc. The numerical values, such as 05, designates $v_3' = 0$, and $2v_1' + v_2' = 5$ (i.e., polyad five) etc. The prime, in e.g., 07', designates the upper Renner-Teller component. The equal sign means that the level belongs to two polyads.

y) The unique levels are marked with *.

z) No dominant basis functions could be attributed to these levels; all assignments given in parentheses with quotation marks are only tentative.

Table 4. Assignments of the high resolution VUV-PFI-PE spectrum of $OCS^-(X^2\Pi)$.

Photon energy (eV)	$\Delta\nu$(expt.) (cm^{-1})	$\Delta\nu$(theo.) (cm^{-1})	Assignments (v_1^-, v_2^-, v_3^-)$\leftarrow$(v_1, v_2, v_3)
11.1192	-515	-520	$(0,0,0)^2\Pi_{3/2} \leftarrow (0,1,0)^1\Pi$
11.1589	-195	-168	$(1,0,0)^2\Pi_{3/2} \leftarrow (1,0,0)^1\Sigma^-$
11.1645	-150	-152	$(0,0,0)^2\Pi_{1/2} \leftarrow (0,1,0)^1\Pi$
11.1710	-98	-102	$(0,1,0)^2\Sigma^- \leftarrow (0,1,0)^1\Pi$
(11.1728 sh)[a]	-82	-82	$(0,1,0)^2\Delta_{5/2} \leftarrow (0,1,0)^1\Pi$
11.1831	0.0	0.0	$(0,0,0)^2\Pi_{3/2} \leftarrow (0,0,0)^1\Sigma^-$
11.2050	177	171	$(1,0,0)^2\Pi_{3/2} \leftarrow (0,1,0)^1\Pi$
(11.2083, sh)[a]	203	204	$(1,0,0)^2\Pi_{1/2} \leftarrow (1,0,0)^1\Sigma^-$
11.2171	274	273	$(0,1,0)^2\Delta_{3/2} \leftarrow (0,1,0)^1\Pi$
11.2286	367	368	$(0,0,0)^2\Pi_{1/2} \leftarrow (0,0,0)^1\Sigma^-$
11.2351	419	419	$(0,1,0)^2\Sigma^- \leftarrow (0,0,0)^1\Sigma^-$
(11.2373, sh)[a]	433	438	$(0,1,0)^2\Delta_{5/2} \leftarrow (0,1,0)^1\Sigma^-$
11.2507	545	543	$(1,0,0)^2\Pi_{1/2} \leftarrow (0,1,0)^1\Pi$
11.2562	590	583	$(1,1,0)^2\Sigma^- \leftarrow (0,1,0)^1\Pi$
		600	$(1,1,0)^2\Delta_{5/2} \leftarrow (0,1,0)^1\Pi$
11.2693	695	691	$(1,0,0)^2\Pi_{3/2} \leftarrow (0,0,0)^1\Sigma^-$
11.2813	792	794	$(0,1,0)^2\Delta_{3/2} \leftarrow (0,0,0)^1\Sigma^-$
(11.2860, sh)[a]	830	837	$(0,1,0)^2\Sigma^- \leftarrow (0,0,0)^1\Sigma^-$
11.2878	844	854	$(2,0,0)^2\Pi_{3/2} \leftarrow (0,1,0)^1\Pi$
11.3030	967	968	$(1,1,0)^2\Delta_{3/2} \leftarrow (0,1,0)^1\Pi$
11.3153	1066	1063	$(1,0,0)^2\Pi_{1/2} \leftarrow (0,0,0)^1\Sigma^-$
11.3197	1102	1103	$(1,1,0)^2\Sigma^- \leftarrow (0,0,0)^1\Sigma^-$
(11.3205, sh)[b]	1108	1120	$(1,1,0)^2\Delta_{5/2} \leftarrow (0,0,0)^1\Sigma^-$
11.3352	1227	1230	$(2,0,0)^2\Pi_{1/2} \leftarrow (0,1,0)^1\Pi$
11.3408	1272	1262	$(2,1,0)^2\Sigma^- \leftarrow (0,1,0)^1\Pi$
		1276	$(2,1,0)^2\Delta_{5/2} \leftarrow (0,1,0)^1\Pi$
11.3546	1383	1374	$(2,0,0)^2\Pi_{3/2} \leftarrow (0,0,0)^1\Sigma^-$
11.3667	1481	1488	$(1,1,0)^2\Delta_{3/2} \leftarrow (0,0,0)^1\Sigma^-$
11.3718	1522	1528	$(1,1,0)^2\Sigma^- \leftarrow (0,0,0)^1\Sigma^-$
11.3769	1563	1555	$(0,0,1)^2\Pi_{3/2} \leftarrow (0,1,0)^1\Pi$
11.3888	1659	1654	$(2,1,0)^2\Delta_{3/2} \leftarrow (0,1,0)^1\Pi$
11.3946	1706	1688	$(2,1,0)^2\Sigma^- \leftarrow (0,1,0)^1\Pi$
11.4009	1757	1750	$(2,0,0)^2\Pi_{1/2} \leftarrow (0,0,0)^1\Sigma^-$
(11.4044, sh)[a]	1784	1782	$(2,1,0)^2\Sigma^- \leftarrow (0,0,0)^1\Sigma^-$
11.4056	1795	1796	$(2,1,0)^2\Delta_{5/2} \leftarrow (0,0,0)^1\Sigma^-$
11.4201	1912	1922	$(0,0,1)^2\Pi_{1/2} \leftarrow (0,1,0)^1\Pi$
(11.4236, sh)[a]	1940	1938	$(3,1,0)^2\Sigma^- \leftarrow (0,1,0)^1\Pi$
11.4251	1952	1948	$(3,1,0)^2\Delta_{5/2} \leftarrow (0,1,0)^1\Pi$

Table 4. (continued)

(11.4373, pd)[b]	—	2050	$(3,0,0)^2\Pi_{3/2} \leftarrow (0,0,0)^1\Sigma^+$
11.4396	2069	2075	$(0,0,1)^2\Pi_{3/2} \leftarrow (0,0,0)^1\Sigma^+$
11.4529	2176	2174	$(2,1,0)^2\Delta_{3/2} \leftarrow (0,0,0)^1\Sigma^+$
11.4720	2330	2344	$(0,1,1)^2\Delta_{3/2} \leftarrow (0,1,0)^1\Pi$
(11.4843, pd)[b]	—	2429	$(3,0,0)^2\Pi_{1/2} \leftarrow (0,0,0)^1\Sigma^+$
11.4846	2432	2442	$(0,0,1)^2\Pi_{1/2} \leftarrow (0,0,0)^1\Sigma^+$
(11.4885, sh)[a]	2463	2458	$(3,1,0)^2\Sigma^+ \leftarrow (0,0,0)^1\Sigma^+$
		2468	$(3,1,0)^2\Delta_{5/2} \leftarrow (0,0,0)^1\Sigma^+$
(11.4928, sh)[a]	2498	2489	$(0,1,1)^2\Sigma^+ \leftarrow (0,0,0)^1\Sigma^+$
		2508	$(0,1,1)^2\Delta_{5/2} \leftarrow (0,0,0)^1\Sigma^+$
11.5115	2649	2669	$(1,1,1)^2\Delta_{5/2} \leftarrow (0,1,0)^1\Pi$
11.5260	2766	2765	$(1,0,1)^2\Pi_{3/2} \leftarrow (0,0,0)^1\Sigma^+$
11.5424	2898	2906	$(0,1,1)^2\Sigma^+ \leftarrow (0,0,0)^1\Sigma^+$
11.5577	3021	3039	$(1,1,1)^2\Delta_{3/2} \leftarrow (0,1,0)^1\Pi$
11.5714	3132	3138	$(1,0,1)^2\Pi_{1/2} \leftarrow (0,0,0)^1\Sigma^+$
(11.5741, sh)[a]	3154	3138	$(4,1,0)^2\Delta_{5/2} \leftarrow (0,0,0)^1\Sigma^+$
(11.5776, sh)[a]	3182	3189	$(1,1,1)^2\Delta_{5/2} \leftarrow (0,0,0)^1\Sigma^+$
11.5893	3276	3284	$(5,1,0)^2\Delta_{5/2} \leftarrow (0,1,0)^1\Pi$
11.5952	3324	3345	$(2,1,1)^2\Delta_{5/2} \leftarrow (0,1,0)^1\Pi$
11.6109	3450	3451	$(2,0,1)^2\Pi_{3/2} \leftarrow (0,0,0)^1\Sigma^+$
11.6233	3550	3559	$(1,1,1)^2\Delta_{3/2} \leftarrow (0,0,0)^1\Sigma^+$
11.6268	3579	3580	$(0,0,2)^2\Pi 3/2 \leftarrow (0,1,0)^1\Pi$
11.6509	3773	3804	$(5,1,0)^2\Delta_{5/2} \leftarrow (0,0,0)^1\Sigma^+$
11.6563	3816	3828	$(2,0,1)^2\Pi_{1/2} \leftarrow (0,0,0)^1\Sigma^+$
(11.6608, sh)[a]	3852	3865	$(2,1,1)^2\Delta_{5/2} \leftarrow (0,0,0)^1\Sigma^+$
11.6756	3972	3950	$(0,0,2)^2\Pi_{1/2} \leftarrow (0,1,0)^1\Pi$
11.6893	4083	4100	$(0,0,2)^2\Pi_{3/2} \leftarrow (0,0,0)^1\Sigma^+$
11.7331	4436	4470	$(0,0,2)^2\Pi_{1/2} \leftarrow (0,0,0)^1\Sigma^+$
11.7766	4787	—	—
11.7860	4863	—	—
11.7921	4912	—	—
11.8232	5163	—	—
11.8423	5316	—	—

a) Here "sh" represents shoulder. We note that these assignments are tentative and require future experimental confirmation.

b) "pd" represents predicted.

Figure Captions

Figure 1. PFI-PE spectra for OCS in the energy ranges of (a) 11.090-11.460 eV and (b) 11.460-11.870 eV. The monochromator entrance/exit slits used were 200 and 400 μm for the energy ranges of 11.090-11.360 eV and 11.360-11.870 eV, respectively. At slits of 200 μm, the instrumental PFI-PE resolution is 1.2 meV (FWHM).

Figure 2. PFI-PE spectrum of OCS in the energy range of 11.155-11.292 eV obtained using monochromator entrance/exit slits of 75 μm. The instrumental PFI-PE resolution is 0.6 meV.

Figure 3. Contour plots of the vibrational parts of the vibronic wave functions for three members of the $2v_1^+ + v_2^+ = 5$ polyad in the $^2\Delta_{5/2}$ symmetry. (a) (2,1,0) at 1795.8 cm^{-1}, (b) (1,3,0) at 2448 cm^{-1}, and (c) (0,5,0) at 2695 cm^{-1} [r(CO) = 2.1344 bohr].

Figure 4. Contour plot of a $^2\Phi_{7/2}$ symmetry level at 3756 cm^{-1}, which belongs to a polyad 10 [r(CO)=2.1344 bohr].

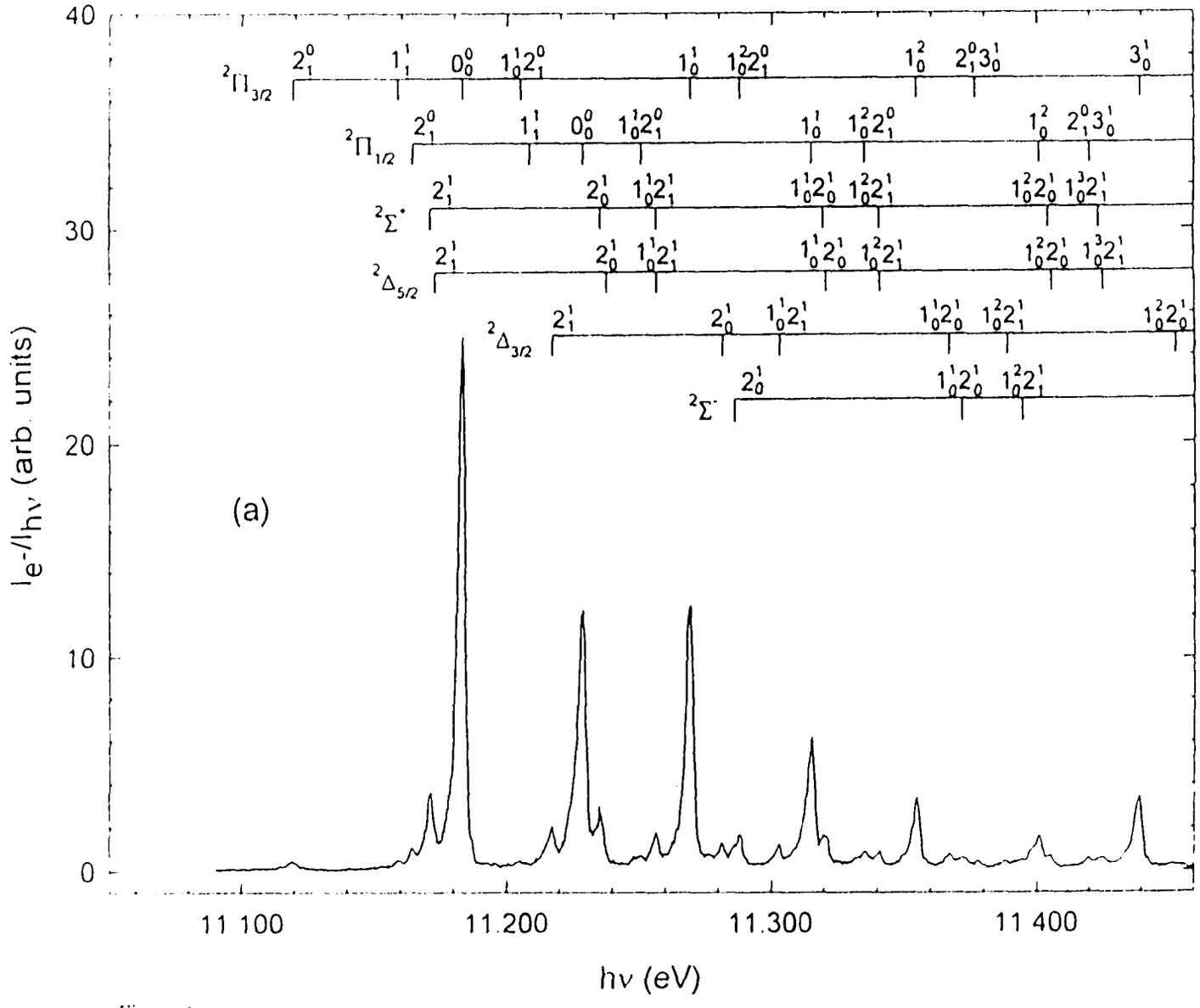
40
30
20
10
0
$I_{e^-}/I_{h\nu}$ (arb. units)
(a)
$^2\Pi_{3/2}$
$^2\Pi_{1/2}$
$^2\Sigma^+$
$^2\Delta_{5/2}$
$^2\Delta_{3/2}$
$^2\Sigma^-$
11 100
11.200
11.300
11 400
hν (eV)

Figure 1.

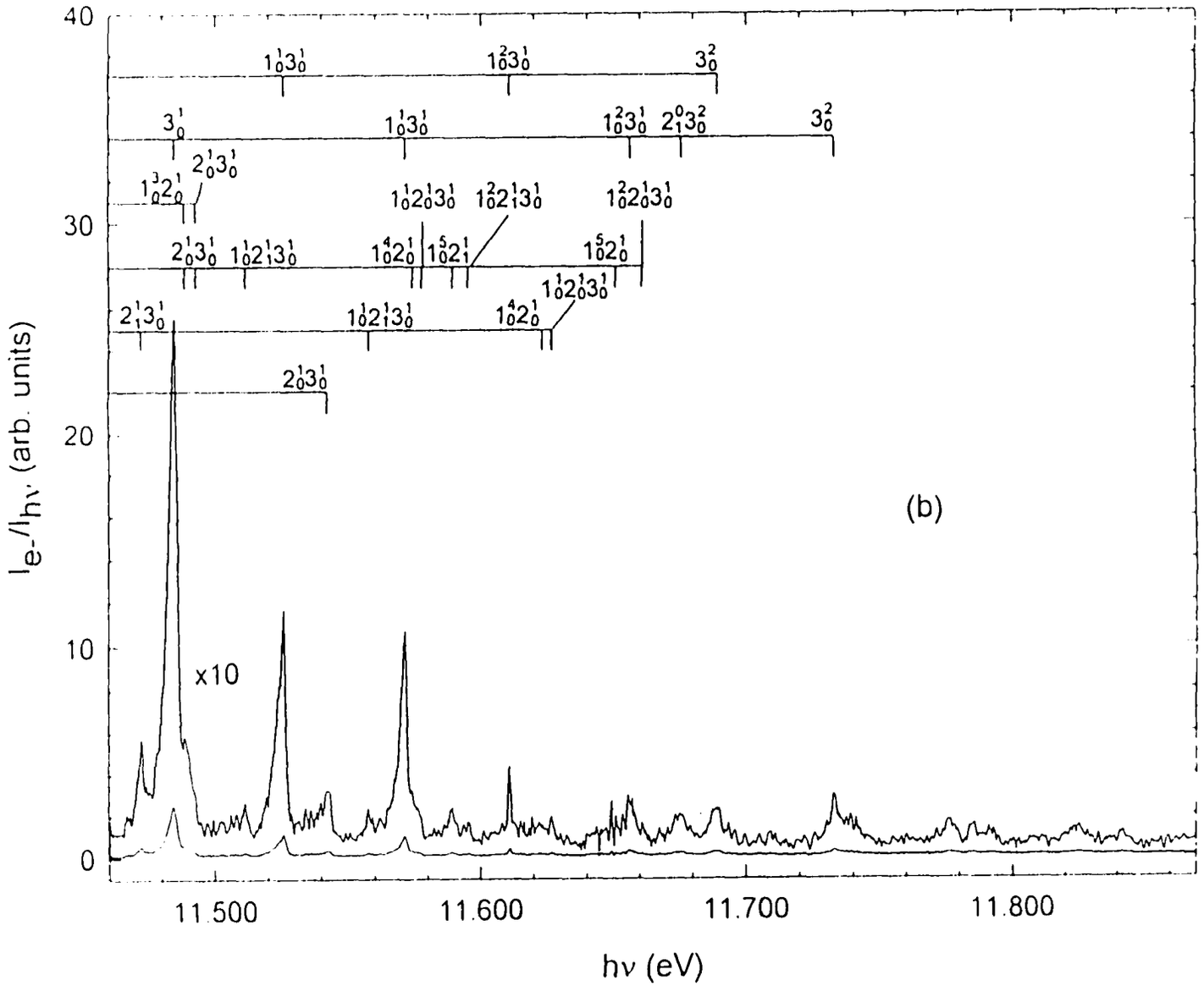

Figure 1. (continued)

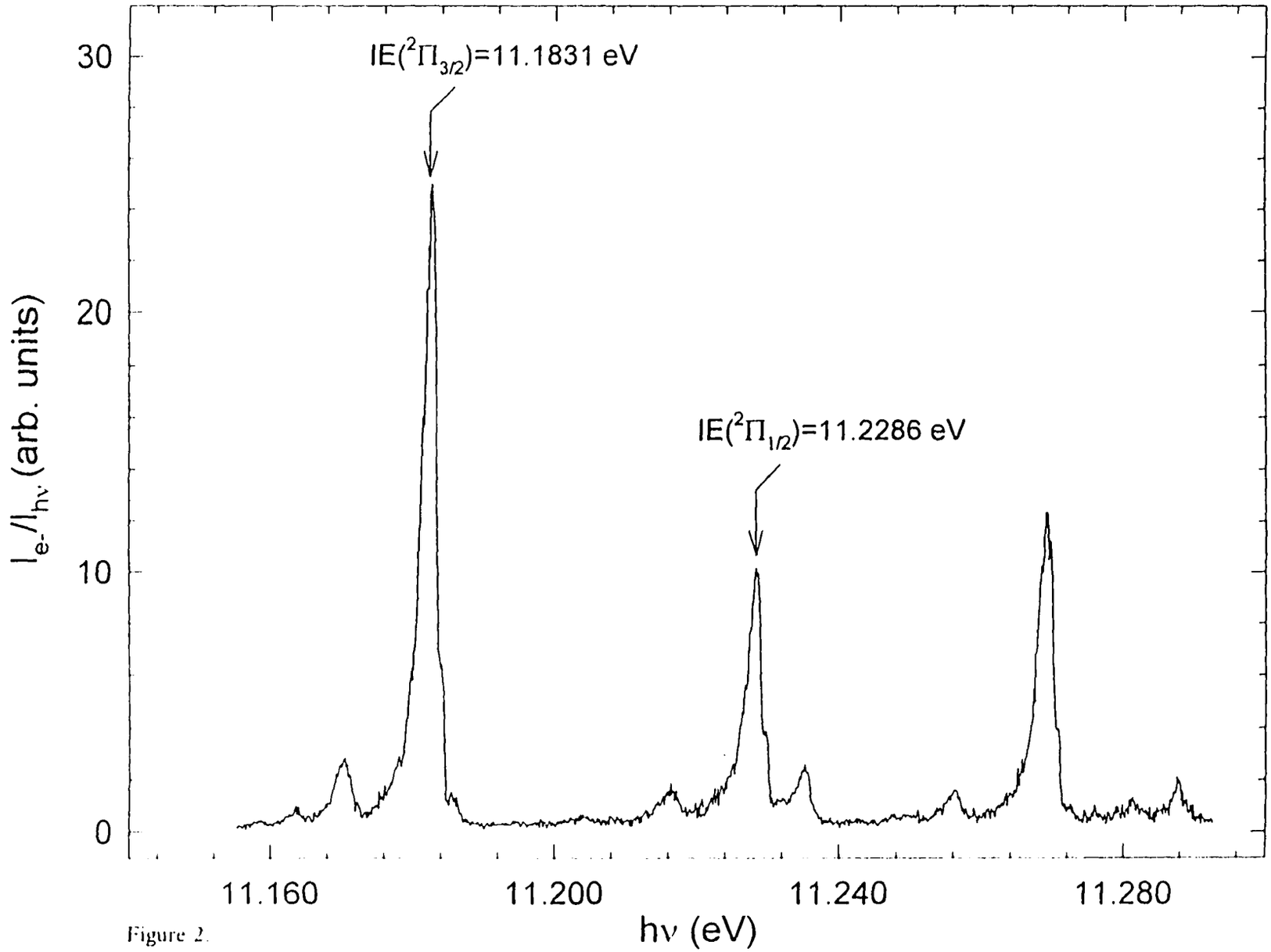
IE($^2\Pi_{3/2}$)=11.1831 eV
IE($^2\Pi_{1/2}$)=11.2286 eV
$I_{e^-}/I_{h\nu}$ (arb. units)
30
20
10
0
11.160
11.200
11.240
11.280
hν (eV)

Figure 2.

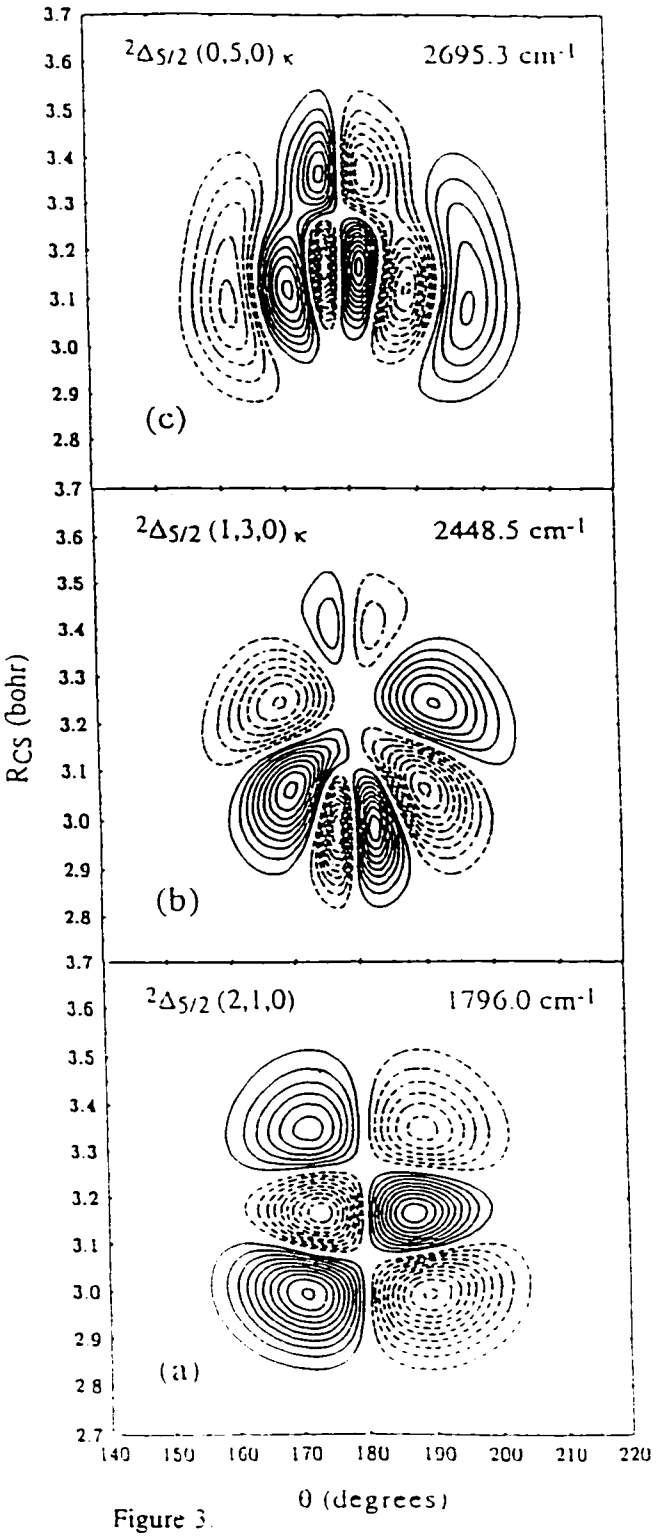
$^2\Delta_{5/2}$ (0,5,0) κ
2695.3 cm^{-1}
(c)
$^2\Delta_{5/2}$ (1,3,0) κ
2448.5 cm^{-1}
(b)
$^2\Delta_{5/2}$ (2,1,0)
1796.0 cm^{-1}
(a)
R_{CS} (bohr)
θ (degrees)
3.7
3.6
3.5
3.4
3.3
3.2
3.1
3.0
2.9
2.8
2.7
140
150
160
170
180
190
200
210
220

Figure 3.

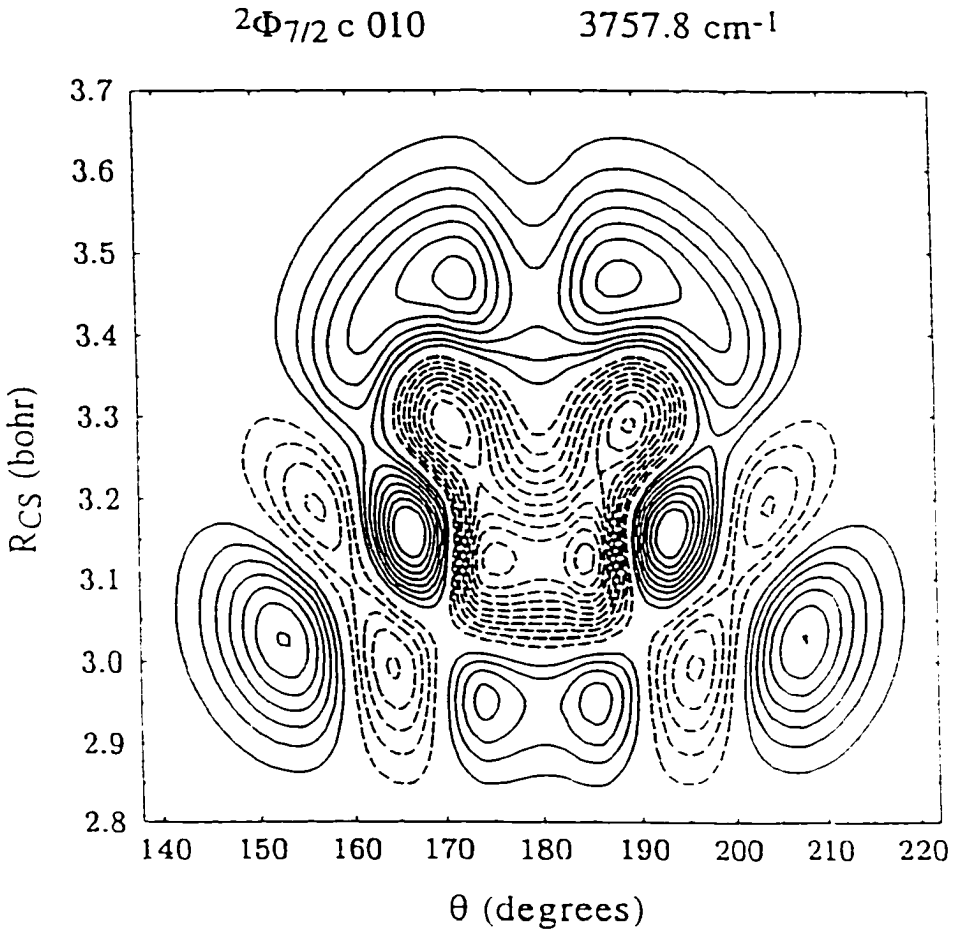
$^2\Phi_{7/2}$ c 010
3757.8 cm^{-1}
3.7
3.6
3.5
3.4
3.3
3.2
3.1
3.0
2.9
2.8
R_{CS} (bohr)
140
150
160
170
180
190
200
210
220
θ (degrees)

Figure 4.

ROTATIONALLY RESOLVED PULSED FIELD IONIZATION PHOTOELECTRON BANDS OF $H_2^+(X^2\Sigma_g^+, v^+=0\text{-}18)$

A paper to be submitted to the Journal of Chemical Physics

S. Stimson,[1] M. Evans,[1] C.-W. Hsu,[2] P. Heimann,[2] and C.Y. Ng[1,3]

Abstract

We have obtained a rotationally resolved pulsed field ionization photoelectron (PFI-PE) spectrum of H_2 at a resolution of 7 cm^{-1} FWHM (full-width-at-half-maximum) in the photon energy range of 15.30-18.09 eV. We present here the assignment of the rotational transitions for the $H_2^+(X^2\Sigma_g^+, v^+ = 0\text{-}18)$ vibronic bands and their simulation using the Buckingham-Orr-Sichel (BOS) model. The BOS simulation shows that the perturbation of PFI-PE rotational line intensities due to near-resonance autoionization decreases as v^+ increases. From the experimental data, B_{v^+}, D_{v^+}, and $\Delta G(v^++1/2)$, were determined and used to calculate the ionic vibrational and rotational constants (ω_e, $\omega_e x_e$, $\omega_e y_e$, $\omega_e z_e$, B_e, and α_e), the internuclear separation (r_e), and the dissociation energy (D_0). In agreement with previous experimental and theoretical investigations, only the $\Delta N^+ = 0$ and ± 2 rotational branches were observed in the PFI-PE spectrum of H_2.

[1] Ames Laboratory, USDOE and Department of Chemistry, Iowa State University, Ames, IA 50011, USA.

[2] Chemical Sciences Division and Advanced Light Source Accelerator and Fusion Research Division, Lawrence Berkeley National Laboratory, Berkeley, CA 94720, USA.

[3] Author to whom correspondence should be addressed. E-mail addresses: CYN: <CYNG@Ameslab.gov>.

Introduction

Being the simplest neutral and cationic molecular system, the potential energy surfaces and spectroscopic constants for H_2 and H_2^+ in their ground and excited rovibronic states have been calculated with high accuracy.[1-8] Reliable and extensive predictions for the bound rovibronic energies of H_2^+ have been obtained at different levels of theory.[2-4] For example, the stated accuracy of the adiabatic calculations[2,3] for the bound state levels of H_2^+ is 0.1-0.2 cm^{-1}. This is better than the accuracy of previous measurements using photoelectron spectroscopic techniques.[11-13] Partly for these reasons, the H_2/H_2^+ system has been the choice for detailed experimental[12-18] and theoretical[19-23] studies of molecular photoionization dynamics.

Due to the large rotational constants for H_2 and H_2^+, partial rotationally resolved photoelectron spectra for H_2 have long been observed using conventional NeI[11] and HeI[12,13] photoelectron spectroscopic techniques. A full rotationally resolved spectrum of H_2^+ has only been reported recently using the vacuum ultraviolet (VUV) laser pulsed field ionization photoelectron (PFI-PE) spectroscopic method,[15] which achieved a PFI-PE energy resolution of 6 cm^{-1} (FWHM). However, the latter study reported only the ionization transitions $H_2^+(X^2\Sigma_g^+, v^+ = 2, N^+ = 0\text{-}3) \leftarrow H_2(X^1\Sigma_g^+, v'' = 0, J'' = 0\text{-}3)$. The photoionization efficiency (PIE) spectrum for H_2 is overwhelmingly dominated by autoionization Rydberg structures in the region of 15.3-16.7 eV.[9,10] The majority of these Rydberg features were assigned based on comparison with predictions from multichannel quantum defect theory (MQDT).[20-22] The couplings between high-n (n>100) Rydberg (pseudocontinuum) states, lying at a few wavenumbers below an ionization limit, and low-n Rydberg (interloper) states in near-energy resonance with the pseudocontinuum states are expected to have a significant affect on the observed PFI-PE intensities.[19,23] Hence, the rotational components of the PFI-PE vibrational band should show different intensities, compared to those resolved in conventional HeI and NeI studies. The PFI-PE band of $H_2^+(X^2\Sigma_g^+, v^+ = 2)$ has been simulated using MQDT. The results of which have confirmed the near-resonance perturbation mechanism.[19]

Although VUV laser radiation with useful intensities can in principle be generated up to ≈17.7 eV, the processes involved remains inefficient for routine experimentation[24-27] compared with the ease in tuning VUV synchrotron radiation. Recently, we have developed a broadly tunable, high resolution synchrotron source associated with the Chemical Dynamics Beamline at the Advanced Light Source (ALS).[28,29] An experimental scheme for PFI-PE detection using the multibunch synchrotron source has also been implemented.[30-33] As demonstrated in recent PFI-PE experiments[31-33] on Ne, Ar, Kr, and O_2, the photoelectron energy resolution achieved was 3-6 cm^{-1} (FWHM). This is comparable to the

resolution obtained in VUV laser studies.[24,25,27] Using the newly implemented PFI-PE experimental scheme, we have obtained a rotationally resolved photoelectron spectrum of H_2 from 15.3-18.09 eV.

Experiment

The design and performance of the Chemical Dynamics Beamline at the ALS has been described previously.[28-31] The major components for the high resolution photoionization beamline includes a 10 cm period undulator, a gas harmonic filter, a 6.65m off-plane Eagle mounted monochromator, and a photoion-photoelectron apparatus. In the present experiment, helium was used in the harmonic gas filter where higher undulator harmonics with photon energies greater than 24.59 eV were suppressed, thereby eliminating interference by photoionization/photoexcitation effects caused by higher order undulator radiation. The fundamental light from the undulator is then directed into the 6.65 m monochromator and dispersed by an Os coated 4800 l/mm grating (dispersion = 0.32 Å/mm) before entering the experimental apparatus. The monochromator entrance/exit slits used were 150/150 μm (v^+=0-14), corresponding to a wavelength resolution of 0.048 Å (FWHM) (or 0.9 meV at 800 Å) and 100/100 μm (v^+=15-18), corresponding to a wavelength resolution of 0.032 Å (FWHM) (or 0.6 meV at 800Å).

Both a continuous molecular beam and an effusive beam of pure H_2 were used in this experiment. The continuous molecular beam was produced by supersonic expansion through a stainless steel nozzle (diameter = 0.127 mm) at a stagnation pressure of 330 Torr and a nozzle temperature of 298 K. The molecular beam was then skimmed by a conical skimmer (diameter = 1 mm) before intersecting the monochromatic VUV light beam 7 cm downstream in the photoionization region. The beam source chamber and photoionization chambers were evacuated by turbomolecular pumps with pumping speeds of 3000 L/s and 1200 L/s, respectively. The electron spectrometer used in this experiment is located in the photoelectron chamber, which was separately evacuated by a turbomolecular pump with a pumping speed of 400 L/s. The rotational temperature was between 250-280 K for the molecular beam

The H_2 effusive beam was introduced into the photoionization region through a metal orifice (diameter=0.5 mm) at room temperature and 0.5 cm from the photoionization region. The pressures maintained in the photoionization chamber and the photoelectron chamber were $1x10^{-6}$ and $1x10^{-7}$, respectively. The main chamber and photoelectron chambers were evacuated by turbomolecular pumps with pumping speeds of 1200 L/s and 3400 L/s, respectively. The rotational temperature was 298 K for the effusive beam.

The ALS storage ring is capable of filling 328 electron buckets in a period of 656 ns. Each electron bucket emits a light pulse of 50 ps with a time separation of 2 ns between successive buckets. In each storage ring period, a dark-gap (48 ns or 60 ns) consisting of 24 or 30 consecutive unfilled buckets exists for the ejection of cations from the orbit. The present experiment[31-36] was performed in the multibunch mode with 304 or 298 bunches in the synchrotron orbit, corresponding to an average repetition rate of 464 MHz or 454 MHz, respectively. A pulsed electric field (height = 0.67 V/cm, width = 40 ns, v^+=0-9), (height=1.2 V/cm, width=40 ns, v^+=10-18) was applied to the repeller at the photoionization/photoexcitation region to field ionize high-n Rydberg states and extract photoelectrons toward the detector. The pulsed electric field was applied every 1 ring period (0.656 μs) for vibrational levels v^+=10-18, and delayed by 20 ns with respect to the beginning of a 60 ns dark-gap. For vibrational levels v^+=0-9, the pulsed electric field was applied every 2 ring periods (1.31 μs) and delayed by 8 ns with respect to the beginning of a 48-ns dark-gap. The electron spectrometer, which consists of a steradiancy analyzer and a hemispherical energy analyzer arranged in tandem, was used to filter prompt electrons.[31] Judging from the width of the rotational transitions observed, we concluded that the PFI-PE energy resolution achieved in the present experiment is ≈7-8 cm^{-1} (FWHM), comparable to the VUV photon energy resolution. On the basis of the observed PFI-PE counts at the $Ar^+(^2P_{3/2})$ threshold, the residual electron background counts at the autoionizing Ar(*11s'*) state, and the relative Ar^+ ion intensities measured at the $Ar^+(^2P_{3/2})$ threshold and at the Ar(*11s'*) state,[28,31] we estimated that the suppression factor for prompt electrons is ≈5×10^{-4}. The Ar(*11s'*) state lies about 4.5 meV above the $Ar^+(^2P_{3/2})$ threshold. The suppression factor is expected to decrease as the kinetic energy of the prompt electrons increases.[31] Hence, the suppression factor should be smaller than 5×10^{-4} for autoionizing levels lying at energies greater than 4.5 meV with respect to an ionization threshold. The absolute photon energy scale for the H_2^+ spectra were calibrated using the $Ne^+(^2P_{3/2})$ and the $Ar^+(^2P_{3/2})$ PFI-PE bands measured under the same experimental conditions.[31-33] In the present experiment, the photon energy step size used was in the range of 0.2-0.3 meV. The dwell time at individual steps was in the range of 3-40 s.

Results and Discussion

Assignment of rovibronic transitions

For the one photon ionization process $H_2^+(X\ ^2\Sigma_g^+,\ v^+,\ N^+) \leftarrow H_2(X\ ^1\Sigma_g^+,\ v''=0,\ J'')$, the total wavefunction for the neutral and ion $|\Psi\rangle=|\psi_{el}\chi_{vib}\chi_{rot}\psi_{nucl\ spin}\rangle$ must be antisymmetric under the space-fixed nuclear exchange operation X_N since H_2 nuclei are fermions. The vibrational state $|\chi_{vib}\rangle$ is not

effected by the exchange operator since it only depends on the internuclear distance. The exchange symmetry of $|\psi_{el}\chi_{rot}\rangle$ under $\mathcal{X}_N$ is given by

$$\begin{aligned}\mathcal{X}_N|\psi_{el}\chi_{rot}\rangle &= i_1 i_2|\psi_{el}\chi_{rot}\rangle \\ &= [(-1)^J(+)][+]|\psi_{el}\chi_{rot}\rangle \\ &= (-1)^J|\psi_{el}\chi_{rot}\rangle\end{aligned} \tag{1}$$

where i_1 represents inversion of all particles through the origin and i_2 represents inversion of electrons through the origin. This results in $|\psi_{el}\chi_{rot}\rangle$ being antisymmetric for odd J and symmetric for even J. The effect of $\mathcal{X}_N$ on the nuclear spin function $|\psi_{nucl\ spin}\rangle$ for a diatomic molecule with $(2I+1)^2$ nulcear spin states results in $(2I+1)(I+1)$ symmetric spin states and $(2I+1)I$ antisymmetric spin states where I is the spin of the nucleus. For H_2 (I=1/2) this results in three symmetric and one antisymmetric nuclear spin states.

Since the rovibronic transitions in this experiment involve photoionization we must take into account coupling of the angular momentum for the neutral, ion, and ejected electron. The angular momentum coupling factor Q for a Hund's case b ← b transition can be expressed as[35]

$$Q(\lambda, N^+, N'') = (2N^+ + 1)\begin{pmatrix} N^+ & \lambda & N'' \\ -\Lambda^+ & \Delta\Lambda & \Lambda'' \end{pmatrix}^2 \tag{2}$$

where $\Delta\Lambda$ is the difference in orbital angular momenta between the ion and the neutral, and the rotational angular momentum of the ion and neutral are represented by N^+ and N'', respectively. The properties of Equation 2 are such that given Λ^+=0 and Λ''=0, Equation 2 will vanish if $N^+ + N'' + \lambda$ is odd. The general interpretation of λ is the angular momentum transferred to the ejected electron in the photoionization process. The values of λ are constrained by the triangle condition $\Delta N \le \lambda \le N^+ + N''$. An additional constraint on λ is $\lambda = |\ell - 1|, \ldots, |\ell + 1|$, which is due to the dipole selection rule.

The parity selection rule connecting rovibronic states of the neutral and ion is given by[36,37]

$$\Delta J + \Delta S + \Delta p + \ell = \text{even} \tag{3}$$

where $\Delta J=J^+-J''$, $\Delta S=S^+-S''$ is the difference in total spin between the ion and neutral, Δp represents the change in Kronig parity of the initial and final states (p = 0 for Λ^+ or = 1 for Λ^-), and ℓ is the angular momentum of the ejected photoelectron. For a $^2\Sigma_g^+ \leftarrow {}^1\Sigma_g^+$ transition, $\Delta S=1/2$, $\Delta p=0$, and $\Delta J=\Delta N+\Delta S$ (for Hund's case b $\leftarrow$ b). Equation 3 thus reduces to $\Delta N+\ell$ = odd. ℓ must be odd for a g $\leftarrow$ g transition in order for the matrix element $\langle\Psi_{ion}|\langle\Psi_{photoelectron}|\mu|\Psi_{mol}\rangle$ not to vanish. Since ℓ must be odd and $\Delta N+\ell$ = odd, ΔN must be even (0, ±2, ±4, etc.). Only the $\Delta N=0$, ±2 transitions were observed in this experiment. The partial waves of the ejected photoelectron are $\ell=1,3$ for $\lambda=2$, and $\ell=1$ for $\lambda=0$. This means that the Q branch gains intensity through the excitation of a *s*- and a *d*-wave electron, with the majority coming from the *s*-wave electron. However, the O and S branches gain their intensity only from the excitation of a *d*-wave electron. This is due to the constraint on the value of λ, introduced by the triangle condition.

The rotationally resolved PFI-PE spectrum of $H_2^+(X^2\Sigma_g^+, v^+=0\text{-}18)$ is shown in Figure 1. Individual vibrational levels are shown in Figures 2(a)-2(s). Note that the vertical I(e$^-$)/I(hν) scales for these figures have the same units, where I(e$^-$) and I(hν) represent the PFI-PE intensity and the VUV photon intensity, respectively. Using the spectroscopic constants for H_2 obtained from Herzberg[1-34], the rotational energy levels for $v''=0$, $J''=0\text{-}10$ were calculated. The rotation-vibration energy levels for H_2^+ were taken from theoretical calculations by Hunter, Yau, and Pritchard (HYP)[2] and Wolniewicz and Poll[5] (WP). Combining the rovibronic energy levels of H_2 and H_2^+ allowed the calculation of the rovibronic transitions, $H_2^+(X^2\Sigma_g^+, v^+=0\text{-}18, N^+=0\text{-}10) \leftarrow H_2(X^1\Sigma_g^+, v''=0, J''=0\text{-}10)$, which were used to assign the rovibronic transitions observed in this experiment. We found that the IEs for the ionization transitions $H_2^+(X^2\Sigma_g^+, v^+=0\text{-}18, N^+=0) \leftarrow H_2(X^1\Sigma_g^+, v''=0, J''=0)$, i.e., $(N^+, J'')=(0, 0)$, and positions of other (N^+, J'') rotational lines observed in the PFI-PE spectrum of H_2 are in excellent agreement with the HYP[2] and WP[5] predictions and the results of previous experiments.[11-13] The fact that the maximum deviation of $\leq$0.5 meV is found in these comparisons confirms the claimed accuracy of $\leq$ 1 meV for the photon energy calibration procedures.[28,32,33]

Since the cross section for direct photoionization is very low compared to that for autoionization in H_2,[9,10] a suppression factor[31] of 5×10^{-4} s may not be sufficient to completely suppress prompt electrons originating from strong autoionization states. Photoionization of H_2 has been a model system for the detailed experimental and theoretical investigation of the near-resonance autoionization mechanism.[9,15,19,21,22] The

unambiguously that the couplings of high-n Rydberg pseudocontinuum states and near-resonance interloper states converging to higher ionization thresholds have a significant effect on the PFI-PE intensities of rotational transitions. An interesting example revealing this effect is the (1, 1) line of the v^+=0 band shown in Fig. 2(a). This transition is overwhelmingly the most intense peak observed in the entire PFI-PE spectrum with an electron counting rate >5×10^4 counts/s and is ≈500 times higher than that of the (0, 0) peak. The high intensity for this (1, 1) line is due to the fact that the $H_2^+(X^2\Sigma_g^+, v^+=0, N^+=1)$ ionization threshold coincides with a strong autoionizing resonance.[9,10]

Photoelectron peaks in Figs. 2(a)-2(f), which are not assigned to (N^+, J'') ionization thresholds, can be attributed to prompt electron background features from autoionizing Rydberg levels of H_2.[9,10] The contamination by prompt electron peaks is expected to be less serious at higher v^+ states because strong autoionizing Rydberg states are mostly concentrated in the energy range (≈15.3-16.7 eV) covering the lower v^+ (<6) states.[9,10] This expectation is confirmed by the PFI-PE spectra of Figs. 2(a)-2(f). The v^+ = 0-5 PFI-PE bands exhibit many strong near-resonance autoionization peaks that cannot be assigned to rotational transitions, whereas the PFI-PE bands for v^+ = 6-18 are nearly free from such autoionization features. Although corresponding autoionization Rydberg peaks resolved in the PIE spectrum[9,10] of H_2 can be identified as background electron peaks found in the PFI-PE spectra of Figs. 2(a)-2(f), the relative intensities of the background electron peaks are not in proportion with the relative intensities of the autoionization ion peaks.

Rotational Intensities

As indicated above, H_2 was introduced into the photoionization/photoexcitation region in the form of a molecular beam and an effusive beam at 298 K. We have compared the PFI-PE spectra recorded using the H_2 supersonic beam with those obtained using an effusive H_2 beam. On the basis of this comparison, we concluded that the rotational temperature for the H_2 molecular beam is in the range of 250-280 K. Since ortho-hydrogen (odd J'') and para-hydrogen (even J'') exist in the ratio of 3:1, we estimated the rotational population ratios for $(J''=0) : (J''=1) : (J''=2) : (J''=3) : (J''=4) : (J''=5)$ to be 0.1447 : 0.6842 : 0.1049 : 0.0639 : 0.0021 : 0.0003 at 265K for the molecular beam and 0.1301 : 0.6605 : 0.1168 : 0.0880 : 0.0038 : 0.0008 at 298 K for the effusive beam. The rotational transition intensities are expected to roughly reflect the thermal distribution of rotational levels at such a temperature if the near-resonance autoionization mechanism does not play a role in the production of PFI-PEs.

As shown in Figs. 2(a)-2(s), the dominant rotational transitions for v^+=0-18 are $\Delta N = 0$, i.e., (0, 0), (1, 1), (2, 2), and (3, 3). In general, the PFI-PE intensity for (1, 1) is higher than that for (0, 0) within a given vibrational band. This observation and the low PFI-PE intensities for transitions involving $J'' \geq 4$ are in general accord with the thermal distribution of J'' for H_2. Weak transitions attributable to $\Delta N = \pm 2$, i.e., (2, 0), (3, 1), (0, 2), (4, 2), (1, 3), and (5, 3) are also observed. The dominance of the rotational transitions with $\Delta N = 0$ over that with $\Delta N = \pm 2$ is consistent with the results of previous experiments[8-13] and theoretical[2] calculations.

BOS Simulation

The Buckingham-Orr-Sichel (BOS) model[35] is described by the formula

$$\sigma(N^+ \leftarrow N'') \propto \Sigma_\lambda Q(\lambda, N^+, N'')C_\lambda \quad . \tag{4}$$

This model was derived to predict rotational line strengths $\sigma(N^+ \leftarrow N'')$ observed in one photon ionization of diatomic molecules. The rotational line strength is separated into two factors. The factor C_λ is associated with the electronic transition moments, which are the linear combination of electron transition amplitudes for the possible angular momenta ℓ of the ejected electron. The general interpretation of λ is that of the angular momentum transfer in the photoionization process. The other factor, Q, is determined by the standard angular momentum coupling constants, which were calculated using the formula for a Hund's case (*b*) to (*b*) transition in the present study and given by Equation 2. The known spectroscopic constants for the $H_2(X^1\Sigma_g^+, v'' = 0)$ were used.[1] The best fits for the PFI-PE bands for $H_2^+(X\,^2\Sigma_g^+, v^+ = 0\text{-}18)$ are depicted as dashed curves in Figs. 2(a)-2(s). The fact that only the $\Delta N = 0, \pm 2$ rotational branches are observed implies that only the BOS coefficients C_0 and C_2 are nonzero. The C_0 and C_2 values for the simulated spectra shown in Figs. 2(a)-2(s) are listed in Table 1. The dominance of the $\Delta N = 0$ or Q-branch observed in the experimental spectra is consistent with the significantly higher C_0 values than the corresponding C_2 values. As expected, the BOS simulation, which does not take into account the effect of near-resonance autoionization, cannot account for the overwhelming intensity of the (1, 1) transition observed in the v^+=0 PFI-PE band. Surprisingly, general agreement is found between the experimental spectra and the BOS simulation of the PFI-PE bands for $v^+ \geq 1$ states. In general, the agreement becomes better for higher vibrational levels. For example, the relative intensities for rotational transitions observed for the $v^+ = 11$ band are in excellent accord with the BOS simulated spectrum (see Fig. 2(l)). Furthermore, disregarding the

C_0 and C_2 values for the $v^+=0$ band, we find that the C_0 value in general increases compared to the C_2 value as v^+ increases. Such a trend is consistent with the observation that the $\Delta N = \pm 2$ rotational branch diminishes as v^+ increases.

The intensities for the rotational transitions, $(N^+ - J'')$, $J'' = 0$-3 and $N^+ = 0$-5, associated with the $v^+=0$, 1, 2, 5, and 8 bands have been calculated by Itikawa[16] at photoionization wavelengths of 584 Å HeI and 736 Å NeI. These calculations, which have not taken into account the coupling of interloper states, are in qualitative agreement with the HeI[12,13] and NeI[11] results. A careful comparison of the PFI-PE, HeI, NeI, and theoretical results for the $v^+=2$ vibrational band have been made by Softley and co-workers.[15,19] These experimental and theoretical intensities are given again in Table 2 to compare with the PFI-PE results and the BOS simulation obtained in the present study. The relative PFI-PE intensities observed here for the $v^+=2$ band are in reasonable agreement with those of Merkt and Softley[15] except that our experiment shows a much weaker (0, 2) transition and stronger (2, 0) and (3, 1) transitions. These differences can be partly ascribed to the different PFI schemes used in the two experiments. A sequential two-pulse Stark field ionization scheme was used in the experiment of Merkt and Softley,[15] where the first pulse V_1 and second pulse V_2 vary in the range of 0.1-3 V/cm and 2-12 V/cm, respectively. It was demonstrated by Merkt and Softley[15] that different combinations of these pulses yielded different PFI-PE line shapes. Since V_2 is significantly higher than the extraction pulse used in our experiment, interloper states lying <20 cm^{-1} with respect to the ionization threshold may be observed in the experiment by Merkt and Softley,[15] and thus affect the PFI-PE intensities. Note that the BOS simulation accounts well for all the relative rotational intensities except that for the (2, 0) transition.

Another important factor that could affect the PFI-PE intensities is the effective lifetime for high-n Rydberg states involved in the PFI-PE measurements. If the effective lifetime is shorter than the time interval for adjacent Stark field pulses, the measured PFI-PE intensity would be lower than the actual threshold photoelectron intensity. We examined several PFI-PE bands obtained at time intervals of 0.656, 1.31, and 1.97 μs, corresponding to the times of applying the Stark field pulse every one, two, and three periods, respectively. Since the relative rotational intensities observed in the one, two, and three period operations were in agreement, we concluded that the rotational intensities resolved in the PFI-PE spectra shown in Figs. 2(a)-2(s) were not influenced by the Rydberg lifetime effect.

Vibrational and Rotational Energy Levels

The vibrational energy levels are defined by the equation

$$G_v = \omega_e(v+1/2) - \omega_e x_e(v+1/2)^2 + \omega_e y_e(v+1/2)^3 + \omega_e z_e(v+1/2)^4 + \ldots \quad (5)$$

The vibrational constants, ω_e, $\omega_e x_e$, $\omega_e y_e$ and $\omega_e z_e$ for H_2^+ were determined by fitting the experimental PFI-PE vibrational energy level differences (ΔG) listed in Table 3 to the equation

$$\begin{aligned}\Delta G_{v+1/2} &= G(v+1) - G(v) \\ &= \omega_e - 2\omega_e x_e (v+1) + \omega_e y_e(3v^2+6v+13/4) + \omega_e z_e(4v^3+12v^2+13v+5) \quad . \end{aligned} \quad (6)$$

The resulting vibrational constants are listed in Table 4 along with the results obtained in the HeI photoelectron study by Pollard *et al.*[13] The HYP[2] and WP[5] theoretical energy levels were also fit to Equation 6 and are listed in Table 4 for comparison. A plot of the PFI-PE and HYP $\Delta G_{v^+ +1/2}$ vs. $(v^+ +1/2)$ is shown in Figure 3. Both curves show a positive curvature at low $(v^+ +1/2)$ and a negative curvature at high $(v^+ +1/2)$ with a point of inflection at $\approx 7\frac{1}{2}$, as was observed in the HeI photoelectron study.[13] This can be seen clearly in Figure 4 where a linear term is subtracted from the $\Delta G_{v^+ +1/2}$. As expected, the results of the present experiment are in good agreement with the theoretical[2-5] results and the HeI photoelectron study.[13]

We have obtained the rotational constants B_{v^+} and D_{v^+} for $H_2^+(X^2\Sigma_g^+, v^+=0\text{-}17)$ by fitting the rotational structures resolved in Figs. 2(a)-2(s) to

$$\nu = \nu_0 + B_{v^+}N(N+1) - D_{v^+}N^2(N+1)^2 - B_v''J(J+1) + D_v''J^2(J+1)^2 \quad . \quad (7)$$

The values of B_v'' and D_v'' for $H_2\ X^1\Sigma_g^+$, v=0 were obtained from Huber and Herzberg.[1] The resulting ionic rotational constants are compared with those reported in the HeI photoelectron study of Pollard et al[13] and to theoretical calculations[2,3,5] in Table 5. Figure 5 shows the B_{v^+} rotational constants determined from this experiment along with the theoretical results by Beckel, Hansen, and Peek[3] and Wolniewicz and Poll.[5] As expected, the results of the present experiment and the theoretical calculations[2,3,5] are in excellent agreement.

In addition, B_e and α_e for H_2^+ were determined by fitting the experimental B_{v^+} values $(v^+=0\text{-}17)$ to the equation, $B_{v^+} = B_e - \alpha_e(v^+ +1/2)$. Based on the results of this calculation, the internuclear distance (r_e) was calculated using

$$r_e = \sqrt{h/8\pi^2\mu B_e} \quad (8)$$

The resulting B_e, α_e, and r_e values are listed in Table 6 along with those obtained in the HeI photoelectron study by Pollard et al[13] and those by Huber and Herzberg.[1] As shown, our results are consistent with previous results. The experimental dissociation energy (D_0) for H_2^+ was also determined. The resulting dissociation energy, as well as other experimental and theoretical dissociation energies, are listed in Table 7.

Conclusions

We presented here the rotationally resolved PFI-PE spectra of $H_2^+(X^2\Sigma_g^+, v^+=0\text{-}18)$. The analysis of which has provided the rovibronic energies for $v^+=0$-18, the vibrational constants (ω_e, $\omega_e x_e$, $\omega_e y_e$, and $\omega_e z_e$), the rotational constants (B_{v^+}, D_{v^+}, B_e, and α_e), the internuclear separation (r_e), and the dissociation energy, (D_0). The simulated photoelectron bands based on the BOS model are in good agreement with the PFI-PE bands of higher v^+ states, indicating that the strong perturbation of the relative intensities for rotational transitions occurs mainly at lower v^+ (<6) states.

Acknowledgements

This work was supported by the Director, Office of Energy Research, Office of Basic Energy Sciences, Chemical Science Division of the U.S. Department of Energy under Contract No. W-7405-Eng-82 for the Ames Laboratory and Contract No. DE-AC03-76SF00098 for the Lawrence Berkeley National Laboratory. M.E. and S.S. acknowledge the GAANN Fellowship support for 1994-1995 and 1996-1997. M.E. is a recipient of the Dow Fellowship for 1997-1998.

References

1. K. P. Huber and G. Herzberg, "Molecular Spectra and Molecular Structure, Vol. IV, Constants of Diatomic Molecules" (Van Nostrand, New York, 1979).
2. G. Hunter, A. W. Yau, and H. O. Pritchard, *At. Data Nucl. Data Tables* **14**, 11 (1974).
3. C. L. Beckel, B. D. Hansen, and J. M. Peek, *J. Chem. Phys.* **53**, 3681 (1970).
4. G. Hunter and H. O. Pritchard, *J. Chem. Phys.* **46**, 2153 (1967).
5. L. Wolniewicz and J. D. Poll, *Mol. Phys.*, **59**, 953-964, (1986).

6. D. M. Bishop and L. M. Cheung, *Phys. Rev.* A**16**, 640 (1977)

7. D. M. Bishop, *Mol. Phys.* **28**, 1397 (1974).

8. D. M. Bishop and L. M. Cheung, *J. Chem. Phys.* **75**, 3155 (1981).

9. P. M. Dehmer and W. A. Chupka, *J. Chem. Phys.* **65**, 2243 (1976).

10. J. Berkowitz, "Photoabsorption, Photoionization, and Photoelectron Spectroscopy" (Academic, New York, 1979), unpublished results.

11. L. Åsbrink, *Chem. Phys. Lett.* **7**, 549 (1970).

12. Y. Morioka, S. Hara, and M. Nakamura, *Phys. Rev. A* **22**, 177 (1980).

13. J. E. Pollard, D. J. Trevor, J. E. Reutt, Y. T. Lee, and D. A. Shirley, *J. Chem. Phys.* **77**, 34 (1982).

14. J. Berkowitz ad R. Spohr, *J. Electron Spectrosc.* **2**, 143 (1973).

15. F. Merkt and Softley, *J. Chem Phys.* **96**, 4149 (1992).

16. Y. Itikawa, *Chem. Phys.* **30**, 109 (1978); ibid. **28**, 461 (1978); **37**, 401 (1979).

17. A. L. Ford, K. K. Docken, and A. Dalgarno, *Astrophys. J.* **195**, 819 (1975).

18. S. V. O'Neil and W. P. Reinhardt, *J. Chem. Phys.* **69**, 2126 (1978).

19. T. P. Softley and A. J. Hudson, *J. Chem. Phys.* **101**, 923 (1994).

20. M. J. Seaton, *Rep. Prog. Phys.* **46**, 167 (1983).

21. C. H. Greene and Ch. Jungen, *Adv. At. Mol. Phys.* **21**, 51 (1985).

22 L. Wolniewicz and J. D. Poll, *Mol. Phys.* **59**, 953 (1986).

23. F. Merkt, H. Xu, and R. N. Zare, *J. Chem. Phys.* **104**, 950 (1996).

24. See R. T. Weidmann and M. G. White, in "High Resolution Laser Photoionization and Photoelectron Studies", edited by I. Powis, T. Baer, and C. Y. Ng, *Wiley Series in Ion Chem. and Phys.* (Wiley, Chichester, 1995), p. 79.

25. F. Merkt and T. P. Softley, in "High Resolution Laser Photoionization and Photoelectron Studies", edited by I. Powis, T. Baer, and C. Y. Ng, *Wiley Series in Ion Chem. and Phys.* (Wiley, Chichester, 1995), p. 119.

26. J. W. Hepburn, in "Vacuum Ultraviolet Photoionization and Photodissociation of Molecules and Clusters", edited by C. Y. Ng (World Scientific, Singapore, 1991), p. 435.

27. J. W. Hepburn, in "Laser Techniques in Chemistry", edited by A. Meyers and T. R. Rizzo (Wiley, New York, 1994).

28. C.-W. Hsu, M. Evans, P. Heimann, K. T. Lu, and C. Y. Ng, *J. Chem. Phys.* **105**, 3950 (1996).

29. P. Heimann, M. Koike, C.-W. Hsu, M. Evans, K. T. Lu, C. Y. Ng, A. Suits, and Y. T. Lee, *Rev. Sci. Instrum.*, **68**, 1945 (1997).

30. M. Evans, C. Y. Ng, C.-W. Hsu, and P. Heimann, *J. Chem. Phys.* **106**, 978 (1997).

31. C.-W. Hsu, M. Evans, P. A. Heimann, and C. Y. Ng, *Rev. Sci. Instrum.*, **68**, 1694 (1997).

32. C.-W. Hsu, P. A. Heimann, M. Evans, S. Stimson, T. Fenn, and C. Y. Ng, *J. Chem. Phys.* **106**, 8931 (1997).

33. C.-W. Hsu, P. A. Heimann, M. Evans, S. Stimson, and C. Y. Ng, *Chem. Phys.*, accepted.

34. G. Herberg, "Molecular Spectra and Molecular Structures, Vol.I. Spectra of Diatomic Molecules" (Van Nostrand, Princeton, 1950).

35. A. D. Buckingham, B. J. Orr, J. M. Sichel, *Phil. Trans. Roy. Soc. Lond. A* **268**, 147 (1970).

36. J. Xie and R.N. Zare, *J. Chem. Phys.*, **93**, 3033 (1990).

37. K.Wang and V. McKoy, *J. Phys. Chem.*, **99**, 1643-1648, (1995).

Table 1. BOS coefficients for the best fit [see dashed curves of Figs. 2(a)-2(s)] to the $H_2^+(X^2\Sigma_g^+$, v^+=0-18) PFI-PE bands. The sum of the C_λ values for a given v^+ state is arbitrarily normalized to 100.

	BOS Coefficients	
v^+	C_0	C_2
0	90	10
1	70	30
2	75	25
3	70	30
4	90	10
5	50	50
6	60	40
7	95	50
8	50	50
9	85	15
10	85	15
11	90	10
12	85	15
13	90	10
14	85	15
15	90	10
16	95	5
17	98	2
18	98	2

Table 2. Comparison of the relative rotational line intensities for the $H_2^+(X\,^2\Sigma_g^+, v^+=2)$ photoelectron bands. The intensities for $(N^+, J'')= (1, 1)$ are arbitrarily normalized to 100.

(N^+, J'')	PFI-PE[a]	BOS	Merkt[15]	MQDT[19]	Åsbrink[11]	Morioka[12]	Itikawa[16]
(0, 0)	21.1	17.3	15	15	42	27	19
(2, 0)	86.3[b]	6.9	51	21(59)[c]	6.2	10.5	2.8
(1, 1)	100.0	100.0	100	100	100	100	100
(3, 1)	15.8	17.5	9.5	20	4.5	—	5.7
(0, 2)	1.2	1.0	8.3	4.8	2.2	—	0.6
(2, 2)	20.5	17.3	20	15	31	21	17
(1, 3)	0.9[d]	1.7	—	0.23	—	—	0.5
(3, 3)	12.1	13.9	16	12	15	14	13
(5, 3)	1.9	1.9	1.1	1.3	—	—	0.9

a) Relative intensities obtained in PFI-PE measurements. Estimated uncertainties are ±0.8.

b) The (4, 2) transition lies at the high-energy shoulder of the (2, 0) peak.

c) The MQDT value in parentheses was obtained by shifting the perturbing resonance to its correct energy. See Ref. 19.

d) (1, 3) overlaps with (4, 4) in the present experiment. Thus, this intensity is a combined intensity for (1, 3) and (4, 4).

Table 3. Comparison of the vibrational differences $\Delta G(v^{+}+1/2)$ for the $H_2^{+}\ ^2\Sigma_g^{+}$ ground state in cm^{-1}.

$v^{+}+1/2$	PFI-PE	HYP[2]	WP[5]	HeI[13]
0.5	2196.29	2191.32	2191.13	2190.9
1.5	2066.12	2064.09	2063.91	2065.2
2.5	1941.19	1941.08	1940.92	1941.8
3.5	1820.69	1821.64	1821.50	1822.1
4.5	1703.78	1705.13	1705.00	1706.2
5.5	1589.63	1590.90	1590.79	1591.1
6.5	1477.40	1478.32	1478.23	1477.7
7.5	1366.28	1366.75	1366.68	1367.0
8.5	1255.42	1255.51	1255.46	1257.8
9.5	1143.99	1143.88	1143.85	1145.8
10.5	1031.17	1031.09	1031.09	1031.9
11.5	916.12	916.31	916.34	913.3
12.5	798.02	798.59	798.65	796.6
13.5	676.02	676.86	676.98	676.4
14.5	549.31	549.97	550.12	548.4
15.5	417.04	416.62	416.84	415.4
16.5	278.40	275.96	276.25	280.3
17.5	132.54	131.26	131.58	------

Table 4. Comparison of experimental PFI-PE, theoretical, and HeI experimental ionic vibrational constants. Theoretical constants were obtained by fitting published values to Equation 6.

	PFI-PE (cm^{-1})	HYP[2] (cm^{-1})	WP[5] (cm^{-1})	HeI[13] (cm^{-1})
ω_e	2332.26 ± 3.26	2326.72	2326.51	2324.4 ± 2.6
$\omega_e x_e$	69.77 ±0.72	68.75	68.74	67.84 ±0.64
$\omega_e y_e$	1.152 ±0.058	1.089	1.089	1.000 ±0.059
$\omega_e z_e$	-0.0346 ±0.0015	-0.0334	-0.0346	-0.0308±0.0017

Table 5. Comparison of the rotational constants for $H_2^+(X^2\Sigma_g^+, v^+)$. Using the rovibronic positions given by HYP[2], we have obtained the B_{v^+} and D_{v^+} values for $H_2^+(X^2\Sigma_g^+, v^+=0\text{-}18)$. The B_{v^+} and D_{v^+} values for HYP[2] and WP[5] were calculated by fitting their reported energy levels of the rovibronic transitions.

	PFI-PE		Theory[2,3]		Hel[13]		Wolniewicz & Poll[5]	
v^+	B_{v^+} (cm^{-1})	D_{v^+} (cm^{-1})	B_{v^+} (cm^{-1})	D_{v^+} (cm^{-1})	B_{v^+} (cm^{-1})	D_{v^+} (cm^{-1})	B_{v^+} (cm^{-1})	D_{v^+} (cm^{-1})
0	29.112±0.150	0.0151±0.0058	29.157_1	$0.01948_{.1}$	29.6±2.5	0.03±0.08	29.073	0.0167
1	27.678±0.068	0.0192±0.0042	27.622_1	0.01866_2	28.1±1.1	0.04±0.04	27.539	0.0160
2	26.091±0.132	0.0150±0.0054	26.140_1	0.01789_2	26.4±1.1	0.03±0.03	26.054	0.0151
3	24.680±0.127	0.0172±0.0052	24.703_1	0.01716_2	24.8±0.5	0.02±0.02	24.624	0.0146
4	23.295±0.096	0.0176±0.0040	23.304_1	0.01650_2	23.6±1.1	0.03±0.04	23.224	0.0140
5	21.773±0.088	0.0113±0.0036	21.934_1	0.01587_2	22.3±0.4	0.03±0.01	21.857	0.0134
6	20.614±0.104	0.0153±0.0057	20.586_1	0.01528_2	21.0±1.3	0.02±0.04	20.512	0.0129
7	19.247±0.142	0.0153±0.0057	19.252_2	0.01473_4	19.0±0.3	0.00±0.01	19.175	0.0123
8	17.957±0.149	0.0116±0.0057	17.923_2	0.01424_4	18.3±0.5	0.04±0.03	17.843	0.0117
9	16.672±0.235	0.0126±0.0098	16.591_2	0.01380_4	17.2±0.6	0.05±0.03	16.511	0.0114
10	15.153±0.238	0.0163±0.0130	15.245_2	0.01343_4	15.0±0.8	0.00±0.04	15.173	0.0112
11	13.835±0.129	0.0148±0.0052	13.873_2	0.01312_4	14.5±0.5	---	13.802	0.0109
12	12.488±0.179	0.0280±0.0110	12.462_2	0.01293_4	12.8±0.6	---	12.383	0.0105
13	11.009±0.204	0.0145±0.0082	10.994_1	0.01284_6	11.1±0.5	---	10.915	0.0105
14	9.558±0.040	0.0294±0.0038	9.447_1	0.01295_8	9.9±1.4	---	9.377	0.0109
15	7.788±0.171	0.0169±0.0069	7.794	0.01337	8.3±1.0	---	7.718	0.0112
16	5.947±0.049	0.0294±0.0038	5.992	0.01426	---	---	5.923	0.0124
17	3.991±0.075	0.0158±0.0031	3.985	0.01629	---	---	3.921	0.0152
18	1.489±0.107	---	1.751	0.0200	---	---	1.598	0.0112
19	---	---	0.3	---	---	---	---	---

Table 6. Comparison of H_2^+ rotational constants and the internuclear distance.

	PFI-PE	Rydberg Series[1]	HeI[13]
B_e (cm^{-1})	29.87 ± 0.17	30.2_1	29.99 ± 0.30
α_e (cm^{-1})	1.424±0.0162	1.68_5	1.388±0.033
r_e (Å)	1.058±0.003	1.052	1.056±0.005

Table 7. Comparison of experimental and theoretical H_2^- molecular ion dissociation energies. (D_0) in cm^{-1}. The first three entries are experimental and the last three are theoretical.

	H_2^-
PFI-PE	21381
Hel[13]	21375
Huber & Herzberg[1]	21379.8
HYP[2]	21379.17
Bishop[7]	21379.39
Wolniewicz & Poll[5]	21380.81

Figure Captions

Figure 1. Rotationally resolved PFI-PE spectrum of $H_2^+(X\,^2\Sigma_g^+, v^+=0\text{-}18)$. Note that the relative intensity for the (1, 1) transition of $v^+=0$ is to 8873.

Figure 2. Rotationally resolved PFI-PE bands of $H_2^+(X\,^2\Sigma_g^+)$. (a) $v^+=0$, (b) $v^+=1$, (c) $v^+=2$, etc. The BOS fits are depicted by the dashed curves. All spectra have the same units of $I(e^-)/I(h\nu)$. Note that the relative intensity for the (1, 1) transition of $v^+=0$ is to 8873.

Figure 3. Vibrational energy level differences, $\Delta G_{v^+,1/2}$, of H_2^+ for PFI-PE (•), H., Y., & P.[2] (---), and Wolniewicz and Poll[5] (—).

Figure 4. Vibrational energy level differences, $\Delta G_{v^+,1/2}$, of H_2^+ for PFI-PE (•), H., Y., & P.[2] (---), and Wolniewicz and Poll[5] (—) with a linear term subtracted (-2249.0-116.87(v+1/2)).

Figure 5. Rotational constant, B_{v^+}, for H_2^+ $v^+=0\text{-}17$. The circles (•) represent the PFI-PE values, the squares (□) represents the theoretical values of Beckel, Hansen, and Peek[3], and the solid line (—) represents the theoretical values of Wolniewicz and Poll.[5]

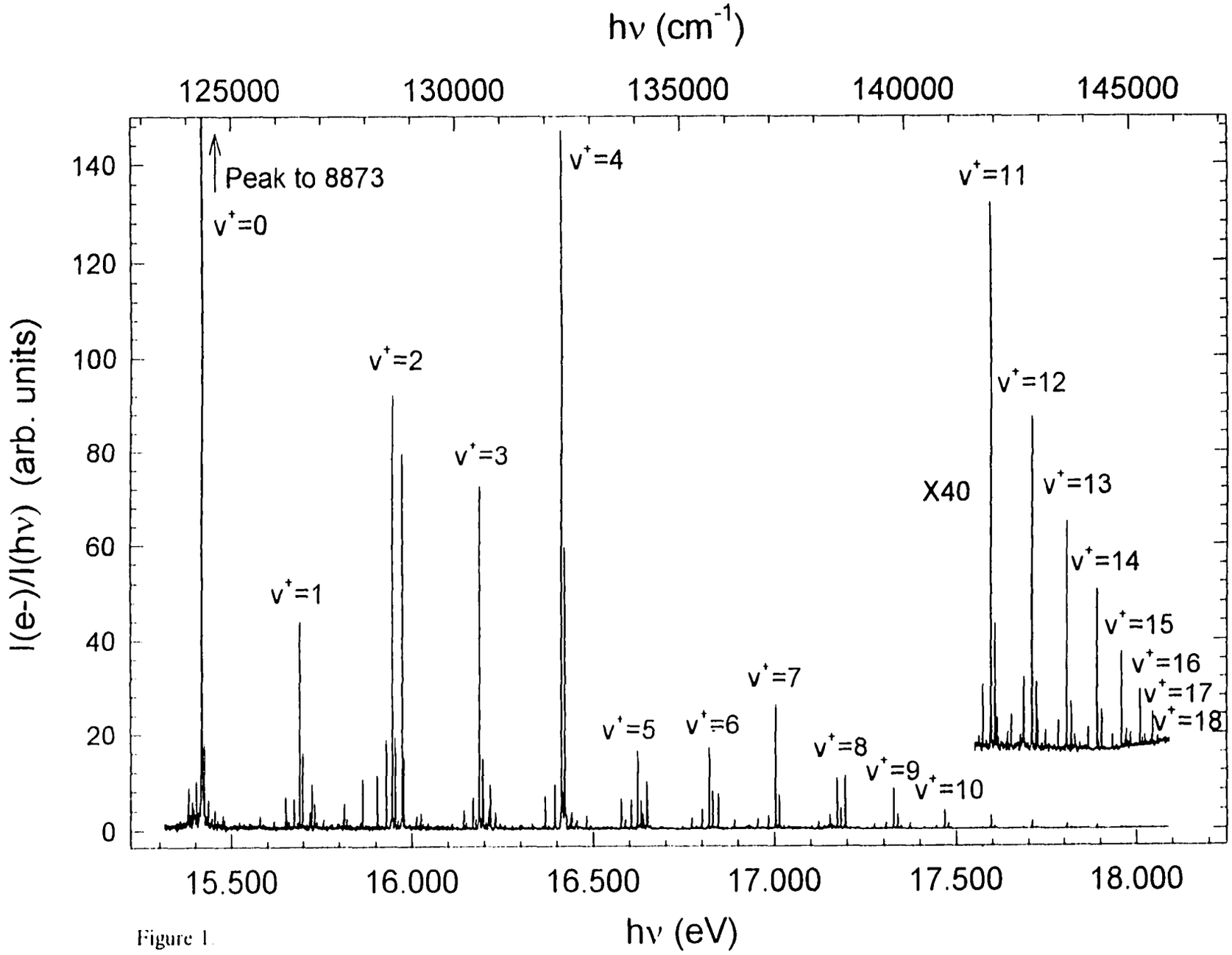
hν (cm-1)
125000
130000
135000
140000
145000
I(e-)/I(hν) (arb. units)
140
120
100
80
60
40
20
0
Peak to 8873
v+=0
v+=1
v+=2
v+=3
v+=4
v+=5
v+=6
v+=7
v+=8
v+=9
v+=10
v+=11
v+=12
v+=13
v+=14
v+=15
v+=16
v+=17
v+=18
X40
15.500
16.000
16.500
17.000
17.500
18.000
hν (eV)

Figure 1

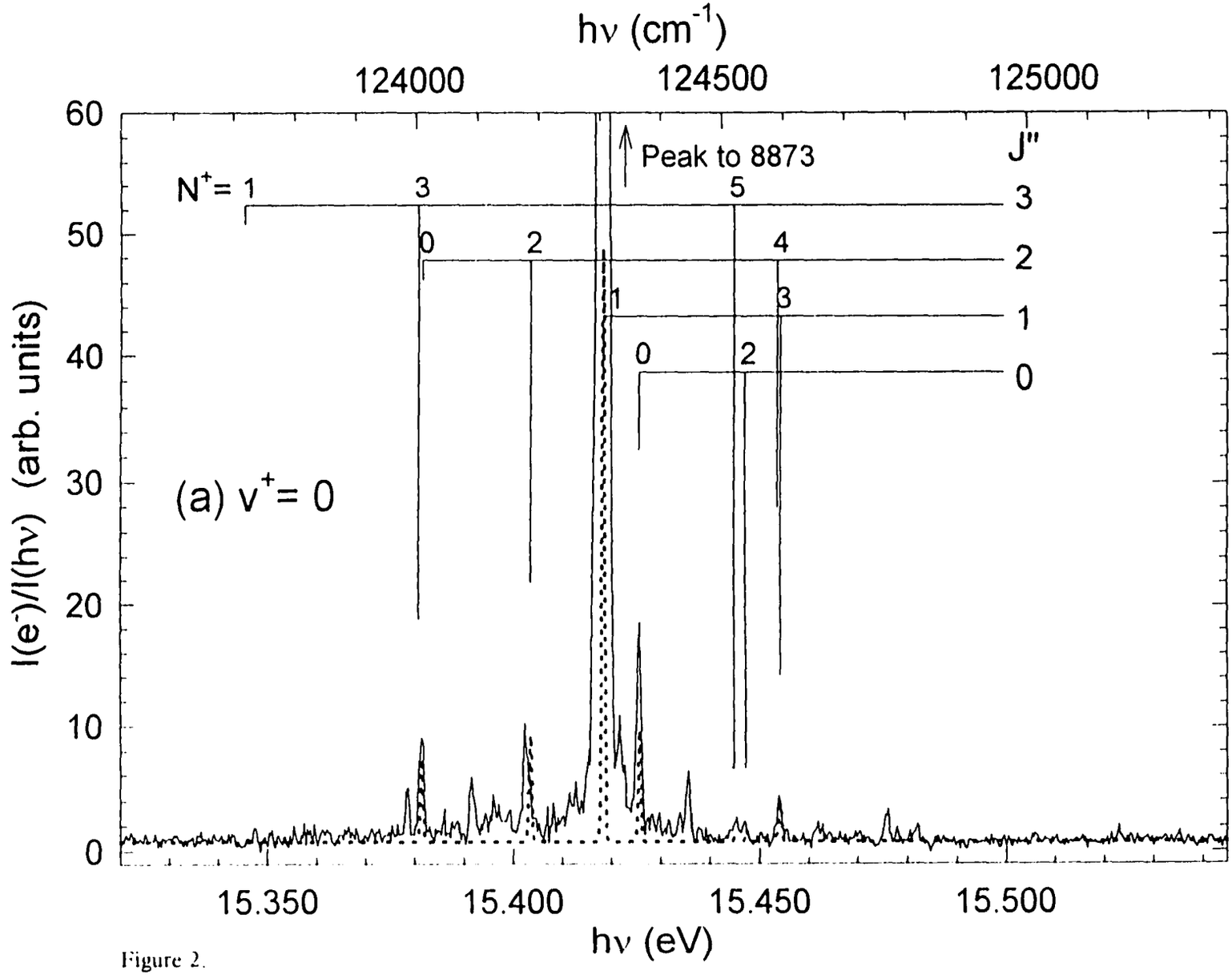
hν (cm-1)
124000
124500
125000
60
50
40
30
20
10
0
I(e-)/I(hν) (arb. units)
Peak to 8873
J"
N+= 1
3
5
3
0
2
4
2
1
3
1
0
2
0
(a) v+= 0
15.350
15.400
15.450
15.500
hν (eV)

Figure 2.

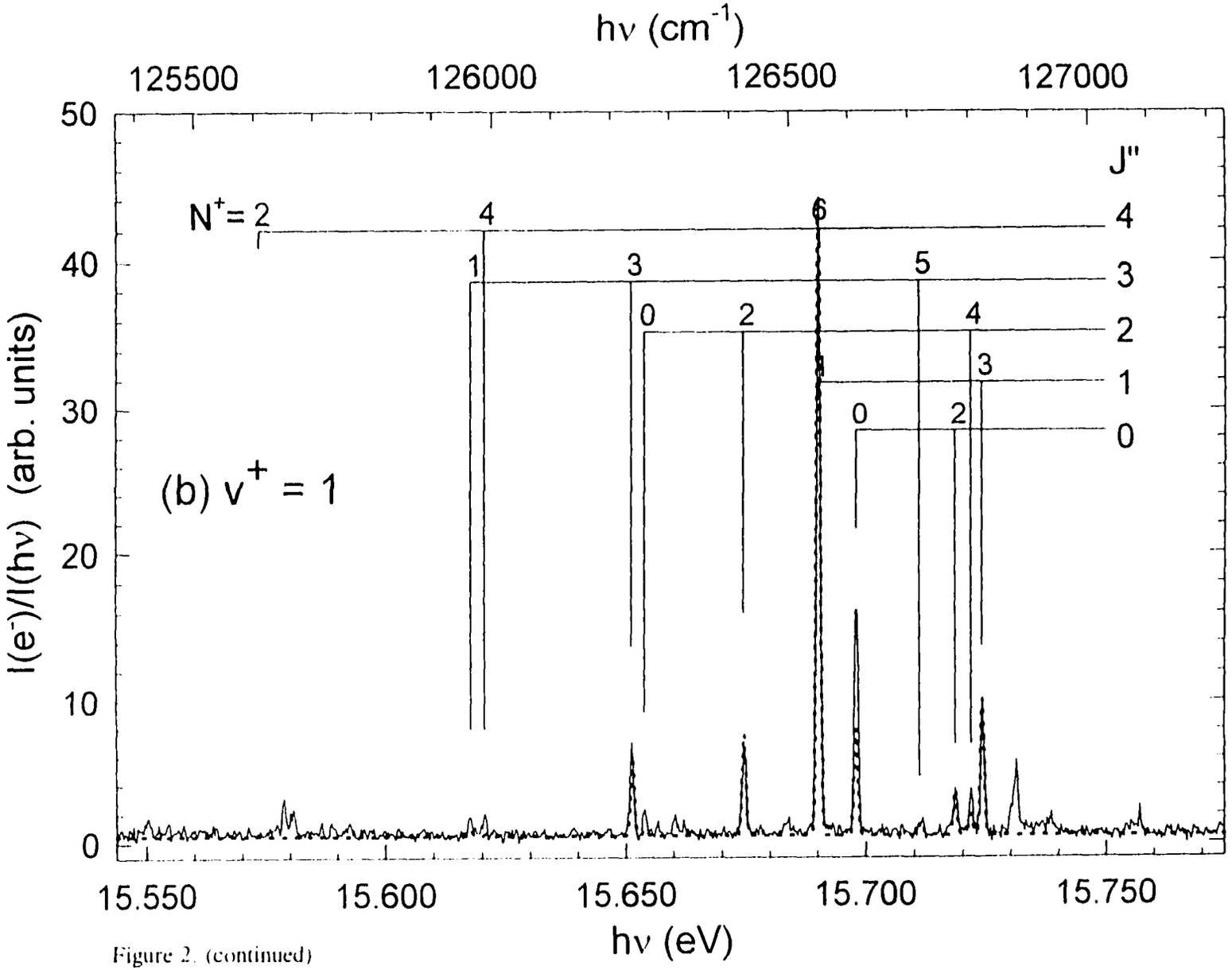

Figure 2. (continued)

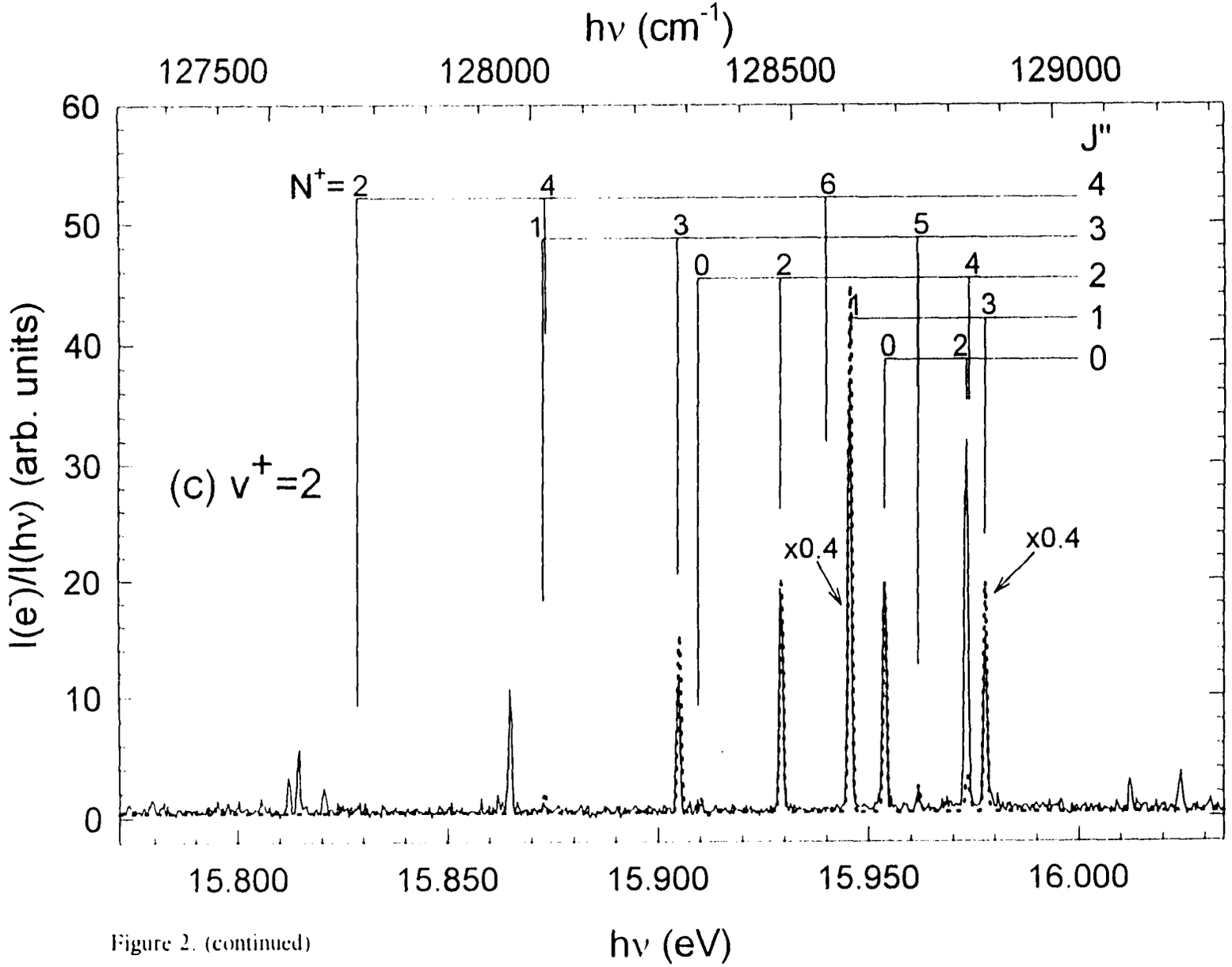

Figure 2. (continued)

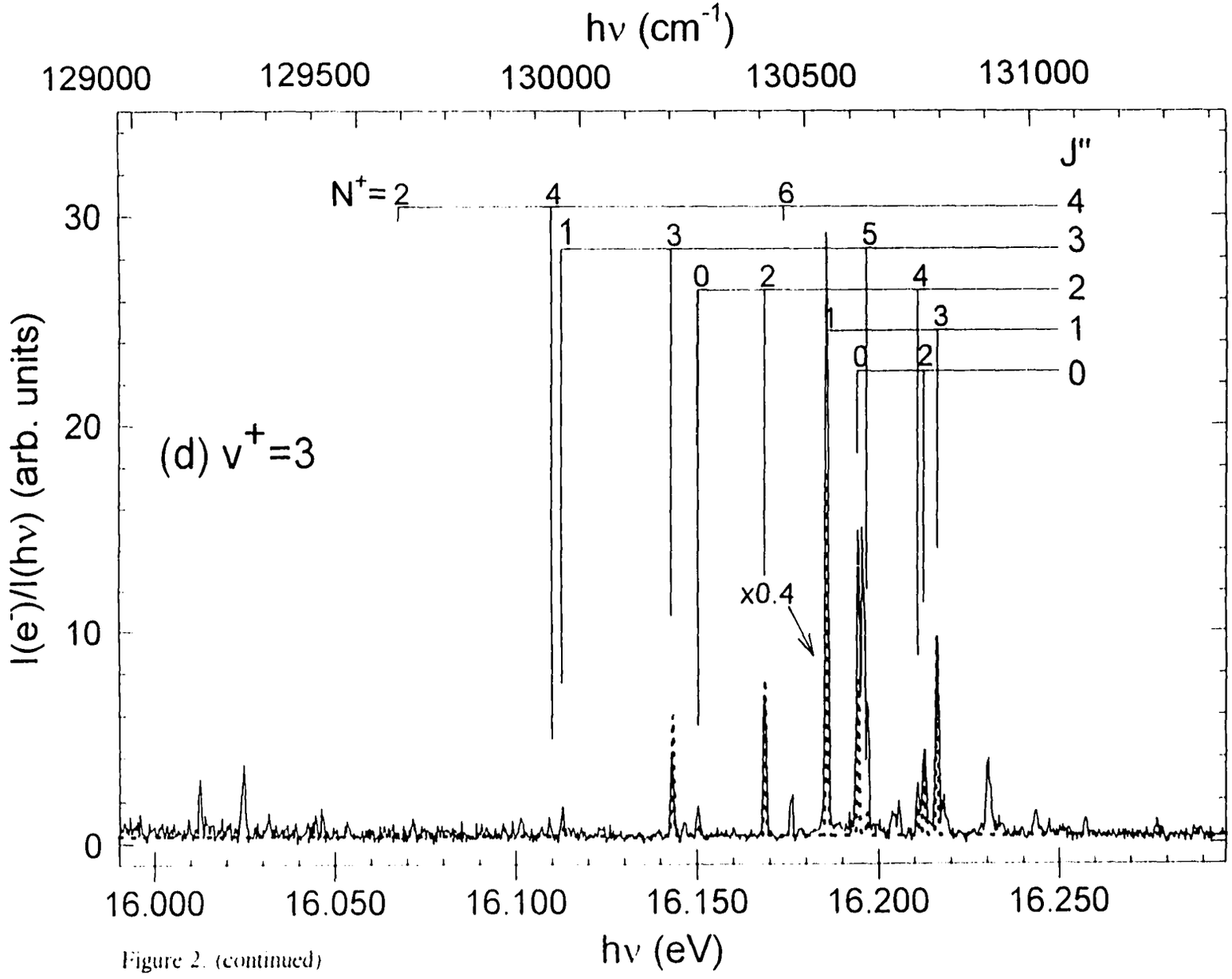

Figure 2. (continued)

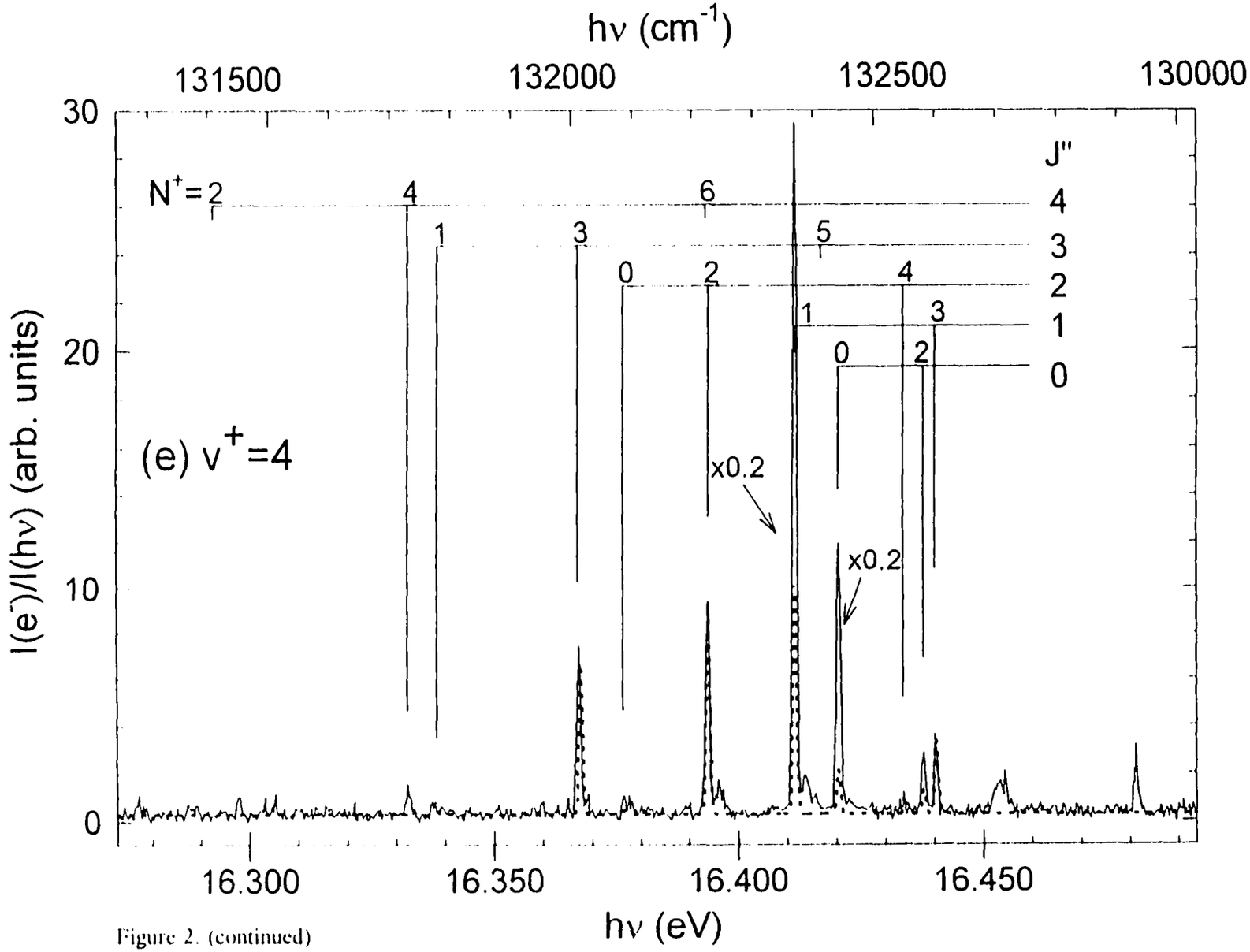

Figure 2. (continued)

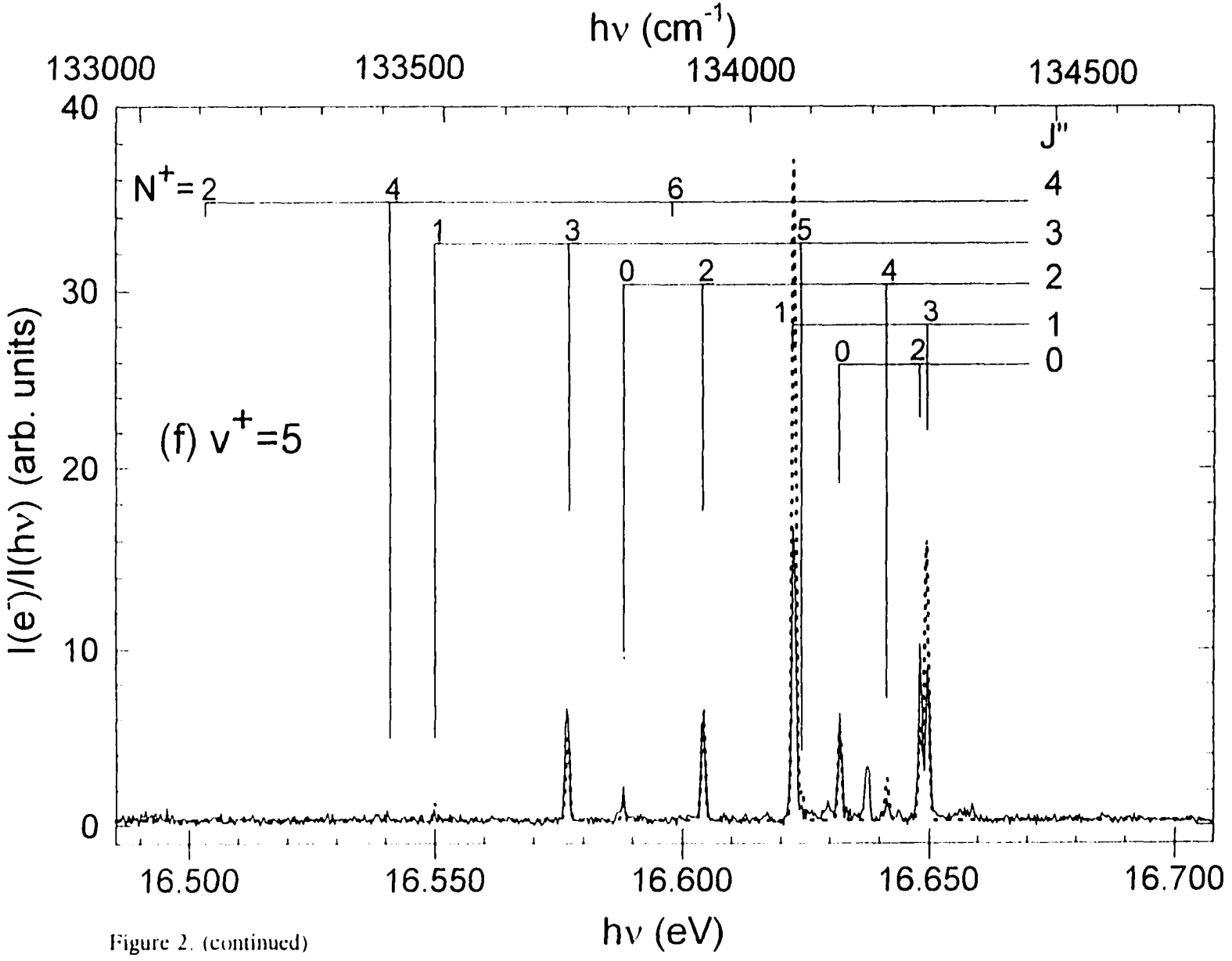

Figure 2. (continued)

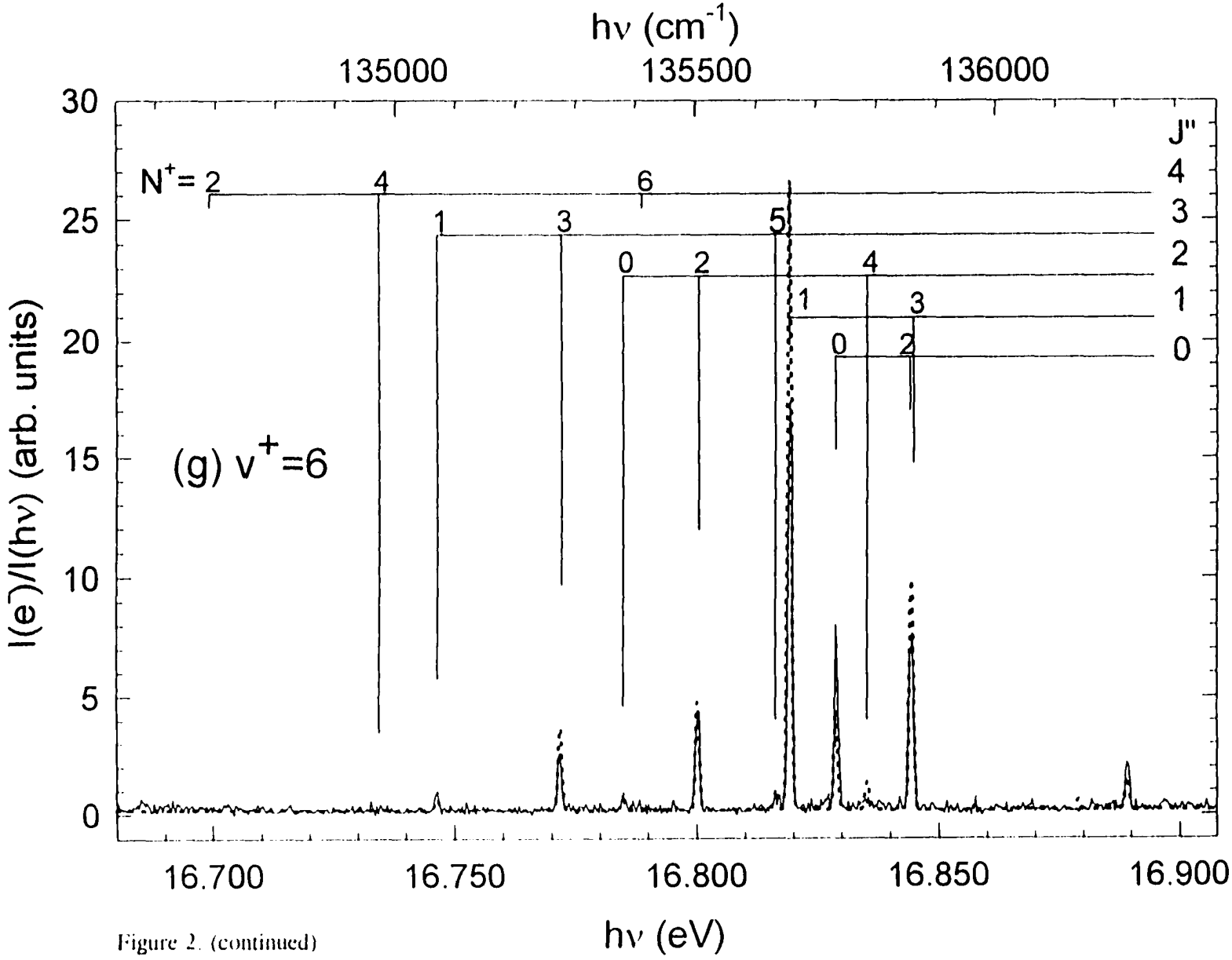

Figure 2. (continued)

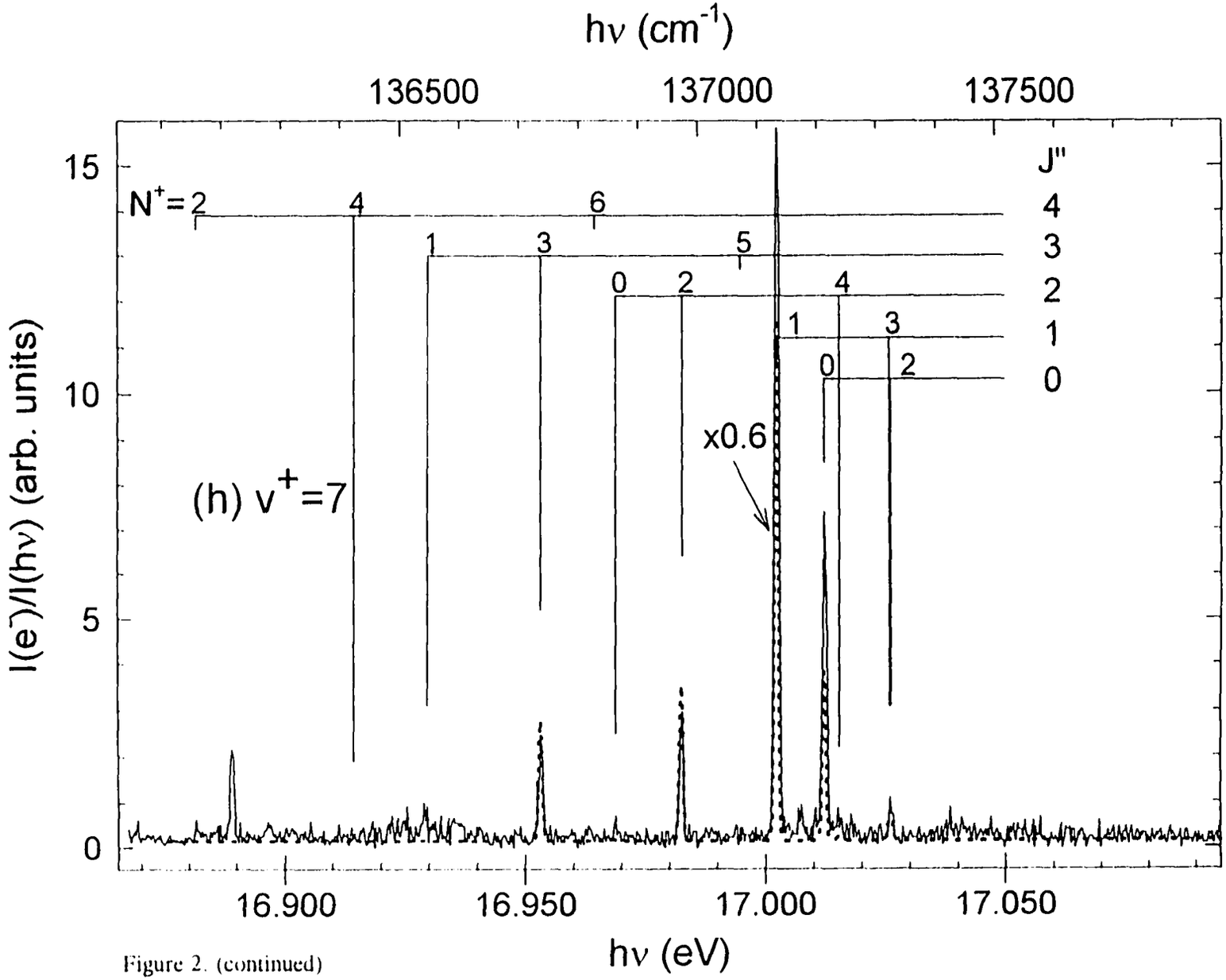

Figure 2. (continued)

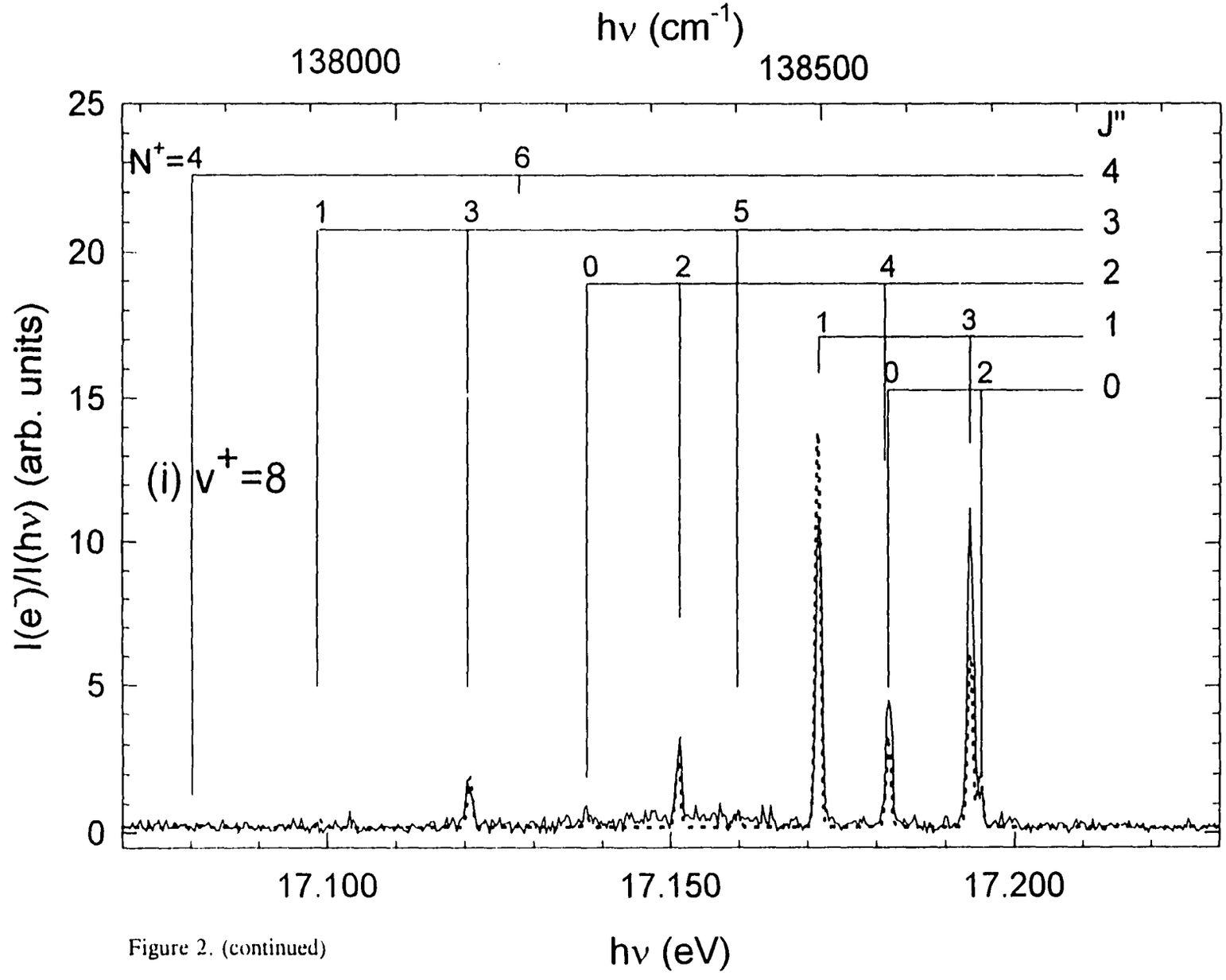

Figure 2. (continued)

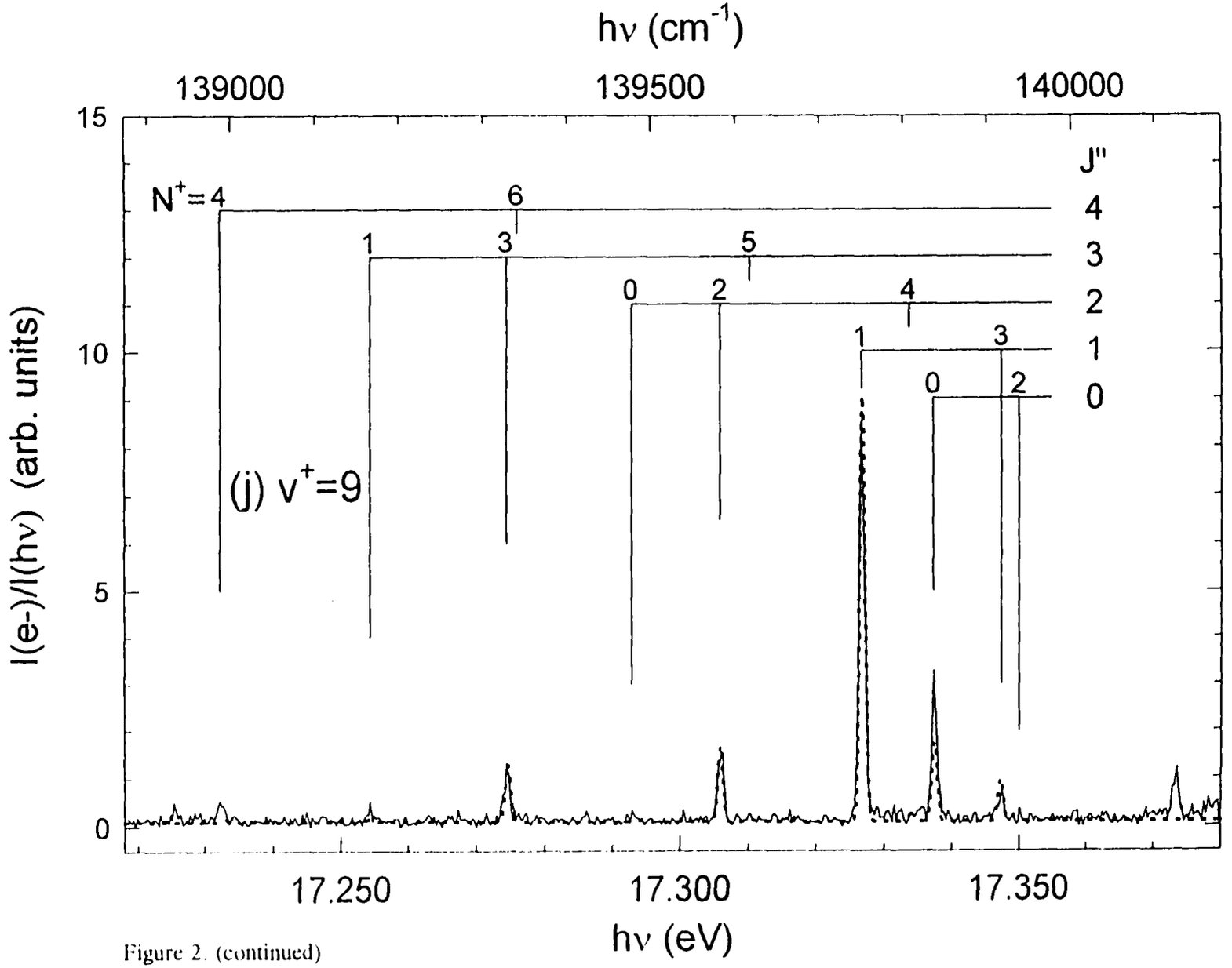

Figure 2. (continued)

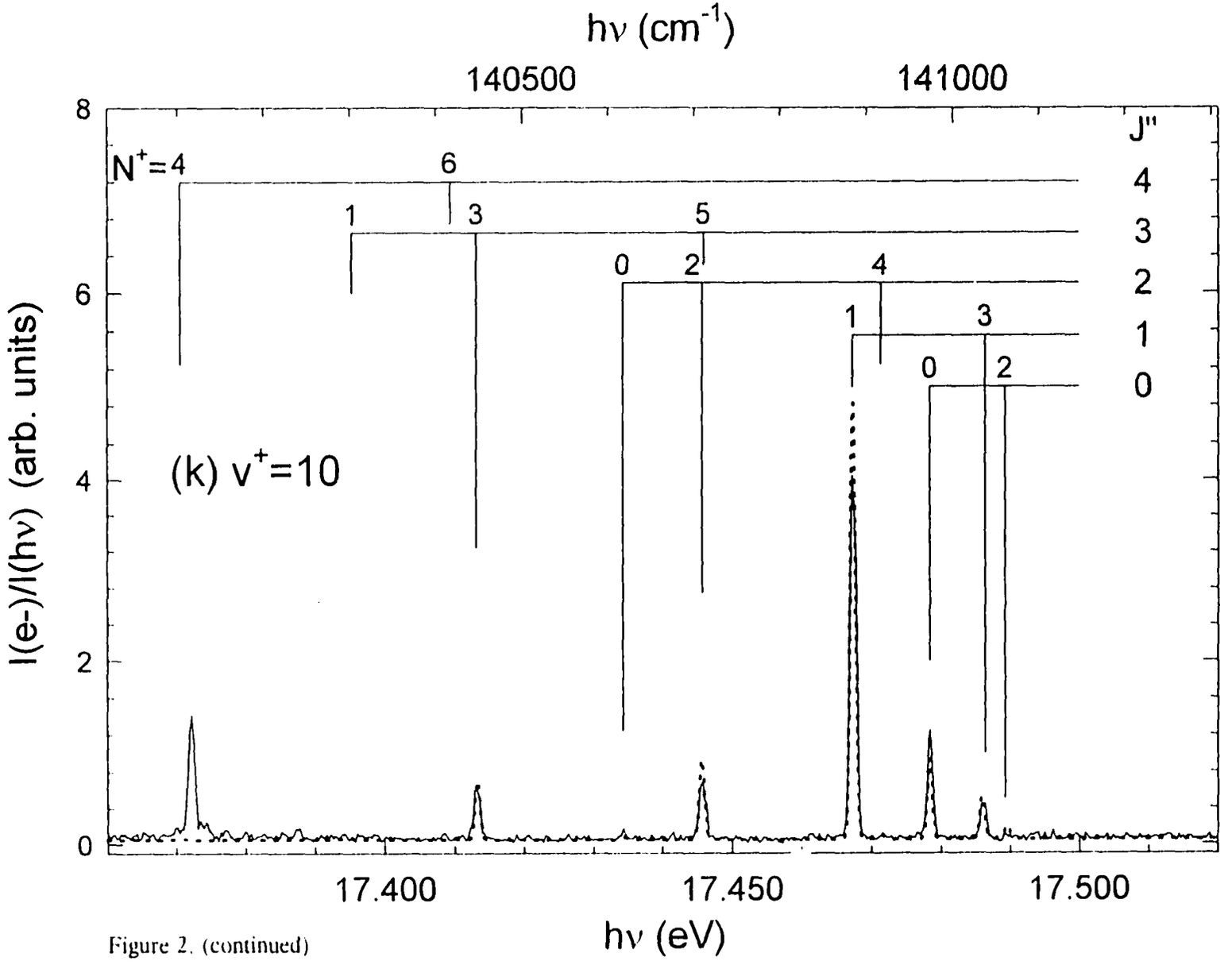

Figure 2. (continued)

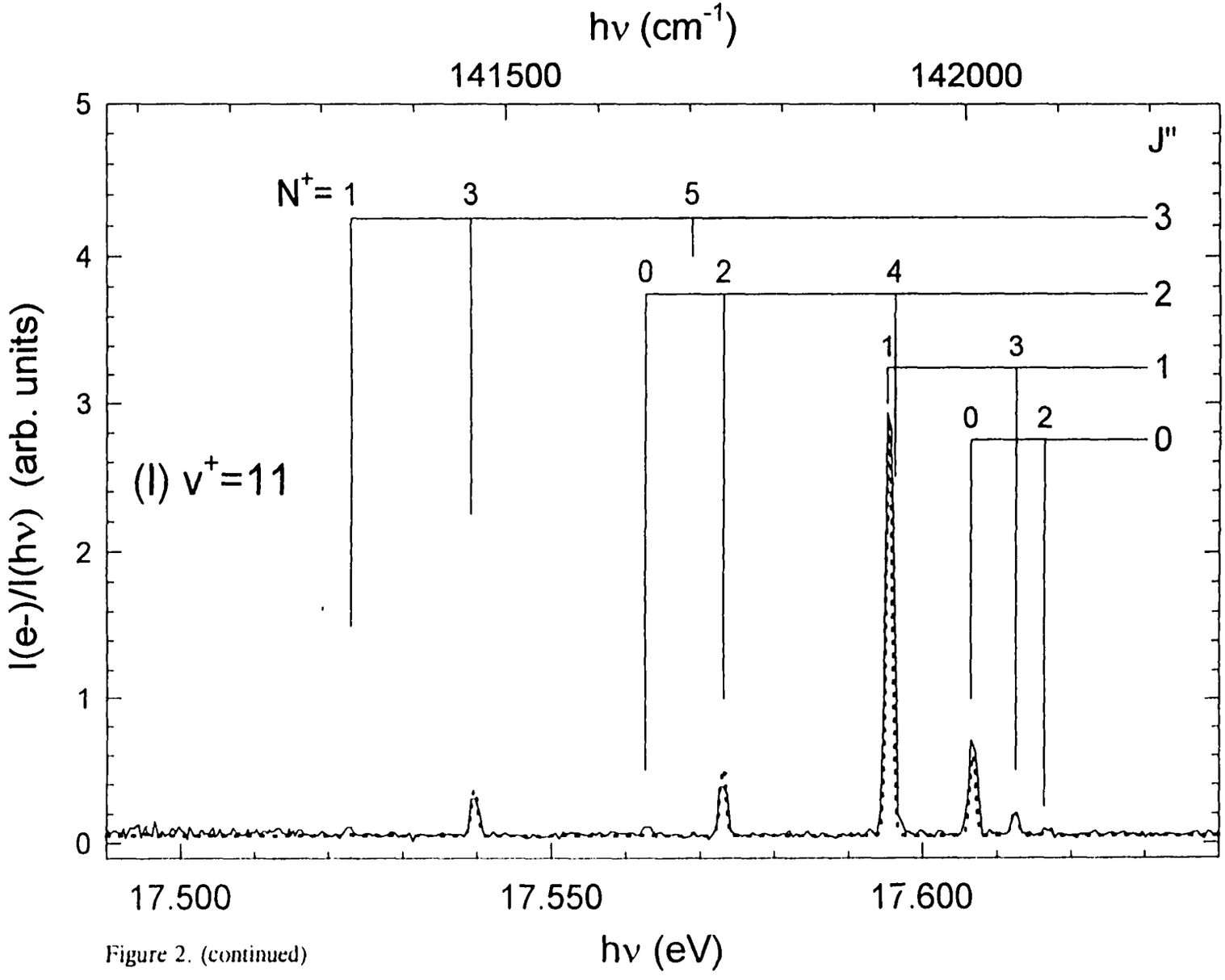

Figure 2. (continued)

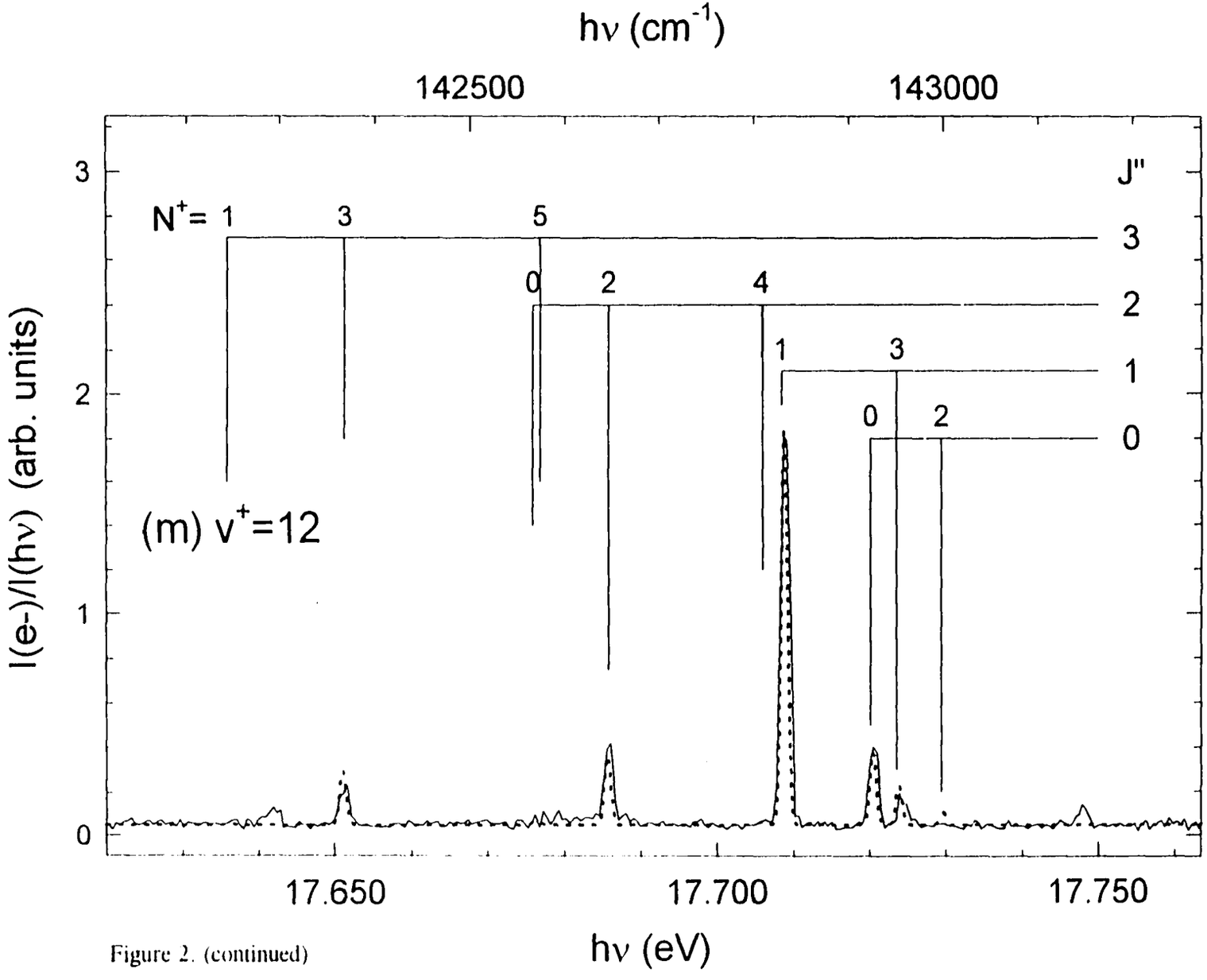

Figure 2. (continued)

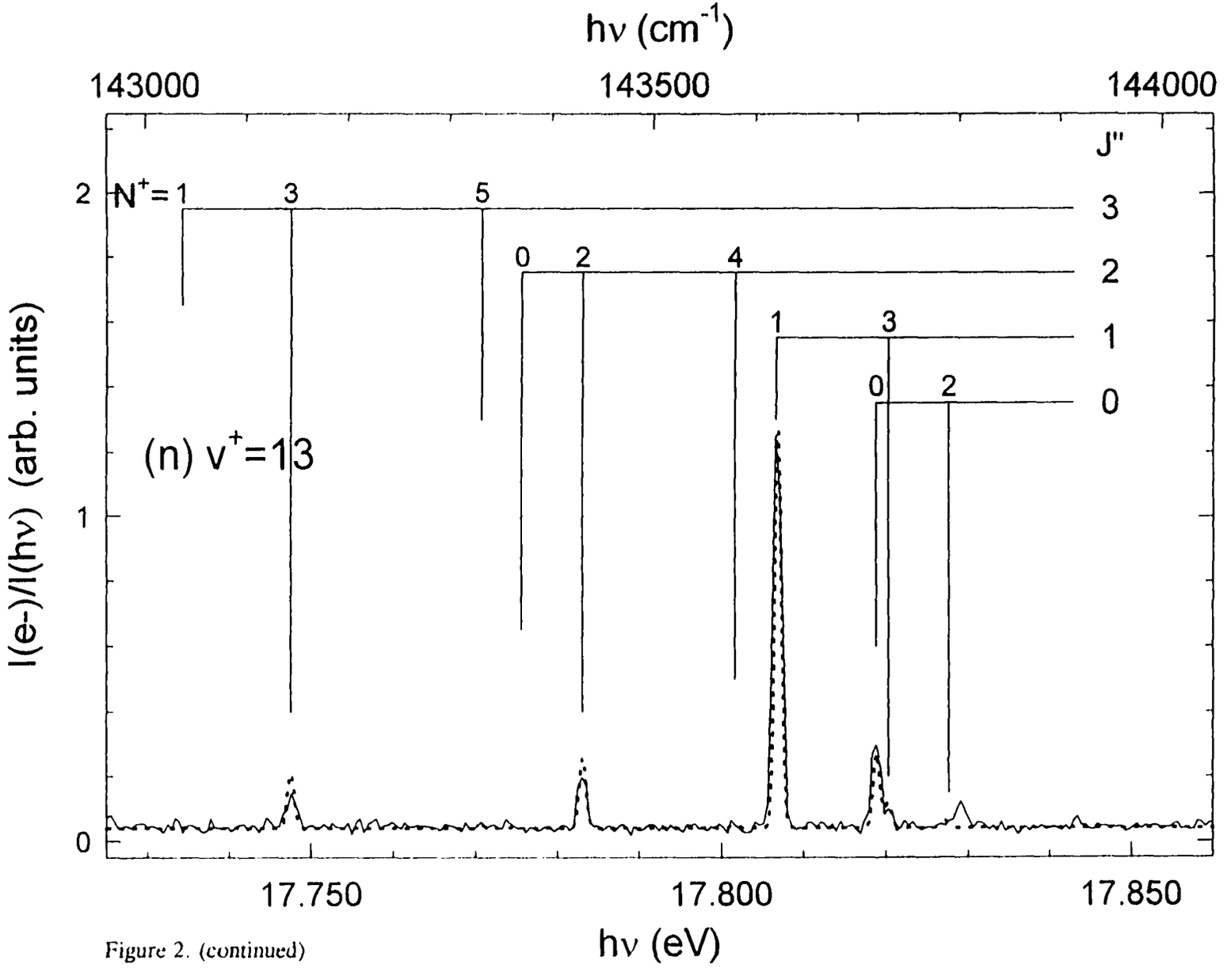

Figure 2. (continued)

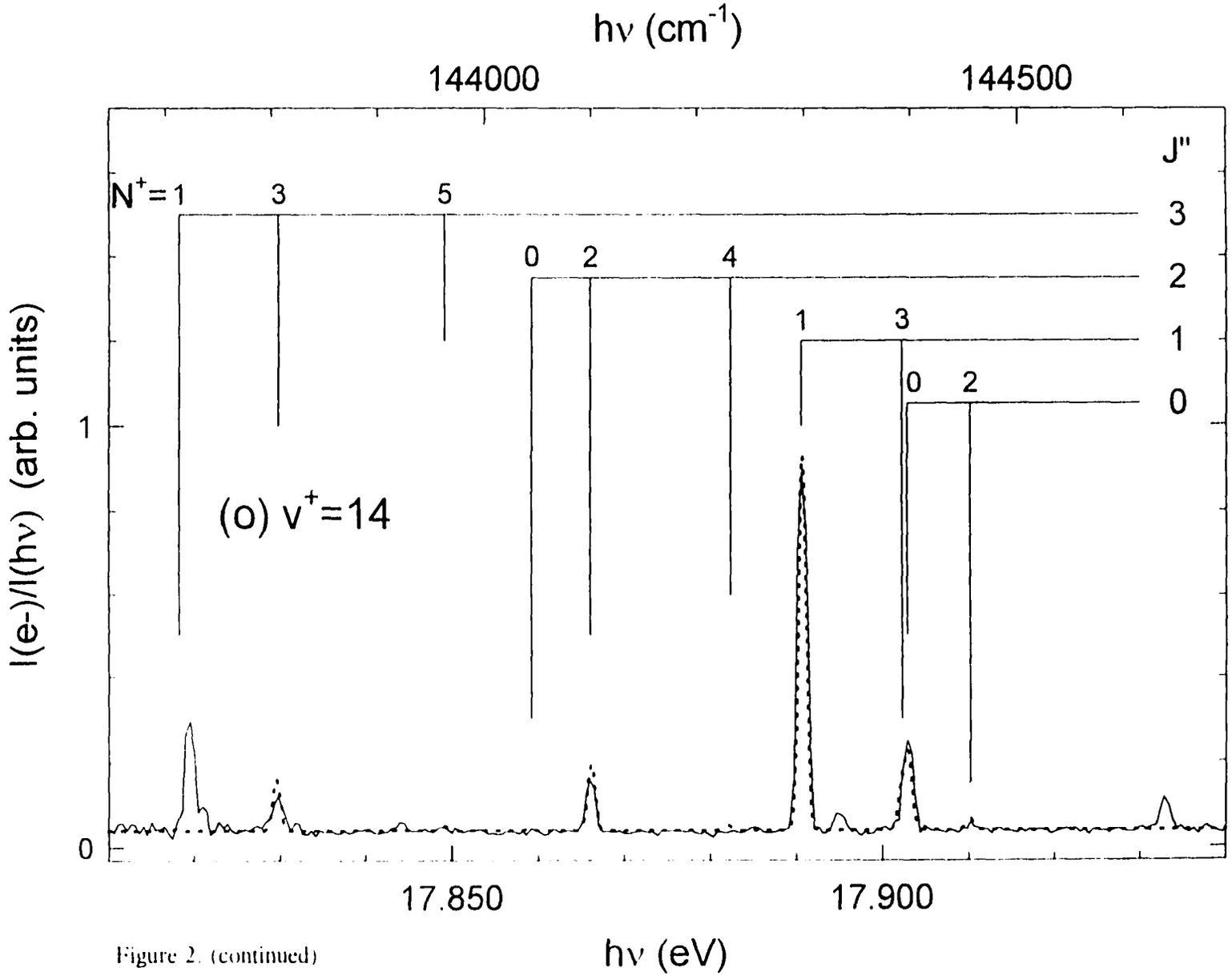

Figure 2. (continued)

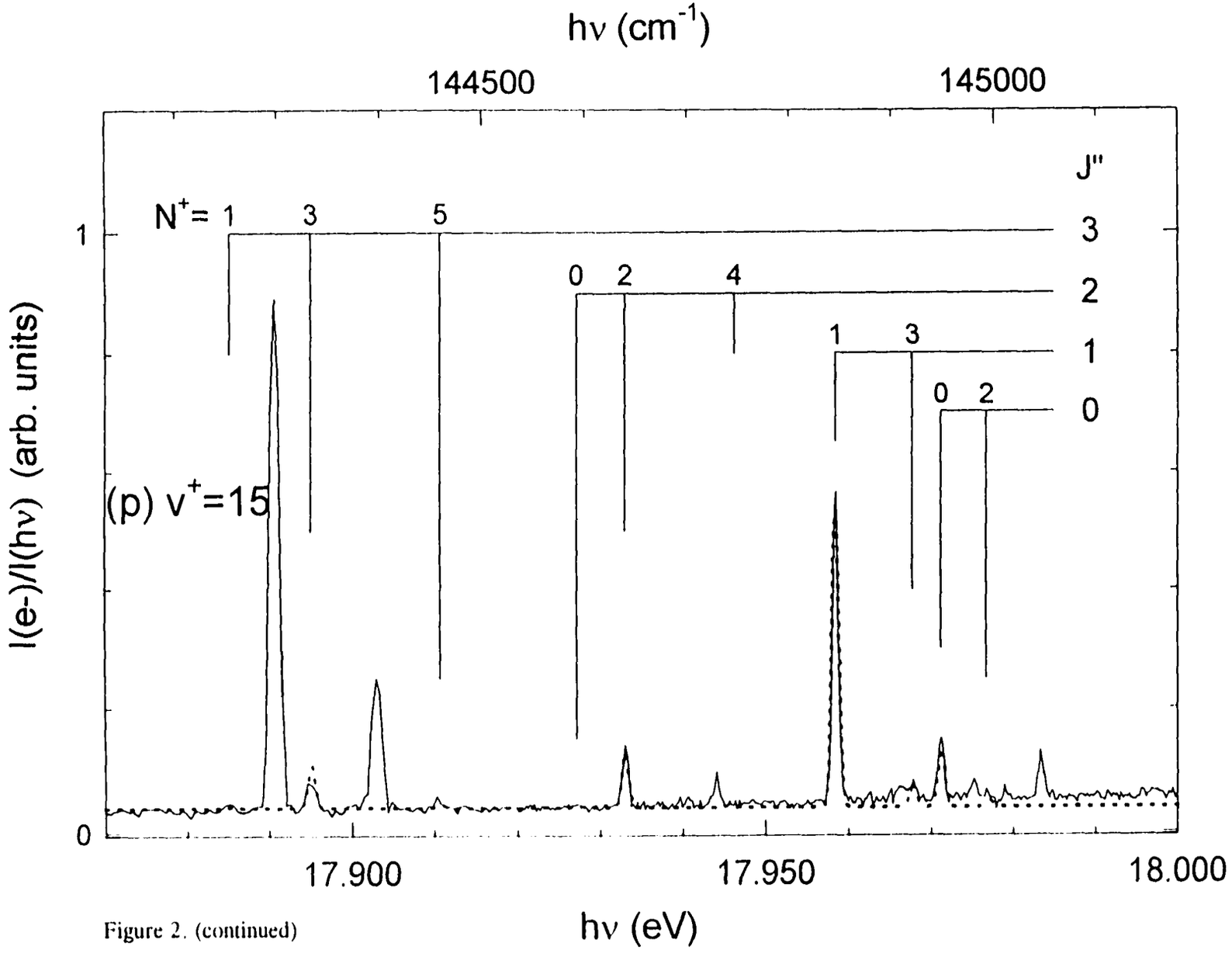

Figure 2. (continued)

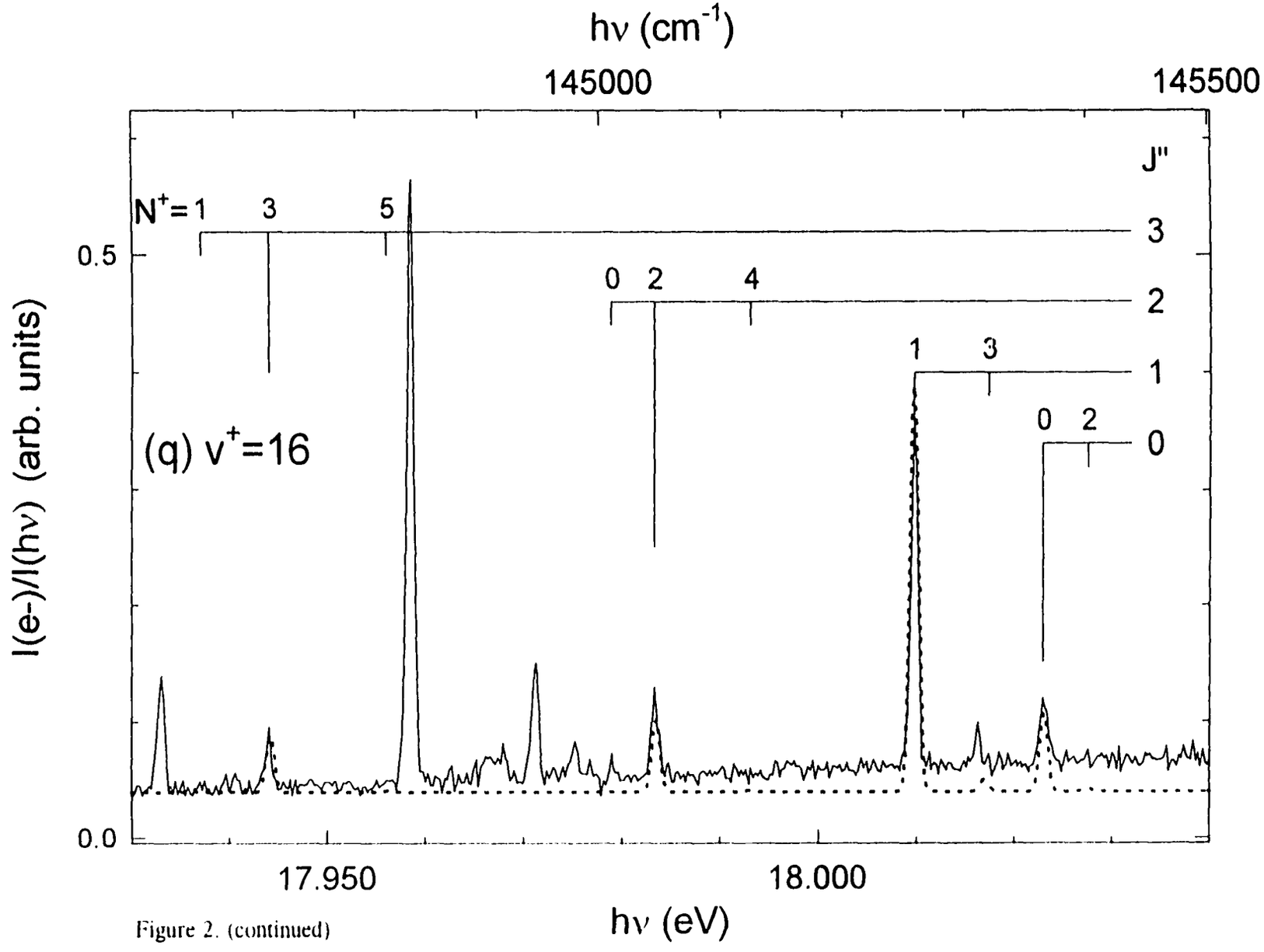

Figure 2. (continued)

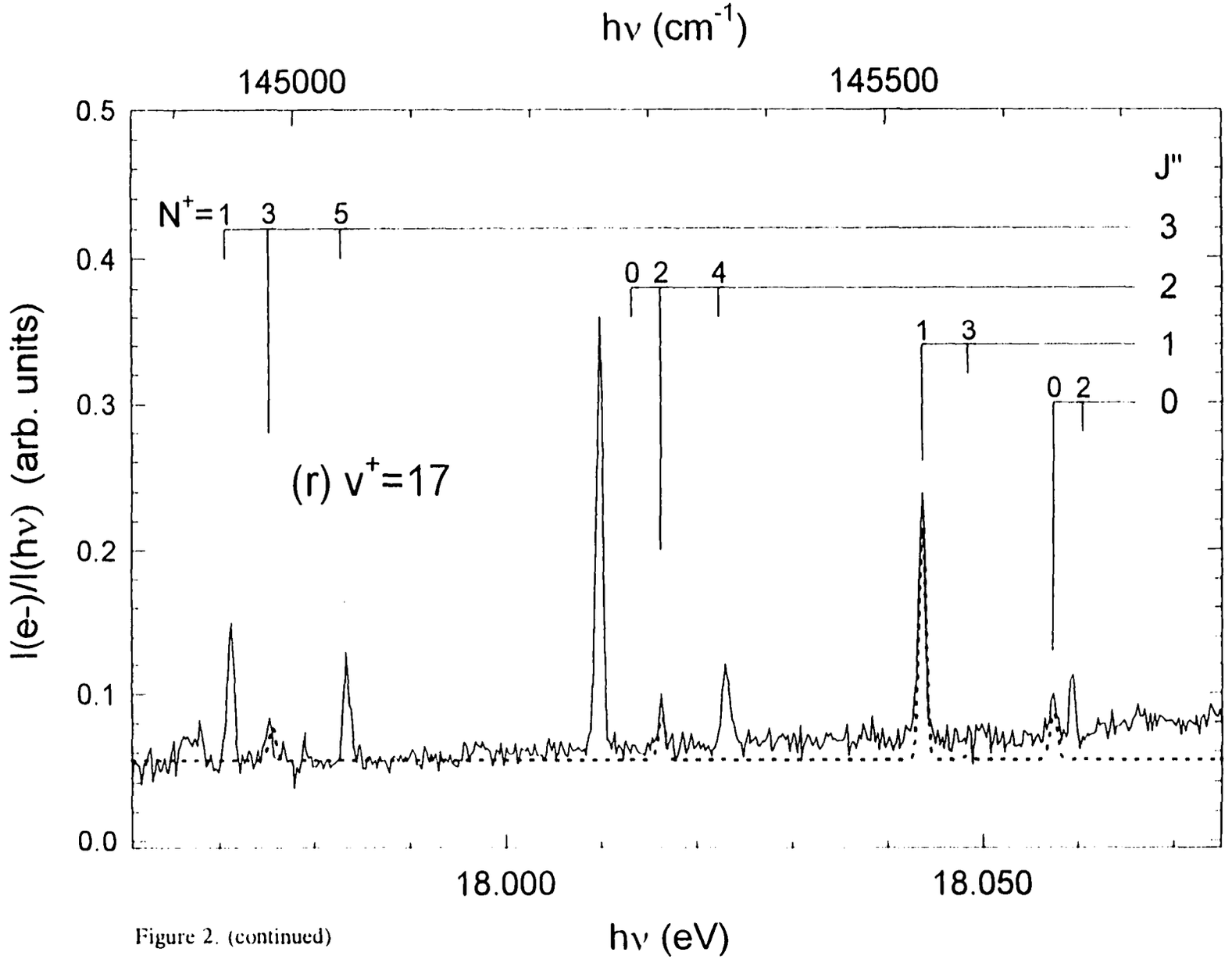

Figure 2. (continued)

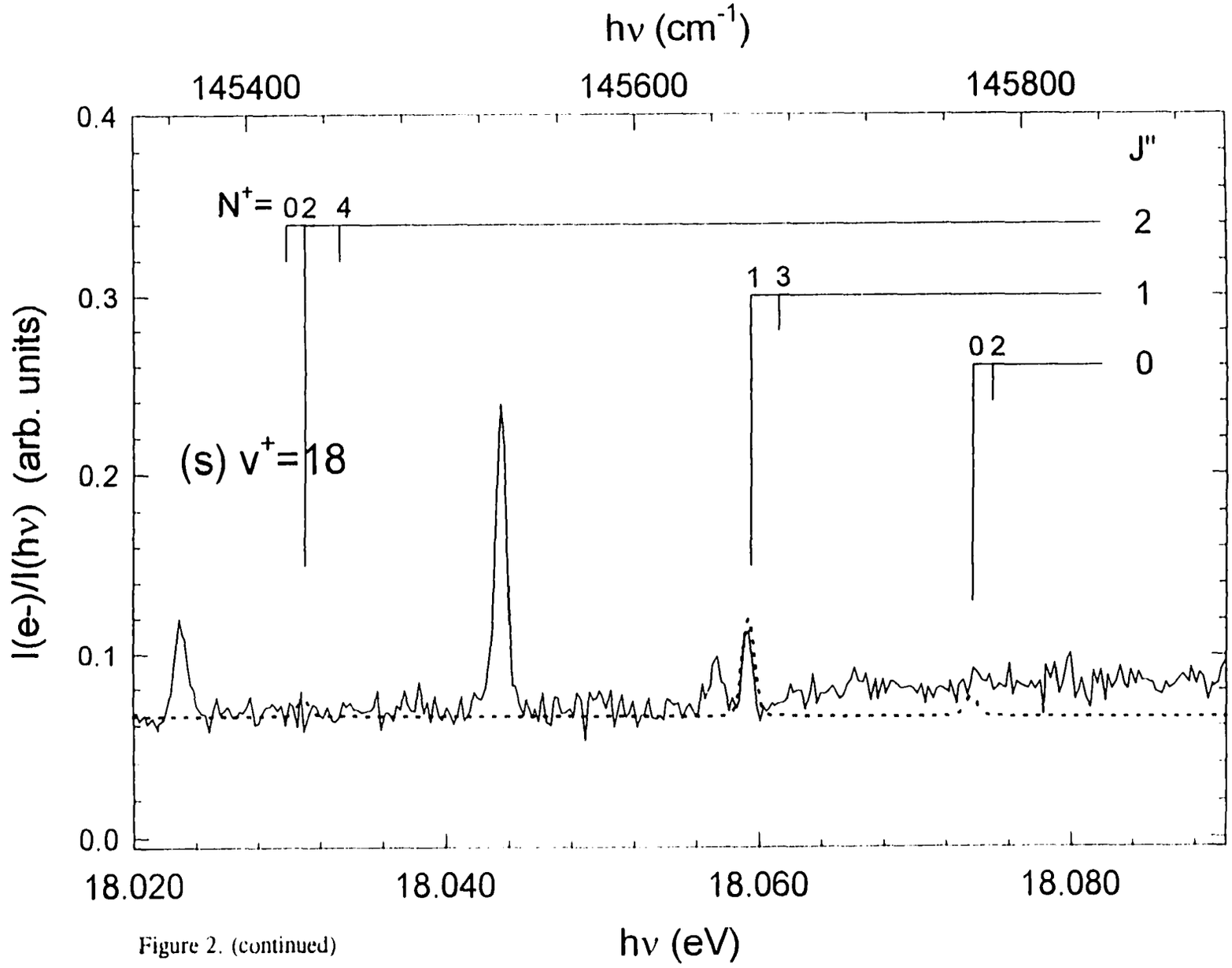

Figure 2. (continued)

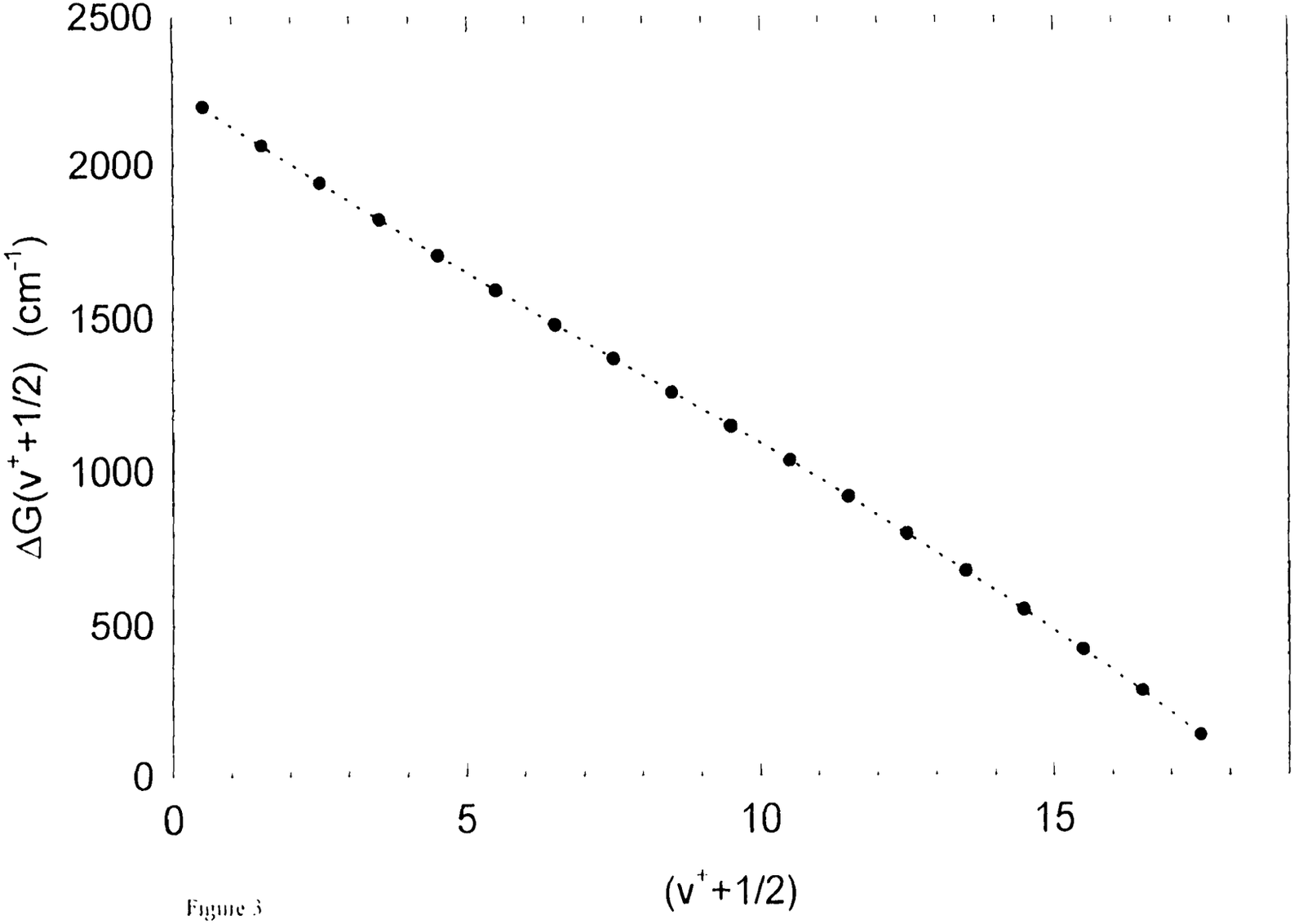

Figure 3

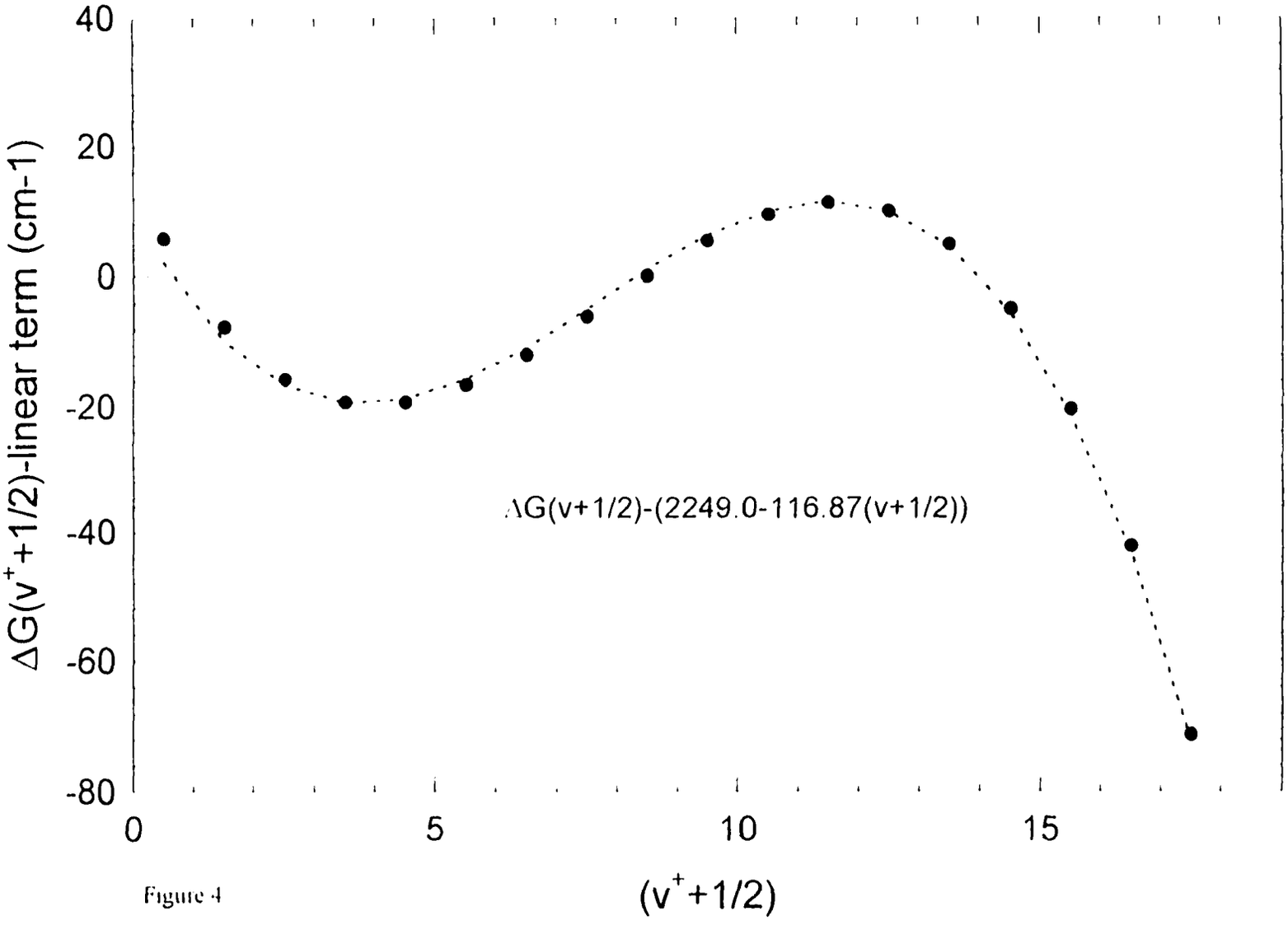
40
20
0
-20
-40
-60
-80
0
5
10
15
ΔG(v+1/2)-(2249.0-116.87(v+1/2))
ΔG(v⁺+1/2)-linear term (cm-1)
(v⁺+1/2)

Figure 4

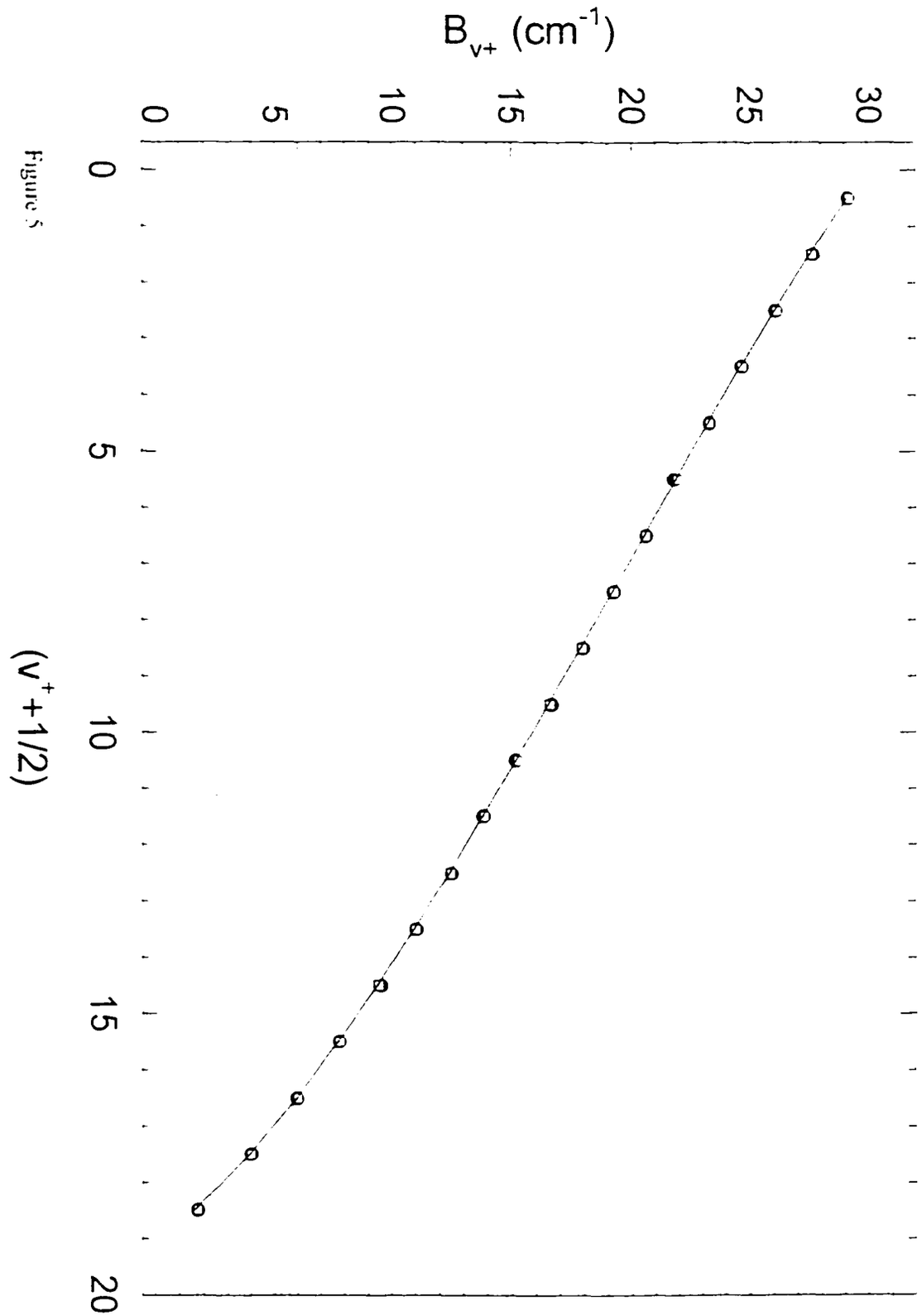

Figure 5

ROTATIONALLY RESOLVED PULSED FIELD IONIZATION PHOTOELECTRON BANDS OF $HD^+(X^2\Sigma^+, v^+=0\text{-}21)$

A paper to be submitted to the Journal of Chemical Physics

S. Stimson, M. Evans, C.-W. Hsu,[2] P. Heimann,[2] and C.Y. Ng[1,3]

Abstract

We have obtained the rotationally resolved pulsed field ionization photoelectron (PFI-PE) spectrum of HD at a resolution of ≈7 cm^{-1} FWHM (full-width-at-half-maximum) in the photon energy range of 15.29-18.11 eV. Presented here is the assignment of rotational transitions for the $HD^+(X^2\Sigma^+, v^+ = 0\text{-}21)$ vibronic bands and their simulation using the Buckingham-Orr-Sichel (BOS) model. The BOS simulation shows that the perturbation of PFI-PE rotational line intensities due to near-resonance autoionization decreases as v^+ increases. From the experimental data, $\Delta G(v^+ + 1/2)$, B_{v^+}, and D_{v^+} were determined and used to calculate the ionic vibrational and rotational constants (ω_e, $\omega_e x_e$, $\omega_e y_e$, $\omega_e z_e$, B_e, and α_e), the internuclear separation (r_e), and the dissociation energy (D_0). In agreement with previous experimental and theoretical investigations, the $\Delta N^+ = 0, \pm 1, \pm 2, \pm 3$, and ± 4 rotational branches were observed in the PFI-PE spectrum of HD.

[1] Ames Laboratory, USDOE and Department of Chemistry, Iowa State University, Ames, IA 50011, USA.

[2] Chemical Sciences Division and Advanced Light Source Accelerator and Fusion Research Division, Lawrence Berkeley National Laboratory, Berkeley, CA 94720, USA.

[3] Author to whom correspondence should be addressed. E-mail addresses: C.Y. Ng: <CYNG@Ameslab.gov>.

Introduction

The vibration and rotation transition frequencies and spectroscopic constants for HD and HD^- in their ground and excited rovibronic states have been calculated.[1-14,34] Reliable and extensive calculations for the rovibronic energies of HD^- have been obtained at different levels of theory.[2-5,9,10,12] For example, the stated accuracy of the adiabatic calculations including nonadiabatic, relativistic, and radiative effects performed by Wolniewicz and Poll[3,5] and Balint-Kurti *et al*[9] for the bound state levels of HD^- was 0.001 cm^{-1}. The accuracy of measurements by Wing *et al*[22] using an ion-beam laser-resonance method was very high, within 0.002 cm^{-1}, but only a few rovibronic transitions were observed. Measurements by Pollard *et al*[15] using photoelectron spectroscopic techniques were accurate to within 2 cm^{-1}. Partly for these reasons, the HD/HD^- system has been the choice for detailed experimental[15-22,38-44] and theoretical[1-14] studies of molecular photoionization dynamics.

Due to the large rotational constants of HD and HD^-, partial rotationally resolved photoelectron spectra for HD have been observed. Autoionization Rydberg structures in the region from 15.40-17.74 eV,[18,21,23,46,47] have also been observed. The majority of these Rydberg features were assigned based on comparison with predictions from multichannel quantum defect theory (MQDT).[45] The couplings between high-n ($n>100$) Rydberg (pseudocontinuum) states, lying at a few wavenumbers below an ionization limit, and low-n Rydberg (interloper) states in near-energy resonance with the pseudocontinuum states are expected to have a significant affect on the observed PFI-PE intensities.[23] Hence, the rotational components of the PFI-PE vibrational band should show different intensities compared to those resolved in previous experiments utilizing other ionization sources.

Although VUV laser radiation with useful intensities can in principle be generated up to ≈17.7 eV, the processes involved remains inefficient for routine experimentation[24-27] compared with the ease in tuning VUV synchrotron radiation. Recently, we have developed a broadly tunable, high resolution synchrotron source associated with the Chemical Dynamics Beamline at the Advanced Light Source (ALS).[28,29] An experimental scheme for PFI-PE detection using the multibunch synchrotron source has also been implemented.[30-33] As demonstrated in recent PFI-PE experiments[31-33] on Ne, Ar, Kr, and O_2, the photoelectron energy resolution achieved was 3-6 cm^{-1} (FWHM). This is comparable to the resolution obtained in VUV laser studies.[24,25,27] Using the newly implemented PFI-PE experimental scheme, we have obtained a rotationally resolved photoelectron spectrum of HD from 15.29-18.11 eV.

Experiment

The design and performance of the Chemical Dynamics Beamline at the ALS has been described previously.[28-31] The major components for the high resolution photoionization beamline includes a 10 cm period undulator, a gas harmonic filter, a 6.65m off-plane Eagle mounted monochromator, and a photoion-photoelectron apparatus. In the present experiment, helium was used in the harmonic gas filter where higher undulator harmonics with photon energies greater than 24.59 eV were suppressed, thereby eliminating interference by photoionization/photoexcitation effects caused by higher order undulator radiation. The fundamental light from the undulator is then directed into the 6.65 m monochromator and dispersed by an Os coated 4800 l/mm grating (dispersion = 0.32 Å/mm) before entering the experimental apparatus. The monochromator entrance/exit slits used were between 100/100 μm and 200/200 μm, corresponding to a wavelength resolution of 0.032 Å (FWHM) (or 0.6 meV at 800 Å) and 0.064 Å (FWHM) (or 1.2 meV at 800Å), respectively.

An effusive beam of HD was used in this experiment. The HD was obtained from Cambridge Isotope Laboratories with a reported purity greater than 98%. The HD effusive beam was introduced into the photoionization region through a metal orifice (diameter=0.5 mm) at room temperature and 0.5 cm from the photoionization region. The pressures maintained in the photoionization chamber and the photoelectron chamber were $1x10^{-6}$ and $1x10^{-7}$, respectively. The main chamber and photoelectron chambers were evacuated by turbomolecular pumps with pumping speeds of 1200 L/s and 3400 L/s, respectively. The rotational temperature was ≈298 K for the effusive beam.

The ALS storage ring is capable of filling 328 electron buckets in a period of 656 ns. Each electron bucket emits a light pulse of 50 ps with a time separation of 2 ns between successive buckets. In each storage ring period, a dark-gap (80 ns) consisting of 40 consecutive unfilled buckets exists for the ejection of cations from the orbit. The present experiment[31-36] was performed in the multibunch mode with 288 bunches in the synchrotron orbit, corresponding to an average repetition rate of 439 MHz. A pulsed electric field (height = 1.2 V/cm, width = 40 ns) was applied to the repeller at the photoionization/photoexcitation region to field ionize high-n Rydberg states and extract photoelectrons toward the detector. The pulsed electric field was applied every 1 ring period (0.656 μs) and delayed by 20 ns with respect to the beginning of the 80 ns dark-gap. The electron spectrometer, which consists of a steradiancy analyzer and a hemispherical energy analyzer arranged in tandem, was used to filter prompt electrons.[31] Judging from the width of the rotational transitions observed, we concluded that the

PFI-PE energy resolution achieved in the present experiment was ≈7-8 cm^{-1} (FWHM), comparable to the VUV photon energy resolution. On the basis of the observed PFI-PE counts at the $Ar^-(^2P_{3/2})$ threshold, the residual electron background counts at the autoionizing $Ar(11s')$ state, and the relative Ar^- ion intensities measured at the $Ar^-(^2P_{3/2})$ threshold and at the $Ar(11s')$ state,[28,31] we estimated that the suppression factor for prompt electrons is $\approx 5\times10^{-4}$. The $Ar(11s')$ state lies about 4.5 meV above the $Ar^-(^2P_{3/2})$ threshold. The suppression factor is expected to decrease as the kinetic energy of the prompt electrons increases.[31] Hence, the suppression factor should be smaller than 5×10^{-4} for autoionizing levels lying at energies greater than 4.5 meV with respect to an ionization threshold. The absolute photon energy scale for the HD^- spectra was calibrated using the $Ne^-(^2P_{3/2})$ and the $Ar^-(^2P_{3/2})$ PFI-PE bands measured under the same experimental conditions.[31-33] In the present experiment, the photon energy step size used was in the range of 0.2-0.3 meV. The dwell time at individual steps was in the range of 2-50 s.

Results and Discussion

Assignment of rovibronic transitions

For the one photon ionization process $HD^-(X\,^2\Sigma^-, v^-, N^-) \leftarrow HD(X\,^1\Sigma^-, v''=0, J'')$, $|\psi_{el}\chi_{rot}\rangle$ can be classified by its behavior under molecule-fixed reflection (σ_v). For Σ^- states,

$$\sigma_v|\psi_{el}\chi_{rot}\rangle = (+)(-1)^J|\psi_{el}\chi_{rot}\rangle . \qquad (1)$$

The effect of σ_v on the dipole moment, μ, is

$$\sigma_v\,\mu = -\mu . \qquad (2)$$

This results in the requirement that the upper, $|\psi^-_{el}\chi^-_{rot}\rangle$ and lower, $|\psi''_{el}\chi''_{rot}\rangle$ states must have opposite reflection under σ_v to ensure that $\langle\psi^-_{el}\chi^-_{rot}|\,\mu\,|\psi''_{el}\chi''_{rot}\rangle$ doesn't vanish.

Since the rovibronic transitions in this experiment involve photoionization we must take into account coupling of the angular momentum for the neutral, ion, and ejected electron. The angular momentum coupling factor Q for a Hund's case b ← b transition can be expressed as[35]

$$Q\left(\lambda, N^+, N''\right) = \left(2N^+ + 1\right)\begin{pmatrix} N^+ & \lambda & N'' \\ -\Lambda^+ & \Delta\Lambda & \Lambda'' \end{pmatrix}^2 . \qquad (3)$$

The general interpretation of λ is the angular momentum transferred to the ejected electron in the photoionization process and it is constrained by the triangle condition $\Delta N \leq \lambda \leq N^+ + N''$. An additional constraint on λ is $\lambda = |\ell - 1|, \ldots, |\ell + 1|$, which is due to the dipole selection rule. $\Delta\Lambda$ is the difference in orbital angular momenta between the ion and the neutral. The rotational angular momentum of the ion and neutral are represented by N^+ and N'', respectively. The properties of Equation 3 are such that given $\Lambda^+ = 0$ and $\Lambda'' = 0$, Equation 3 will vanish if $N^+ + N'' + \lambda$ is odd.

The parity selection rule connecting rovibronic states of the neutral and ion is given by[36,37]

$$\Delta J + \Delta S + \Delta p + \ell = \text{even} \qquad (4)$$

where $\Delta J = J^+ - J''$, $\Delta S = S^+ - S''$ is the difference in total spin between the ion and neutral, Δp represents the change in Kronig parity of the initial and final states ($p = 0$ for Λ^+ or $= 1$ for Λ^-), and ℓ is the angular momentum of the ejected photoelectron. For a $^2\Sigma^+ \leftarrow {}^1\Sigma^+$ transition, $\Delta S = 1/2$, $\Delta p = 0$, and $\Delta J = \Delta N + \Delta S$ (for Hund's case b $\leftarrow$ b). Equation 3 reduces to $\Delta N + \ell$ = odd. Thus, when ΔN is even, ℓ must be odd and vice versa. Transitions of $\Delta N = 0, \pm 1, \pm 2, \pm 3$, and ± 4 were observed in this experiment. The partial waves of the ejected photoelectron are $\ell = 1$ for $\lambda = 0$, $\ell = 0,2$ for $\lambda = 1$, $\ell = 1,3$ for $\lambda = 2$, $\ell = 2,4$ for $\lambda = 3$, and $\ell = 3,5$ for $\lambda = 4$,. This means that the Q branch, $\Delta N = 0$, gains intensity through the excitation of a *s*-, *d*-, and a *g*-wave electron, with the majority coming from the *s*-wave electron. The P and R branches, $\Delta N = \pm 1$, gain their intensity from the excitation of a *p*- and an *f*-wave electron. The O and S branches, $\Delta N = \pm 2$, gain their intensity from the excitation of a *d*- and a *g*-wave electron. However, the N and T branches, $\Delta N = \pm 3$, gain their intensity only from the excitation of an *f*-wave electron and the M and U branches, $\Delta N = \pm 4$, gain their intensity only from the excitation of a *g*-wave. This is due to the constraint on the value of λ introduced by the triangle condition.

The rotationally resolved PFI-PE spectrum of $HD^+(X^2\Sigma^+, v^+ = 0\text{-}21)$ is shown in Figure 1. Individual vibrational levels are shown in Figures 2(a)-2(v). Note that the vertical $I(e^-)/I(h\nu)$ scales for these figures have the same units, where $I(e^-)$ and $I(h\nu)$ represent the PFI-PE intensity and the VUV photon intensity, respectively. Using the spectroscopic constants for HD obtained from Herzberg[1,34], the rotational energy levels for $v'' = 0$, $J'' = 0\text{-}8$ were calculated. The rotation-vibration energy levels for HD^+ were taken from theoretical calculations by Wolniewicz and Poll (WP)[3] ($N^+ = 0\text{-}8$). Combining the rovibronic energy levels of HD and HD^+ allowed the calculation of the rovibronic transitions

$HD^+(X^2\Sigma^+, v^+=0\text{-}21, N^+=0\text{-}8) \leftarrow HD(X^1\Sigma^+, v''=0, J''=0\text{-}8)$, which were used to assign the rovibronic transitions observed in this experiment. We found that the IEs for the ionization transitions $HD^+(X^2\Sigma^+, v^+=0\text{-}21, N^+=0) \leftarrow HD(X^1\Sigma^+, v''=0, J''=0)$, i.e. $(N^+, J'') = (0, 0)$, and positions of other (N^+, J'') rotational lines observed in the PFI-PE spectrum of HD are in excellent agreement with the calculations of WP,[3] HYP,[2] and Balint-Kurti *et* al.[9] and the results of previous experiments.[15,22] The fact that the maximum deviation of ≤0.5 meV is found in these comparisons confirms the claimed accuracy of ≤ 1 meV for the photon energy calibration procedures.[28,32,33]

Since the cross section for direct photoionization is very low compared to that for autoionization in HD,[46] a suppression factor[31] of 5×10^{-4} may not be sufficient to completely suppress prompt electrons originating from strong autoionization states. Photoelectron peaks in Figs. 2(a)-2(v), which are not assigned to (N^+, J'') ionization thresholds, can be partly attributed to prompt electron background features from autoionizing Rydberg levels of HD.[18,23,45,46] In addition, the HD sample appears to have been contaminated with a small amount of H_2. This produced observable photoelectron peaks attributable to strong autoionizing Rydberg states of H_2 observed in the lower $v^+ \leq 2$ HD^+ states. The contamination by prompt electron peaks is expected to be less serious at higher v^+ states because strong autoionizing Rydberg states appear to be mostly concentrated in the energy range (≈15.3-16.7 eV) covering the lower v^+ (≤6) states. This expectation is confirmed by the PFI-PE spectra of Figs. 2(a)-2(v). The $v^+ = 0 - 6$ PFI-PE bands exhibit many strong near-resonance autoionization peaks that cannot be assigned to rotational transitions, whereas the PFI-PE bands for $v^+ = 7\text{-}21$ are nearly free from such autoionization features. Although corresponding autoionization Rydberg peaks resolved in the PIE spectrum[46] of HD can be identified as background electron peaks found in the PFI-PE spectra of Figs. 2(a)-2(g), the relative intensities of the background electron peaks are not in proportion with the relative intensities of the autoionization ion peaks.

Rotational Intensities

As indicated above, HD was introduced into the photoionization/photoexcitation region in the form of an effusive beam at 298 K. We have estimated the rotational population ratios for $(J'' = 0) : (J'' = 1) : (J'' = 2) : (J'' = 3) : (J'' = 4) : (J'' = 5)$ to be 0.2048 : 0.3953 : 0.2728 : 0.1017 : 0.0224 : 0.0030 at 298K. The rotational transition intensities are expected to roughly reflect the thermal distribution of the rotational levels at such a temperature if the near-resonance autoionization mechanism does not play a role in the production of PFI-PEs.

As shown in Figs. 2(a)-2(v), the dominant rotational transitions for v^+=0-21 are $\Delta N = 0$, i.e., (0, 0), (1, 1), (2, 2), and (3, 3). In general, the PFI-PE intensity for (1, 1) is higher than that for (0, 0) and (2, 2), and the PFI-PE intensity for (2, 2) is higher than that for (0, 0) within a given vibrational band. These observations and the low PFI-PE intensities for transitions involving $J'' \geq 4$ are in general accord with the thermal distribution of J'' for HD. Transitions attributable to $\Delta N = \pm 1, \pm 2, \pm 3$, and ± 4 were also observed.

BOS Simulation

The Buckingham-Orr-Sichel (BOS) model[35] is described by the formula,

$$\sigma(N^+ \leftarrow N'') \propto \Sigma_\lambda Q(\lambda, N^+, N'')C_\lambda. \qquad (5)$$

This model was derived to predict rotational line strengths $\sigma(N^+ \leftarrow N'')$ observed in one photon ionization of diatomic molecules. The rotational line strength is separated into two factors. The factor C_λ is associated with the electronic transition moments, which are the linear combination of electron transition amplitudes for the possible angular momenta ℓ of the ejected electron. The general interpretation of λ is that of the angular momentum transferred to the electron in the photoionization process. The other factor, Q, is determined by the standard angular momentum coupling constants, which were calculated using the formula for a Hund's case *b* $\leftarrow$ *b* transition in the present study and given by Equation 3. The known spectroscopic constants for the $HD(X^1\Sigma^+, v'' = 0)$ were used.[1-34] The best fits for the PFI-PE bands for $HD^+(X^2\Sigma^+, v^+ = 0$-21) are depicted as dashed curves in Figs. 2(a)-2(v). The fact that the $\Delta N = 0, \pm 1, \pm 2, \pm 3$, and ± 4 rotational branches were observed implies that the BOS coefficients C_{-4}, C_{-2}, C_0, C_2, and C_4 are nonzero. The C_{-4} values for the simulated spectra shown in Figs. 2(a)-2(v) are listed in Table 1. The dominance of the $\Delta N = 0$, or Q-branch, observed in the experimental spectra is consistent with the significantly higher C_0 values than the corresponding $C_{\pm 4}$ values. As expected, the BOS simulation, which has not taken into account the effect of near-resonance autoionization, cannot account for the variations in intensity of the observed transitions. Surprisingly, general agreement is found between the experimental spectra and the BOS simulation of the PFI-PE bands for $v^+ \geq 3$ states. In general, the agreement becomes better for higher vibrational levels. For example, the relative intensities of rotational transitions observed for the $v^+ = 12$ band are in excellent accord with the BOS simulated spectrum (see Fig. 2(m)). Furthermore, disregarding the C_0 values for the v^+=10 and 11 bands, we find that the C_0 value in general increases compared to the $C_{\pm 4}$ values as v^+ is increased. Such

a trend is consistent with the observation that the $\Delta N = \pm 1, \pm 2, \pm 3$, and ± 4 rotational branches diminish as v^+ increased.

Another important factor that could affect the PFI-PE intensities is the effective lifetime of high-n Rydberg states involved in the PFI-PE measurements. If the effective lifetime is shorter than the time interval for adjacent Stark field pulses, the measured PFI-PE intensity would be lower than the actual threshold photoelectron intensity. Lifetime measurements of Rydberg states located a few wavenumbers below the ionization threshold of HD^{25} ($n>100$) indicate that the lifetime of these states is greater than 10 μs. Since the lifetime of the Rydberg states is longer than the time interval for adjacent Stark field pulses, we concluded that the rotational intensities resolved in the PFI-PE spectra shown in Figs. 2(a)-2(v) were not influenced by the Rydberg lifetime effect.

Vibrational and Rotational Energy Levels

The vibrational energy levels are defined by the equation,

$$G_{v^+} = \omega_e(v+1/2) - \omega_e x_e(v+1/2)^2 + \omega_e y_e(v+1/2)^3 + \omega_e z_e(v+1/2)^4 + \ldots \quad (6)$$

The vibrational constants, ω_e, $\omega_e x_e$, $\omega_e y_e$, and $\omega_e z_e$ for HD^+ were determined by fitting the experimental PFI-PE vibrational energy level differences (ΔG) listed in Table 2 to the equation

$$\begin{aligned}\Delta G_{v^+ +1/2} &= G(v+1) - G(v) \\ &= \omega_e - 2\omega_e x_e (v+1) + \omega_e y_e (3v^2+6v+13/4) + \omega_e z_e (4v^3+12v^2+13v+5). \end{aligned} \quad (7)$$

The resulting vibrational constants are listed in Table 3 along with the results obtained in the HeI photoelectron study by Pollard *et al.*[15]. The HYP,[2] WP,[3] and Balint-Kurti *et al.*[9] theoretical energy levels were also fit to Equation 7 and the results are listed in Table 4 for comparison. As expected, the results of the present experiment are in good agreement with the HeI photoelectron study[15] and the theoretical results of HYP,[2] WP,[3] and Balint-Kurti *et al.*[9] A plot of the PFI-PE, HYP,[2] WP,[3] and Balint-Kurti *et al.*[9] $\Delta G_{v^+ +1/2}$ vs. $(v^+ +1/2)$ is shown in Figure 3. A positive curvature at low $(v^+ +1/2)$ and a negative curvature at high $(v^+ +1/2)$ with a point of inflection at ≈ 9 ½ were observed in all of the curves. This was also observed in the HeI study[15] and can be seen clearly when a linear term is subtracted from the $\Delta G_{v^+ +1/2}$ values as shown in Figure 4.

We have obtained the rotational constants B_{v^+} and D_{v^+} for $HD^+(X^2\Sigma^+, v^+=0\text{-}20)$ by fitting the rotational structures resolved in Figs. 2(a)-2(v) to

$$\nu = \nu_0 + B_{v^+}N(N+1) - D_{v^+}N^2(N+1)^2 - B_{v''}J(J+1) + D_{v''}J^2(J+1)^2. \quad (8)$$

The values of $B_{v''}$ and $D_{v''}$ for $X^2\Sigma^+$, $v''=0$ of HD were obtained from Huber and Herzberg.[1,24] The resulting ionic rotational constants are compared with those reported in the HeI photoelectron study of Pollard et al.[15] and to theoretical calculations[2,3,9] in Table 4. Figure 5 shows the B_{v^+} rotational constants determined from this experiment along with those calculated from the vibration-rotation energy levels reported by HYP[2] and Wolniewicz and Poll.[3] As expected, the results of the present experiment and the theoretical calculations[2,3] are in excellent agreement.

In addition, B_e and α_e for HD^+ were determined by fitting the experimental B_{v^+} values ($v^+=0\text{-}20$) to the equation $B_{v^+} = B_e - \alpha_e(v^+ + 1/2)$. Based on the results of this calculation, the internuclear distance (r_e) was calculated using

$$r_e = \sqrt{h/8\pi^2\mu B_e} \quad . \quad (9)$$

The resulting B_e, α_e, and r_e values are listed in Table 5 along with those obtained in the HeI photoelectron study by Pollard *et al.*[15] those by Huber and Herzberg,[1] and those determined from the rotational constants calculated from the vibration-rotation energy levels reported by HYP[2] and WP.[3] As shown, our results are consistent with previous results. The experimental dissociation energy (D_0), for HD^+ was also determined. The resulting dissociation energy, as well as other experimental and theoretical dissociation energies, are listed in Table 6.

Conclusions

We presented here the rotationally resolved PFI-PE spectra of $HD^+(X^2\Sigma^+, v^+=0\text{-}21)$. The analysis of which has provided the rovibronic energies for $v^+=0\text{-}21$, the vibrational constants (ω_e, $\omega_e x_e$, $\omega_e y_e$, and $\omega_e z_e$), the rotational constants (B_{v^+}, D_{v^+}, B_e, and α_e), the internuclear separation (r_e), and the dissociation energy (D_0). The simulated photoelectron bands based on the BOS model are in good agreement with the PFI-PE bands of higher v^+ states, indicating that the strong perturbation of the relative intensities for rotational transitions occurs mainly at lower v^+ (≤ 6) states.

Acknowledgements

This work was supported by the Director, Office of Energy Research, Office of Basic Energy Sciences, Chemical Science Division of the U.S. Department of Energy under Contract No. W-7405-Eng-82 for the Ames Laboratory and Contract No. DE-AC03-76SF00098 for the Lawrence Berkeley National Laboratory. M.E. and S.S. acknowledge the GAANN Fellowship support for 1994-1995 and 1996-1997. M.E. is a recipient of the Dow Fellowship for 1997-1998.

References

1. K. P. Huber and G. Herzberg, "Molecular Spectra and Molecular Structure, Vol. IV, Constants of Diatomic Molecules" (Van Nostrand, New York, 1979).
2. G. Hunter, A. W. Yau, and H. O. Pritchard, *At. Data Nucl. Data Tables* **14**, 11 (1974).
3. L. Wolniewicz and J. D. Poll, *Mol. Phys.* **59**, 953 (1986).
4. G. Hunter and H. O. Pritchard, *J. Chem. Phys.* **46**, 2153 (1967).
5. L. Wolniewicz and J. D. Poll, *J. Chem. Phys.* **73**, 6225 (1980).
6. D. M. Bishop and L. M. Cheung, *Phys. Rev.* A**16**, 640 (1977).
7. D. M. Bishop, *Mol. Phys.* **28**, 1397 (1974).
8. D. M. Bishop and L. M. Cheung, *J. Chem. Phys.* **75**, 3155 (1981).
9. Balint-Kurti *et al*, *Phys. Rev. A***41**, 4913 (1989).
10. D. M. Bishop, *At. Data Nucl. Data Tables* **18**, 521 (1976).
11. D. M. Bishop and R. W. Wetmore, *J. Mol. Spectrosc.* **46**, 502 (1973).
12. E. A. Colbourn and P. R. Bunker, *J. Mol. Spectrosc.* **63**, 155 (1976).
13. L. Wolniewicz, *J. Chem Phys.* **78**, 6173 (1983).
14. Y. Itikawa, *Chem. Phys.* **28**, 461 (1978).
15. J. E. Pollard, D. J. Trevor, J. E. Reutt, Y. T. Lee, and D. A. Shirley, *J. Chem. Phys.* 77, 34 (1982).
16. J. Berkowitz and R. Spohr, *J. Electron Spectrosc.* **2**, 143 (1973).
17. A. L. Ford, K. K. Docken, and A. Dalgarno, *Astrophys. J.* **195**, 819 (1975).
18. S. Takezawa and Y. Tanaka, *J. Chem. Phys.* **56**, 6125 (1972).
19. L. Wolniewicz and T. Kowalski, *Chem. Phys. Lett.* **18**, 55 (1973).
20. I. Dabrowski and G. Herzberg, *Can. Journ. Phys.* **54**, 525 (1976).
21. W. Chupka, P. Dehmer, and W. Jivery, *J. Chem. Phys.* **63**, 3929 (1975).

22 W. H. Wing, G. A. Ruff, W. E. Lamb, and J. J. Spezeski, *Phys.Rev. Lett.* **36**, 1488 (1976).

23. F. Merkt, H. Xu, and R. N. Zare, *J. Chem. Phys.* **104**, 950 (1996).

24. See R. T. Weidman and M. G. White, in "High Resolution Laser Photoionization and Photoelectron Studies", edited by I. Powis, T. Baer, and C. Y. Ng, *Wiley Series in Ion Chem. and Phys.* (Wiley, Chichester, 1995), p. 79.

25. F. Merkt and T. P. Softley, in "High Resolution Laser Photoionization and Photoelectron Studies", edited by I. Powis, T. Baer, and C. Y. Ng, *Wiley Series in Ion Chem. and Phys.* (Wiley, Chichester, 1995), p. 119.

26. J. W. Hepburn, in "Vacuum Ultraviolet Photoionization and Photodissociation of Molecules and Clusters", edited by C. Y. Ng (World Scientific, Singapore, 1991), p. 435.

27. J. W. Hepburn, in "Laser Techniques in Chemistry", edited by A. Meyers and T. R. Rizzo (Wiley, New York, 1994).

28. C.-W. Hsu, M. Evans, P. Heimann, K. T. Lu, and C. Y. Ng, *J. Chem. Phys.* **105**, 3950 (1996).

29. P. Heimann, M. Koike, C.-W. Hsu, M. Evans, K. T. Lu, C. Y. Ng, A. Suits, and Y. T. Lee, *Rev. Sci. Instrum.* **68**, 1945 (1997).

30. M. Evans, C. Y. Ng, C.-W. Hsu, and P. Heimann, *J. Chem. Phys.* **106**, 978 (1997).

31. C.-W. Hsu, M. Evans, P. A. Heimann, and C. Y. Ng, *Rev. Sci. Instrum.*, **68**, 1694 (1997).

32. C.-W. Hsu, P. A. Heimann, M. Evans, S. Stimson, T. Fenn, and C. Y. Ng, *J. Chem. Phys.* **106**, 8931 (1997).

33. C.-W. Hsu, P. A. Heimann, M. Evans, S. Stimson, and C. Y. Ng, *Chem. Phys.*, accepted.

34. G. Herzberg, "Molecular Spectra and Molecular Structures, Vol.I, Spectra of Diatomic Molecules" (Van Nostrand, Princeton, 1950).

35. A. D. Buckingham, B. J. Orr, J. M. Sichel, *Phil. Trans. Roy. Soc. Lond.* A**268**, 147 (1970).

36. J. Xie and R.N. Zare, *J. Chem. Phys.* **93**, 3033 (1990).

37. K. Wang and V. McKoy, *J. Phys. Chem.* **99**, 1643 (1995).

38. A. Carrington, I. McNab, and C. Montgomerie, *J. Chem. Phys.* **87**, 3246 (1987).

39. A. Carrington and R. Kennedy, *Mol. Phys.* **56**, 935 (1985).

40. A. Carrington and J. Buttenshaw, *Mol. Phys.* **44**, 267 (1981).

41. A. Carrington, J. Buttenshaw, and P. Roberts, *Mol. Phys.* **38**, 267 (1979).

42. P. Essenwanger and H. P. Gush, *Can. J. Phys.* **62**, 1680 (1984).

43. A. R. McKellar, J. W. C. Johns, W. Majewski, and N. H. Rich, *Can. J. Phys.* **62**, 1673 (1984).

44. R. A. Durie and G. Herzberg, *Can. J. Phys.* **38**, 806 (1960).

45. N. Y. Du and C. H. Greene, *J. Chem. Phys.* **85**, 5430 (1986).

46. P. M. Dehmer and W. A. Chupka, *J. Chem. Phys.* **79**, 1569 (1983).

47. V. H. Dibeler, R. M. Reeses, and M. Krauss, *J. Chem. Phys.* **42**, 2045 (1965).

Table 1. BOS coefficients for the best fit [see dashed curves of Figs. 2(a)-2(s)] to the $HD^+(X^2\Sigma^+, v^+=0\text{-}21)$ PFI-PE bands. The sum of the C_k values for a given v^+ state is arbitrarily normalized to 100.

	BOS Coefficients				
v^+	C_0	C_1	C_2	C_3	C_4
0	57	10	25	3	5
1	58	10	25	3	4
2	66	2	24	6	2
3	65	5	22	5	3
4	69	3	17	9	2
5	63	8	24	3	2
6	82	5	10	2	1
7	52	10	34	2	2
8	58	4	34	2	2
9	72	3	21	2	2
10	53	3	40	1	3
11	54	2	42	1	1
12	76	4	16	2	2
13	79	5	10	2	4
14	70	10	20	0	0
15	67	7	26	0	0
16	78	7	15	0	0
17	75	7	18	0	0
18	74	11	15	0	0
19	74	11	15	0	0
20	75	10	15	0	0
21	75	10	15	0	0

Table 2. Comparison of the vibrational differences $\Delta G(v^{+}+1/2)$ for the $HD^{+}(^{2}\Sigma^{+})$ ground state in cm^{-1}.

$v^{+}+1/2$	PFI-PE	Hel[15]	HYP[2]	Balint-Kurti *et al*[7]	Wolniewicz *et al*[3]
0.5	1912.66	1913.1	1913.14	1912.9954	1912.993
1.5	1818.78	1817.2	1817.00	1816.8609	1816.860
2.5	1720.38	1722.7	1723.70	1723.5874	1723.586
3.5	1634.88	1631.8	1632.92	1632.7999	1632.798
4.5	1544.55	1543.0	1544.23	1544.1337	1544.132
5.5	1456.63	1456.8	1457.33	1457.2308	1457.231
6.5	1372.75	1372.0	1371.81	1371.7348	1371.734
7.5	1288.07	1287.5	1287.36	1287.2880	1287.287
8.5	1204.18	1201.7	1203.58	1203.5243	1203.523
9.5	1117.88	1119.4	1120.11	1120.0673	1120.066
10.5	1034.00	1035.2	1036.55	1036.5217	1036.521
11.5	956.65	951.3	952.48	952.4693	952.470
12.5	864.99	866.2	867.46	867.4592	867.459
13.5	781.99	779.8	780.97	781.0020	781.003
14.5	692.75	693.2	692.52	692.5562	692.557
15.5	600.80	600.6	601.46	601.5236	601.524
16.5	506.60	507.2	507.14	507.2358	507.238
17.5	409.97	409.0	408.88	408.9736	408.974
18.5	306.41	306.1	305.98	306.0275	306.031
19.5	196.80	203.0	198.40	198.0256	198.029
20.5	82.11	—	90.63[a]	83.8426	83.845

a) Hunter, Yau, and Pritchard[2] report that an error of up to 15 cm^{-1} is expected as the dissociation limit is approached.

Table 3. Comparison of experimental PFI-PE, HeI experimental, and theoretical ionic vibrational constants. Theoretical constants were obtained by fitting published values to Equation 7.

	PFI-PE (cm^{-1})	HeI[15] (cm^{-1})	HYP[2] (cm^{-1})	Theory[3,9] (cm^{-1})
ω_e	2016.6 ± 2.6	2014.6 ± 1.8	2015.0	2016.2
$\omega_e x_e$	51.97 ± 0.49	51.42 ± 0.39	51.48	51.88
$\omega_e y_e$	0.744 ± 0.034	0.687 ± 0.030	0.699	0.736
$\omega_e z_e$	-0.0198 ± 0.0008	-0.0181 ± 0.0007	-0.0186	-0.0196

Table 4 Comparison of the rotational constants for HD ($X\ ^1\Sigma^+, v$) The B_v and D_v values for HYP[2] and WP[3] were calculated by fitting their reported energy levels of the rovibronic transitions

	PFI-PE		Hel[1]	Hunter, Yau, & Pritchard[2]		Wolniewicz & Poll[3]	
v	B_v (cm^{-1})	D_v (cm^{-1})	B_v (cm^{-1})	B_v (cm^{-1})	D_v (cm^{-1})	B_v (cm^{-1})	D_v (cm^{-1})
0	21 910±0 021	0 0102±0 0003	22 6±1 7	21 9525	0 01093	21 9524	0 01097
1	20 991±0 021	0 0109±0 0003	21 5±1 0	20 9504	0 01053	20 9505	0 01057
2	19 915±0 019	0 0093±0 0003	20 3±1 1	19 9788	0 01015	19 9789	0 01019
3	19 122±0 023	0 0102±0 0004	19 8±1 2	19 0347	0 00981	19 0352	0 00987
4	18 065±0 016	0 0086±0 0002	18 7±0 9	18 1103	0 00942	18 1140	0 00953
5	17 180±0 016	0 0086±0 0003	18 0±0 4	17 2081	0 00911	17 2100	0 00918
6	16 362±0 014	0 0091±0 0002	16 9±0 6	16 3242	0 00886	16 32b3	0 00897
7	15 425±0 015	0 0079±0 0002	16 6±0 5	15 4447	0 00850	15 4448	0 00850
8	14 542±0 017	0 007b±0 0003	15 6±0 3	14 5790	0 00827	14 5810	0 00833
9	13 629±0 022	0 0066±0 0004	14 0±0 4	13 7164	0 00803	13 7171	0 00807
10	12 858±0 020	0 0076±0 0003	14 0±0 5	12 8522	0 00781	12 8533	0 00785
11	12 11b±0 028	0 0089±0 0004	14 4±1 6	11 9830	0 00762	11 9839	0 00765
12	11 062±0 018	0 0068±0 0003	11 4±0 5	11 102b	0 00744	11 1037	0 00748
13	10 322±0 032	0 0089±0 0008	11 9±0 8	10 2054	0 00731	10 2068	0 00734
14	9 273±0 035	0 0078±0 0011	9 5±0 7	9 2849	0 00722	9 2858	0 00725
15	8 346±0 029	0 0079±0 0010	9 9±1 3	8 3307	0 00717	8 3325	0 00721
16	7 331±0 028	0 0067±0 0009	7 5±1 0	7 3346	0 00721	7 3362	0 00725
17	6 420±0 034	0 0098±0 0011	6 1±1 0	6 2812	0 00734	6 2833	0 00739
18	5 190±0 035	0 0093±0 0011	6 1±1 0	5 1524	0 00758	5 1557	0 00769
19	3 841±0 029	0 0068±0 0009	---	3 9233	0 00802	3 9265	0 00820
20	2 754±0 034	0 0148±0 0011	---	2 5692	0 00935	2 5525	0 00914
21	0 894±0 071	---	---	---	---	0 8565	0 01402

Table 5. Comparison of the HD^+ rotational constants B_e (cm^{-1}) and α_e (cm^{-1}), and the internuclear distance r_e (Å).

	PFI-PE	Rydberg Series[1]	HeI[15]	HYP[2]	Wolniewicz & Poll[3]
B_e	22.43 ±0.12	22.45_2	23.03 ±0.63	22.45	22.59
α_e	0.926±0.010	1.00_1	0.901±0.057	0.931	0.949
r_e	1.058±0.003	1.057	1.044±0.014	1.057	1.054

Table 6. Comparison of experimental and theoretical HD^+ molecular ion dissociation energies D_0 (cm^{-1}). The first three entries are experimental and the last four are theoretical.

	HD^+
PFI-PE	21516
HeI[15]	21515
Huber & Herzberg[1]	21516.4
HYP[2]	21515.91
Bishop[7]	21515.99
Wolniewicz & Poll[3]	21516.071
Balint-Kurti *et al*[9]	21516.069

Figure Captions

Figure 1. Rotationally resolved PFI-PE spectrum of $HD^+(X\,^2\Sigma^+)$ v^+=0-21.

Figure 2. Rotationally resolved PFI-PE bands of $HD^+(X\,^2\Sigma^+)$. (a) v^+=0, (b) v^+=1, (c) v^+=2, etc. The BOS fits are depicted by the dashed curves. All spectra have the same units for $I(e^-)/I(h\nu)$.

Figure 3. Vibrational energy level differences, $\Delta G_{v^+ +1/2}$, of HD^+ for PFI-PE (•), H., Y., & P.[2] (□), W. & P.[3] (—), and Balint-Kurti *et al*[9] (---).

Figure 4. Vibrational energy level differences, $\Delta G_{v^+ +1/2}$, of HD^+ for PFI-PE (•), H., Y., & P.[2] (□), W. & P.[3] (—), and Balint-Kurti *et al*[9] (---) with a linear term subtracted (-1950.83-87.68(v+1/2)).

Figure 5. Rotational constant B_{v^+} for HD^+ v^+=0-20. The circles (•) represent the PFI-PE values, the squares (□) represent the theoretical values of H., Y., & P.,[2] and the solid line (—) represents the theoretical values of W. & P.[3]

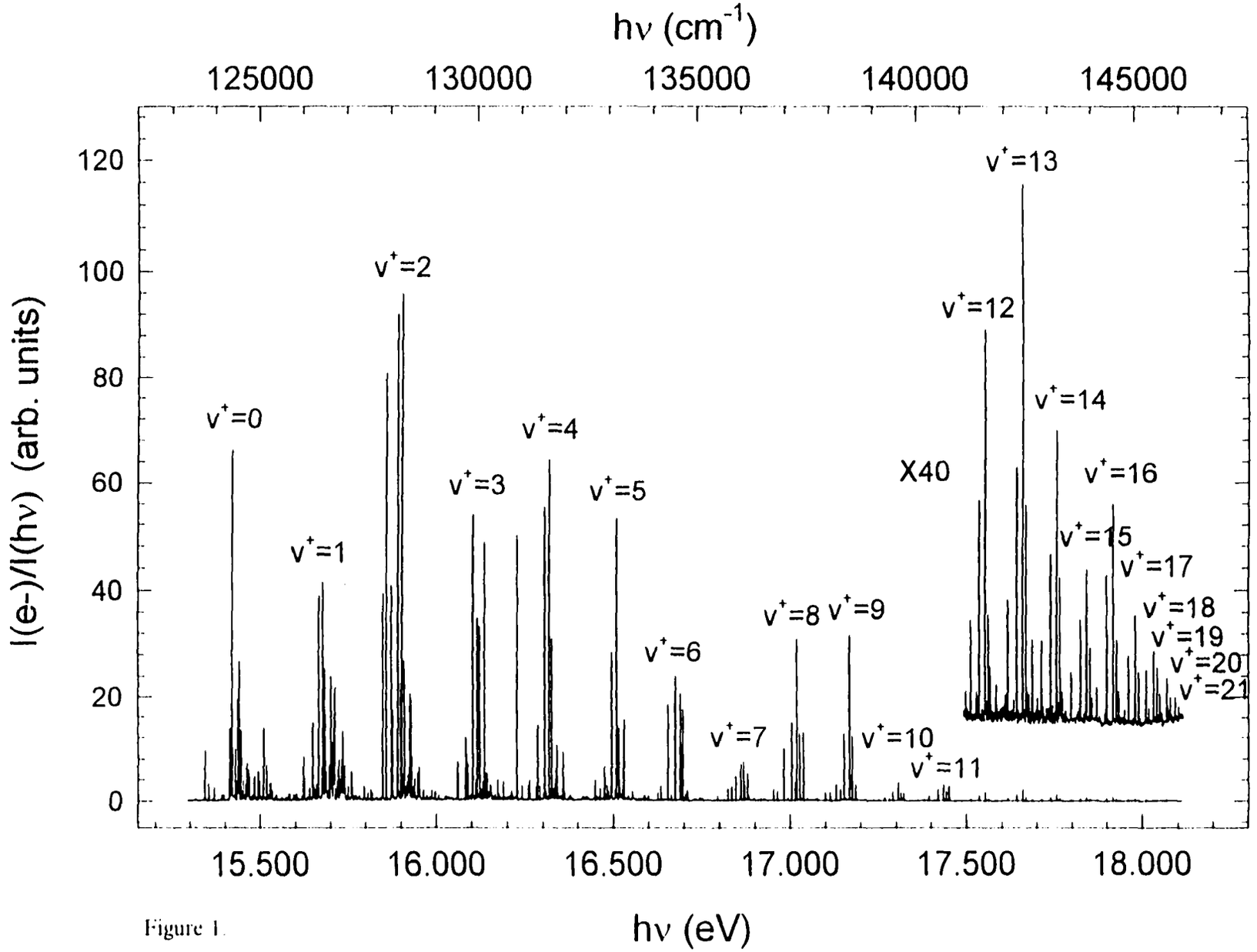
hν (cm^{-1})
125000
130000
135000
140000
145000
I(e-)/I(hν) (arb. units)
120
100
80
60
40
20
0
v$^+$=0
v$^+$=1
v$^+$=2
v$^+$=3
v$^+$=4
v$^+$=5
v$^+$=6
v$^+$=7
v$^+$=8
v$^+$=9
v$^+$=10
v$^+$=11
v$^+$=12
v$^+$=13
v$^+$=14
v$^+$=15
v$^+$=16
v$^+$=17
v$^+$=18
v$^+$=19
v$^+$=20
v$^+$=21
X40
15.500
16.000
16.500
17.000
17.500
18.000
hν (eV)

Figure 1.

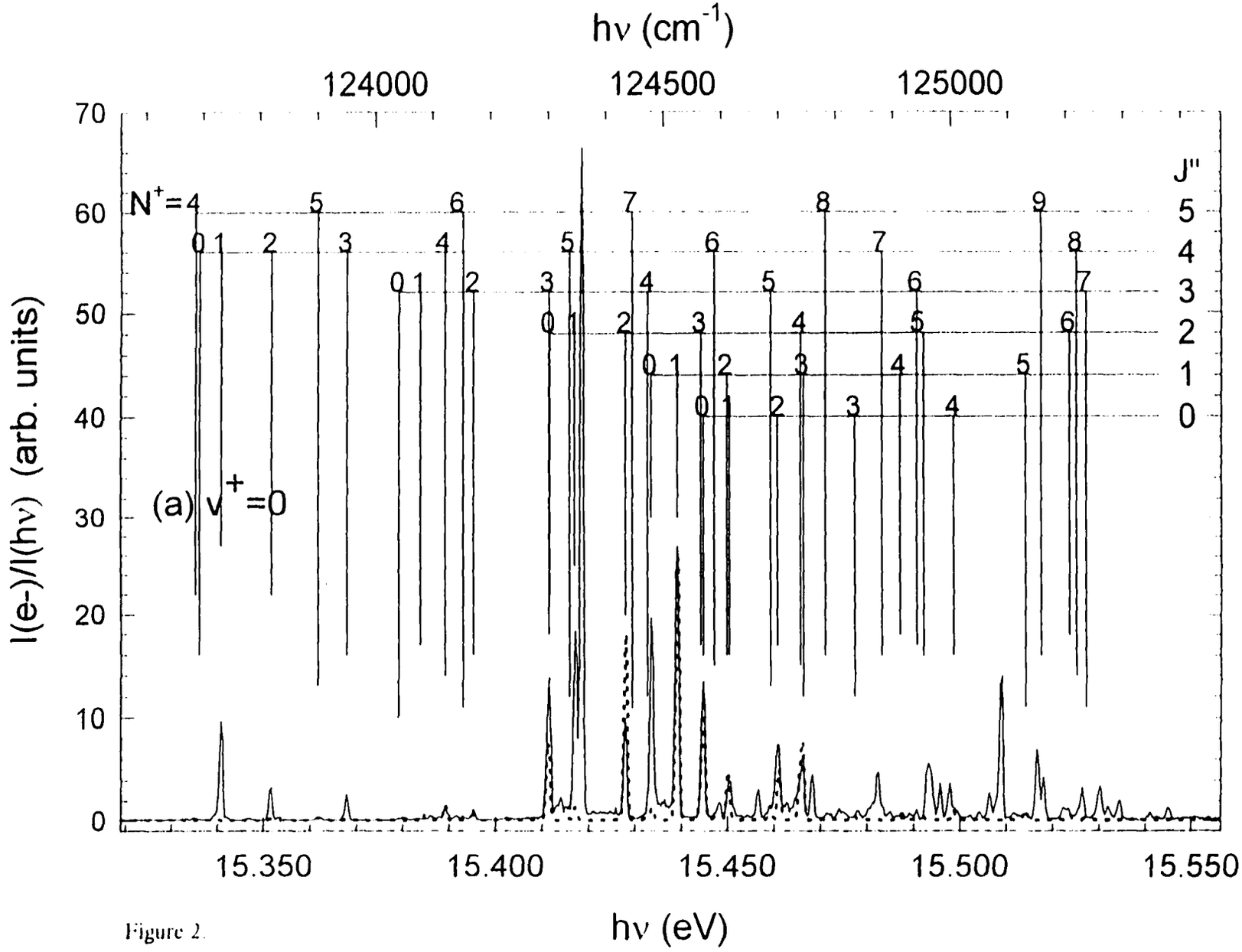
hν (cm-1)
124000
124500
125000
70
60
50
40
30
20
10
0
I(e-)/I(hν) (arb. units)
N+=4
(a) v+=0
J"
5
4
3
2
1
0
15.350
15.400
15.450
15.500
15.550
hν (eV)

Figure 2.

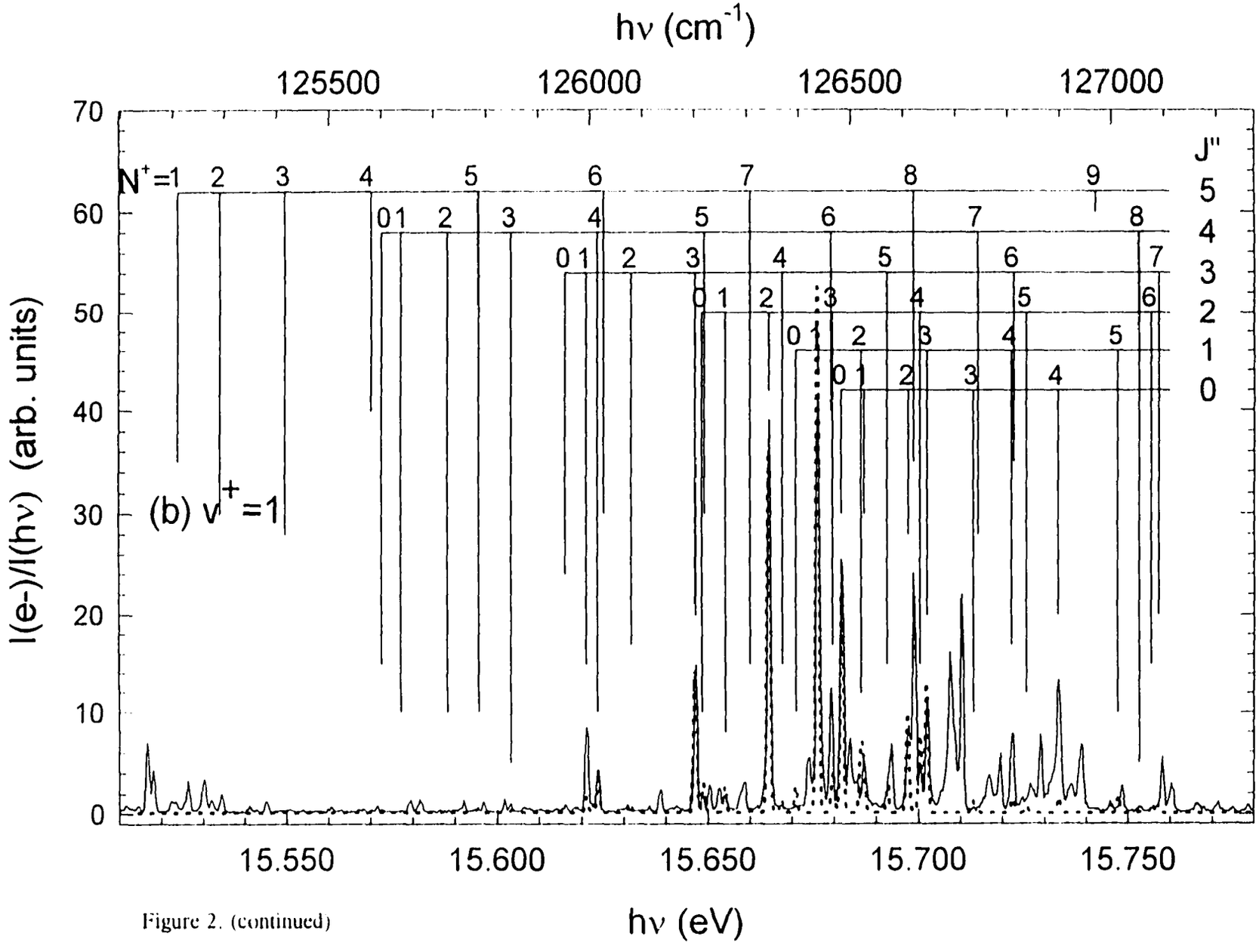

Figure 2. (continued)

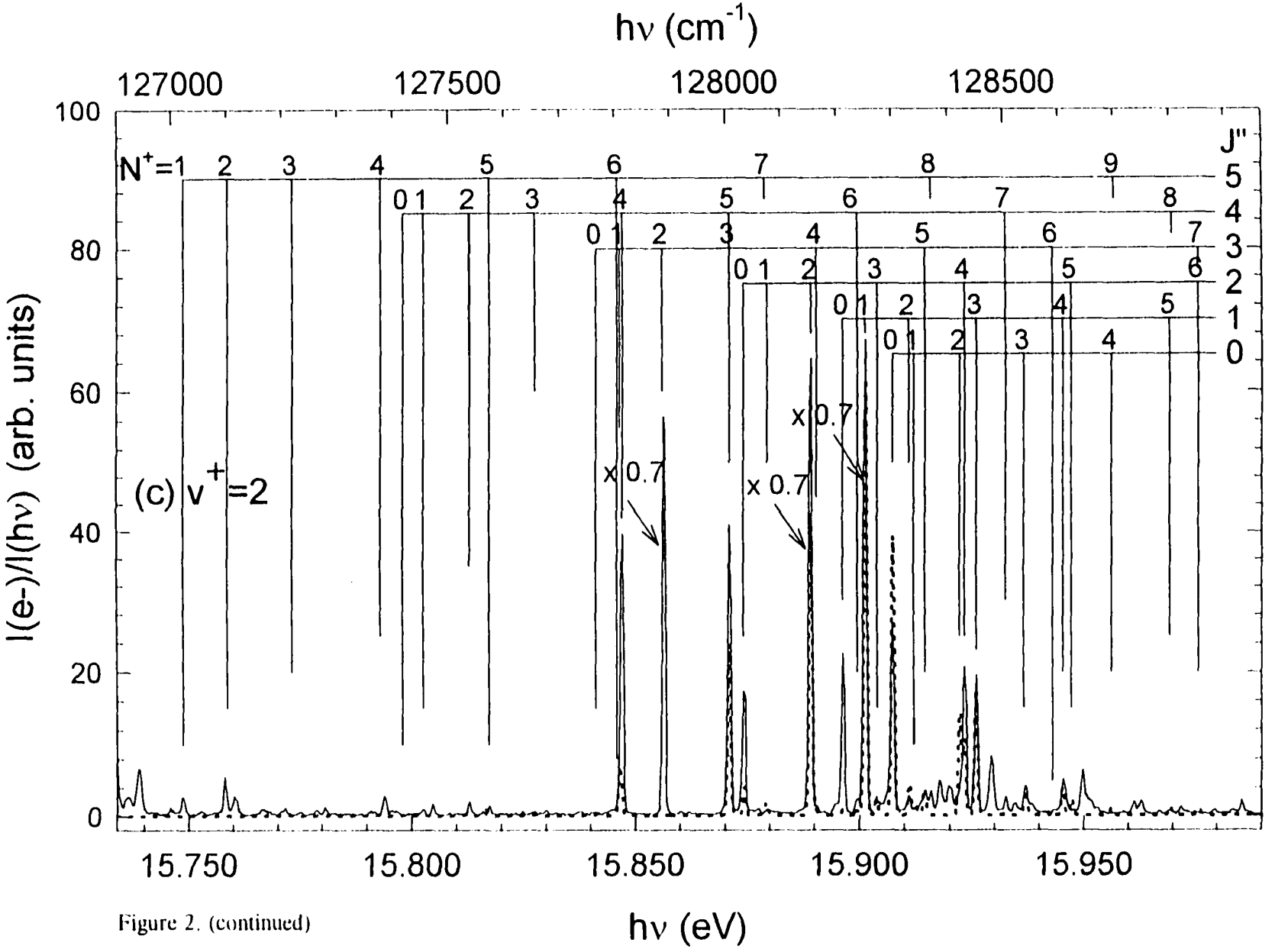

Figure 2. (continued)

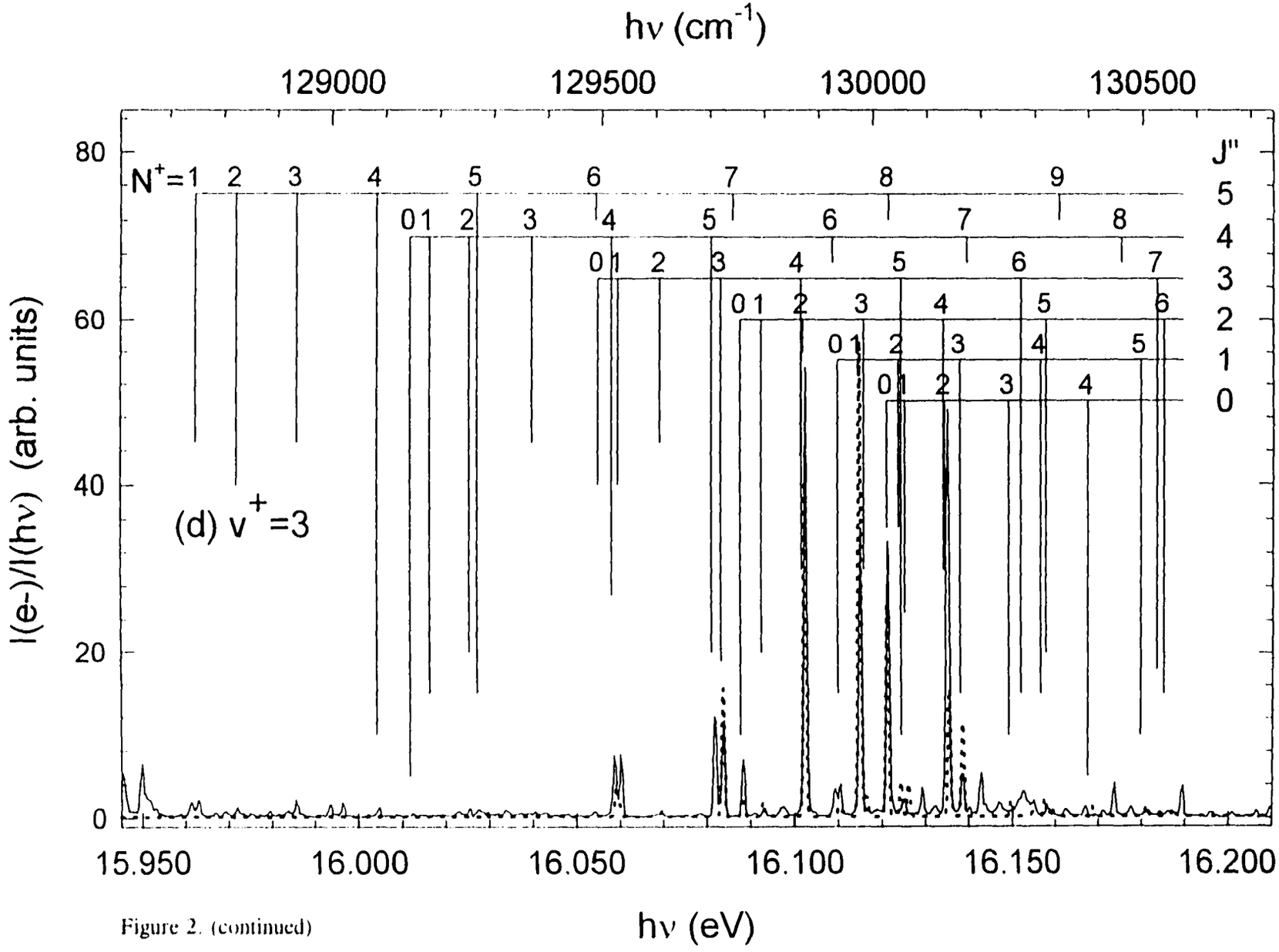

Figure 2. (continued)

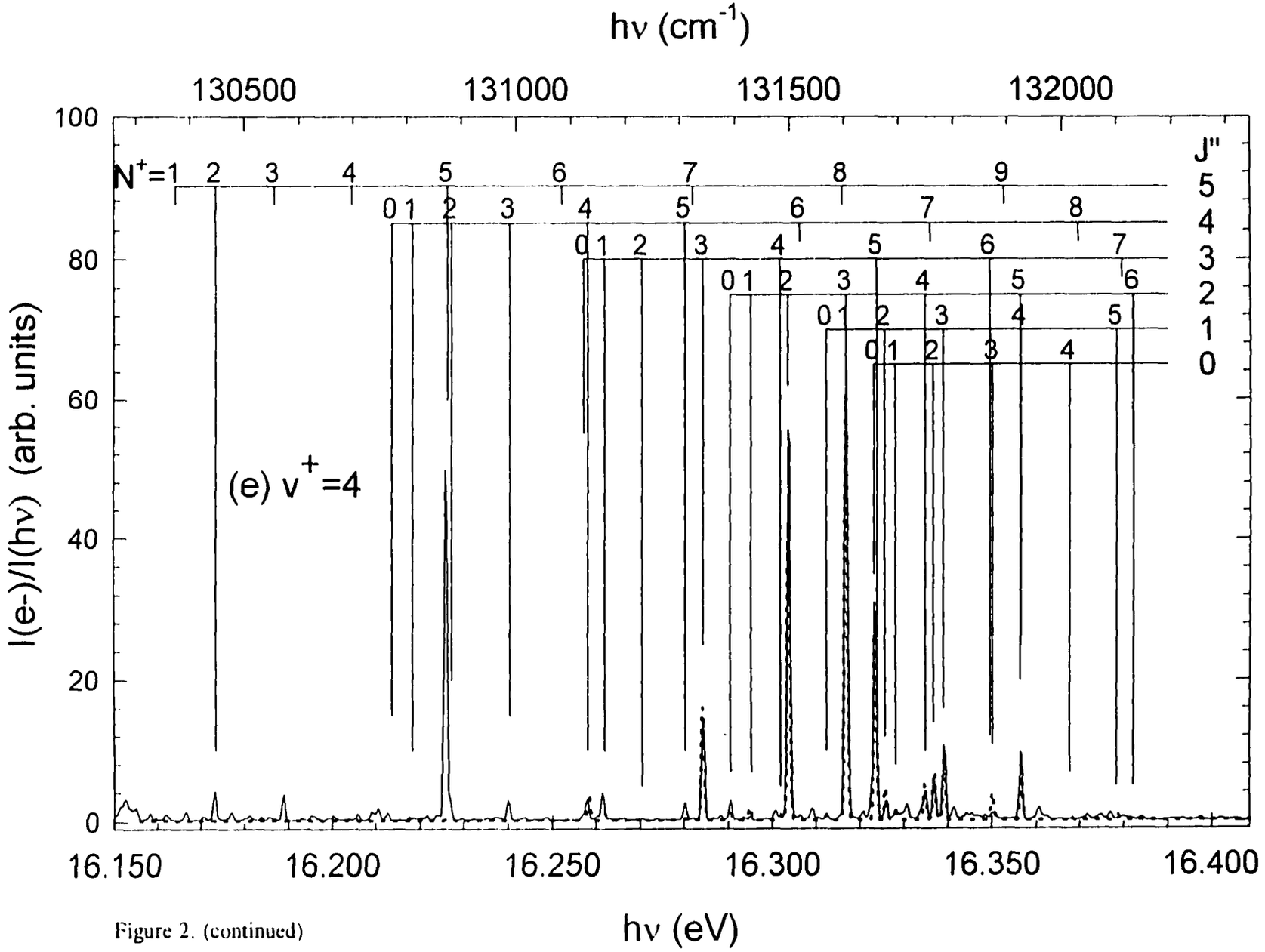

Figure 2. (continued)

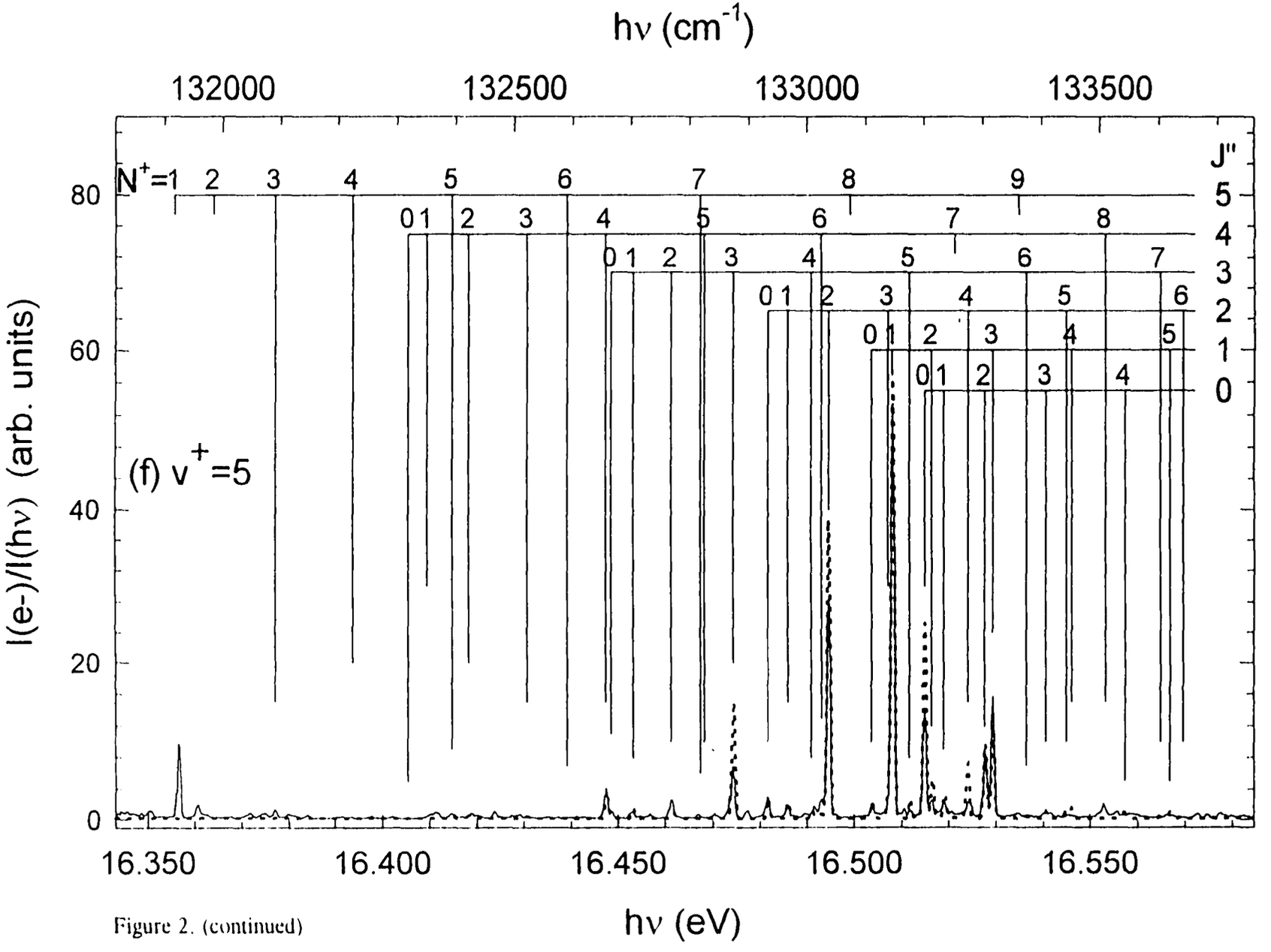

Figure 2. (continued)

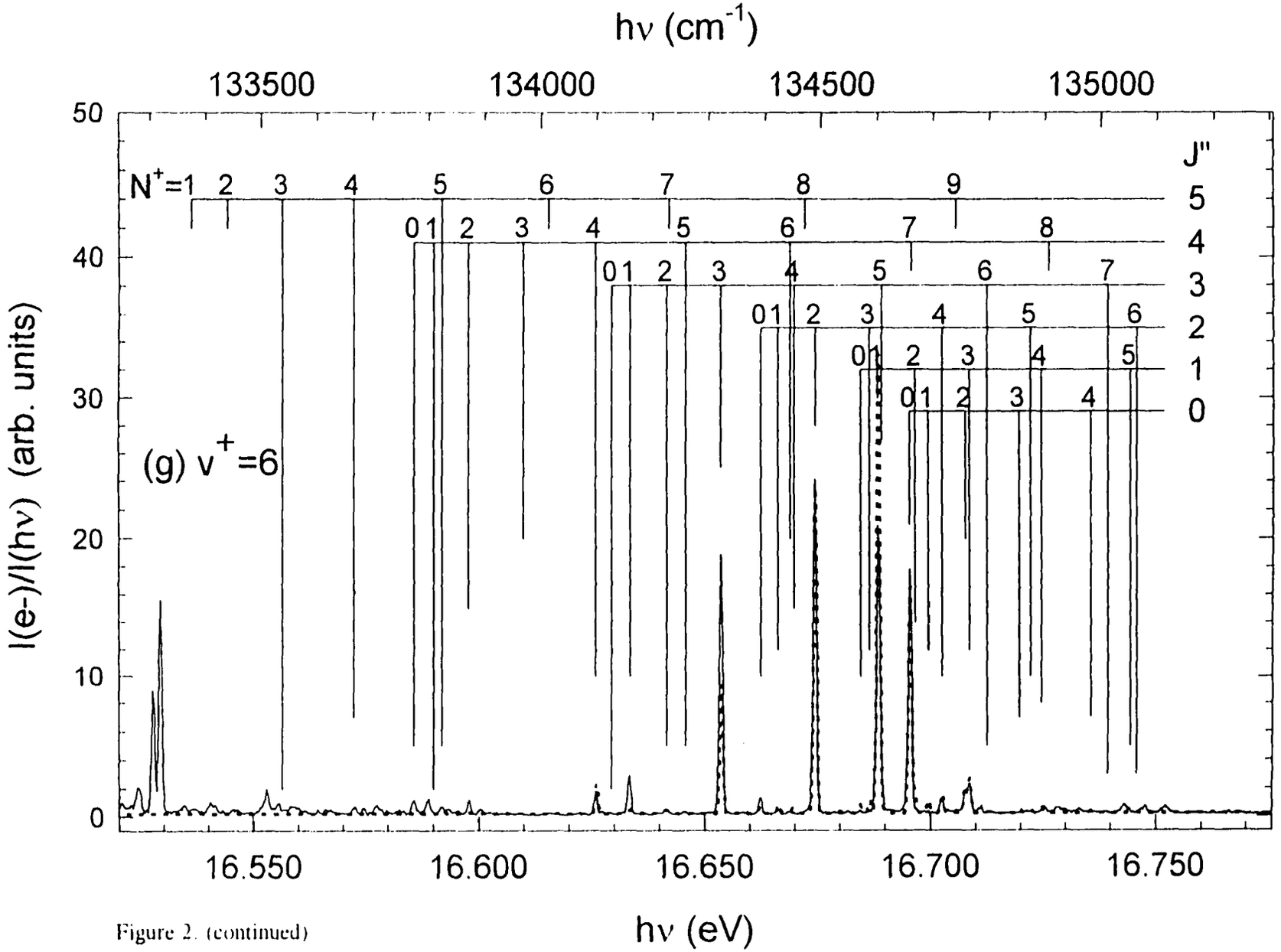

Figure 2. (continued)

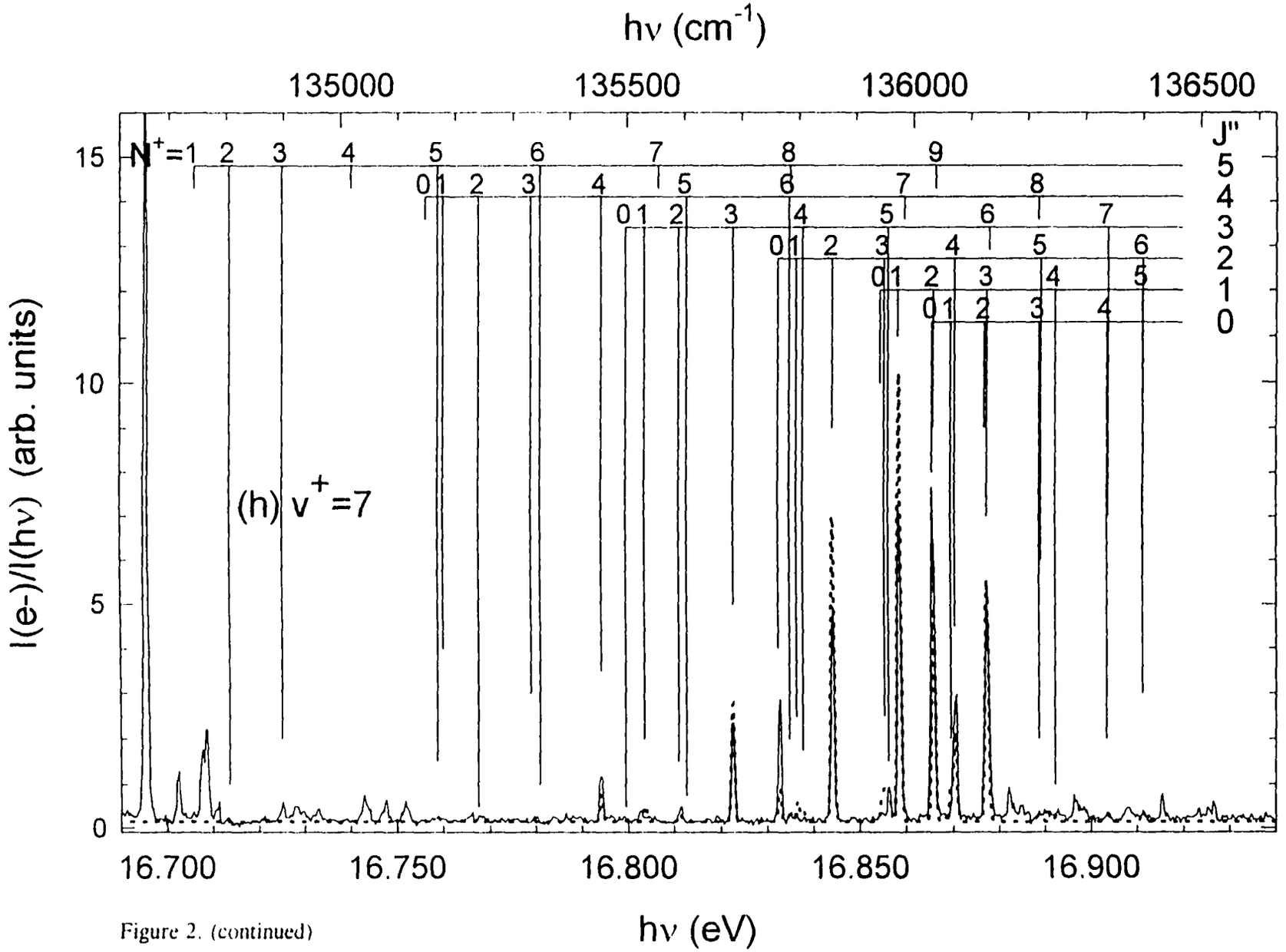

Figure 2. (continued)

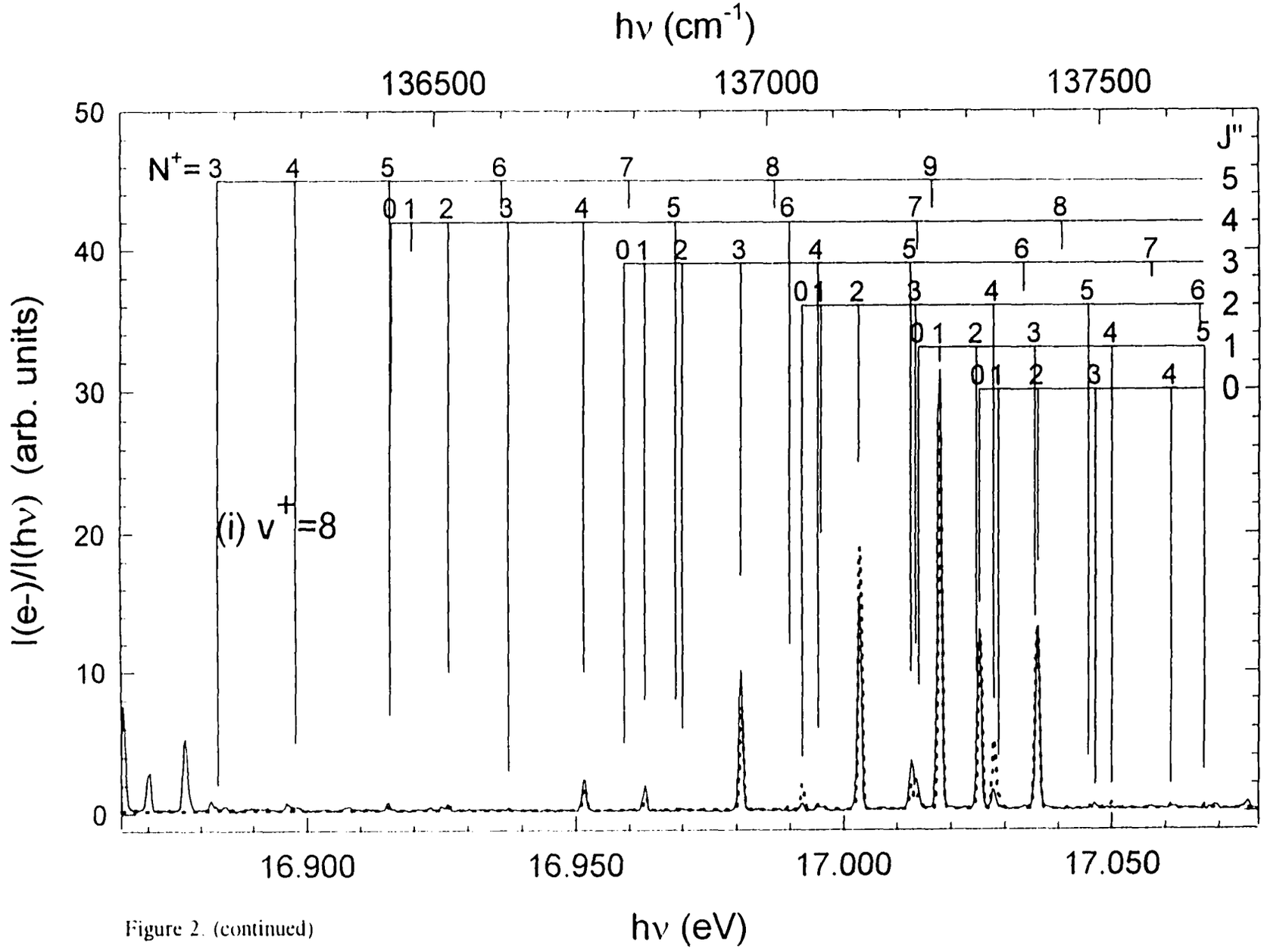

Figure 2. (continued)

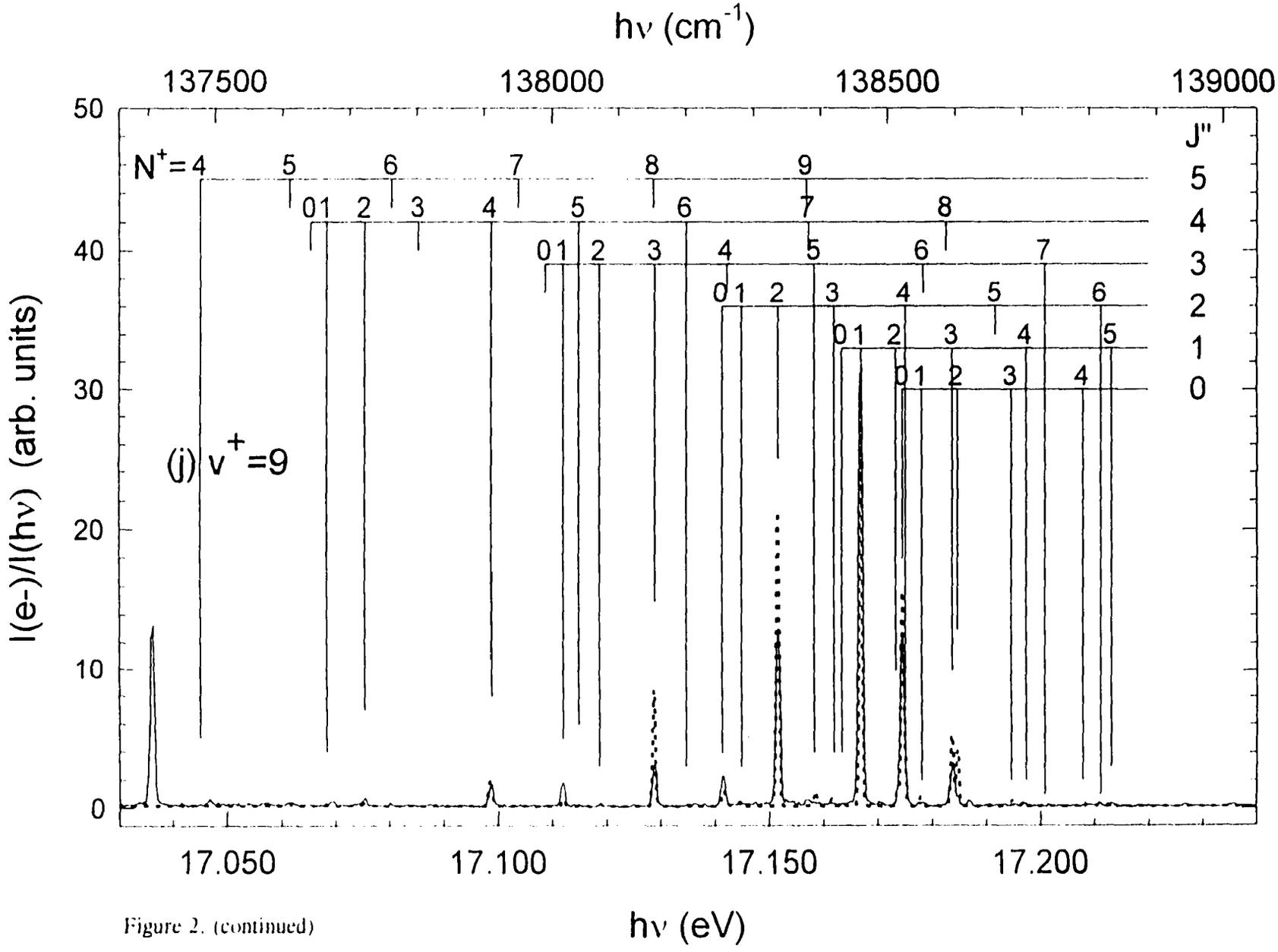

Figure 2. (continued)

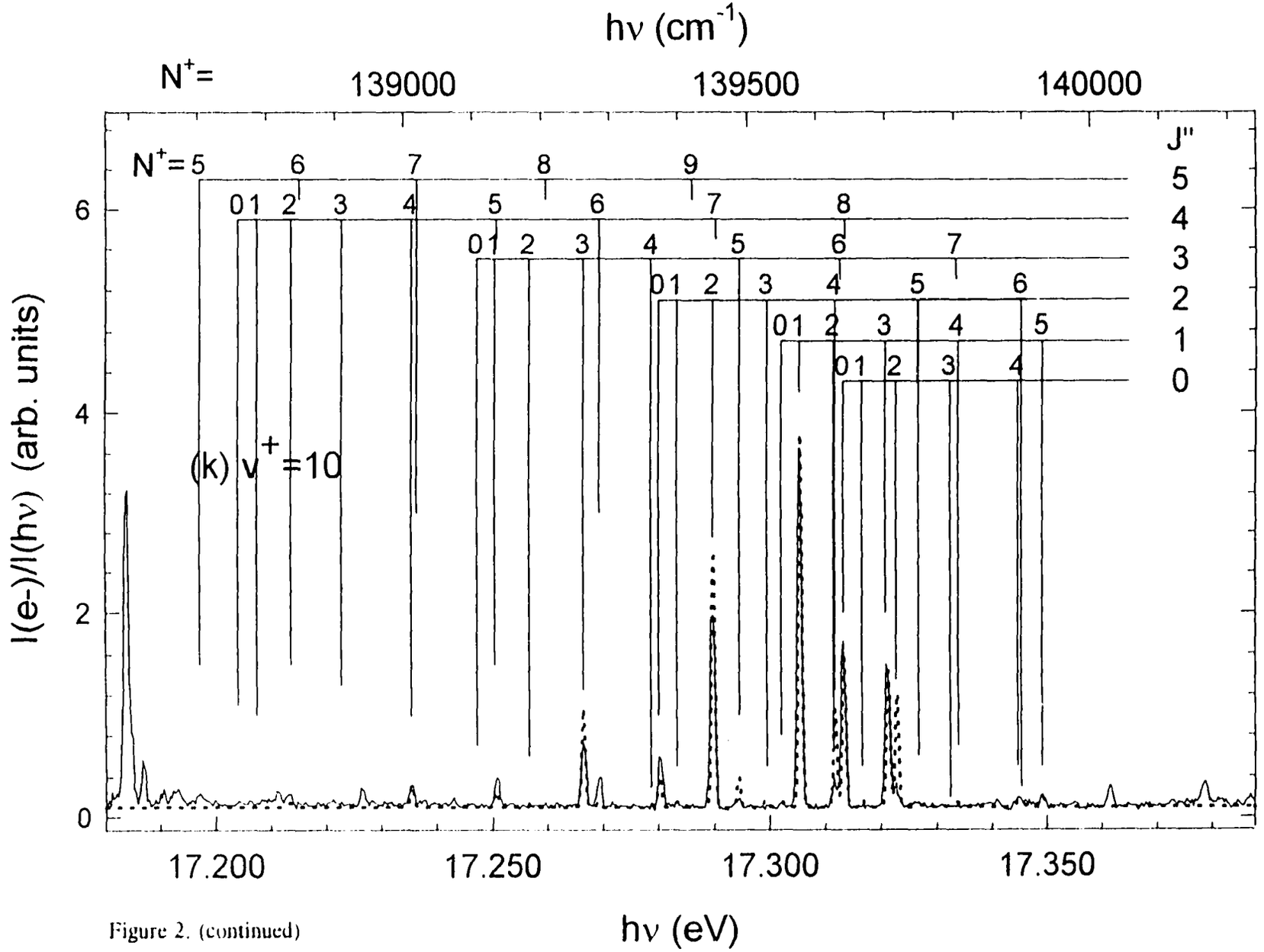

Figure 2. (continued)

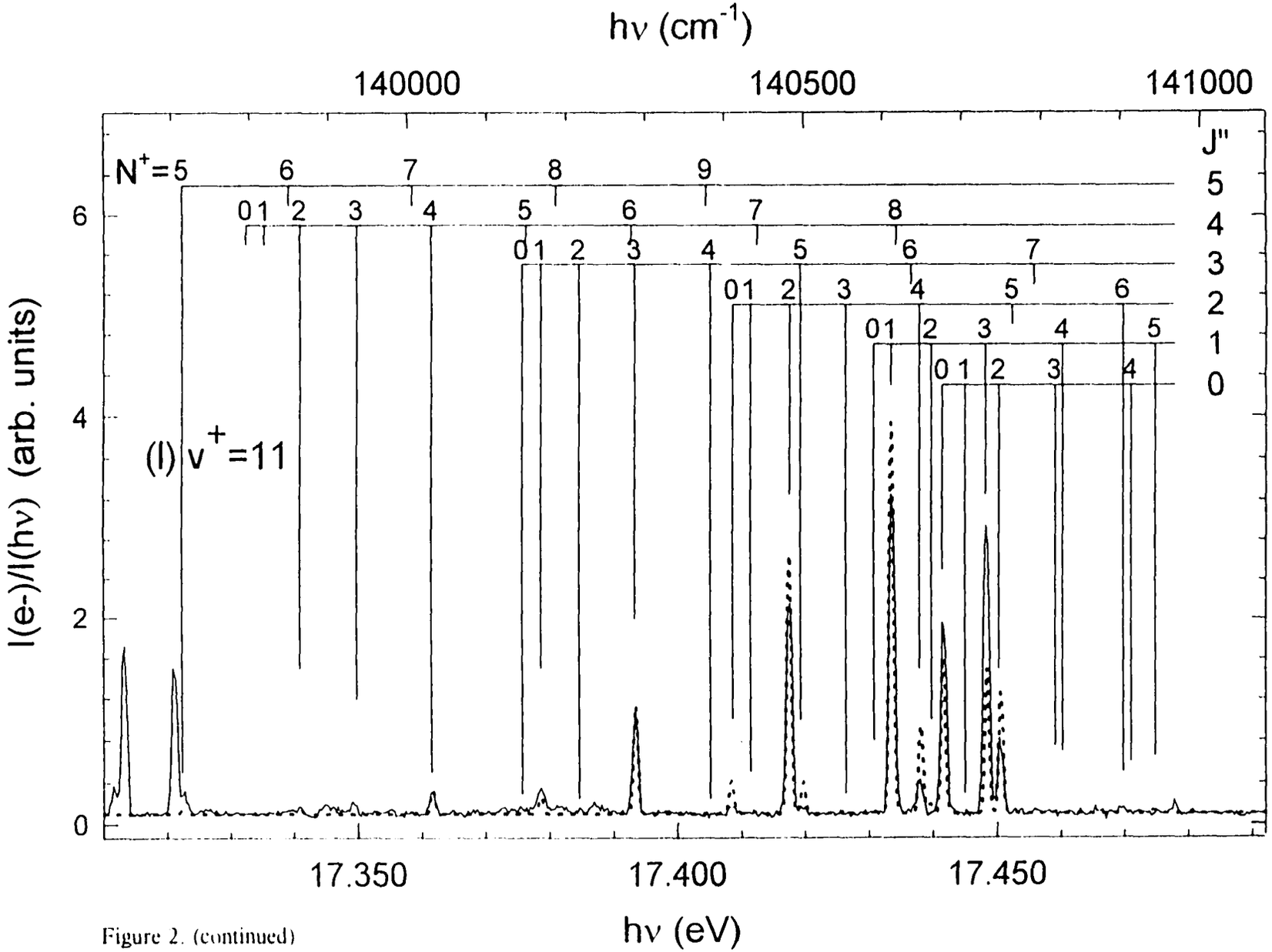

Figure 2. (continued)

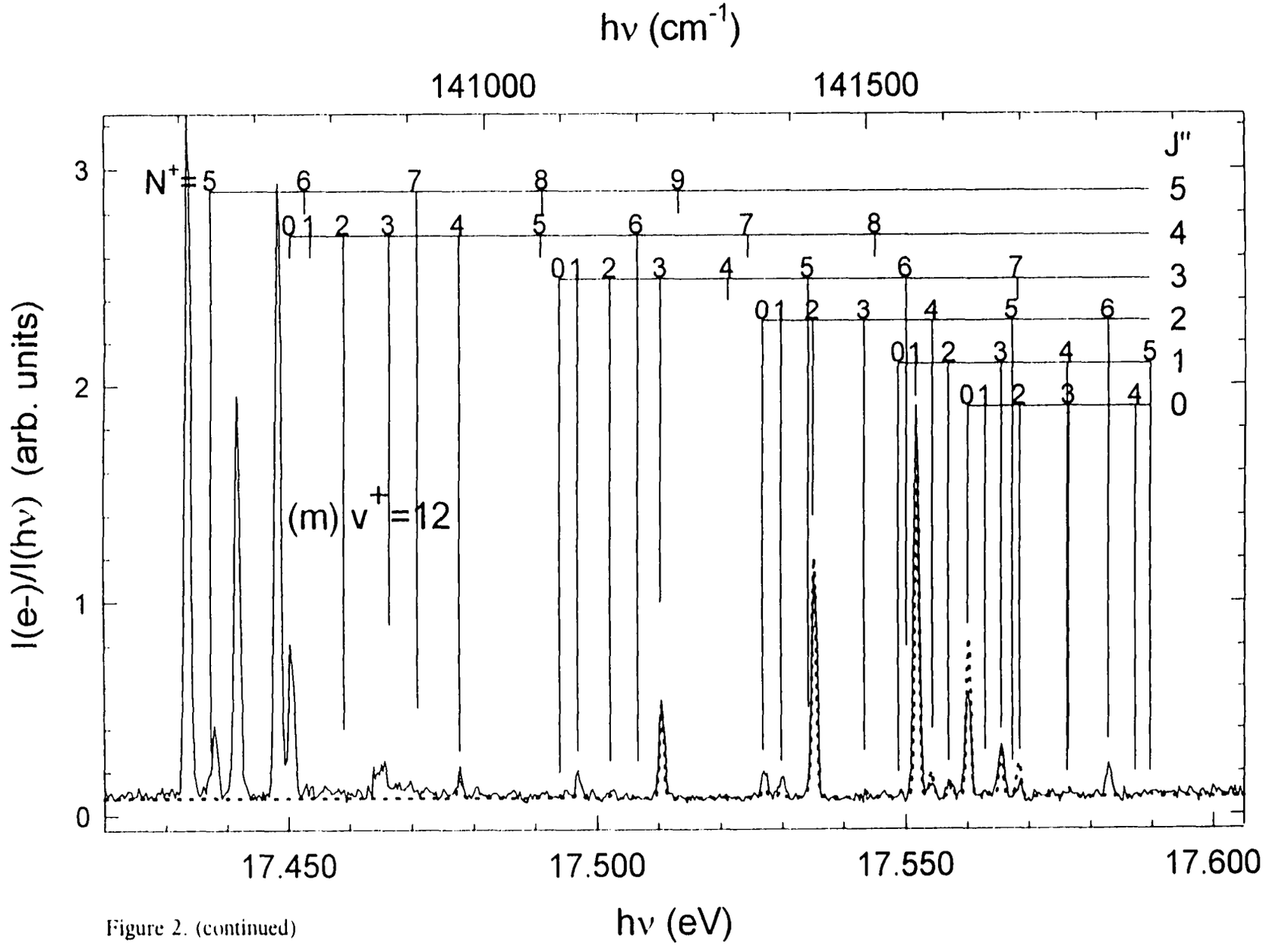

Figure 2. (continued)

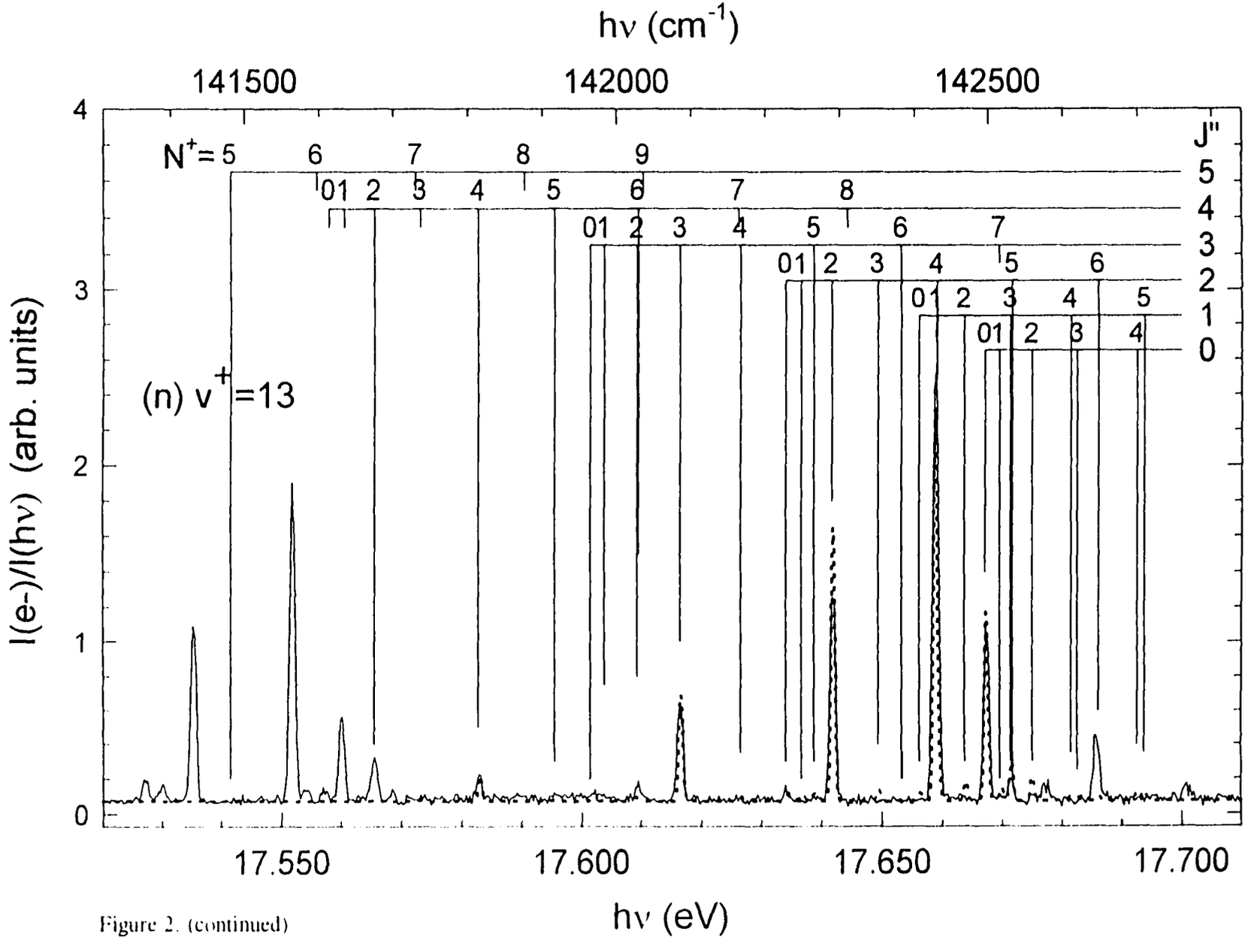

Figure 2. (continued)

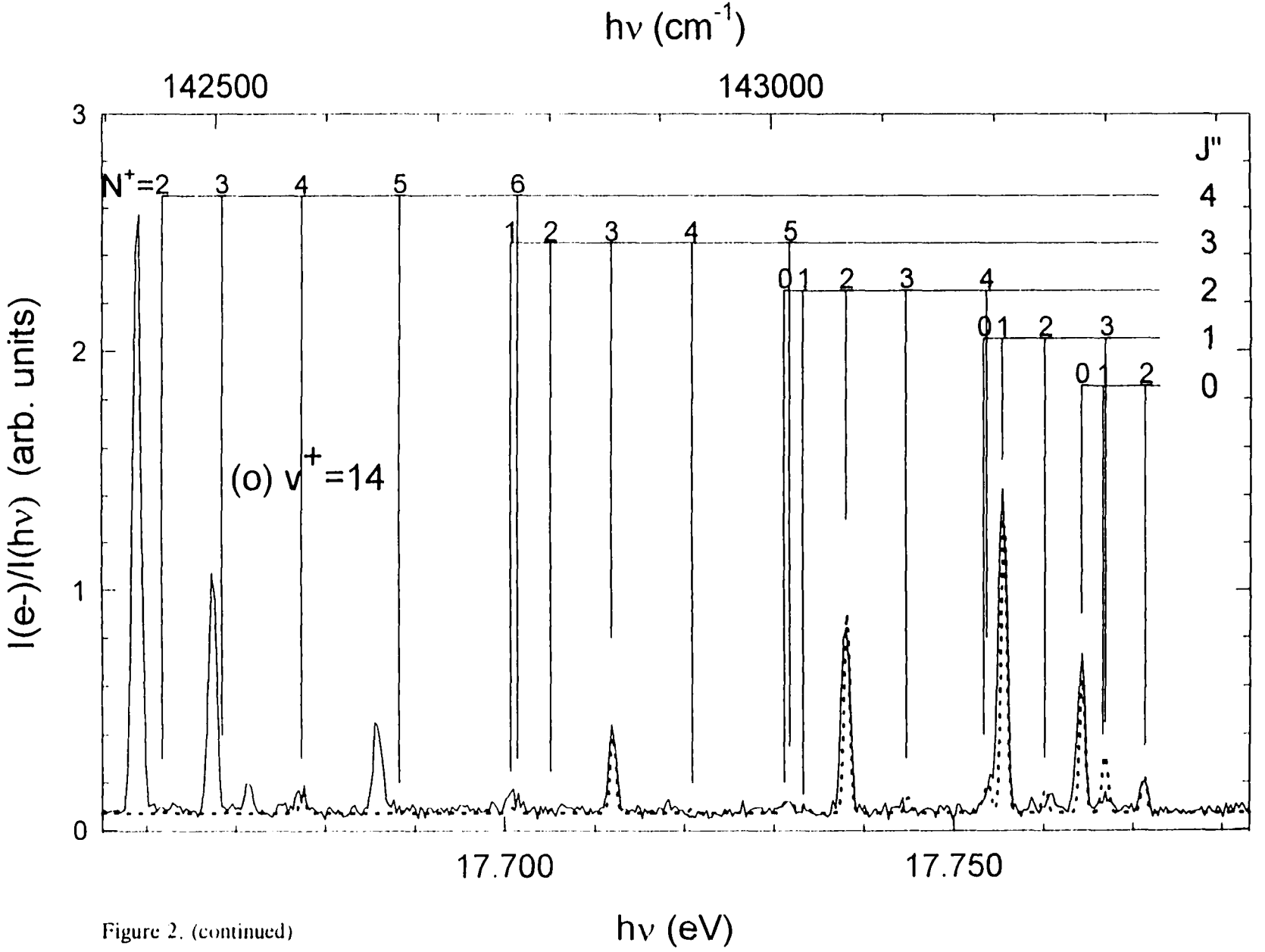

Figure 2. (continued)

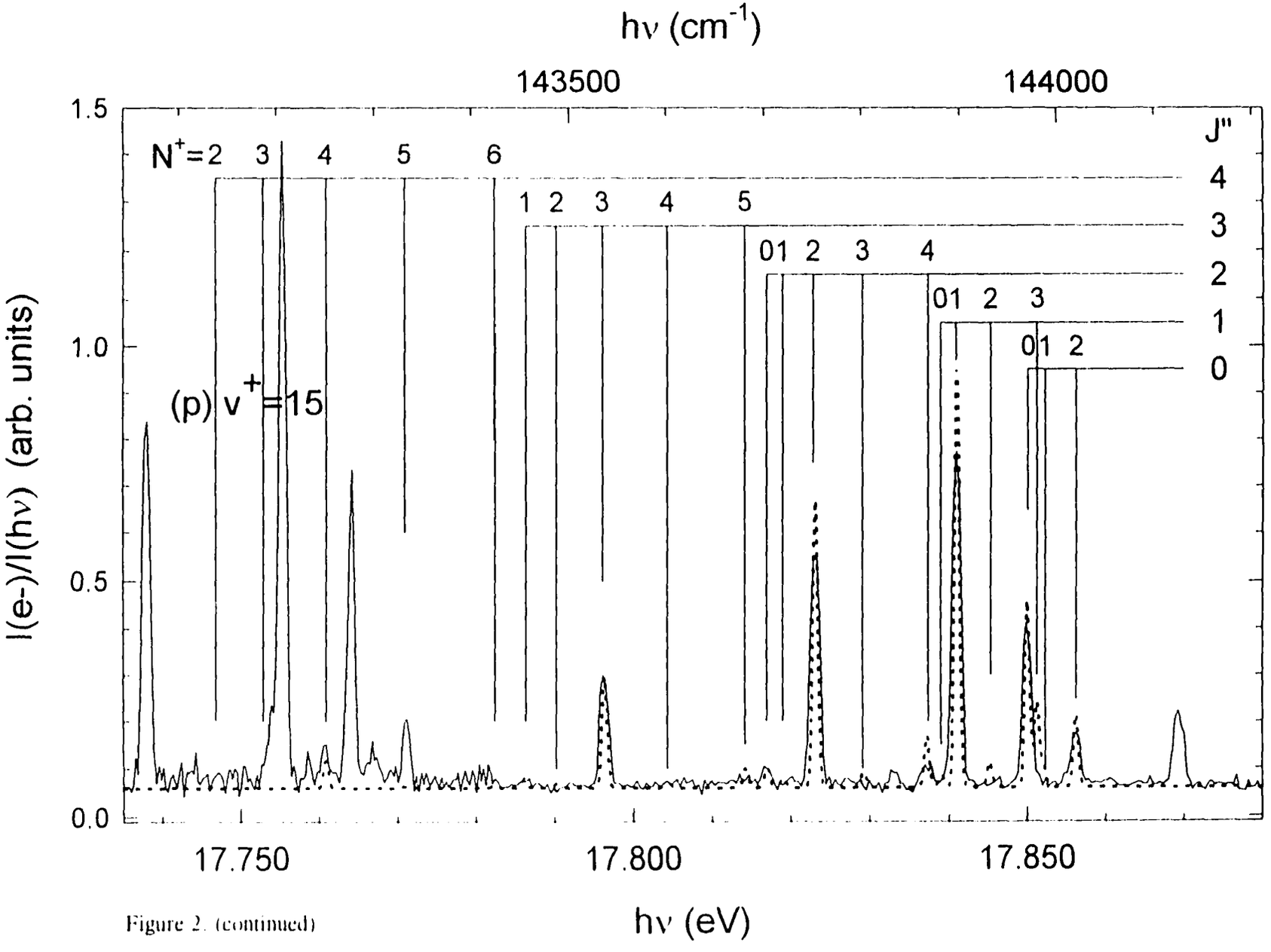

Figure 2. (continued)

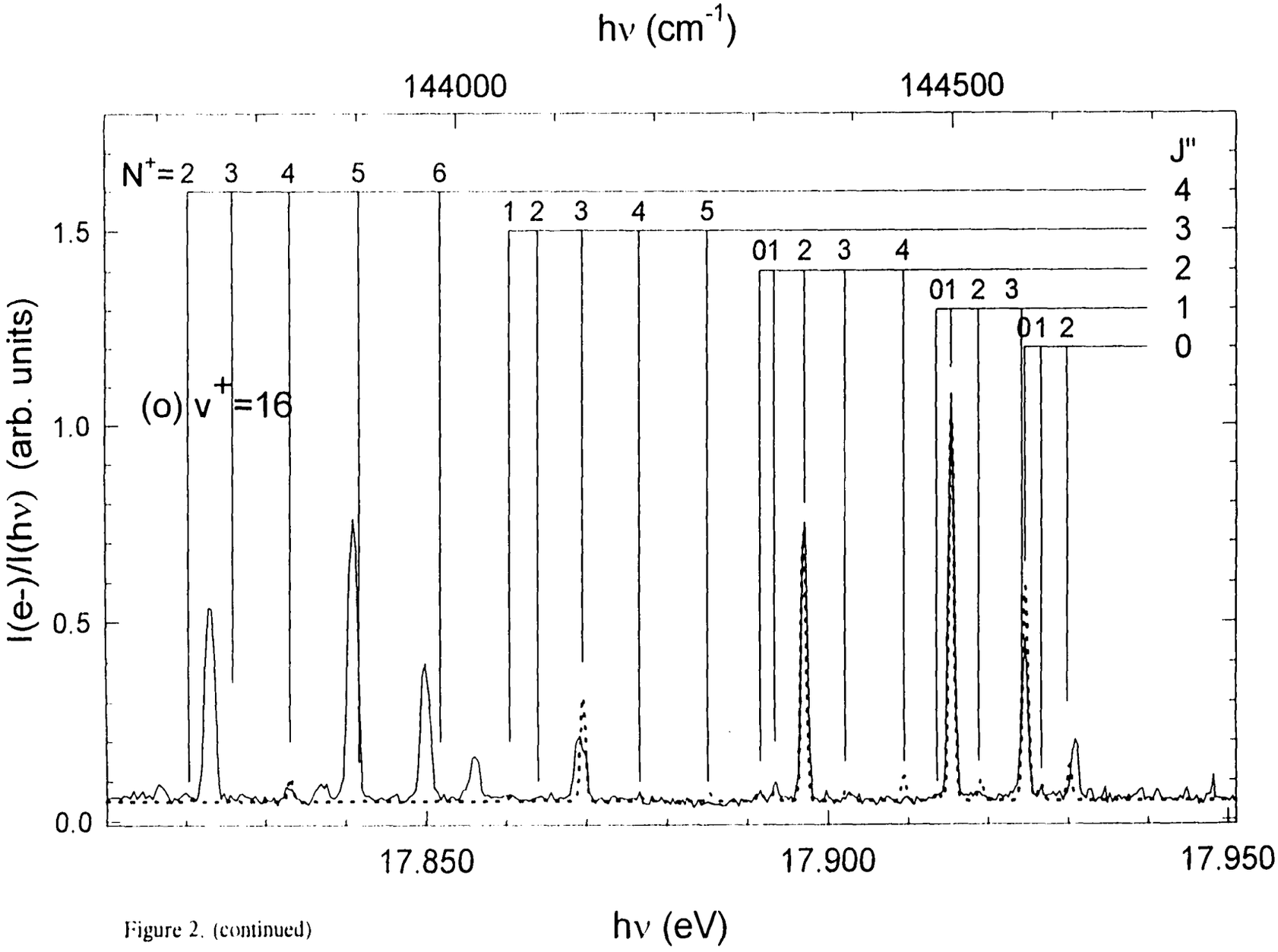

Figure 2. (continued)

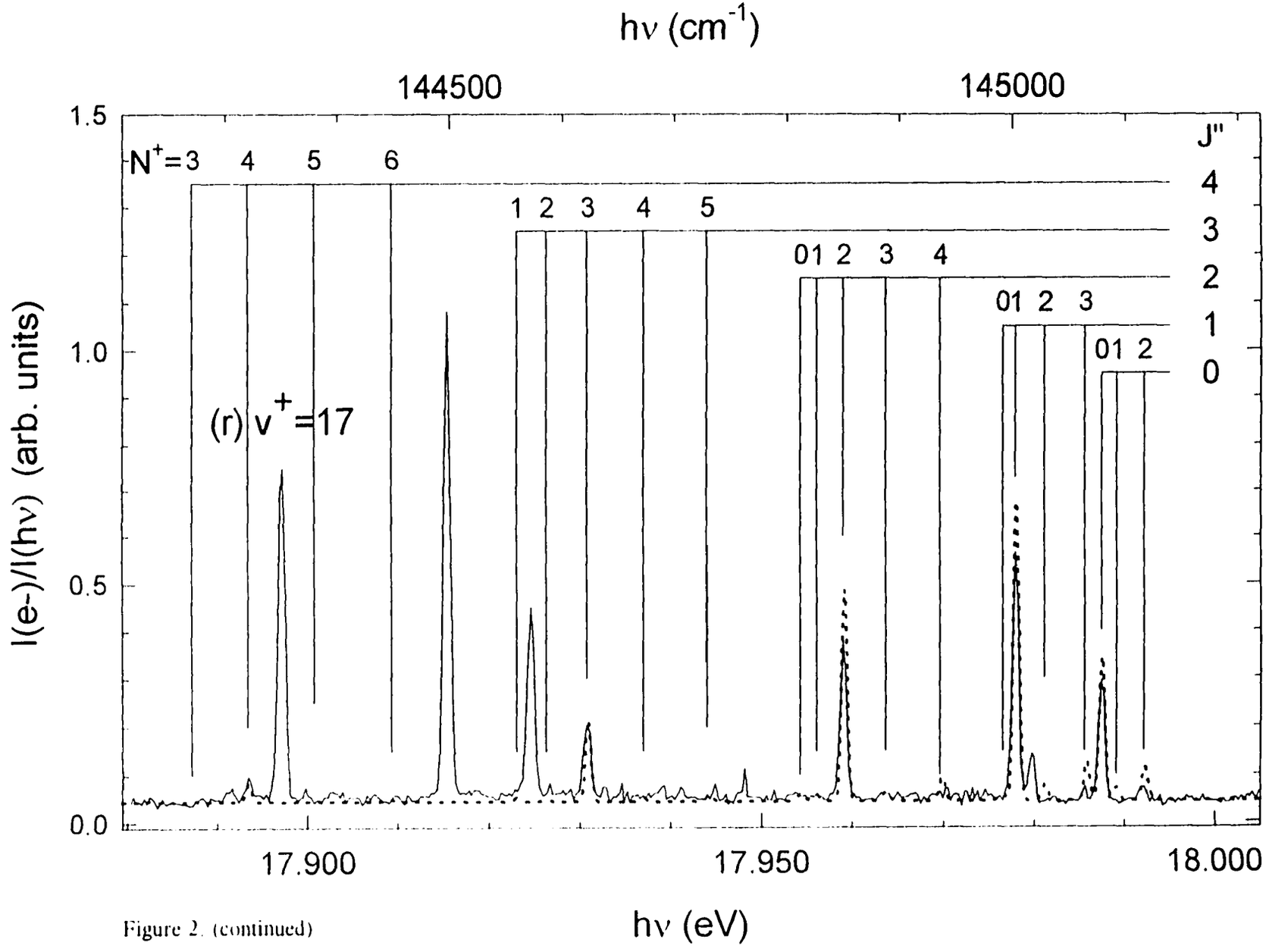

Figure 2. (continued)

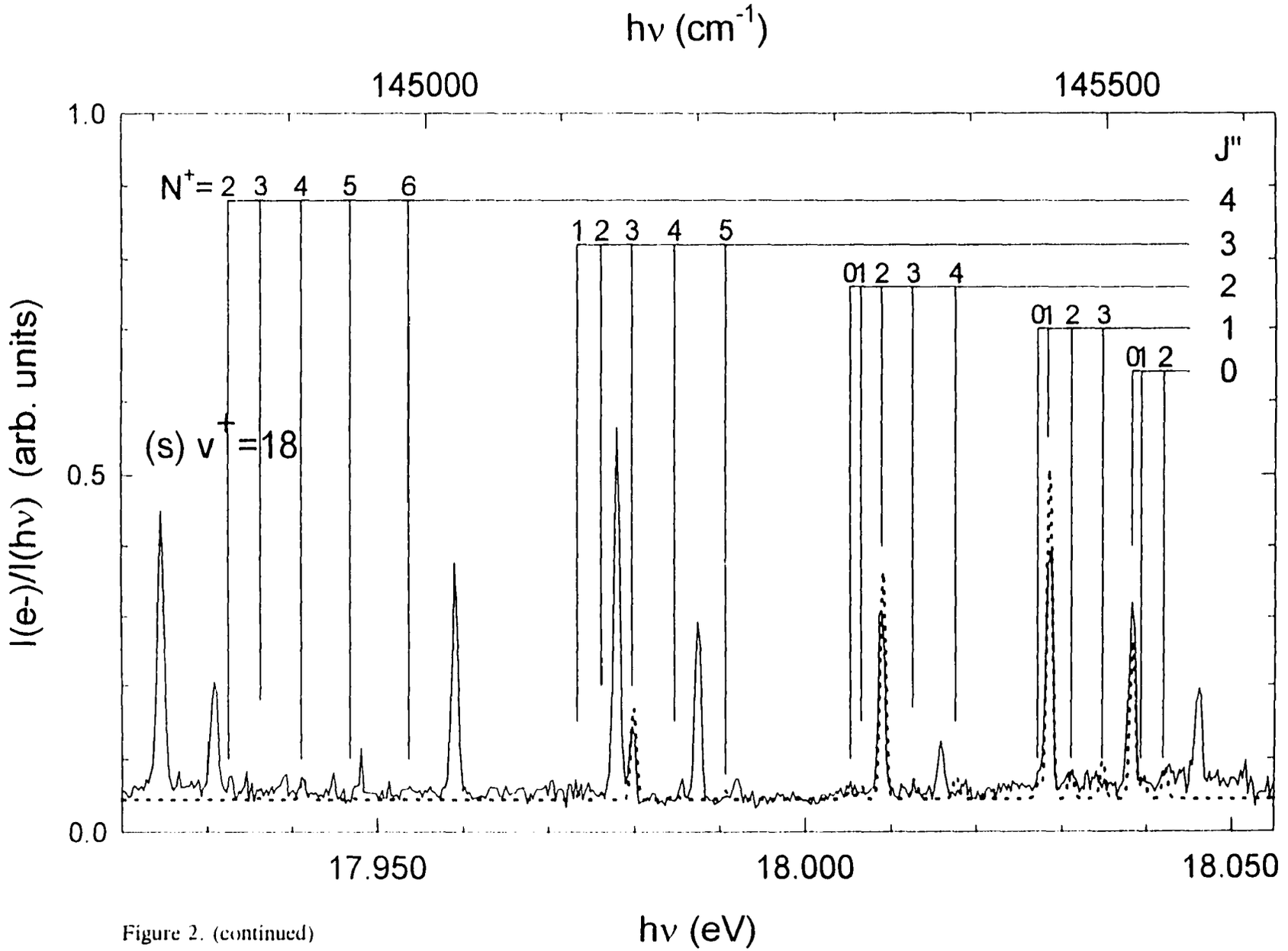

Figure 2. (continued)

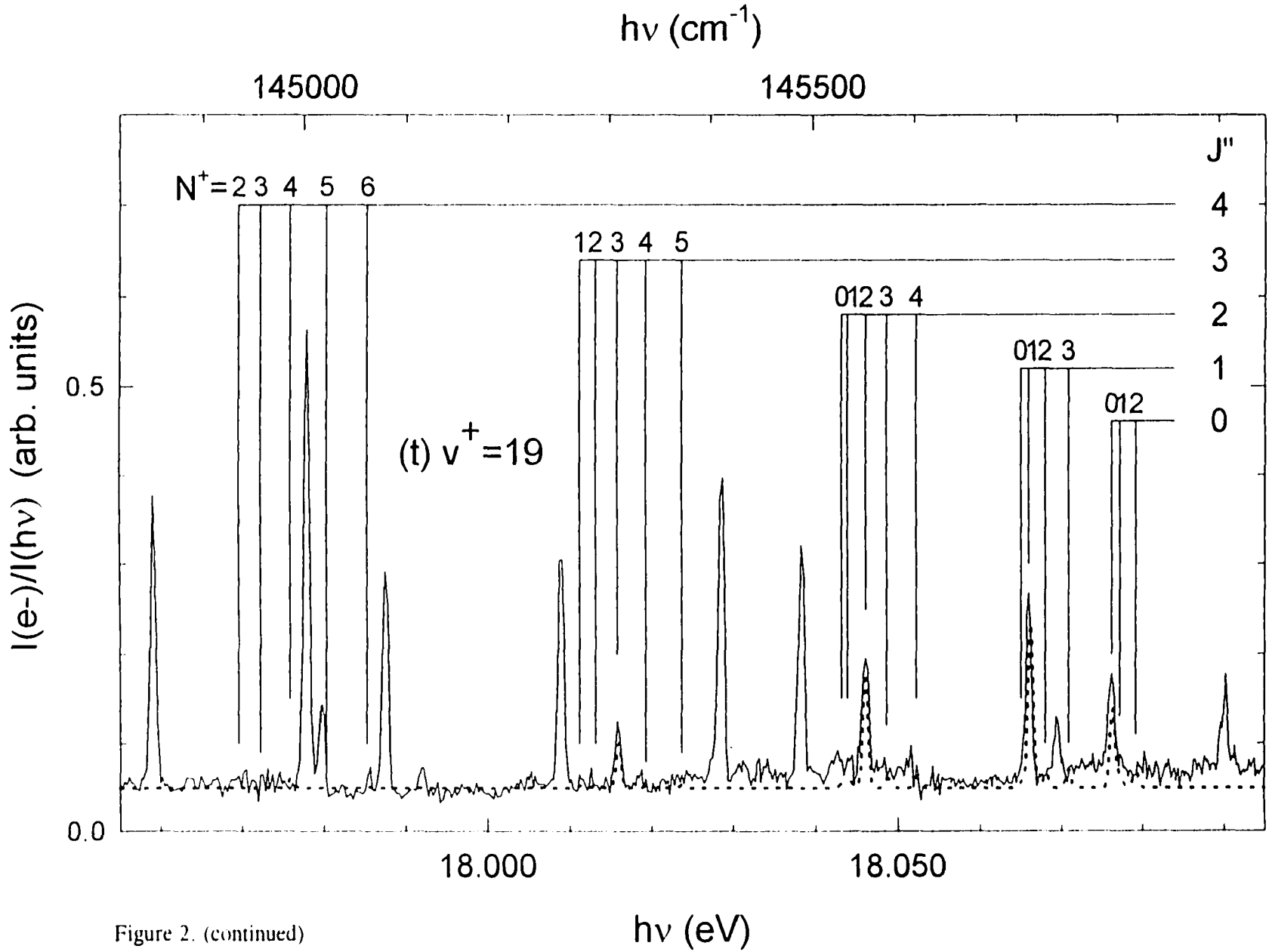

Figure 2. (continued)

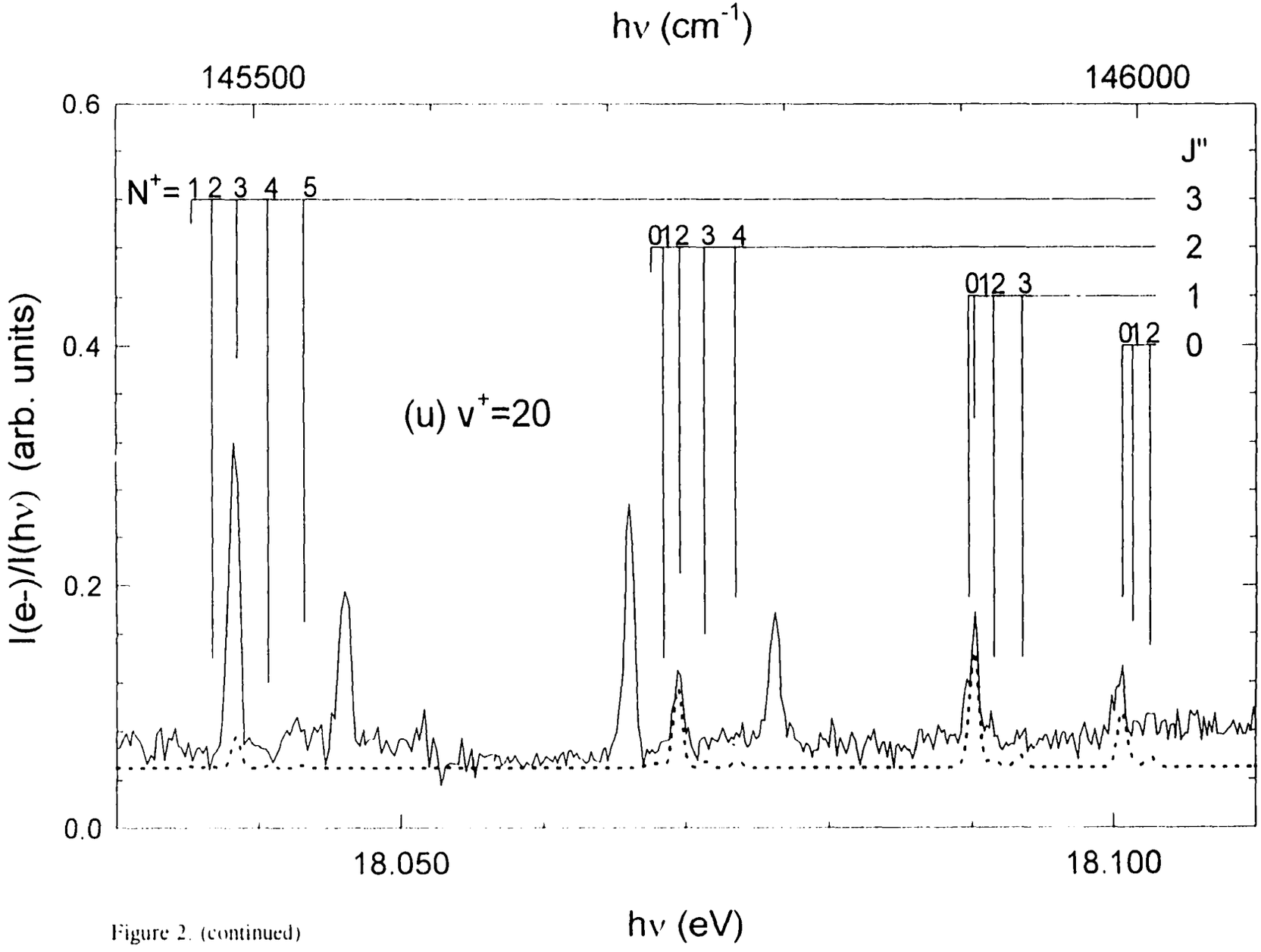

Figure 2. (continued)

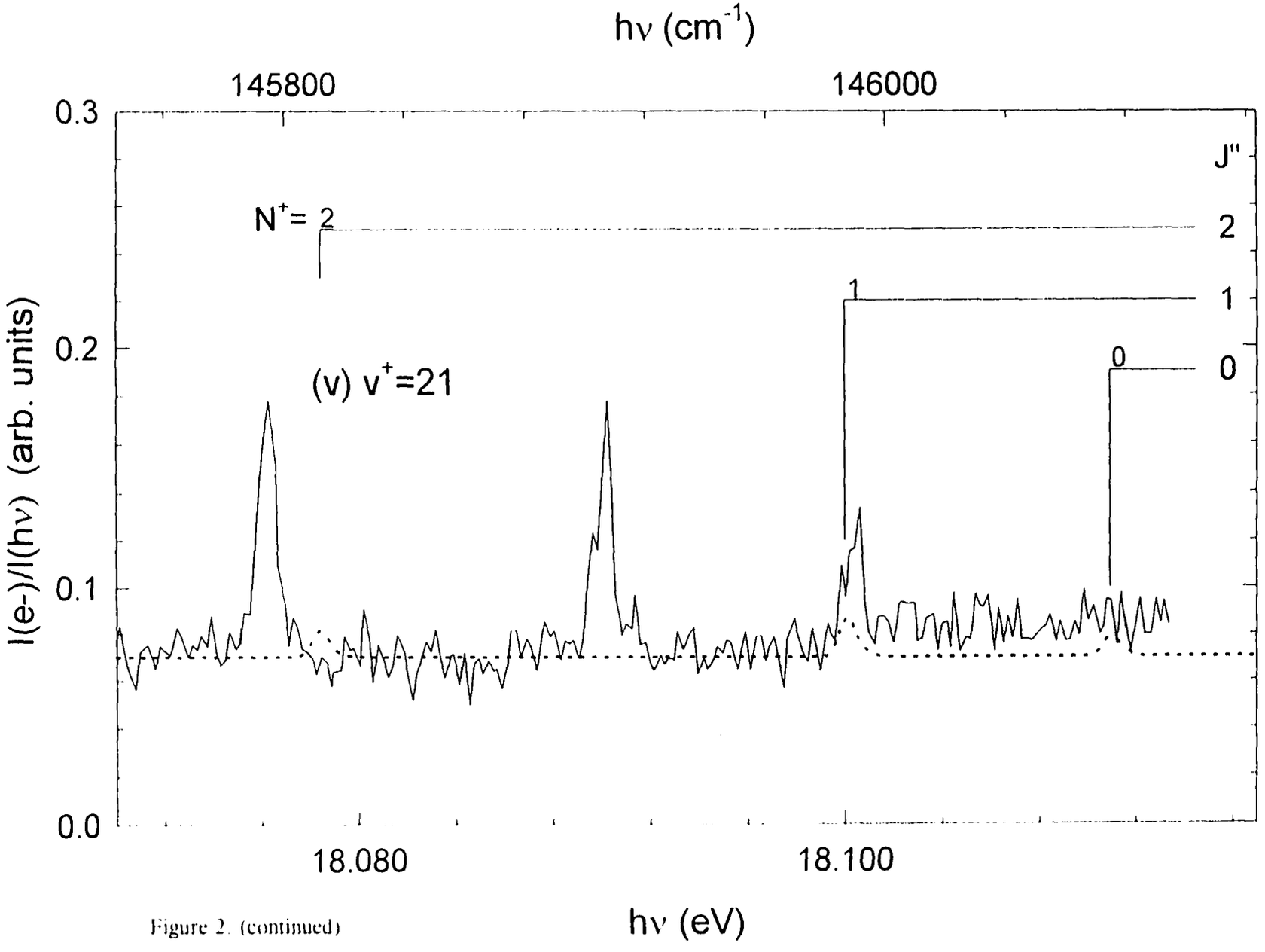

Figure 2. (continued)

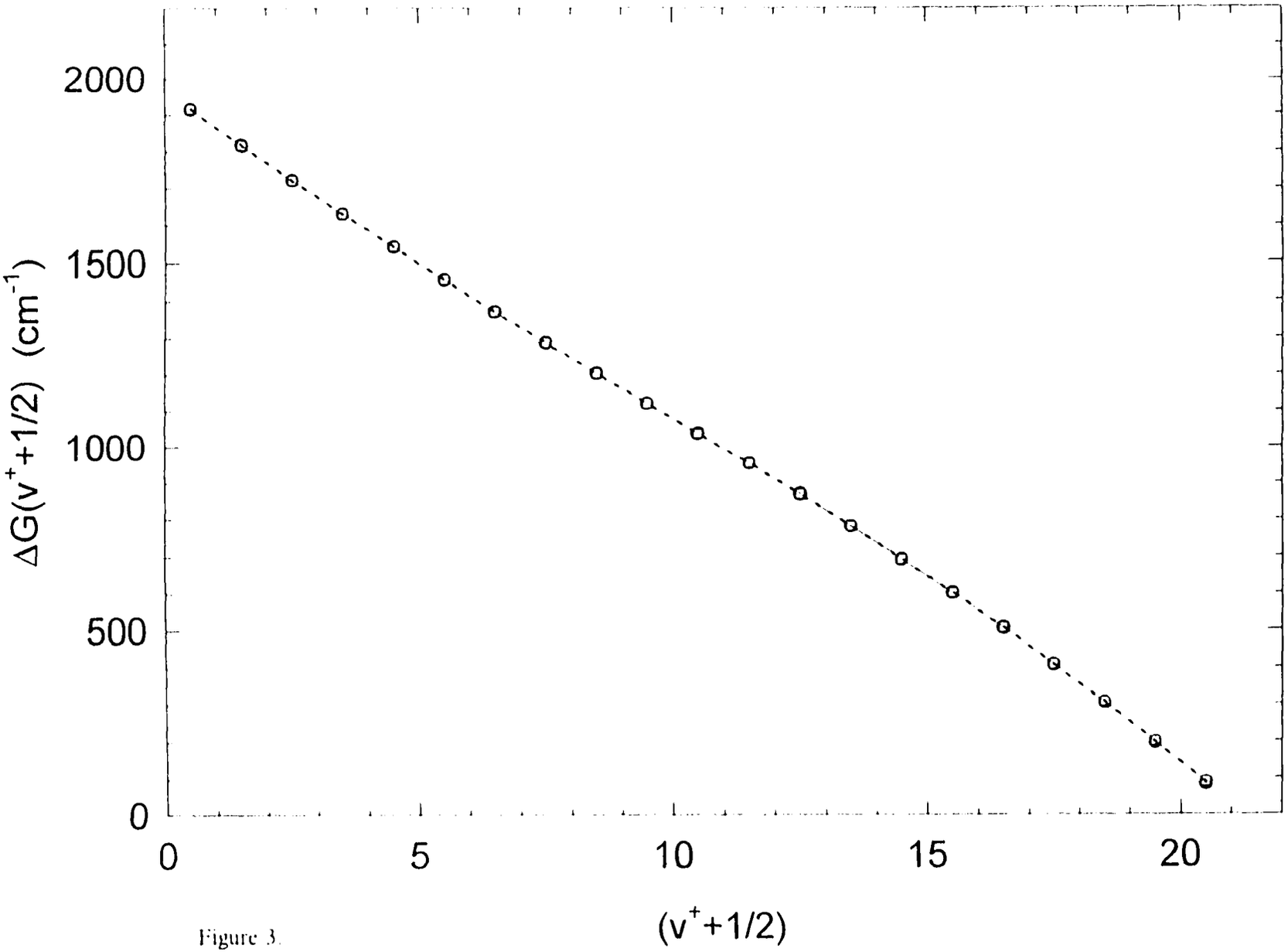

Figure 3.

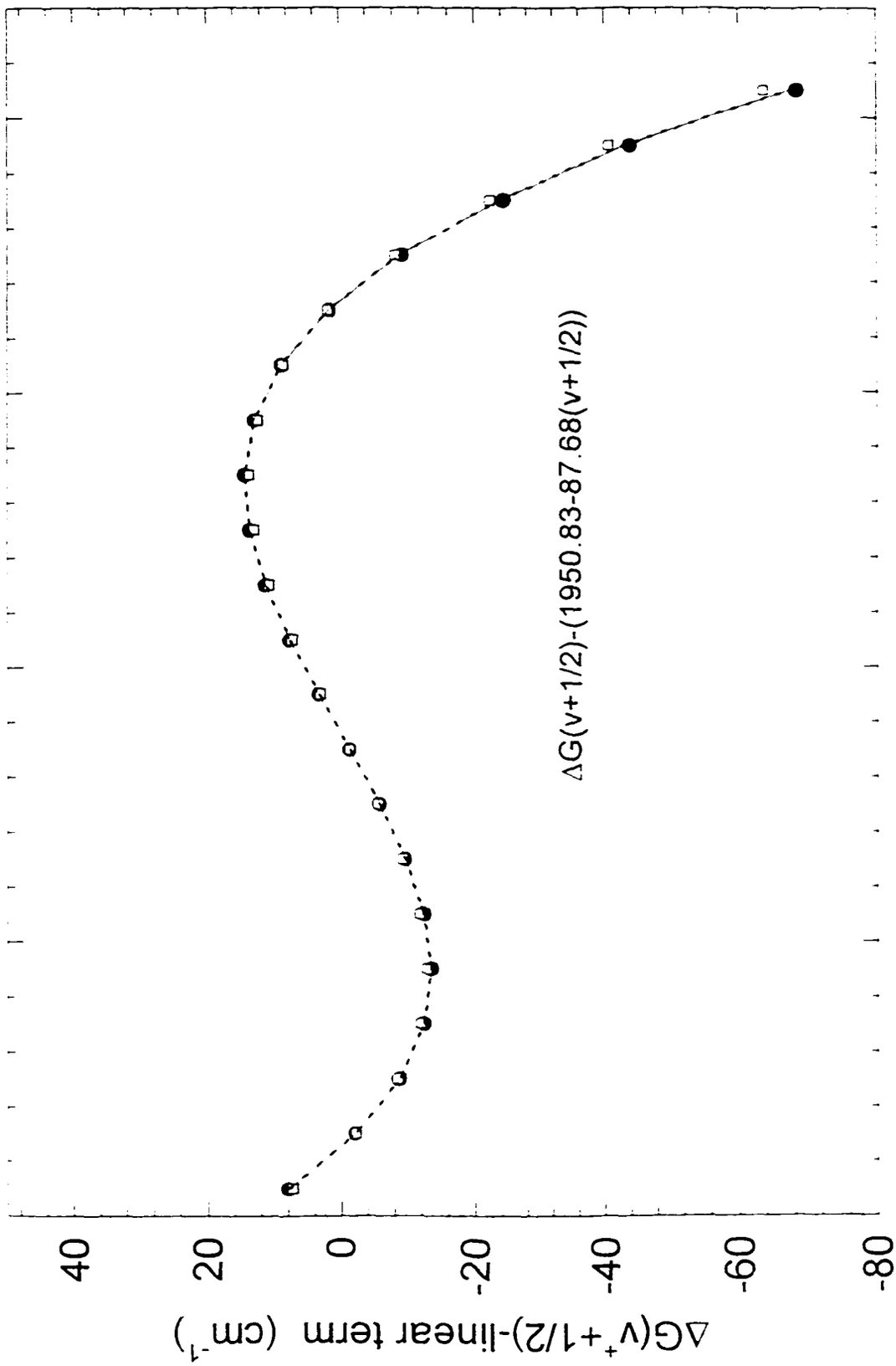
ΔG(v+1/2)-(1950.83-87.68(v+1/2))
ΔG(v+1/2)-linear term (cm-1)
v+1/2
40
20
0
-20
-40
-60
-80
0
5
10
15
20

Figure 4.

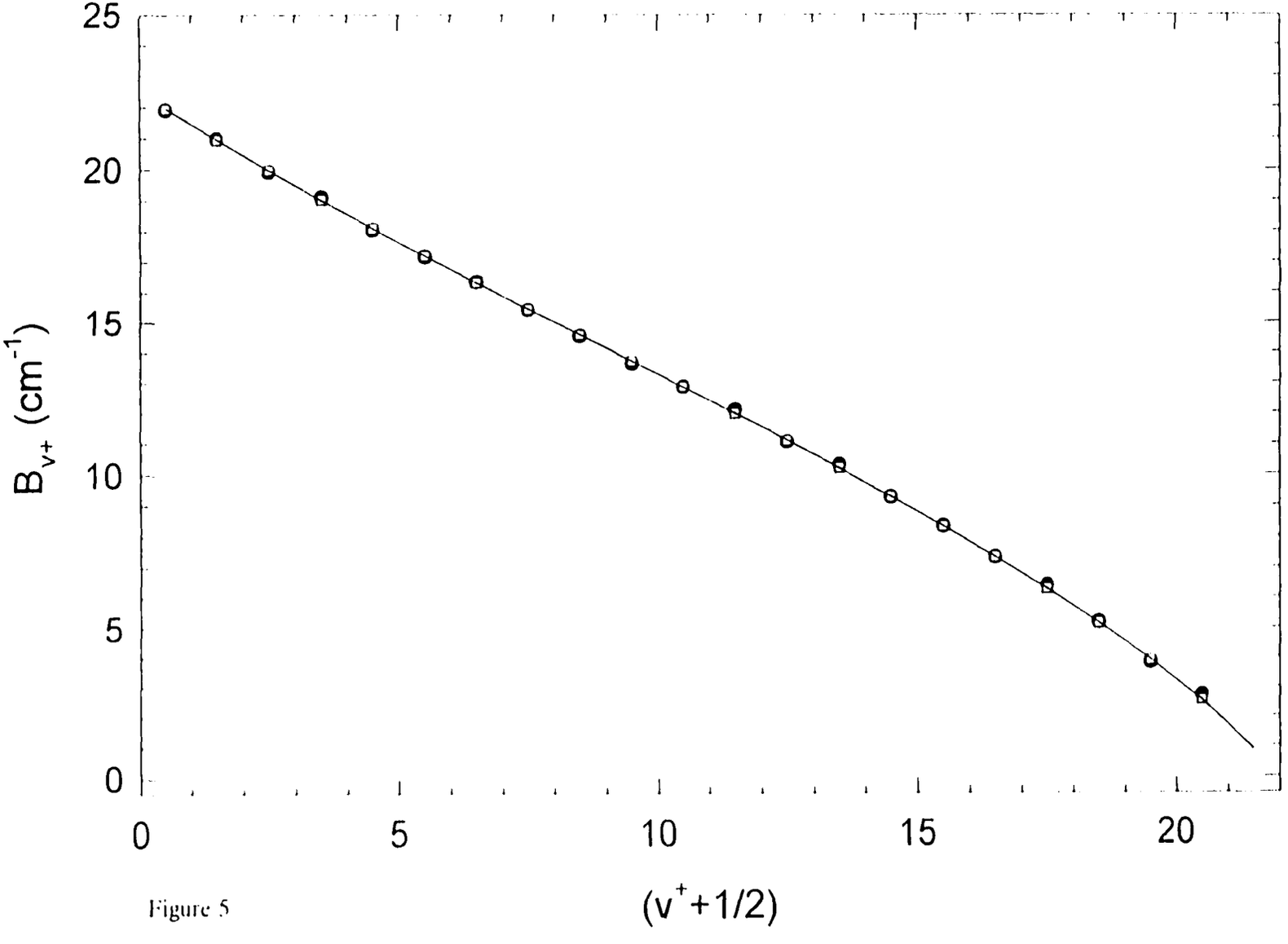

Figure 5

GENERAL CONCLUSIONS

We have examined the CID reaction of CH_3SH^+ + Ar in the E_{cm} range of 2-36 eV. The fragment ions observed were in general agreement with those observed in previous charge exchange and photoionization studies. The most interesting observation of this CID study was that CH_3^+ + SH was found to be the dominant product channel, which is contrary to the QET prediction and results of previous charge exchange and photoionization measurements. Stemming from the fact that the dissociation energy for the CH_3^+-SH bond is greater than that of the H-CH_2SH^+ bond, this observation clearly indicates non-statistical behavior in the CID of $CH_3SH^+(1^2A'')$. In effect, this system is an example of bond selective dissociation via collisional activation.

A high resolution PFI-PE spectrum for OCS in the energy range of 11.09-11.87 eV was obtained. In addition to strong photoelectron bands assigned to $(v_1^+, 0, v_3^+)\ ^2\Pi_{3/2}$ and $(v_1^+, 0, v_3^+)\ ^2\Pi_{1/2}$ for $OCS^+(X^2\Pi)$, weaker Renner-Teller structures were observed for the first time. Accurate theoretical predictions for the Renner-Teller levels of the $OCS^+(X^2\Pi)$ state were also obtained. The observed transitions in the PFI-PE spectrum were assigned satisfactorily by using the calculated energy positions of the vibronic levels.

In addition, the rotationally resolved PFI-PE spectra of $H_2^+(X^2\Sigma_g^+, v^+=0\text{-}18)$ and $HD^+(X^2\Sigma^+, v^+=0\text{-}21)$ were obtained. The analysis of which provided the rovibronic energies, the vibrational constants (ω_e, $\omega_e x_e$, $\omega_e y_e$, and $\omega_e z_e$), the rotational constants (B_v, D_v, B_e, and α_e), the internuclear separation (r_e), and the dissociation energy, (D_0). The simulated photoelectron bands based on the BOS model are in good agreement with the PFI-PE bands of higher v^+ states, indicating that the strong perturbation of the relative intensities for rotational transitions occurs mainly at lower v^+ (≤ 6) states.

IMAGE EVALUATION
TEST TARGET (QA-3)

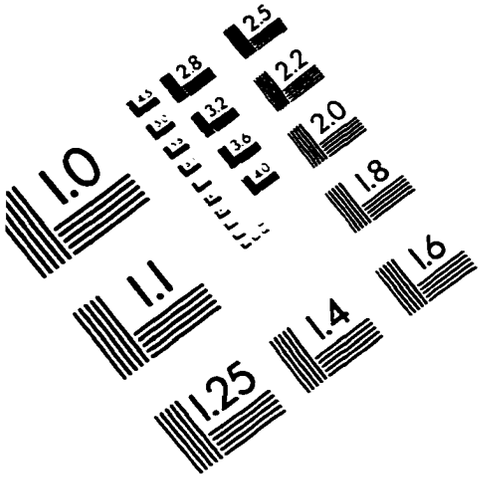

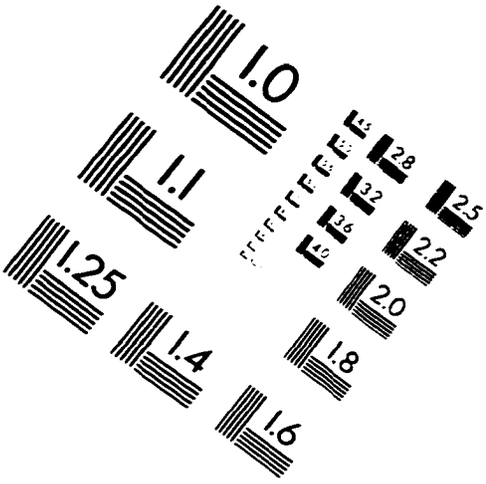

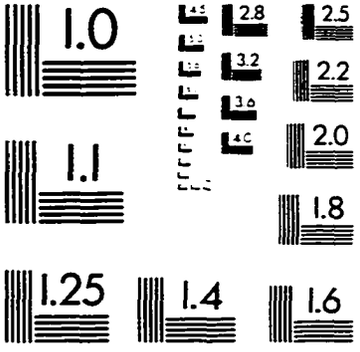

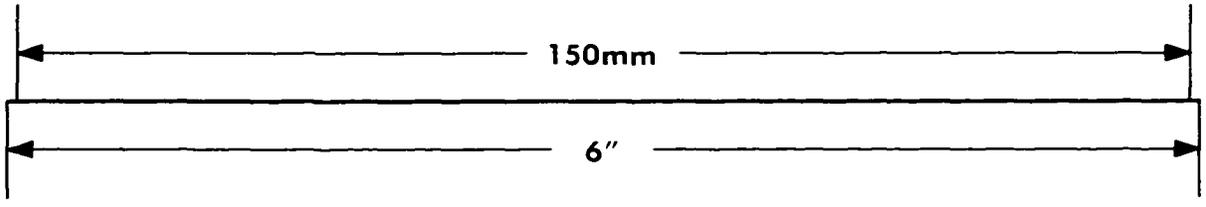

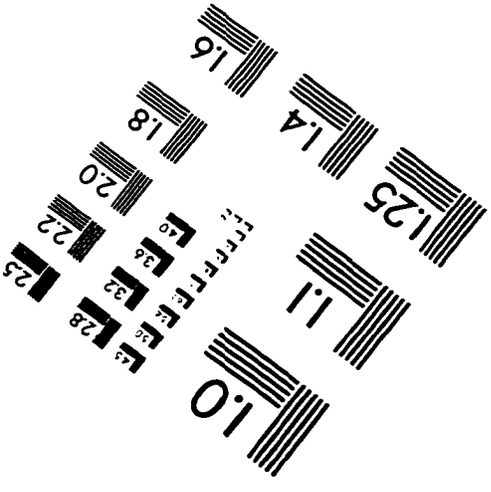

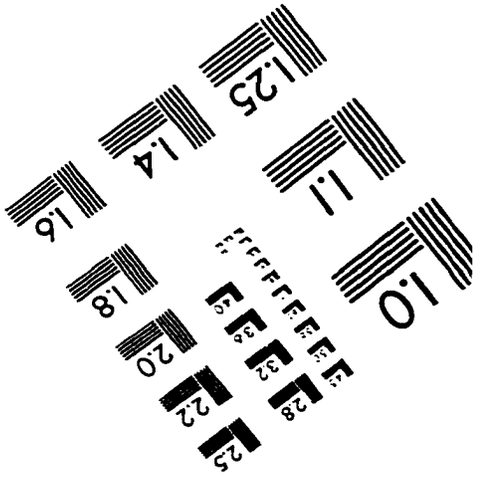

APPLIED IMAGE, Inc
1653 East Main Street
Rochester, NY 14609 USA
Phone: 716/482-0300
Fax: 716/288-5989